GDSA Repository Systems Analysis Investigations in FY 2022

Spent Fuel and Waste Disposition

Prepared for
US Department of Energy
Spent Fuel and Waste Science and Technology

Tara LaForce, Eduardo Basurto, Kyung W. Chang, Mohamed Ebeida, William Eymold, Christopher Faucett, Richard Jayne, Nicholas Kucinski, Rosie Leone, Paul Mariner, Frank V. Perry*
** ORNL*

Sept 2, 2022
M2SF-22SN010304102
SAND2022-12771 R

Sandia National Laboratories

Sandia National Laboratories is a multi-mission laboratory managed and operated by National Technology & Engineering Solutions of Sandia, LLC., a wholly owned subsidiary of Honeywell International, Inc., for the U.S. Department of Energy's National Nuclear Security Administration under contract DE-NA0003525.

APPENDIX E

NFCSC DOCUMENT COVER SHEET[1]

Name/Title: GDSA Repository Systems Analysis Investigations in FY2022

Deliverable/Milestone/Revision No.: M2SF-22SN010304102

Work Package Title and Number: GDSA-Repository Systems Analysis SNL / SF-22SN01030410

Work Package WBS Number: 1.08.01.03.04

Responsible Work Package Manager: Tara LaForce (Name/Signature)

Date Submitted: 09/02/2022

Quality Rigor Level for Deliverable/Milestone[2]	☐ QRL-1 ☐ Nuclear Data	☐ QRL-2	☒ QRL-3	☐ QRL-4 Lab QA Program[3]

This deliverable was prepared in accordance with Sandia National Laboratories
(Participant/National Laboratory Name)

QA program which meets the requirements of

☒ DOE Order 414.1 ☐ NQA-1 ☒ Other

This Deliverable was subjected to:

☒ Technical Review ☐ Peer Review

Technical Review (TR)	**Peer Review (PR)**
Review Documentation Provided	**Review Documentation Provided**
☐ Signed TR Report or,	☐ Signed PR Report or,
☐ Signed TR Concurrence Sheet or,	☐ Signed PR Concurrence Sheet
or,	
☒ Signature of TR Reviewer(s) below	☐ Signature of PR Reviewer(s)
below	

Name and Signature of Reviewers

Michael Nole Michael Nole	Paul Mariner Paul Mariner
Sections 1-6, 8	Section 7

NOTE 1: *Appendix E should be filled out and submitted with the deliverable. Or, if the PICS:NE system permits, completely enter all applicable information in the PICS:NE Deliverable Form. The requirement is to ensure that all applicable information is entered either in the PICS:NE system or by using the NFCSC Document Cover Sheet.*

☐ *In some cases there may be a milestone where an item is being fabricated, maintenance is being performed on a facility, or a document is being issued through a formal document control process where it specifically calls out a formal review of the document. In these cases, documentation (e.g., inspection report, maintenance request, work planning package documentation or the documented review of the issued document through the document control process) of the completion of the activity, along with the Document Cover Sheet, is sufficient to demonstrate achieving the milestone.*

NOTE 2: *If QRL 1, 2, or 3 is not assigned, then the QRL 4 box must be checked, and the work is understood to be performed using laboratory QA requirements. This includes any deliverable developed in conformance with the respective National Laboratory / Participant, DOE or NNSA-approved QA Program.*

NOTE 3: *If the lab has an NQA-1 program and the work to be conducted requires an NQA-1 program, then the QRL-1 box must be checked in the work Package and on the Appendix E cover sheet and the work must be performed in accordance with the Lab's NQA-1 program. The QRL-4 box should not be checked.*

EXECUTIVE SUMMARY

The Spent Fuel and Waste Science and Technology (SFWST) Campaign of the U.S. Department of Energy Office of Nuclear Energy, Office of Spent Fuel and Waste Disposition (SFWD), has been conducting research and development on generic deep geologic disposal systems (i.e., geologic repositories). This report describes specific activities in the Fiscal Year (FY) 2022 associated with the Geologic Disposal Safety Assessment (GDSA) Repository Systems Analysis (RSA) work package within the SFWST Campaign. The overall objective of the GDSA RSA work package is to develop generic deep geologic repository concepts and system performance assessment (PA) models in several host-rock environments, and to simulate and analyze these generic repository concepts and models using the GDSA Framework toolkit, and other tools as needed.

A summary of the specific objectives in FY2022:

- Develop the technical bases for representing generic repository reference case concepts in GDSA Framework simulations for deep geologic disposal in any of four possible host-rock environments: argillite, crystalline, bedded salt, and unsaturated zone formations.
- Ensure that generic repository concepts include potential disposal of large, high-decay-heat waste packages.
- Incorporate relevant near field and far field processes as well as geologic/material properties and stratigraphic information developed in conjunction with geologic framework models (GFMs).
- Perform GDSA Framework PA simulations and, in collaboration with the GDSA Uncertainty and Sensitivity Analysis Methods work package, conduct the associated uncertainty and sensitivity analyses for generic repository reference case concepts containing high-decay-heat waste packages.
- Include, as needed, detailed coupled processes in the engineered barrier system (EBS; e.g., waste form and waste package degradation, EBS flow and transport, disturbed rock zone (DRZ) evolution) and natural system (e.g., near-field and far-field flow and transport, multi-phase flow).
- Reference case development, simulation, and analysis, as appropriate, for international collaborations, including for example, DECOVALEX, the Integration Group for the Safety Case (IGSC) sensitivity analysis task group, and the long-standing US-German collaboration on PA methodology applied to generic repositories in salt.

Section 1 of this report is a brief introduction. Section 2 discusses progress to date on the international Development of Coupled models and their Validation against Experiments (DECOVALEX) 2023 Task F performance assessment comparison, which is being led by the GDSA team on behalf of the US DOE's SFWST Campaign. Section 3 utilizes recently developed near-field modelling capability, investigating how the EBS and host rock influence each other when thermal dependence of rock properties is included in the simulation model. Section 4 develops a shallow-geosphere model for the crystalline environment. Section 5 discusses deterministic simulations of a PA-scale model for the unsaturated alluvium reference case under development. Section 6 compares the thermal output of the generic pressurized water reactor (PWR) assembly used in GDSA PA simulations with updated ORIGEN modelling for real and hypothetical high energy waste packages. Section 7 documents the continuing investigation into PFLOTRAN simulations on Voronoi meshes, demonstrating a simplified PA case including geological uncertainty in a shale GFM model. Finally, Section 8 summarizes the FY22 research and discusses potential future work for FY23 and beyond.

This page is intentionally left blank

ACKNOWLEDGEMENTS

This work was supported by the U.S. Department of Energy (DOE) Office of Nuclear Energy, through the Office of Spent Fuel and Waste Science and Technology (SFWST), within the Office of Spent Fuel and Waste Disposition (DOE NE-8).

Thanks go to our DOE customer for their support of this work. Thank you to David Sevougian (retired) for leading the Repository Systems Analysis team until 2020. Thank you to LianGe Zheng and Jonny Rutqvist of Lawrence Berkeley National Laboratory for input to the shale geomechanical analysis. Finally, thanks to our technical reviewers, Michael Nole and Paul Mariner, for comments and suggestions that improved the report.

This report incorporates principal contributions from the following coauthors:

Eduardo Basurto (Section 5, Section 7.2.6)

Kyung Chang (Section 3)

Mohamed Ebeida (Section 7.1)

William Eymold (Section 7.2)

Christopher Faucett (Section 6.1)

Nicholas Kucinski (Section 6.2)

Tara LaForce (Sections 1, 2, 6, 7, 8)

Rosie Leone (Section 2.1)

Richard Jayne (Section 2.2)

Paul Mariner (Section 2)

Frank Perry (Section 4)

This page is intentionally left blank

CONTENTS

EXECUTIVE SUMMARY v

ACKNOWLEDGEMENTS vii

NOMENCLATURE xix

1. INTRODUCTION 21

2. DECOVALEX REFERENCE CASES 25
    2.1 Crystalline Reference Case (Task F1) 25
        2.1.1 Geological Setting 25
        2.1.2 Emplacement Concept and Repository Layout 26
        2.1.3 Host Rock (Natural Barrier System) 27
        2.1.4 Conservative Tracer Transport 28
        2.1.5 DFN Generation 29
        2.1.6 Upscaling 30
        2.1.7 Repository Discretization 31
        2.1.8 Output Metrics 33
        2.1.9 Preliminary Results 34
    2.2 Salt Reference Case (Task F2) 42
        2.2.1 Geologic Setting 43
        2.2.2 Natural Barrier System 44
        2.2.3 Geochemical Environment 44
        2.2.4 Engineered Barrier System 44
        2.2.5 Emplacement Drifts 45
        2.2.6 Non-waste Area Seals and Backfill 45
        2.2.7 Shaft Seal 46
        2.2.8 Outputs for Comparison 47
        2.2.9 Simulation Model Construction 47
        2.2.10 Preliminary Results 51
        2.2.11 Look Ahead 55

3. SMALL-SCALE REFERENCE CASE STUDIES 57
    3.1 Model Setting 57
        3.1.1 Model Domain 57
        3.1.2 Heat Source 60
        3.1.3 Stress-dependent DRZ Permeability 61
        3.1.4 Saturation-temperature-dependent Thermal Conductivity 62
    3.2 Results 63
        3.2.1 Hydro-thermal Impacts on Tracer Transport 63
        3.2.2 Impact of Numerical Domain Scale 66
    3.3 Findings & Future Work 69

4. Geology and Hydrology of Glacial Deposits to Support Biosphere Modeling in a Crystalline Rock Environment 71
    4.1 Description of the Example Watershed 71
    4.2 Geology and Hydrology 72

4.2.1 Aquifers 74
4.2.2 Water Well Characteristics 74
4.2.3 Precipitation and Recharge 75
4.2.4 Groundwater Contribution to Streams 76
4.3 Agricultural Framework 79
4.3.1 Water Sources 79
4.3.2 Water Requirements 80
4.4 Consideration of Future Climate and Landscape Evolution Scenarios 81
4.4.1 Periglacial Climate 81
4.4.2 Landscape Evolution 81
4.5 Conclusions 82

5. UNSATURATED ALLUVIUM 83
5.1 Model Setting 83
5.2 Simulation 85
5.2.1 Newton Trust-Region Dogleg Cauchy Nonlinear Solver Update 87
5.2.2 Nuclear Waste Transport Mode 87
5.2.3 Initial Conditions 87
5.2.4 Boundary Conditions 88
5.2.5 Material Properties 88
5.3 Simulation Results and Discussion 88
5.4 Conclusions and Considerations for Future Work 93

6. NEW WASTE FORM SOURCE TERMS 95
6.1 SNL ORIGEN modelling of Spent Fuel Cask 95
6.1.1 ORIGEN modelling results 99
6.1.2 Comparison with existing PWR model 102
6.2 ORNL ORIGEN Modelling SNF Decay 103
6.2.1 Comparison with existing PWR decay heat 103
6.3 Conclusions and Future Work 104

7. VOROCRUST MESHING AND SIMULATION 107
7.1 Improvements to VoroCrust 107
7.2 Shale Performance Assessment 109
7.2.1 Simplifications 109
7.2.2 Geosphere/Natural Barriers 111
7.2.2.1 Shale GFM 112
7.2.2.2 Uncertainty in Stratigraphy of a GFM 112
7.2.3 Multiple PA-Scale Geological Models from the GFM 113
7.2.3.1 Searching for suitable PA-scale model regions 113
7.2.4 Deterministic Case 113
7.2.4.1 Partially automated creation of a model realization 113
7.2.4.2 Deterministic Model Meshing Results 117
7.2.4.3 Deterministic Model Numerical Implementation 120
7.2.4.4 Monitoring Tracer Transport 121

7.2.5 Stochastic Cases 122
7.2.6 Simulation Results 123
7.2.6.1 Deterministic Results 123
7.2.6.2 Probabilistic Results 124
7.2.6.2.1 Simulation Statistics 125
7.2.6.2.2 Tracer Results 125
7.2.6.3 Comparison with Previous Shale PA case 130
7.3 Conclusions and Future Work 132

8. SUMMARY AND CONCLUSIONS 134
8.1 Future Work 135

9. References 136

Appendix A 144

DPC Calculations from ORNL 144

This page is intentionally left blank.

LIST OF FIGURES

Figure 1-1. Information flow and the role of performance assessment for RD&D prioritization during a single stage of repository development. (Taken from Sevougian et al. 2019b) 23
Figure 1-2. Schematic the GDSA Framework. The RSA work package focuses primarily on flow and transport modelling, but also works closely with VoroCrust, dfnWorks and Dakota for processing and computational support. (Mariner et al. 2021)........ 24
Figure 2-1. Elevation profile and corresponding pressure boundary condition (top) and depth zones in the domain (bottom) (after LaForce et al., 2022). 26
Figure 2-2. Repository layout for the crystalline reference case. (Black outline around the repository is not a tunnel). 27
Figure 2-3. Deterministic fractures (represent HCD) in the model domain. 28
Figure 2-4. One realization of the stochastic fractures, colored by fracture family. Depth zones correspond to different colors. 28
Figure 2-5. Upscaled fracture domain using cell size of 20 m. 31
Figure 2-6. Discretization of the repository with 20 m far field size........ 32
Figure 2-7. Discretization of the deposition holes and drifts with 20 m far field size........ 32
Figure 2-8. Upscaled fractures near the repository using cell size of 20/3 m........ 33
Figure 2-9. Surfaces on top of domain used for output metrics. 34
Figure 2-10. Steady state flow solution. 34
Figure 2-11. Steady state flow for high point (green), hillslope (red), and low point (black) for 20 m grid (dashed) and 25 m grid (solid) on Realization 1. 35
Figure 2-12. Steady state flow for all realizations on the 25 m grid of high point (dotted), hillslope (dashed), and low point (solid)........ 36
Figure 2-13. Tracer 1 moving through the domain at a cutaway of y=1000 m at 100 years for Realization 1. 36
Figure 2-14. Tracer 2 moving through the domain at a cutaway of y=1000 m at 100 years for Realization 1. 37
Figure 2-15. Mass of Tracer 1 (left) and Tracer 2 (right) remaining in the repository on the 20 m grid (dashed) and 25 m grid (solid) on Realization 1. 38
Figure 2-16. Mass of Tracer 1 (left) and Tracer 2 (right) remaining in the repository for all realizations on the 25 m grid........ 38
Figure 2-17. Cumulative mass flow (left) and mass flow rate (right) across the hillslope on Realization 1 for both the 20 and 25 m grid resolution. 39
Figure 2-18. Cumulative mass flow (left) and mass flow rate (right) across the low point on Realization 1 for both the 20 and 25 m grid resolution. 39
Figure 2-19. Cumulative mass flow (left) and mass flow rate (right) across the hillslope for all fracture network realizations on the 25 m grid. 40
Figure 2-20. Cumulative mass flow (left) and mass flow rate (right) across the low point for all fracture network realizations on the 25 m gird. 40
Figure 2-21. Cumulative mass flow at the point on the low point where the maximum mass flow occurred on the 20 m grid in Realization 1........ 41

Figure 2-22. Cumulative mass flow at the point on the low point where the maximum mass flow occurred on the 25 m grid in Realization 1 ... 42

Figure 2-23. Geological cross-section with model units for the generic salt reference case. The model units are simplified from Bertrams et al. (2020). The repository location and initial model conditions are shown. ... 44

Figure 2-24. Schematic of the waste repository in a generic salt dome. The drifts outlined in yellow will be for used for comparisons between each teams' results. ... 45

Figure 2-25. Shaft seal for generic salt dome repository (modified from Rübel et al. (2016) by Richard Jayne). ... 47

Figure 2-26. The geologic repository mined components created with LaGriT. This surface object is used by Vorocrust to create the full mesh. ... 49

Figure 2-27. Mesh created by Vorocrust. This slice is parallel to the repository at a depth of 795m. Note the high-resolution meshing near the repository and coarsening outwards. ... 50

Figure 2-28. Zoomed in slices of the (A) repository and (B) disposal drifts showing the mesh. ... 51

Figure 2-29. General mode results for pressure (left) and saturation (right) at 10,000, 20,000, and 30,000 years. ... 52

Figure 2-30. Richard's mode results for pressure (left) and saturation (right) for 10,000, 20,000, and 30,000 years. ... 53

Figure 2-31. Average pressure and saturation for the regions of interest in the model comparison. (A) Pressure in the SNF drift, (B) Liquid saturation in the SNF drift, (C) Pressure in the vitrified waste drift, (D) Liquid saturation in the vitrified drift, (E) Pressure in the drift seal, and (F) Liquid saturation in the drift seal. ... 54

Figure 2-32. Shaft saturation in General mode at 5,000, 10,000, and 15,000 years. ... 55

Figure 3-1. Model description and setting. (A) Schematic description of the model domain consisting of waste package (wp), buffer/spacer, DRZ, and shale host rock. (B) Numerical domain with mesh setting. The temporal evolution of concentration of radioactive isotopes are obtained at points H1 and H2 at 2.94 m and 4.315 m in x-direction within the buffer and DRZ, respectively. ... 58

Figure 3-2. Heat source. (A) Transient decay heat curve for waste package heat source term from the 10th, 50th, and 75th percentiles of frequency distribution of heat outputs that are predicted at the selected canisters in Jones et al. (2021). The heat source is scaled based on the volume of a quarter of waste package modeled in this study. (B) Temporal evolution of average temperature within WP for three types of heat source as stored in the shale. ... 60

Figure 3-3. Thermal conductivity changes as a function of liquid saturation and temperature. The values of dry and wet thermal conductivities are for the DRZ in this study. The solid black line represents the default thermal conductivity independent of temperature changes. ... 62

Figure 3-4. Temporal evolution of average (A to B) liquid mobility, (C to D) liquid saturation, and (E to F) aqueous concentration of tracer (Cl^-) within the buffer and DRZ for five cases. ... 64

Figure 3-5. Spatial distribution of aqueous phase concentration of Cl- [mol/m^3-liq] at t = 60 years for three types of heat source ... 65

Figure 3-6. Spatial distribution of (A to B) Liquid saturation and (C to D) aqueous concentration of tracer Cl$^-$ at points H1 and H2 within the buffer and DRZ (refer to Figure 3-1A), respectively for five cases. 66

Figure 3-7. Model description and setting. (A) Schematic description of the vertically extended model domain consisting of waste package (wp), buffer/spacer, DRZ, and shale host rock. (B) Numerical domain and geometry. 67

Figure 3-8. The effect of the model domain size. Temporal evolution of average (A to B) temperature, (C to D) mobility of liquid phase, (E to F) liquid saturation, and (G to H) aqueous concentration of tracer (Cl$^-$) within the buffer and DRZ for the cases of 50th percentiles of heat output with a vertically reduced and extended domain. 68

Figure 4-1. Shaded relief map showing the boundary of the watershed and the incision of the glacial deposits by the main stream and its tributaries (streams shown in blue). 72

Figure 4-2. Simplified geologic map of glacial deposits within the region of the watershed and distribution of water wells within the watershed. Line B-B’ is the location of the cross-section shown in Figure 4-3. 73

Figure 4-3. Stratigraphic relationships and thicknesses of glacial deposits along geologic cross-section B-B’ from Figure 4-2. Modified from Nielsen and Locke (2015). 74

Figure 4-4. Well Depth versus well yield for bedrock and gravel wells within the example watershed. 75

Figure 4-5. Monthly streamflow estimates for the example watershed using two estimation methods, from Nielsen and Locke (2015). 77

Figure 4-6. Schematic representation of stratigraphy and groundwater flow in a watershed with three types of glacial deposits (not to scale). Groundwater flow from the upper sand and gravel aquifer contributes approximately 90% of the water to the total streamflow. Arrows are general indicators of flow velocities based on differences in permeability. Question marks indicate uncertainty in the amount of radionuclide transport in glacial deposits. 78

Figure 4-7. Schematic representation of groundwater flow for a simple stratigraphy of till overlying crystalline basement rock. Groundwater flow from till contributes approximately 40% of the water to the total streamflow. Arrows are general indicators of groundwater flow. Question marks indicate uncertainty in the amount of radionuclide transport in glacial deposits. 79

Figure 5-1. A schematic showing a potential unsaturated zone geologic repository. Figure 5-2 of Mariner et al. (2018). A possible location for a repository would be in the playa deposits, which are impermeable fine-grained sediments and are located towards the center of this schematic. Also notice the lithologic heterogeneity depicted here that is expected in basin-fill valleys where alluvial fans, fluvial systems, spring discharge areas, and playas are common features. 84

Figure 5-2. Schematic cross section of the unsaturated zone model (Mariner et al., 2018). UZ = unsaturated zone; SZ = saturated zone 85

Figure 5-3. Configuration of the repository and natural barrier system generated using Cubit, simulated in PFLOTRAN and visualized on ParaView. Turquoise color (material ID 3) represents the ubf_conf units (the centermost contains the repository as seen there), green (material ID 4) represents UBF, dark blue (material ID 2) represents the UBF aquifer, and blue (material ID 1) represents LBF. Distances along the axes are in meters, where 1000 m is land surface and 0 m is the bottom of the model domain. The left side of the figure represents a western direction. 86

Figure 5-4. XY slice through the repository colored by material ID. The repository is assumed to be 250 meters below the surface. The zoom in box on the top left shows a close-up of four waste packages (WPs), colored in red, buffer in yellow, DRZ in burgundy, and ubf_conf in turquoise. Visualized using ParaView..................... 87

Figure 5-5. Temperature, gas saturation, gas pressure and liquid saturation history plots at observation point “Fwp_inside” for the three PFLOTRAN simulations. 90

Figure 5-6. XY slice through the repository colored by liquid saturation at 300 years for the NWT simulation. Saturation range has been rescaled over all timesteps and no longer shows a negative lower range value as FY21 runs did. 92

Figure 5-7. XZ slice through the center of the repository at “Fwp_inside” colored by Material ID (top left) and Total Tracer (M) at 2350, 3000, 4000, 10200, and 100k years for the “GIRT” simulation. Tracer concentration range has been rescaled over all timesteps. 92

Figure 5-8. Total Tracer molar concentration history at observation point “Fwp_inside” for the “GIRT” simulation. 93

Figure 6-1. Reference data from PNNL thermal simulation of a TN-32B spent fuel cask. (After Fort et al., 2019) 98

Figure 6-2. Thermal energy output vs time for the 18 individual radionuclides and total decay heat for the simulated 32 PWR assembly DPC.. 101

Figure 6-3. Comparison of the decay heats of the simulated 32 assembly DPC and the hypothetical 37 assembly DPC used in previous PA simulations. 101

Figure 6-4. Comparison of the decay heats of the simulated 32 assembly DPC and the hypothetical 37 assembly DPC used in previous PA simulations scaled to 32 assemblies. 102

Figure 6-5. Comparison of the decay heats of the mass-scaled simulated 32 assembly DPC and the hypothetical 37 assembly DPC used in previous PA simulations scaled to 0.435 MTIHM/assembly. 102

Figure 6-6. Comparison of the decay heat of 4 hypothetical DPCs with burnup and enrichment shown and the heat source used in previous PA simulations. Both are scaled to 32 PWR. 104

Figure 7-1. At the beginning of this fiscal year, VoroCrust was a set of C++ classes that have different functionality and a wide range of applications. There was a great deal of interdependency between the different classes. VoroCrust has a commercial license which poses constraints on our capacity to distribute the code outside Sandia National Laboratories and did not meet the needs of the GDSA to distribute the code as part of its open-source earth science package. 108

Figure 7-2. Schematic of the current workflow for incorporating geological uncertainty into simplified PA. 109

Figure 7-3. Top: Geological framework model of the Pierre Shale sequence stratigraphy at 10x vertical exaggeration at 250 m grid resolution (after Sevougian et al., 2019b). Bottom: Subsurface geological horizons at 10x vertical exaggeration upscaled to 1000 m grid resolution (Overburden Top surface not included). The dimensions of the region are 69 km (E-W) by 83 km (N-S). Stratigraphy color scale is the same for both subfigures. 111

Figure 7-4. Development of an example simulation mesh for the base case (Realization r1). (a) Surfaces selected for the PA model. From the top they are Top Overburden, Top Host Shale, Top Silty Shale, Top Underlying Shale, Top Limestone aquifer, and Top Lower Shale. A flat model base is added at z = -1200 m. (b) Model volume and surfaces from LaGriT clipped to show the box containing the repository box in the interior. (c) VoroCrust simulation surface mesh. (d) VoroCrust simulation mesh showing colored by material ID where 1 = Limestone, 2 = Underlying Shale, 3 = Silty Shale, 4 = Host Shale, 5 = Overburden, 6 = repository (not shown), and 7 = Lower Shale. 117

Figure 7-5. The Overburden formation for the base case (Realization r1) of the shale PA model at 10x vertical exaggeration. (a) Model volume from LaGriT. (b) Voronoi surface mesh generated by VoroCrust-meshing. (c) Detail of the surface mesh at the thinnest point in the Overburden. 119

Figure 7-6. Top surface of Realizations 2-10 of the shale PA model at 10x vertical exaggeration. 123

Figure 7-7. Tracer 1 (left) and Tracer 2 (right) in the reservoir for the base case (r1). Tracer concentrations above 1×10^{-11} (M) are overlain on the full model colored according to Material ID. Times are a-b) 1 years; c-d) 10,000 years; e-f) 100,000 years; g-h) 200,000 years; i-j) 500,000 years; k-l) 1,000,000 years. 124

Figure 7-8. Concentration of the instant release Tracer 1 (left) and slow-release Tracer 2 (right) at the three downstream monitoring locations as a function of time for the million year simulation. a)-b) Tracers in the Overburden. c)-d) Tracers in the Silty Shale. e)-f) Tracers in the Limestone aquifer. 127

Figure 7-9. Concentration of the instant release Tracer 1 (left) and slow-release Tracer 2 (right) at the monitoring point in the middle of the repository as a function of time for the first 100,000 years of the simulation. Note: Vertical scale on the subplots is not the same. 128

Figure 7-10. Total mass of the instant release Tracer 1 (left) and slow-release Tracer 2 (right) in the repository volume as a function of time for the first 100,000 years of the simulation. Vertical scale on the subplots is not the same. 128

Figure 7-11. Tracer 1 in the reservoir for realization r2 of the model. Tracer concentrations above 1×10^{-11} (M) are overlain on the full model colored according to Material ID. Times are Top: 100,000 years; Bottom: 1,000,000 years. 129

Figure 7-12. Tracer 1 in the reservoir for realization r8 of the model. Tracer concentrations above 1×10^{-11} (M) are overlain on the full model colored according to Material ID. Times are Top: 100,000 years; Bottom: 1,000,000 years. 130

Figure 7-13. Figure 7.2 from Swiler et al., (2019): 2-D cross section of 3-D model domain showing aquifer observation points (pink dots). From top to bottom and left to right: sand_obs 1, sand_obs2, sand_obs3, lime obs 1, lime_obs2, lime obs3. 131

Figure 7-14. ^{129}I concentrations at observation points from Figure 7.3 of Swiler et al. (2019). Only the plots of ‘sand_obs3’ and ‘lime_obs3’ are shown as they are the closest to our Overburden and Limestone aquifer monitoring points, respectively. 131

LIST OF TABLES

Table 2-1. Sizes of parameters meshed in Cubit vs Task Specification. 33
Table 3-1. Model parameter values 59
Table 4-1. Reference permeabilities and thickness of deposits 74
Table 4-2. Monthly Mean Precipitation and Temperature in the area of the watershed 76
Table 4-3. Water Requirements and Sources for Representative Crops in the May-September growing season. 80
Table 5-1. Parameter values used in simulations (Modified from LaForce et al. 2021, Table 5-1). Modification made was setting a more realistic grain density value for the upper basin fill DRZ. 88
Table 5-2. Results for the PFLOTRAN simulations at observation point “Fwp_inside”. 91
Table 6-1. Tabulated data from PNNL thermal simulation of a TN-32B spent fuel cask used for ORIGEN simulations. 97
Table 6-2. Assembly nuclide/isotopic masses used for ORIGEN simulation input. 98
Table 6-3. Mass of select nuclides in simulated 32 assembly DPC at 0.0 yrs. 100
Table 6-4. Selected Burnup and Enrichment Values. 103
Table 7-1. Parameter values used in deterministic simulation, reproduced from Mariner et al., (2017). Thermal properties are not included as current simulations are isothermal. 112
Table 7-2. Model meshing results for the base case (Realization r1) mesh. Material IDs correspond to Figure 7-4 c. 118
Table 7-3. Sampled parameters and their distributions. (Mariner et al., 2017). 121
Table 7-4. Results of DAKOTA sampling for 10 realizations of the shale PA model. 121
Table 7-5. Simulation statistics for the shale uncertain simulations 125
Table A-1. Fuel Assembly Input parameters 145
Table A-2. Cooling time steps as a function of cooling time 145
Table A-3. Example ORIGAMI input file 146
Table A-4. Output Files Format. File: decay_heat.csv – contains decay heat data for 0 to 200 years. The file has a header of 5 lines. The lines contain the variable name in the first column followed by 5 columns of input data. Line 6 is the header for decay heat results. Line 7 and below are results, again in 6 columns where the first column is the decay time in years and columns 2-6 are results in Watts for each corresponding header column. The start of the file is shown. 147
Table A-5. File: isotopes.csv – contains isotopic composition for 55 years cooled fuel. The file has a header of 6 lines. The lines contain the variable name in the first column followed by 5 columns of input data. Line 7 is the header for isotopic composition results. Lines 8 and beyond are results, again in 6 columns where the first column is the isotope name and columns 2-6 are results in grams of isotope for each header column. The start of the file is shown. 147

NOMENCLATURE

AMSL	above mean sea level
ARP	Automatic Rapid Process
CSNF	commercial spent nuclear fuel
DCD	Design Control Document
DOE	U.S. Department of Energy
DPC	dual-purpose canister
DRZ	Disturbed rock zone
EBS	engineered barrier system
ECPM	Equivalent Continuous Porous Medium
FY	fiscal year
GDSA	Geologic Disposal Safety Assessment
GFMs	geologic framework models
GIRT	Global Implicit Reactive Transport
GPM	gallons per minute (GPM)
HCD	Hydraulic Conductor Domains
HLW	high-level radioactive waste
HRD	Hydraulic Rock Mass Domains
LANL	Los Alamos National Laboratories
LBF	lower basin fill
LHS	Latin Hypercube Sampling
MTU	Metric Tons of Uranium
MPC	multi-purpose canister
NBS	natural barrier system (NBS)
NGW	Next Generation Workflow
NRC	Nuclear Regulatory Commission
NTRDC	Newton trust-region dogleg Cauchy
NWT	nuclear waste transport
ORNL	Oak Ridge National Laboratory
PA	Performance Assessment
PWR	pressurized water reactor
R&D	Research and Development
RD&D	Research, Development and Demonstration
RSA	Repository Systems Analysis

SA	sensitivity analysis
SFWD	Spent Fuel and Waste Disposition
SFWST	Spent Fuel Waste Science and Technology
SNF	spent nuclear fuel
SNL	Sandia National Laboratory
SZ	saturated zone
THM	thermal, hydrologic, and mechanical
THMC	thermos-hydro-mechanical-chemical
UBF	upper basin fill
UNF-ST&DARDS	Used Nuclear Fuel – Storage, Transportation & Disposal Analysis Resource and Data Systems
UQ	uncertainty quantification
UZ	Unsaturated Zone
WF	Waste Form

1. INTRODUCTION

The Spent Fuel and Waste Science and Technology (SFWST) Campaign of the U.S. Department of Energy (DOE) Office of Nuclear Energy, Office of Spent Fuel and Waste Disposition (SFWD), is conducting research and development (R&D) on geologic disposal of spent nuclear fuel (SNF) and high-level radioactive waste (HLW). Two of the highest priorities for SFWST disposal R&D are design concept development and disposal system performance assessment (PA) modeling (DOE 2012, Table 6; Sevougian et al., 2019c). Generic design (or reference-case) concepts being considered for SNF and HLW disposal since 2010 include mined repository concepts in bedded salt, argillite (shale), and crystalline rock. An additional option is a potential mined repository in an unsaturated zone (UZ) alluvium. The PA R&D from 2012-2018 mostly focused on disposal of commercial spent nuclear fuel (CSNF) inventory packaged in smaller waste packages, such as 4-PWR and/or 12-PWR waste packages. However, since 2019 a greater emphasis is given to simulating disposal of higher decay-heat waste packages containing 21, 24, or 37 pressurized water reactor (PWR) assemblies.

This report describes accomplishments for the Fiscal Year 2022 (FY22) in the development of generic repository reference cases and PA modeling and analysis by the repository systems analysis (RSA) work package. Prior development and accomplishments are summarized at a high-level in Mariner et al. (2021), with more detail provided in Mariner et al. (2020, 2019, 2018, 2017, 2016, 2015), Sevougian et al. (2016, 2014, 2013, 2012), Freeze et al. (2013), Vaughn et al. (2013). Recent accomplishments of the RSA package are discussed in detail in Sevougian et al. (2019a), Sevougian et al. (2019b), LaForce et al. (2020, 2021).

Sassani et al. (2021) details a 5-year research R&D plan that "provides a strategic guide to the work within the Research, Development, and Demonstration (RD&D) technical areas, focusing on the highest priority technical thrusts" for the SFWST Campaign. The plan discusses the need to focus on four areas (Sassani et al. 2021):

- Capabilities Development and Demonstration
- International Collaboration and Underground Research Laboratories
- EBS Representations
- Evaluation of Potential Direct Disposal of large, high-energy waste packages

The objective of the GDSA RSA work package is to develop generic deep geologic repository concepts and system PA models in line with the current 5-year plan (Sassani et al. 2021) for several host-rock environments, and to simulate and analyze these generic repository concepts and models using the GDSA Framework toolkit (Mariner et al. 2021), and other tools as needed.

Figure 1-1 shows the flow of information and the role of PA in RD&D. The RSA work package focuses primarily on the reference case components, technical bases, and process models, as indicated by the dashed blue lines. Figure 1-2 shows the GDSA framework, which is used by the RSA work package for simulation studies. The pieces of the GDSA framework addressed by RSA in FY22 are flow and transport modelling and investigating integration of the VoroCrust meshing software into the workflow. The work accomplished in FY22 applies to the goals of capabilities development and demonstration, international collaboration, EBSs, and evaluation of disposal of large, high-energy waste packages. The specific goals for FY22 are:

- The GDSA team is leading Task F of the DECOVALEX 2023 project on behalf of the US DOE's SFWST Campaign. This project has nine international partners for the crystalline case and four for the salt case. Both cases involve collaborative development of reference case scenarios for post-closure PA for deep geologic repositories. An overview of the task specification and SNL team progress to date is in Section 2.

- The study on the impact of buffer swelling on the disturbed rock zone (DRZ) in a shale reservoir in Sevougian et al. (2019b) and LaForce et al. (2020, 2021) was continued. This study includes tracer transport, DRZ evolution, thermal dependence on material properties near the waste packages and considers heat sources representative of the 10th, 50th and 75th percentile PWR waste packages in inventory. The results of this study are in Section 3.

- A study of near-surface glacial deposits that overlay crystalline basement rock formations has been conducted in support of the GDSA biosphere modelling effort to evaluate dose to human receptors (Condon et al. 2020). Of particular interest is the contribution of groundwater to surface rivers and lakes, and how much of that water is used in irrigation for agriculture. The results of this study are presented in Section 4.

- Simulations on a deterministic UZ alluvium PA-model have continued. New simulations utilize improved numerical methods and tracer transport has been added to the model using a forward coupled in time approach. The results of this study are shown in Section 5.

- As a first step toward improving the realism of the waste form (WF) heat and radionuclide source in PA simulations, a new WF heat source term has been simulated based on an as-loaded dual-purpose canister (DPC) in inventory, as well as simulations of decay energy for several hypothetical high-energy waste packages. This work is presented in Section 6.

- VoroCrust Voronoi meshing continues to be studied in a stepwise process to improve GDSA capability and to further the goal of having all open-source software in the GDSA Framework workflow. A simplified shale PA model has been developed as a proof-of-concept for including uncertainty in the geological model. This work is presented in Section 7.

- Section 8 summarizes the work done in FY22 and discusses possible future work.

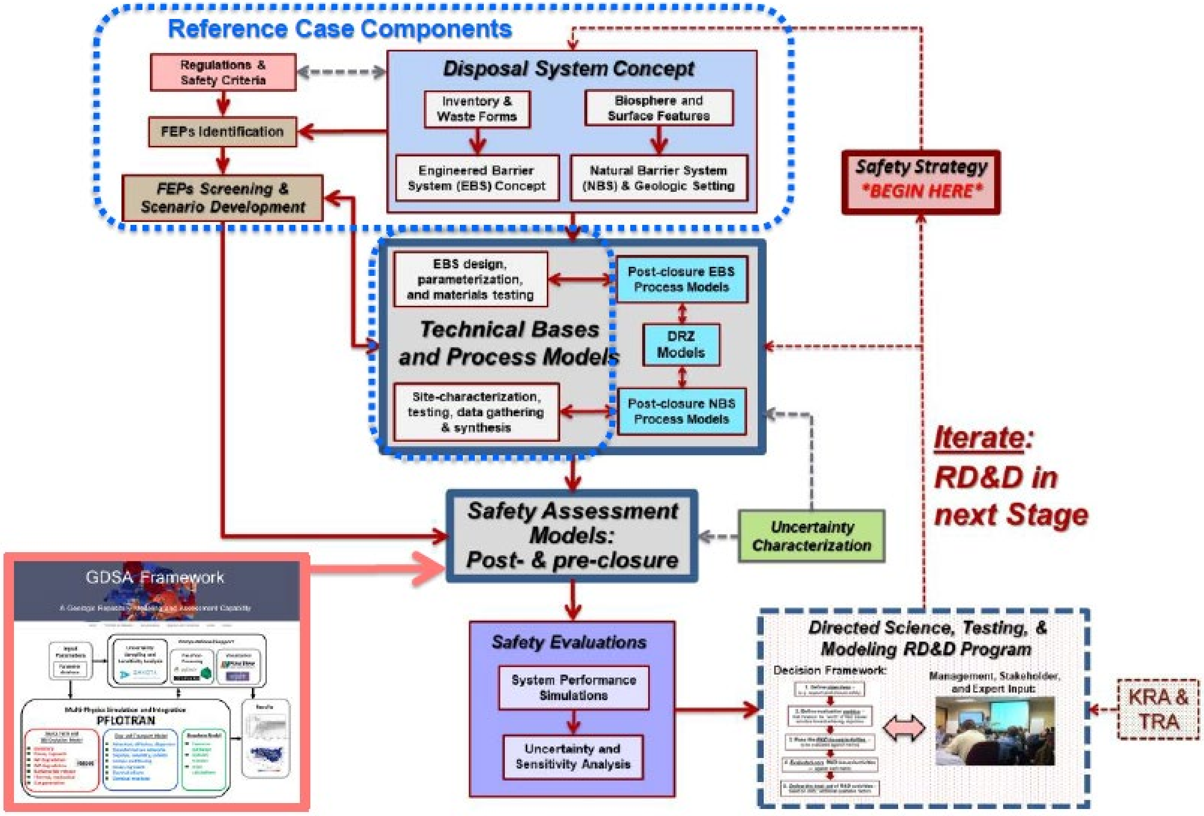

Figure 1-1. Information flow and the role of performance assessment for RD&D prioritization during a single stage of repository development. (Taken from Sevougian et al. 2019b)

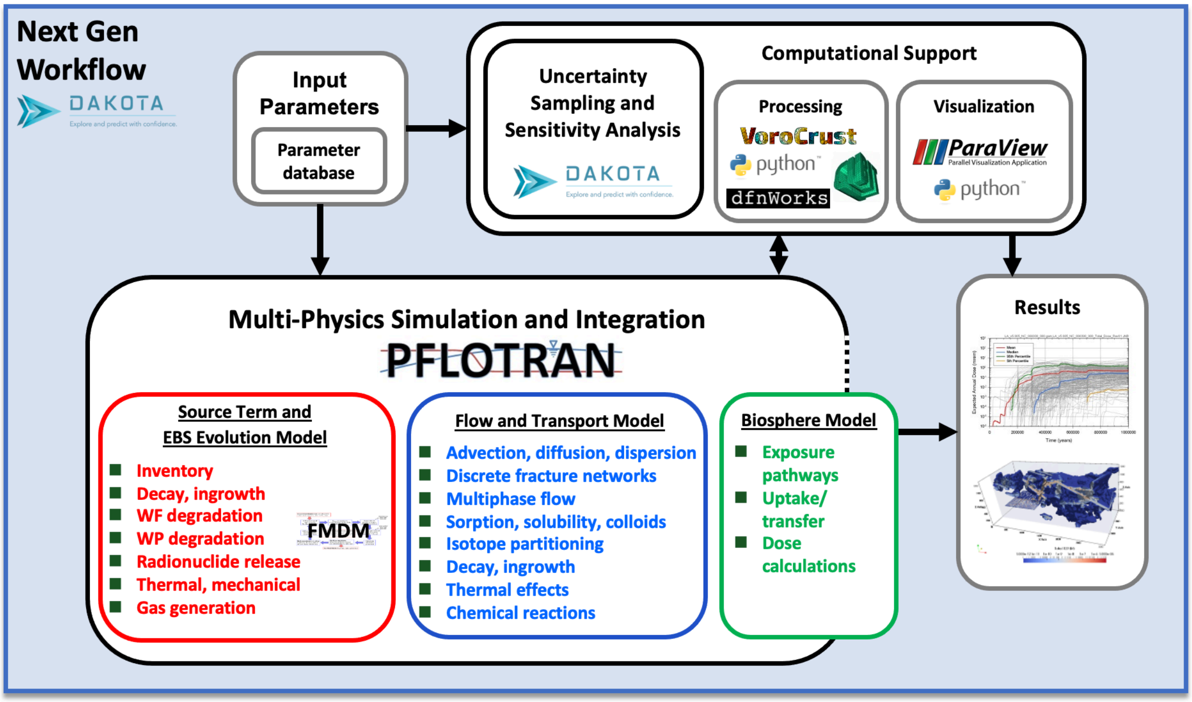

Figure 1-2. Schematic the GDSA Framework. The RSA work package focuses primarily on flow and transport modelling, but also works closely with VoroCrust, dfnWorks and Dakota for processing and computational support. (Mariner et al. 2021)

2. DECOVALEX REFERENCE CASES

DECOVALEX (DEveloping COupled models and their VALidation against Experiments; https://decovalex.org) is an international collaboration initiated in 1992 for the purpose of improving understanding of the coupled thermal, hydrologic and mechanical (THM) processes affecting repository evolution. In recent years chemical processes have also been considered. DECOVALEX activities run in four-year phases. SNL is leading Task F, on behalf of the US DOE's SFWST Campaign, for the DECOVALEX-2023 phase. Task F is a comparison of the models and methods used in deep geologic repository PA.

Task F of DECOVALEX-2023 (LaForce et al. 2022) focuses on comparison of models and methods used for post-closure PA. The goal is to test and build confidence in models, methods, and software used for post-closure PA and to identify additional research and development needed to improve PA methodologies. Task F includes more than 50 participants from 9 countries and 19 organizations. The countries are Canada, Czech Republic, Germany, Korea, Netherlands, Sweden, Taiwan, United Kingdom, and the United States.

In Task F, two hypothetical repositories are being developed: one in crystalline rock (F1) and the other in salt (F2). In the first year, 9 teams from 6 countries participated in the crystalline repository and benchmarking exercises. In the second year, Task F1 gained one additional team. Task F2 was initiated six months later than Task F1, in August 2020, and has five teams from five countries. In year two, the focus of the tasks was on development of the conceptual reference case. As Task F moves into its third year, the F1 and F2 groups are further refining reference case specifications, and teams within these groups have either begun simulations of the reference cases or improvements to their simulations. In addition, as required, internal interim reports were drafted and reviewed for each subtask to capture the work performed to date. These reports were internal to the project, but the SNL contributions to these reports are included as appendices to the most recent iteration of the task specification in LaForce et al. (2022).

Task F will continue to provide numerous opportunities for learning new modeling approaches, developing new models for use in PA simulations, testing uncertainty and sensitivity analysis methods, comparing PA methods, and exchanging ideas with modelers in other programs. Several accomplishments in the past year are highlighted in the subsections below. Because of the success and enthusiasm observed to date, a continuance of Task F for the next four-year phase of DECOVALEX is being pursued.

2.1 Crystalline Reference Case (Task F1)

The Task F1 preliminary reference case for a mined repository in fractured crystalline rock is defined in the Task Specification revision 8 (LaForce et al., 2022). The reference case assumes isothermal conditions, steady state flow, and transient transport of two conservative tracers upon simultaneous breach of all the canisters in the repository. Teams will run the simulation on ten different stochastic fracture realizations and compare tracer transport and steady state flow across the top boundary of the model domain. An overview of the reference case and initial results from the DOE team are provided below.

2.1.1 Geological Setting

The reference case repository is located beneath a gently sloping hill in a domain 5 km in length, 2 km in width, and ~1 km in depth (Figure 2-1). The repository is located near the west (left) side of the domain, and the area of lowest elevation is located near the east (right) side of the domain. Surface elevation decreases 20 m over a distance of 2 km; the hydraulic pressure at the top surface of the domain is used to mimic the topography. All other surfaces are set to no-flow boundaries, forcing upwelling of the fluid near the eastern boundary. Conceptually, the area of lowest elevation represents the location where water would collect at the surface forming a feature such as a lake or wetland; however, in this model, upward vertical flow out of the top layer is effectively swept away with no opportunity for feedback. Fracture intensity and fracture transmissivity decrease with depth. The decrease is implemented by assigning different parameter values to each depth zone (as given in the Task Specification, Section 3.7 of LaForce et al., 2022).

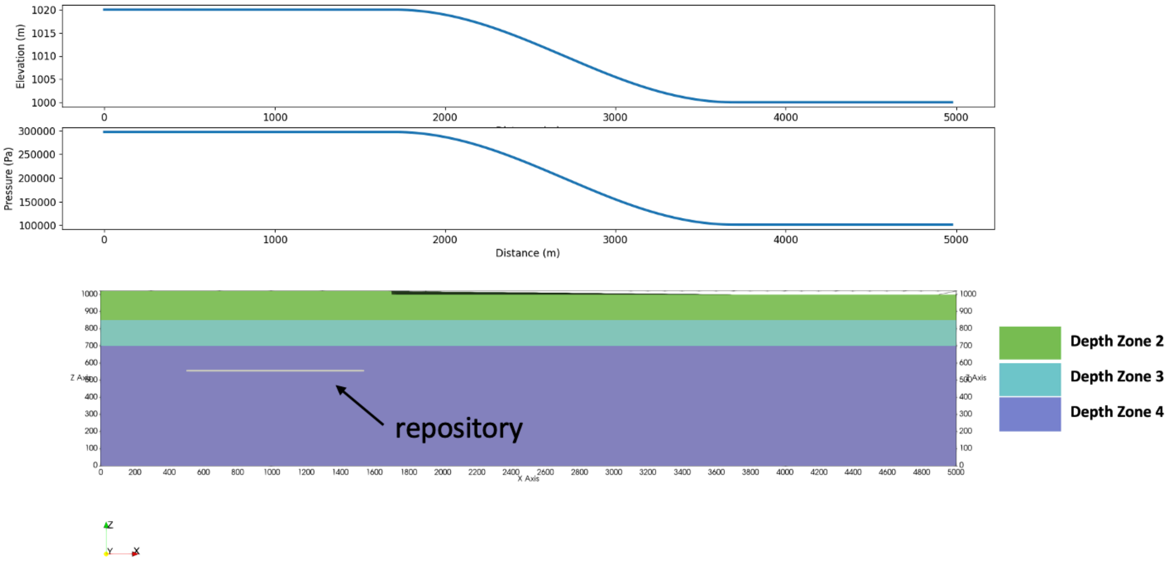

Figure 2-1. **Elevation profile and corresponding pressure boundary condition (top) and depth zones in the domain (bottom) (after LaForce et al., 2022).**

2.1.2 Emplacement Concept and Repository Layout

The generic reference case uses the KBS-3V emplacement concept developed for the Swedish and Finnish repository programs (Pettersson and Lönnerberg, 2008) and adopted by several countries as the reference design for a generic reference case or in the preliminary stages of site investigation (TPC 2017; Choi et al. 2013; NWMO 2012). The KBS-3V concept is developed for a repository mined at a depth of approximately 500 m in sparsely fractured crystalline rock. Copper canisters each containing a nominal inventory of four PWR assemblies are emplaced within rings of compacted bentonite in vertical deposition holes beneath the floor of a deposition tunnel, and tunnels are backfilled.

The waste inventory is 4,350 metric tons uranium (MTU) in the form of PWR SNF. Assuming each PWR assembly contains 0.435 MTU, 2500 4-PWR canisters are required to dispose of the inventory. The waste inventory is deliberately small to reduce the computational burden of simulations.

The repository, located at a depth of approximately 450 m, comprises 50 deposition drifts branching off two parallel access tunnels (Figure 2-2). The deposition drifts are spaced 40 m center-to-center; 50 deposition holes within each tunnel are spaced 6 m center-to-center. This spacing ensures that peak buffer temperatures would not exceed 100ºC (Pettersson and Lönnerberg 2008). The deposition drifts are 306 m in length so that the deposition tunnel extends 6 m beyond the center of the last deposition hole at both ends. There are 50 individual deposition drifts which results in a total of 2,500 deposition boreholes.

Dimensions and properties of the features of the repository (i.e., the engineered barrier system) are given in the Task Specification, Section 3.5 (LaForce et al., 2022).

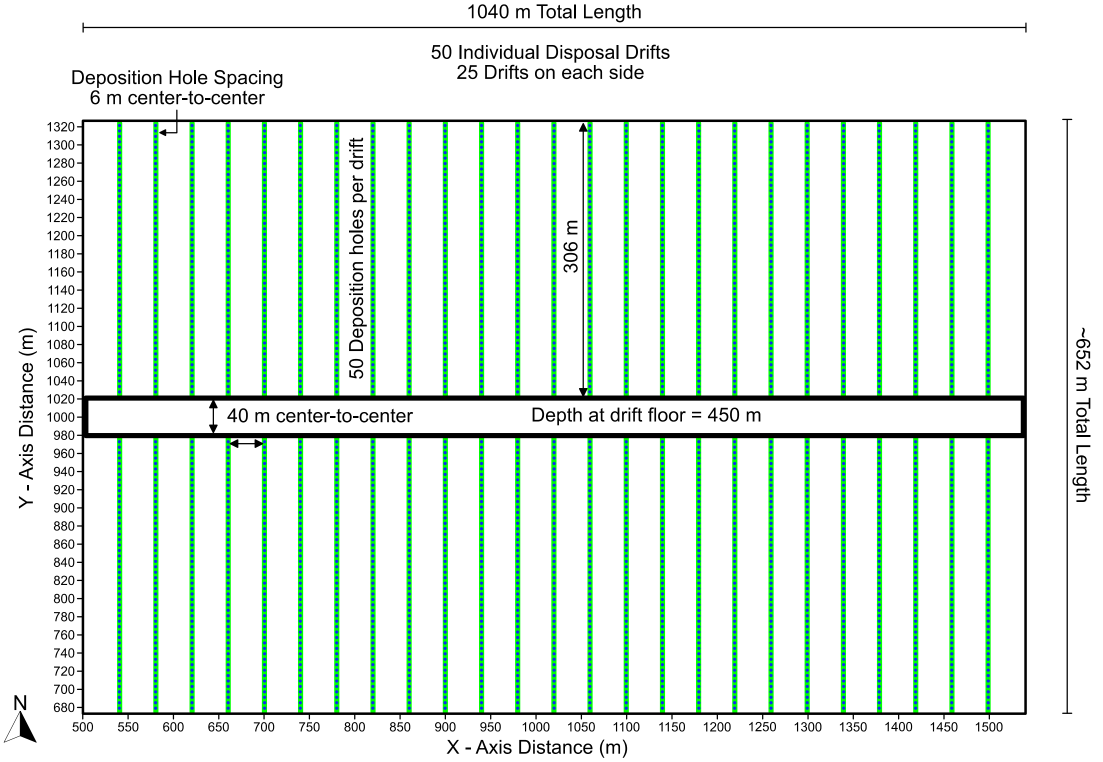

Figure 2-2. Repository layout for the crystalline reference case. (Black outline around the repository is not a tunnel).

2.1.3 Host Rock (Natural Barrier System)

The crystalline host rock is characterized by occurrence of large-scale, highly fractured brittle deformation zones and intervening masses of competent rock containing sparse networks of connected fractures. Following the example of SKB (e.g., Joyce et al. 2010), the former are named Hydraulic Conductor Domains (HCD) and the latter are named Hydraulic Rock Mass Domains (HRD).

The fractures within the HRD are subdivided into three different depth zones, representing vertical variations within the subsurface. Each depth zone contains three different families, representing variations in orientation (strike and dip, or equivalently, trend and plunge) and hydraulic properties.

Conceptually, properties such as transmissivity of individual fractures exhibit a dependence on the present-day stress field. As a result, there is a greater density of fractures, larger proportion of subhorizontal fractures, and higher fracture transmissivity at shallower depths, and lower density of fractures, lower proportion of subhorizontal fractures, and lower fracture transmissivity at greater depths.

The HCD and HRD are described in more detail in the Task Specification Section 3.7 (LaForce et al., 2022). The HCD are treated as deterministic features (i.e., their geometry and properties are the same in all realizations of reference case simulations (Figure 2-3)). Fractures within the HRD are treated as stochastic features (i.e., multiple realizations of the fractured rock mass are generated by sampling probability distributions for fracture radius, fracture orientation, and fracture location (Figure 2-4))

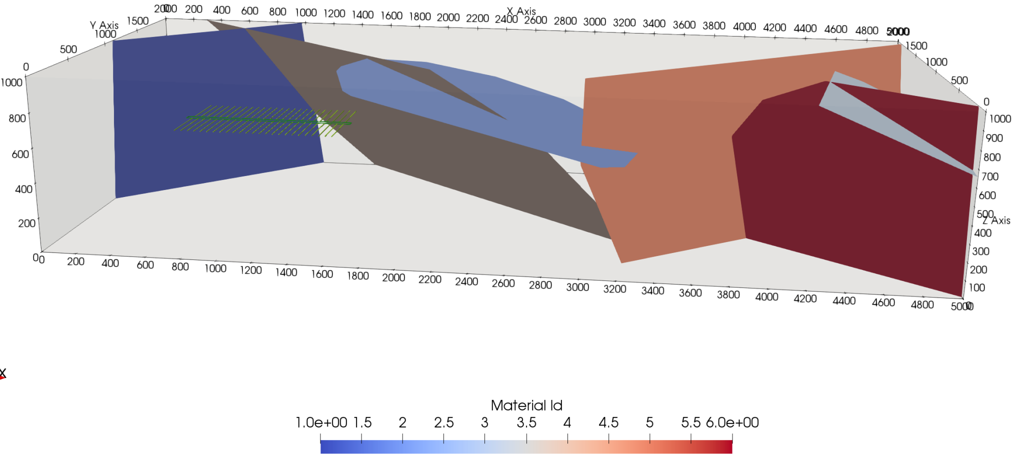

Figure 2-3. **Deterministic fractures (represent HCD) in the model domain.**

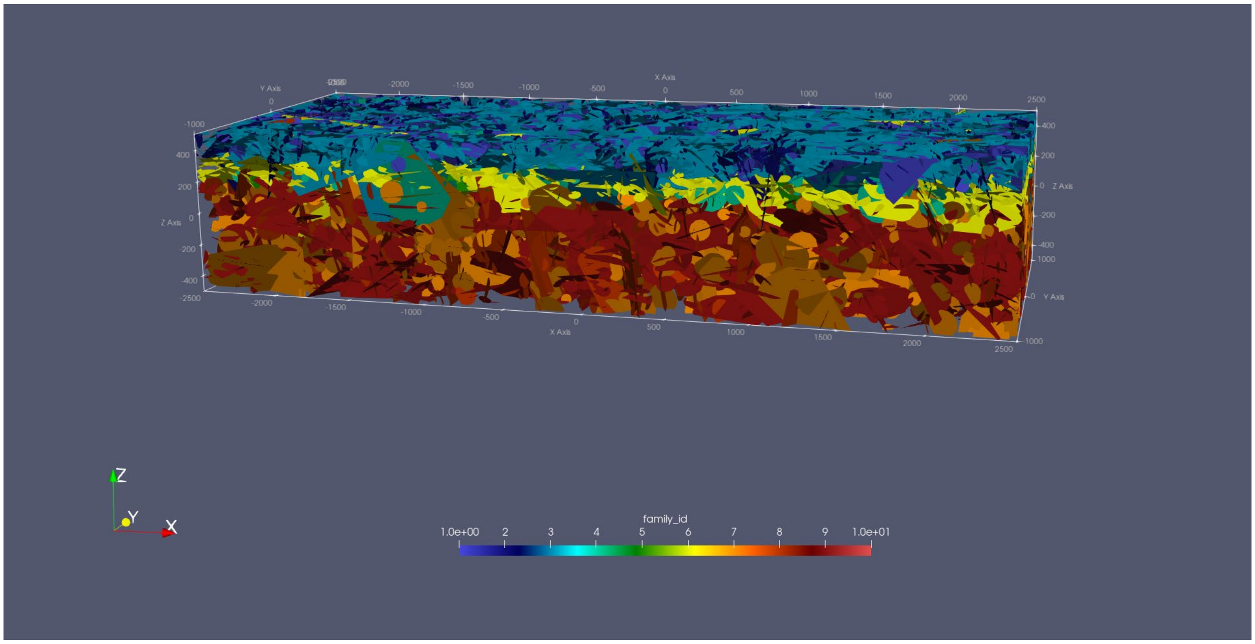

Figure 2-4. **One realization of the stochastic fractures, colored by fracture family. Depth zones correspond to different colors.**

2.1.4 Conservative Tracer Transport

Teams are modeling steady state flow and conservative transport of two tracers. Tracer 1 and Tracer 2 are modeled after ^{129}I but they do not undergo radioactive decay. Both have an atomic weight of 128.9 g/mol. The total inventory of the two tracers in each waste package is 5.45 g (0.0423 moles), equivalent to 1/100th of the expected inventory of ^{129}I in a waste package containing 4 PWR assemblies. The inventory of Tracer 1 is 0.545 g (0.00423 moles), or 10% of the total; it is instantly released at the start of the transport simulation. The inventory of Tracer 2 is 4.90 g (0.038 moles), or 90% of the total; it is released at a fractional rate of 10^{-7}/y throughout the transport simulation. It is assumed all canisters breach at the beginning of the simulation.

Teams first establish a steady state flow solution using a constant pressure (Dirichlet) boundary condition at the top surface of the domain and no flow boundary conditions at all other faces of the domain. Then, transport of the two tracers is simulated for 100,000 years. Initially the domain is empty of tracer everywhere except in the waste packages. Tracer is allowed to advect out of the domain at the top surface. No-flow transport boundary conditions are applied on all other surfaces of the domain, the same as the flow field. Teams ran 10 realizations of the preliminary reference case, varying the network of stochastic fractures. They either used fracture realizations provided by SNL or their own based on probability distributions given in the Task Specification.

2.1.5 DFN Generation

Stochastic and deterministic fractures are generated using Los Alamos National Laboratories (LANL) software dfnWorks (Hyman et al. 2015). dfnWorks takes inputs of probability distributions for fracture radius and orientation, fracture density, and fracture transmissivity. Fracture orientation is sampled from a Fisher distribution which is parameterized by mean direction (characterized by mean trend φ, the angle the projection of the pole onto the x-y plane makes with the x axis and mean plunge θ, the angle the pole makes with x-y plane), and a concentration parameter κ. Fracture radius is sampled through a truncated power law distribution. The fracture radius distribution takes the form (Follin et al. 2007):

$$f(r) = \frac{kr_0^k}{r^{k+1}} \qquad \textbf{Eq (2-1)}$$

where r_0 is the minimum radius and k is a constant, respectively. Fracture intensity is expressed as fracture area per unit volume of rock (P_{32} [m^2/m^3]). P_{32} is related to the average number of fractures per unit volume of rock (n_0) by (Swiler et al. 2020):

$$\begin{aligned} P_{32} &= n_0 \int_{r_0}^{r_{upper}} f(r)\pi r^2 dr \\ &= n_0 \int_{r_0}^{r_{upper}} \frac{kr_0^k}{r^{k+1}} \pi r^2 dr = \frac{n_0 \pi k r_0^k}{2-k} \left[r^{2-k}\right]_{r=r_0}^{r=r_{upper}}. \end{aligned} \qquad \textbf{Eq (2-2)}$$

The P_{32} values for the task specification assume $r_0 = 0.04$ m and maximum radius (r_{max}) of 564 m. The P_{32} over the range $r_0 = 0.04$ m to $r_{max} = 564$ m is equivalent to billions of fractures per km^3, the vast majority of which have radii < 1 m. We calculated the P_{32} for a smaller range of radii (e.g., minimum radius, r_{min} = 30 m to r_{max} = 564 m), by integrating the above over the range r_{min} to r_{max} (Swiler et al. 2020):

$$P_{32}[r_{min}, r_{max}] = \frac{\pi n_0 k r_0^k}{2-k} \left[r_{max}^{2-k} - r_{min}^{2-k}\right]. \qquad \textbf{Eq (2-3)}$$

Fracture transmissivity (T [m^2/s]) is a function of fracture radius. The reference case uses the fully correlated relationship defined in Follin et al. (2007):

$$\log T = \log a r^b \qquad \textbf{Eq. (2-4)}$$

Where *r* is radius [m] and the coefficients *a* and *b* are dimensionless constants. Fracture aperture is calculated from the transmissivity using the cubic law (Bear et al. 1993):

$$\text{aperture} = \left(12T\frac{\mu}{\rho g}\right)^{\frac{1}{3}} \qquad \textbf{Eq. (2-5)}$$

Where μ is viscosity of water [Pa s], ρ is density of water [kg/m^3], and *g* is the acceleration due to gravity [m/s^2]. Permeability (*k* [m^2], not to be confused with the constant in Eqs. 2-1 to 2-3) is defined as,

$$k = \frac{\text{aperture}^2}{12} \qquad \textbf{Eq. (2-6)}$$

The dfnWorks output must be post-processed to compute depth dependent transmissivity, aperture, and permeability. Deterministic fractures are input by specifying normal vectors, radii, and translation from the origin. Stochastic fractures are randomly distributed in the domain until the target fracture density is reached. Isolated fractures and fracture clusters not connected to faces in the domain are discarded. The calculated fracture apertures, permeabilities, normal vectors, and coordinates are output to files.

2.1.6 Upscaling

Fractures are upscaled using a Python script called mapdfn.py (Stein et al. 2017), which takes dfnWorks input and the Equivalent Continuous Porous Medium (ECPM) model domain and discretization (origin, domain, length, and length of cubic grid cells) and outputs grid cell permeability, porosity, and tortuosity. Effective cell properties are calculated by determining the characteristics of the fractures that extend over a given ECPM grid cell. For each fracture in a cell, intrinsic transmissivity (T_f[m^3]) is calculated as:

$$T_f = k_f b_f \qquad \textbf{Eq. (2-7)}$$

where k_f is fracture permeability [m^2] and b_f is fracture aperture [m]. Intrinsic transmissivity is described as a diagonal transmissivity tensor, where the coordinates are then rotated into the coordinates of the grid. Off-diagonal terms are discarded, and the diagonal tensor describing cell permeability is calculated as:

$$\begin{bmatrix} k_{xx} & & \\ & k_{yy} & \\ & & k_{zz} \end{bmatrix} = \frac{1}{d}\sum \begin{bmatrix} T_{xx} & & \\ & T_{yy} & \\ & & T_{zz} \end{bmatrix}_f \qquad \textbf{Eq. (2-8)}$$

where *d* is the length of the cell side, and the sum is over all fractures intersecting the cell. A stairstep correction may be added to the permeability which accounts for the artificially low flux calculated from the ECPM due to fractures being characterized as staircases. The correction is derived from Sweeney et al. (2020), where the amount of correction needed is determined by the dot product between each fracture in the grid cell and the normal vector to each coordinate axis and is applied based on the angle closest to 45°. Fracture porosity for each grid cell is calculated as:

$$\phi = \frac{1}{d}\sum b_f \qquad \textbf{Eq. (2-9)}$$

and cell tortuosity (τ) is calculated so the effective diffusion coefficient (D_e) is homogeneous everywhere in the fractured rock. In PFLOTRAN, tortuosity is a number less than one such that:

$$D_e = \phi \tau D_m \qquad \textbf{Eq. (2-10)}$$

where D_m is the molecular diffusion coefficient in water. Cells not intersected by fractures are assigned matrix permeability and porosity. For the reference case, an upscaled grid cell size of 20 or 25 m is used (Figure 2-7).

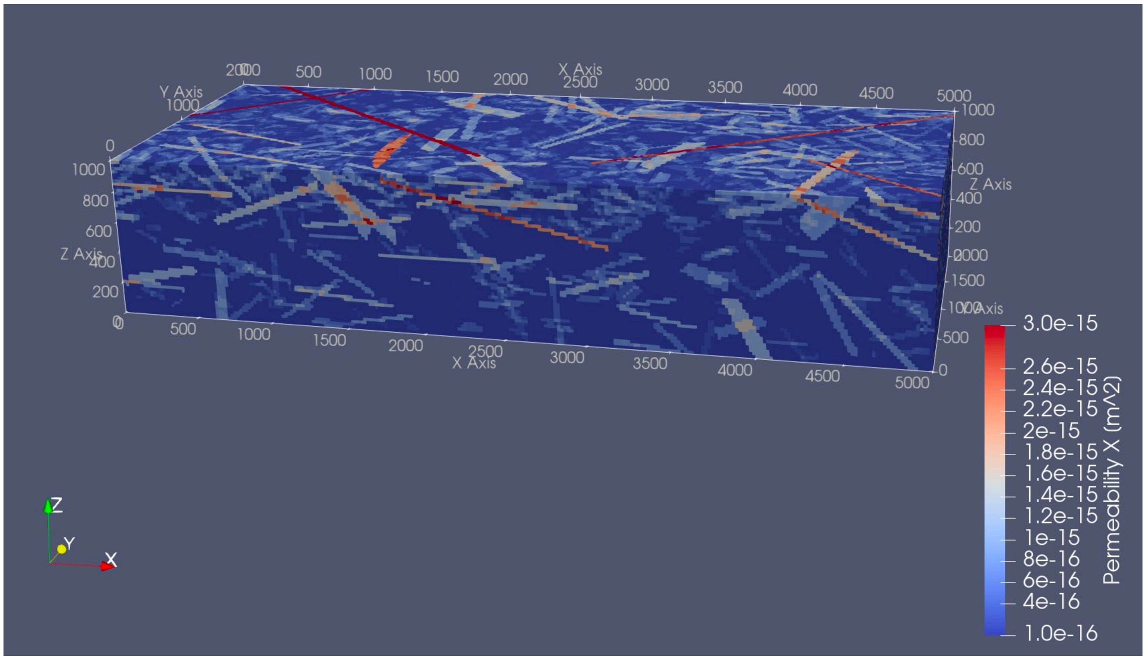

Figure 2-5. Upscaled fracture domain using cell size of 20 m.

2.1.7 Repository Discretization

The mesh is created using Cubit (Skrock et al., 2021) and formatted as an unstructured mesh that can be input into PFLOTRAN, a massively parallel flow and reactive transport modelling software (Hammond et al. 2014). Figure 2-6 shows an image in Paraview of the drifts and deposition holes in the repository. The deposition holes and waste packages are discretized to 25/27 or 20/27 m, the deposition drifts are discretized to 25/9 or 20/9 m, and the near field is discretized to 25/3 or 20/3 m (Figure 2-7). The fractures in the repository were then upscaled to a 25/3 or 20/3 m grid (Figure 2-8). Only the results of the 20 m farfield mesh size are shown.

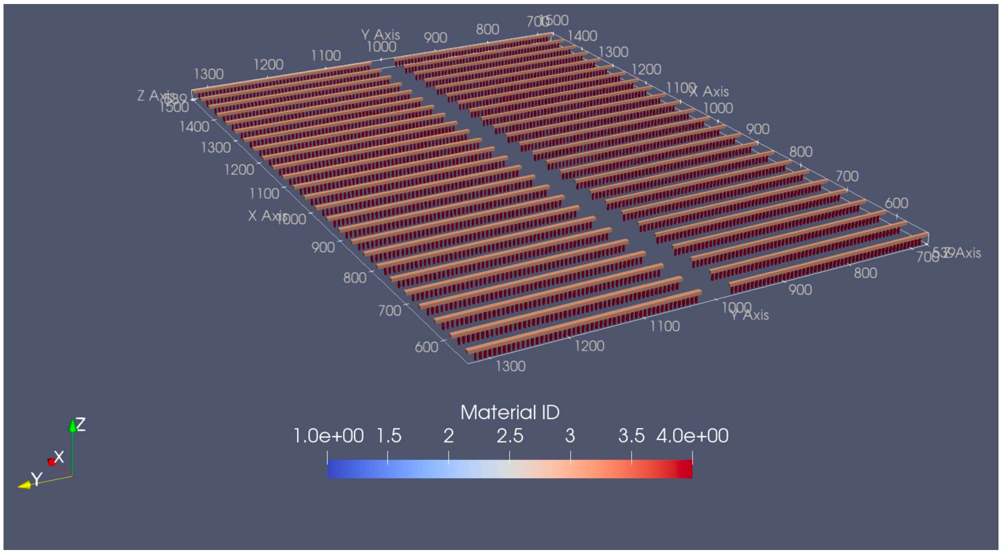

Figure 2-6. **Discretization of the repository with 20 m far field size.**

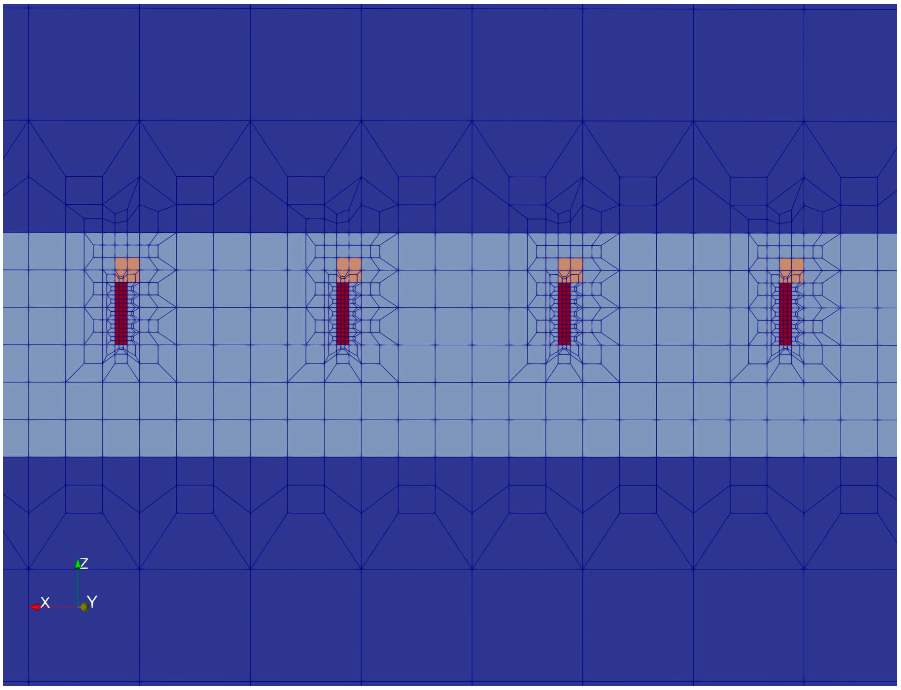

Figure 2-7. **Discretization of the deposition holes and drifts with 20 m far field size.**

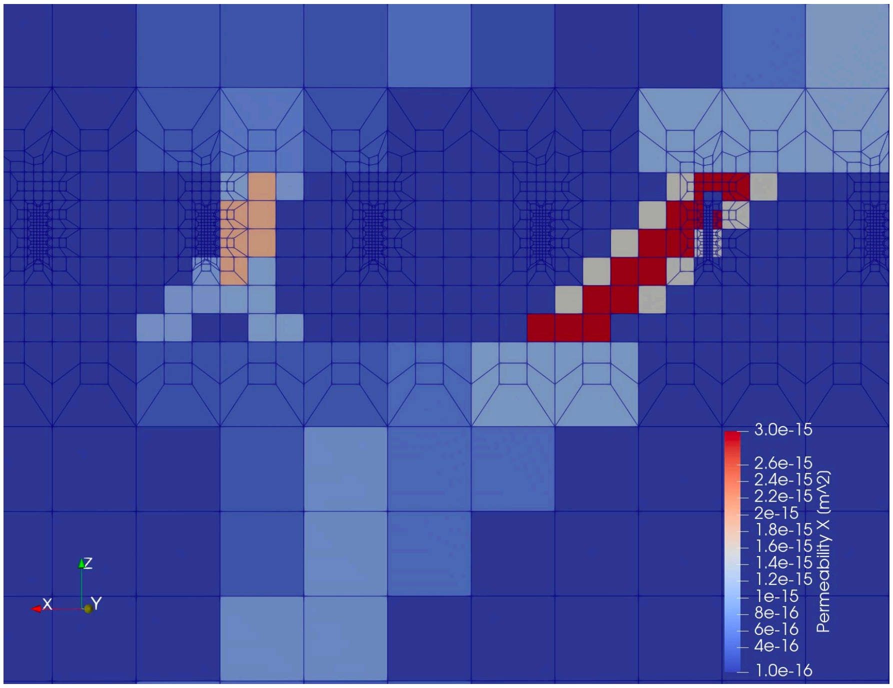

Figure 2-8. Upscaled fractures near the repository using cell size of 20/3 m.

Table 2-1 shows the grid value of each parameter based on a 20 or 25 m grid size vs the value specified in the task specification. The 20 m grid cell size results in closer sizing to the task specification for all parameters except for the volume of the canister. Therefore, both grid sizes are implemented and tested to see if the smaller volume of canister in the 20 m grid affects the transport results.

Table 2-1. Sizes of parameters meshed in Cubit vs Task Specification.

Parameter	Value with Grid Size 20 m [m]	Value with Grid Size 25 m [m]	Value in Task Specification [m]
Deposition hole spacing	5.93	5.55	6
Canister dimensions	0.74 × 5.18	0.9 × 5.55	1.05 × 4.9
Drift spacing	40	41.66	40
Drift floor (z value)	551.11	550	550
Drift tunnel dimensions	4.44 × 4.44	5.55 × 5.55	4.2 × 4.8
Deposition hole dimensions	2.22 × 8.88	2.77 × 8.33	1.75 × 8.155

2.1.8 Output Metrics

Three different surfaces of interest were defined at the top of the domain (z=1000 m) seen in Figure 2-9. The surface of the high point (0 m < x < 1700 m), the surface of the hillslope (1700 m < x < 3700 m), and the surface of the low point (3700 m < x < 5000 m). The performance assessment results are then compared in the following ways: (1) steady state liquid flow across the high point, hillslope, and low point with time, (2) tracer mass flow across the hillslope and low point with time, (3) largest tracer mass flow across the low point and hillslope, and (4) tracer inventory remaining in the repository with time.

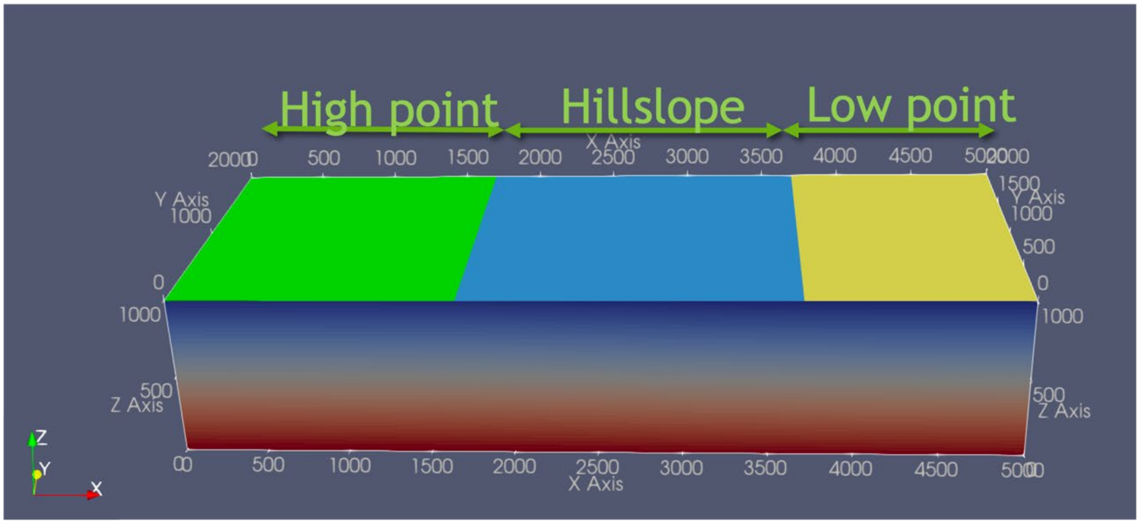

Figure 2-9. **Surfaces on top of domain used for output metrics.**

2.1.9 Preliminary Results

Steady state flow is implemented using PFLOTRAN Richards mode and transport is simulated using PFLOTRAN Global Implicit Reactive Transport (GIRT) mode. The initial conditions for the steady state flow simulation are created by running the top pressure boundary condition on a 2-D model to steady state and using this to populate the 3D model (Figure 2-10). The 3D simulations were run on 8 nodes and 288 processors. The 20 m grid for Realization 1 contains 3,454,936 total cells and the 25 m grid contains 2,051,032 total cells. The 25 m grid completed in ~10 minutes while the 20 m grid took ~496 minutes to complete on Realization 1. Then, an initial test on the effect of the stochastic realizations on the outputs were run for each realization on the 25 m grid.

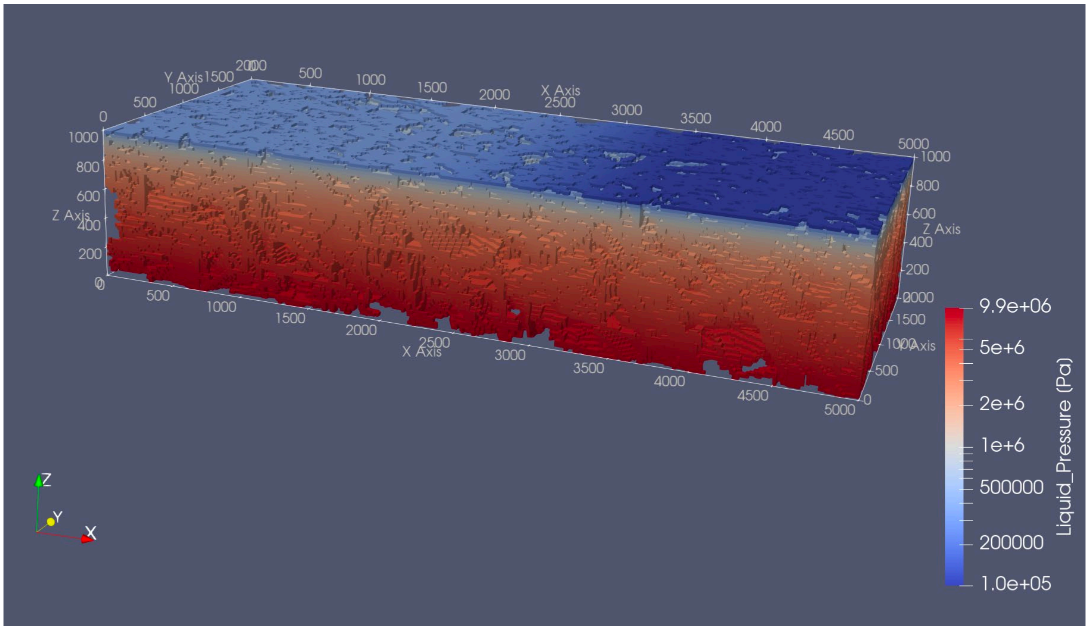

Figure 2-10 **Steady state flow solution.**

The source terms for the tracers are simulated in PFLOTRAN using the Waste Form Process Model. The model contains three main components: the waste form canister, waste form object, and the waste form release mechanism.

- The waste form canister controls the timing of the canister breach and performance of the canister after the breach.
- The waste form object tracks the concentrations of radionuclides in the object. Once the canister breaches, the waste form object dissolves according to the dissolution model defined by the waste form mechanisms.
- The waste form mechanism defines the behavior of each specific waste form type and contains the density, initial radionuclide inventory of the waste form type, and pointer to the waste form dissolution model.

First, the steady state flow of water (kg/y) for each of the three surfaces was calculated for Realization 1 (Figure 2-11). In Figure 2-11 positive values represent outflow and negative values represent inflow. (Recall that flow is driven by the pressure gradient across the top surface shown in Figure 2-1.) The two grid sizes show good agreement with one another. Since simulation results on the two grids are similar, the faster 25 m grid simulations are used for comparison of the fracture network realizations. The flux is then plotted for all upscaled fracture network realizations using the faster 25 m grid (Figure 2-12).

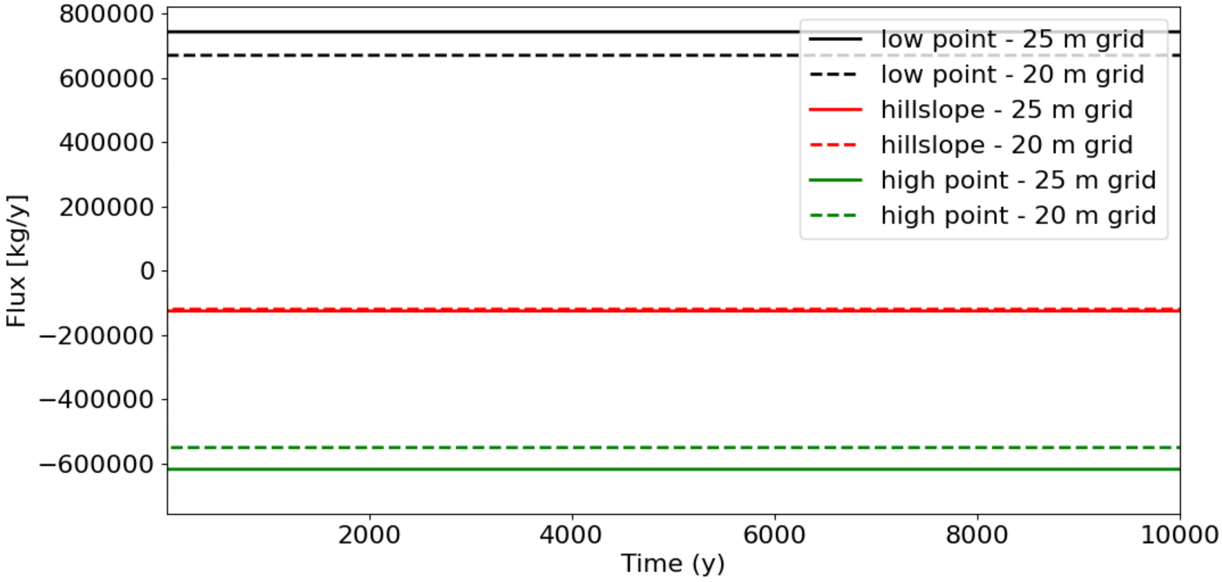

Figure 2-11. Steady state flow for high point (green), hillslope (red), and low point (black) for 20 m grid (dashed) and 25 m grid (solid) on Realization 1.

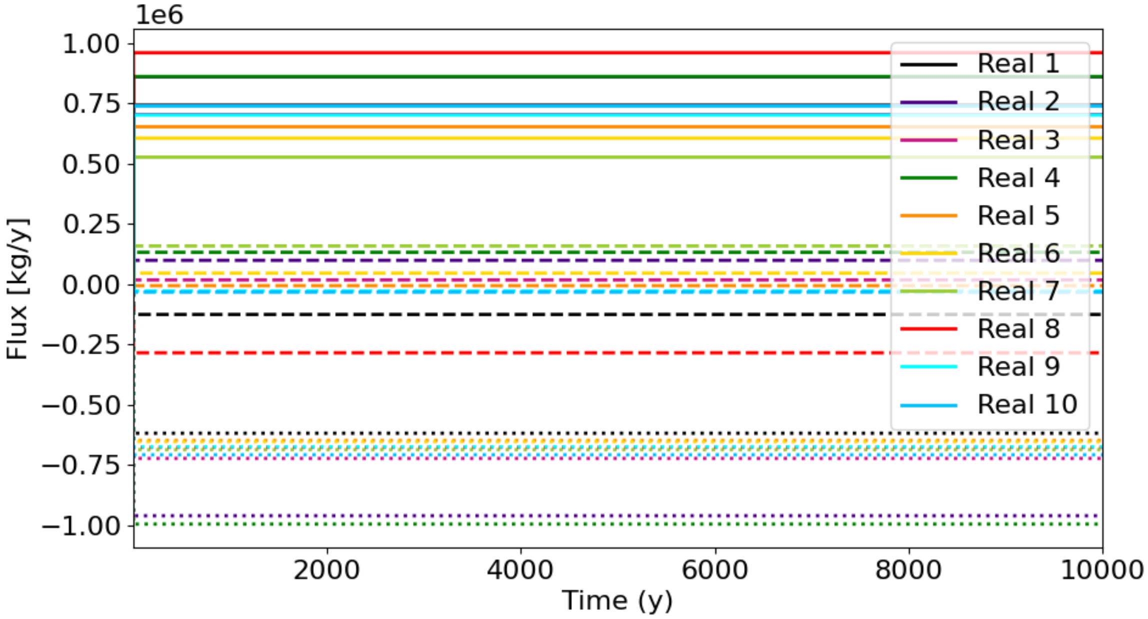

Figure 2-12. **Steady state flow for all realizations on the 25 m grid of high point (dotted), hillslope (dashed), and low point (solid).**

Figure 2-13 and Figure 2-14 show the Tracer 1 and 2 moving through the domain and repository at a cutaway in the domain at y=1000 m at 100 years for Realization 1. After 100 years, significant amounts of Tracer 1 and Tracer 2 still remain in the repository but a portion of both tracers has migrated east through the fractures and exits across the low point of the surface. Higher concentrations of Tracer 1 compared to Tracer 2 are seen at the low point surface. Both figures show that the tracers are largely confined to the fractures.

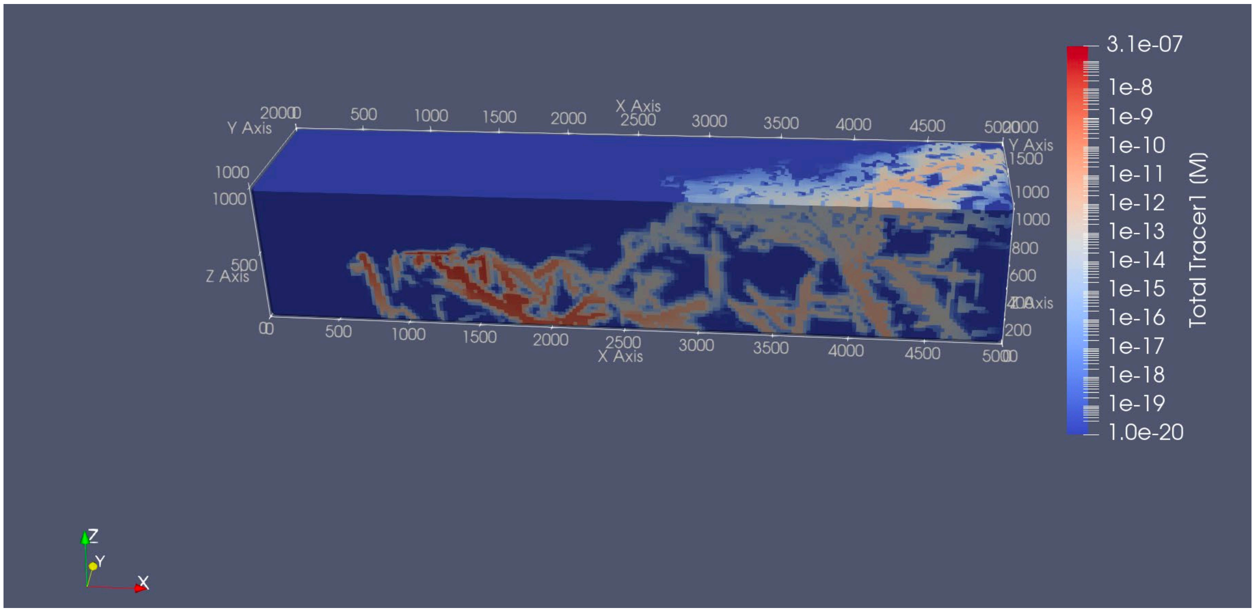

Figure 2-13. **Tracer 1 moving through the domain at a cutaway of y=1000 m at 100 years for Realization 1.**

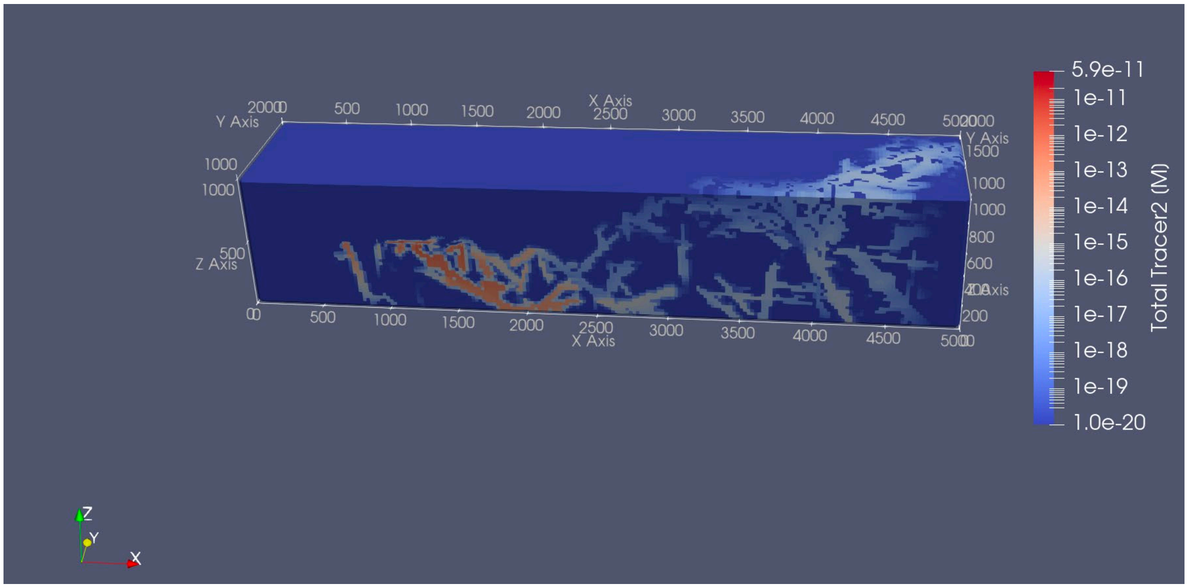

Figure 2-14. Tracer 2 moving through the domain at a cutaway of y=1000 m at 100 years for Realization 1.

Tracer inventory remaining in the repository from the cumulative release of each tracer is calculated at prescribed time intervals using the TOTAL_MASS_REGIONS keyword within the MASS_BALANCE_FILE output in PFLOTRAN. A region spanning the entire repository was defined. Within this region, total mass of each tracer at each time point is calculated and output. Figure 2-15 shows the results for Tracer 1 and Tracer 2 for the 20 and 25 m grid in Realization 1. A large amount of both tracers still remain in the repository at the end of the simulation, with more remaining in the 25 m grid as compared to the 20 m grid. Figure 2-16 shows the mass remaining in the repository for all realizations in the 25 m grid. Tracer 2 behaves similarly for all realizations while Tracer 1 concentration shows increasing spread at later times.

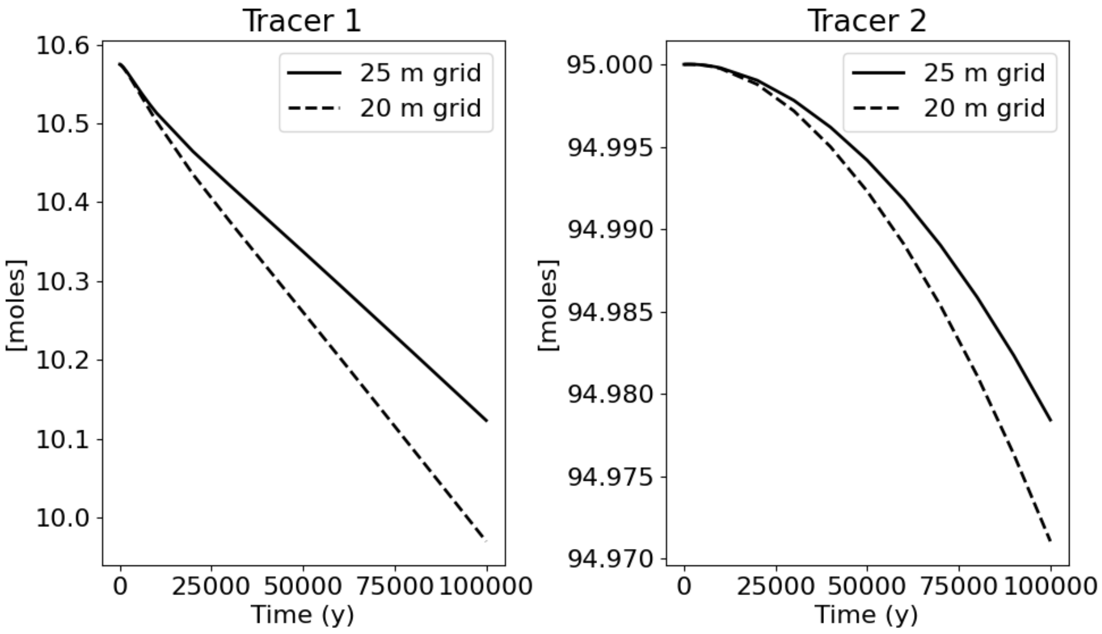

Figure 2-15. Mass of Tracer 1 (left) and Tracer 2 (right) remaining in the repository on the 20 m grid (dashed) and 25 m grid (solid) on Realization 1.

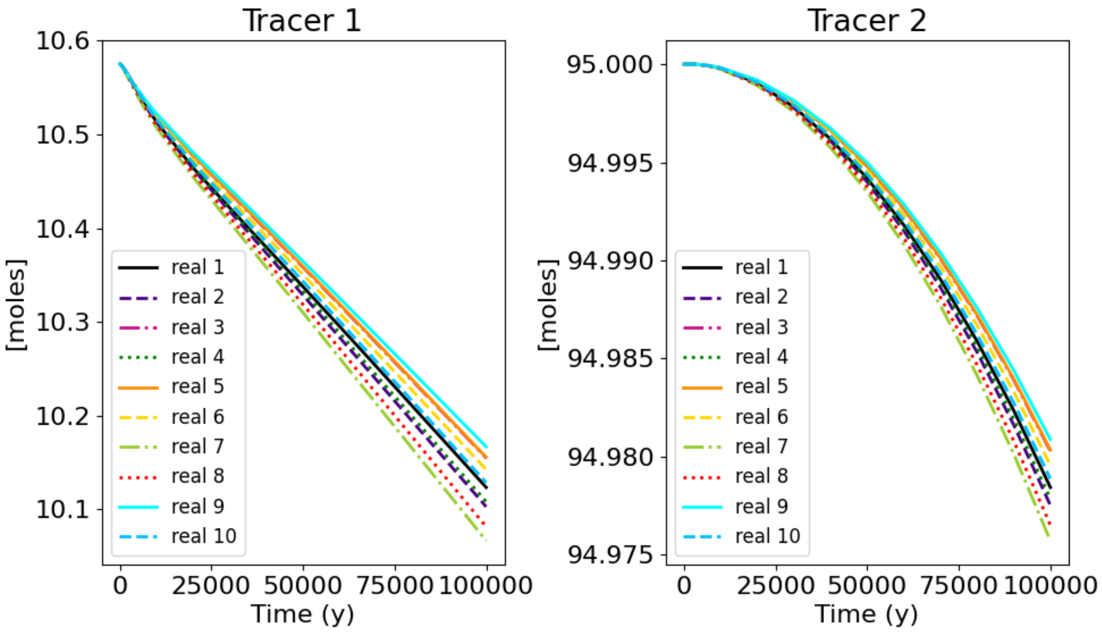

Figure 2-16. Mass of Tracer 1 (left) and Tracer 2 (right) remaining in the repository for all realizations on the 25 m grid.

The cumulative mass (moles) and mass flow (moles/year) across the hillslope and the low point surface can be seen in Figure 2-17 and Figure 2-18 respectively. This was calculated using the INTEGRAL_FLUX card in PFLOTRAN, which integrates fluxes over polygons defined by the surface coordinates of the hillslope and low point. The two grids are in good agreement with one another. The results for the hillslope and low point on all realizations for the 25 m grid can be seen in Figure 2-19 and Figure 2-20 respectively. Cumulative mass flow and mass flow over the hillslope and low point are highly dependent on the stochastic realization.

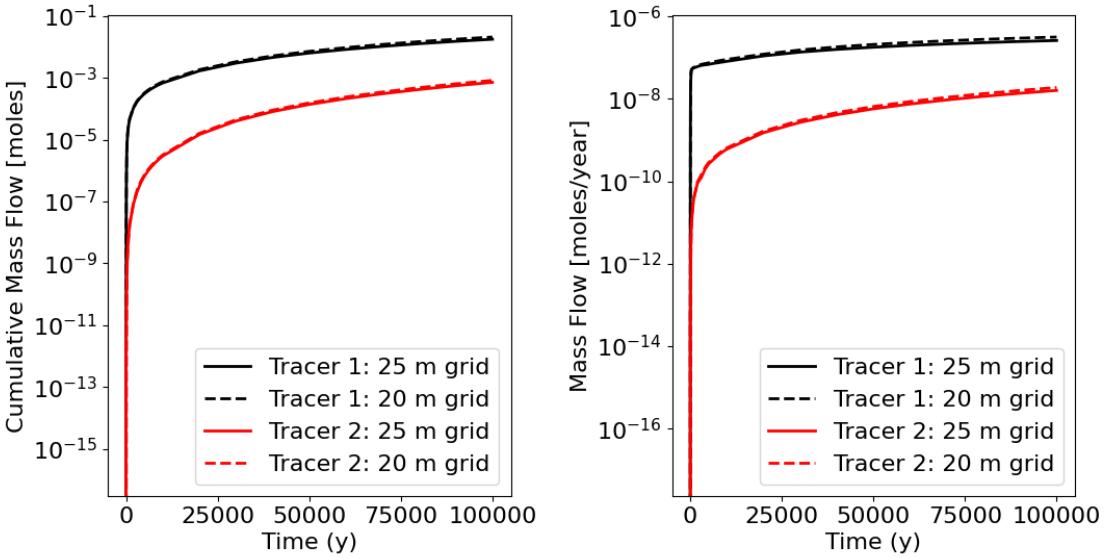

Figure 2-17. **Cumulative mass flow (left) and mass flow rate (right) across the hillslope on Realization 1 for both the 20 and 25 m grid resolution.**

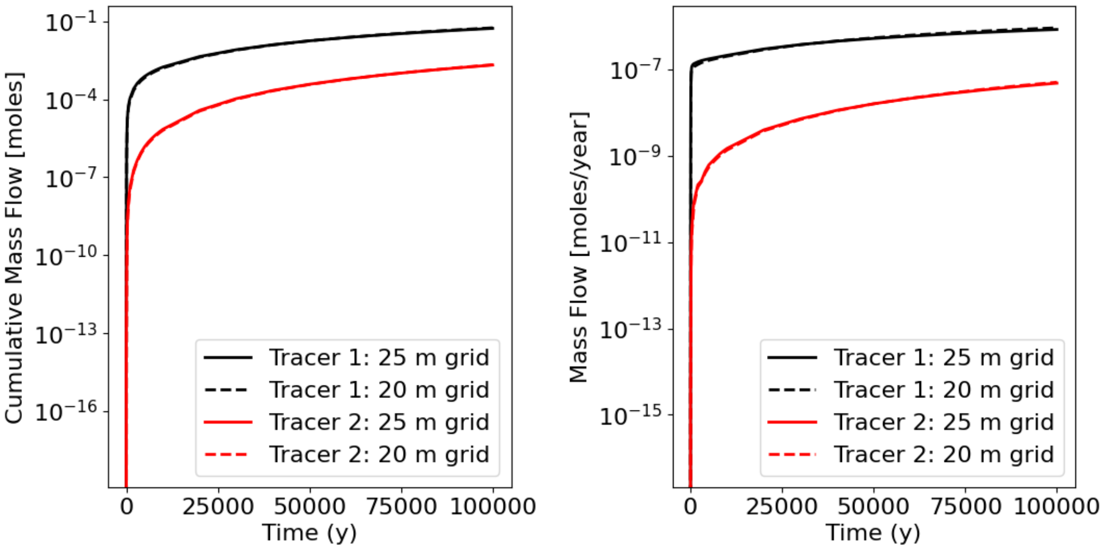

Figure 2-18. **Cumulative mass flow (left) and mass flow rate (right) across the low point on Realization 1 for both the 20 and 25 m grid resolution.**

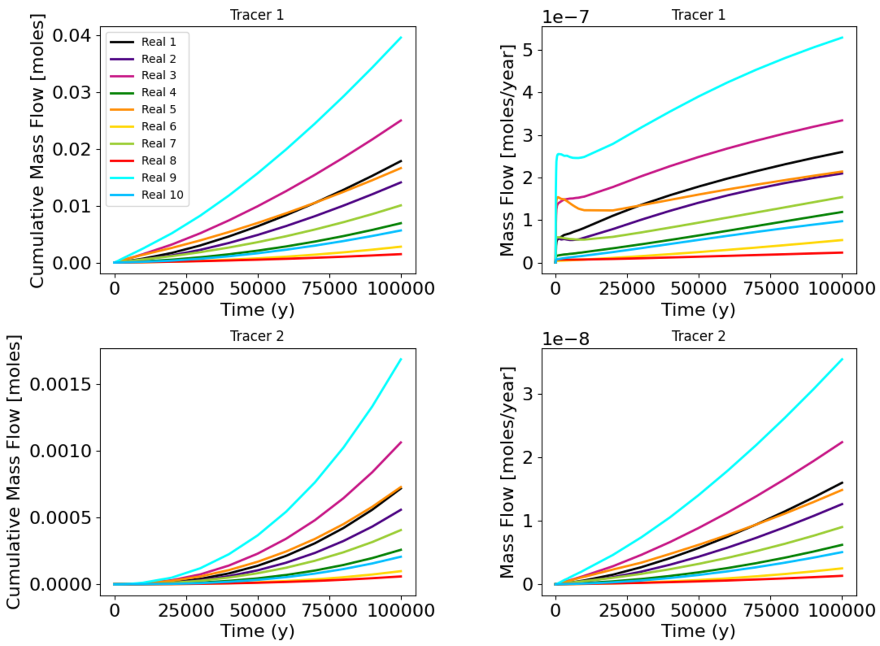

Figure 2-19. Cumulative mass flow (left) and mass flow rate (right) across the hillslope for all fracture network realizations on the 25 m grid.

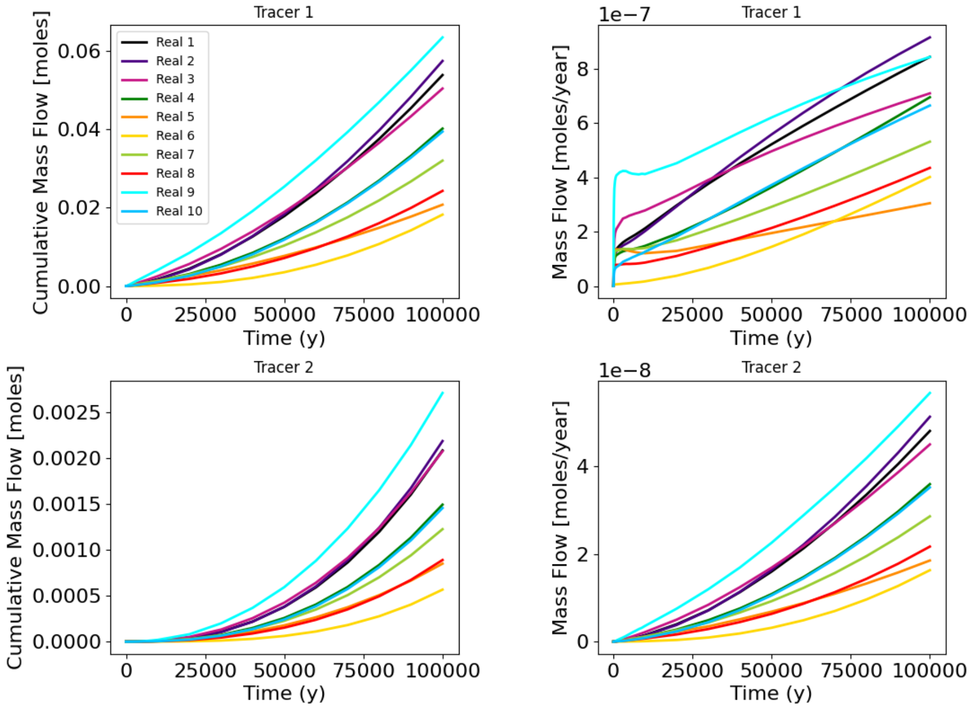

Figure 2-20. Cumulative mass flow (left) and mass flow rate (right) across the low point for all fracture network realizations on the 25 m gird.

The cumulative mass flow over the area on the low point with the largest mass flow is shown in Figure 2-21 for the 20 m grid and Figure 2-22 for the 25 m grid on Realization 1. To calculate where the maximum mass flow occurred, multiple integral flux cards were defined over each cell on the low point and then post processed to find the maximum mass flow. The largest mass flow occurs over areas where deterministic fractures intersect the top surface. For the 20 m grid, the largest mass flow was at the grid cell covering 3880 m < x < 3900 m and 840 m < y < 860 m. For the 25 m grid the largest mass flow was found at the grid cell covering 3900 m < x < 3925 m and 750 m < y< 775 m. This is near the location where the deterministic fracture 5 (peach color in Figure 2-3) intersects the top of the domain. It is also above the flow path from near the repository to the surface created by the intersection of deterministic fracture 2 (light blue in Figure 2-3) and fracture 5. Future work includes post processing the output to find values for the hillslope and the remaining realizations.

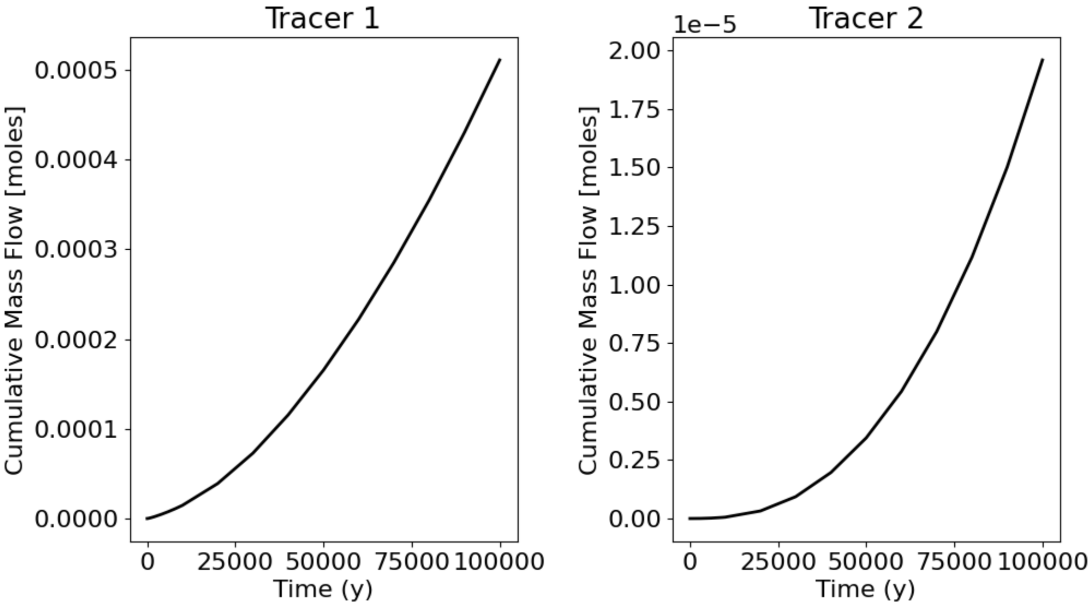

Figure 2-21. Cumulative mass flow at the point on the low point where the maximum mass flow occurred on the 20 m grid in Realization 1.

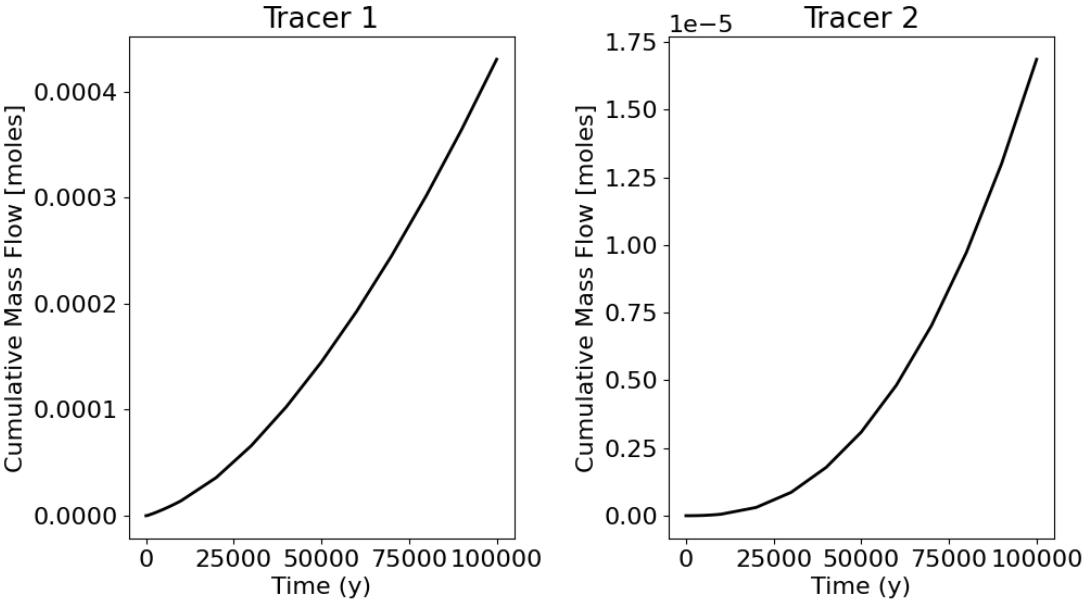

Figure 2-22. Cumulative mass flow at the point on the low point where the maximum mass flow occurred on the 25 m grid in Realization 1.

In conclusion, this year we have made significant progress on completing the Task F1 PA simulations. All ten realization of the mesh have been simulated on the coarser, 25 m mesh. Preliminary results indicate that tracers migrating from the repository mostly discharge in the low point region; however, there is also sizeable discharge in the hillslope region. In FY23 additional work will be performed to pinpoint the locations of the maximum tracer discharge so that the maximum mass flux can be calculated and compared for all fracture network realizations.

Task F1 will continue to evolve as the F1 teams make progress, work through problems, and continue to plan their next steps. Potential additions to the reference case include simulating scenarios involving early vs later waste package failures (due to a low probability of undetected mechanical defects), the addition of matrix diffusion, addition of a radionuclide decay chain, waste package failures due to glacial loading, and emplacement of a pumping well at a receptor location. Propagation of uncertainty and sensitivity analyses could become an increasingly important activity in FY23 depending on teams’ interest and progress. Probabilistic simulation as a major focus of Task F1, however, may be pushed to the next four-year phase of DECOVALEX (2024-2027).

2.2 Salt Reference Case (Task F2)

The salt reference scenario has been developed collaboratively between the Task F2 teams since the initiation of Task F2-Salt in August 2020. Scenario development continues as complexity is added in an incremental fashion. The base case will not focus on an undisturbed scenario for a salt repository. It has been shown through multiple performance assessments (e.g., RESUS, KOMTESS, ISIBEL and VSG – Bollingfehr et al., 2008; Beuth et al., 2012; Bollingfehr et al., 2017; Bollingfehr et al., 2018; Bertrams et al., 2020) that for an undisturbed scenario, there are no radiological consequences within 1,000,000 years for disposal in salt formations because of salt’s very low permeability and moisture content. Additionally, the integrity of rock salt is maintained for at least 1,000,000 years for salt rock barriers greater than 200 m in thickness (i.e., the scenario presented here), which provides no pathway through permeable fractured anhydrite, boudinage, or isolated salt blocks. We model a scenario that assumes the shaft seals fail 1,000 years after repository closure, allowing an influx of brine from overlying aquifers down the shafts and into the repository.

As discussed previously, staged development of models is planned, building up to a full PA. This stepwise process is done to ensure the consistency between each team's modeling efforts as complexities are added. The staged development is:

(1). Flow and radionuclide mobilization and transport (problem description will include variably saturated initial conditions)
(2). Include drift convergence (salt creep and backfill consolidation will be considered)
(3). Include heat flow and temperature-dependence of drift convergence
(4). Include model uncertainty in backfill consolidation model
(5). Include gas generation

The description of the engineered and natural barrier systems in the task specification (LaForce et al., 2022) is being updated as the exercise progresses so that necessary information is available at each stage of model development.

2.2.1 Geologic Setting

The generic geological cross section of a salt dome developed for the RESUS project (Bertrams et al. 2020) is simplified to six homogeneous geologic units for use in this reference case (Figure 2-23). It is assumed that the salt dome geometry shown in Figure 2-23 extends 9 km perpendicular to the plane of the cross section. The ground surface is 50 m above mean sea level (amsl) and the top of the salt dome is roughly -150 m amsl. The base of the salt diapir is at about -3150 amsl and is underlain by basement rock. The repository is mined at a depth of 850 m below the ground surface (-800 m amsl).

The basin fill around the salt diapir is assumed to have a higher permeability and effective porosity than the salt dome. Above the salt structure and cap rock the overburden consists largely of unconsolidated sediments with higher pore volume relative to the deeper units. This model unit is classified as a freshwater aquifer. Advection and dispersion may need to be considered, but as observed in the 2D benchmark case, dispersivity will be likely dependent on grid discretization of the overburden at the PA scale.

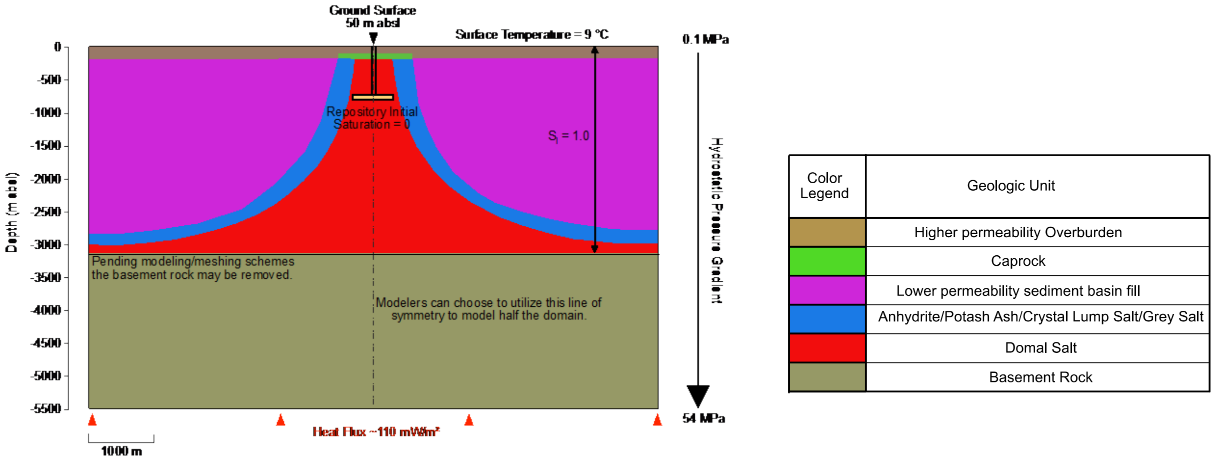

Color Legend	Geologic Unit
🟫	Higher permeability Overburden
🟩	Caprock
🟪	Lower permeability sediment basin fill
🟦	Anhydrite/Potash Ash/Crystal Lump Salt/Grey Salt
🟥	Domal Salt
🟫	Basement Rock

Figure 2-23. Geological cross-section with model units for the generic salt reference case. The model units are simplified from Bertrams et al. (2020). The repository location and initial model conditions are shown.

2.2.2 Natural Barrier System

The natural barrier system is comprised of the five simplified geologic units illustrated in Figure 2-23: the salt dome (which is the host rock); a mixed evaporite sequence flanking the salt dome; the caprock; the lower-permeability basin fill; and the higher-permeability overburden. The basement rock is not considered part of the natural barrier and is omitted from the simulation model. In the geological model of the salt dome, the host rock consists of homogeneous rock salt (halite), which has no connected pore space and thus no permeability greater than 10^{-22} m^2 so that mass transport is determined solely by diffusion (Bertrams et al. 2020).

The flanks of the salt structure consist of a potash seam, an evaporitic sequence of salt and anhydrite, and a clayey strata, represented by a single formation defined by bulk properties with low porosity and permeability. A caprock has formed above the salt structure. This model unit consists largely of gypsum or of the residual formations of the various evaporitic strata following the salt structure and the permeability is assumed to be low.

2.2.3 Geochemical Environment

In a complex geologic system, solubility limits and adsorption behavior would be controlled by local porewater chemistry and mineral assemblage. For the salt reference case, simplifying assumptions are made and radioelement solubility limits throughout the model domain are held constant at values calculated for a concentrated, reducing brine as in previous salt reference case simulations conducted in the U.S. (e.g., LaForce et al. 2020; Clayton et al. 2011). The full details of the geochemical model are not necessary for the results presented here and are in the task specification (LaForce et al. 2022).

2.2.4 Engineered Barrier System

The repository is oriented so the emplacement drifts are perpendicular to the salt dome in Figure 2-23. With the repository oriented this way and positioned in the center of the salt dome there is a line of symmetry through the repository and salt dome that modelers can choose to utilize to reduce the computational resources required for simulation. The repository is accessed by two shafts that extend vertically out of the salt dome formation through the cap rock to the surface. The access shafts are designed this way based on the design of the shaft seal as it is specifically engineered to be an effective seal within a salt formation.

2.2.5 Emplacement Drifts

Within the repository there are three sets of 25 emplacement drifts with a drift spacing of 35 m center-to-center. For heat-generating SNF waste, the waste packages are placed end-to-end in emplacement drifts 90 m long with 10 waste packages per drift for a total of 500 POLLUX-10 waste packages. The vitrified waste emplacement area consists of 25 emplacement drifts with 35-m center-to-center drift spacing. Each 45-m-long drift contains 10 vertical boreholes and two waste packages per borehole, giving a total of 500 vitrified waste packages (Figure 2-24). The spacing of the drifts and waste packages should be sufficient to ensure that peak temperatures do not exceed 100 °C (Bertrams et al., 2020.). Details of the waste canisters and inventories are in LaForce et al. (2022) and are not included here because the current stage of the performance assessment is comparison of the fluid pressure and flow in the repository, which are unaffected by the presence of waste canisters.

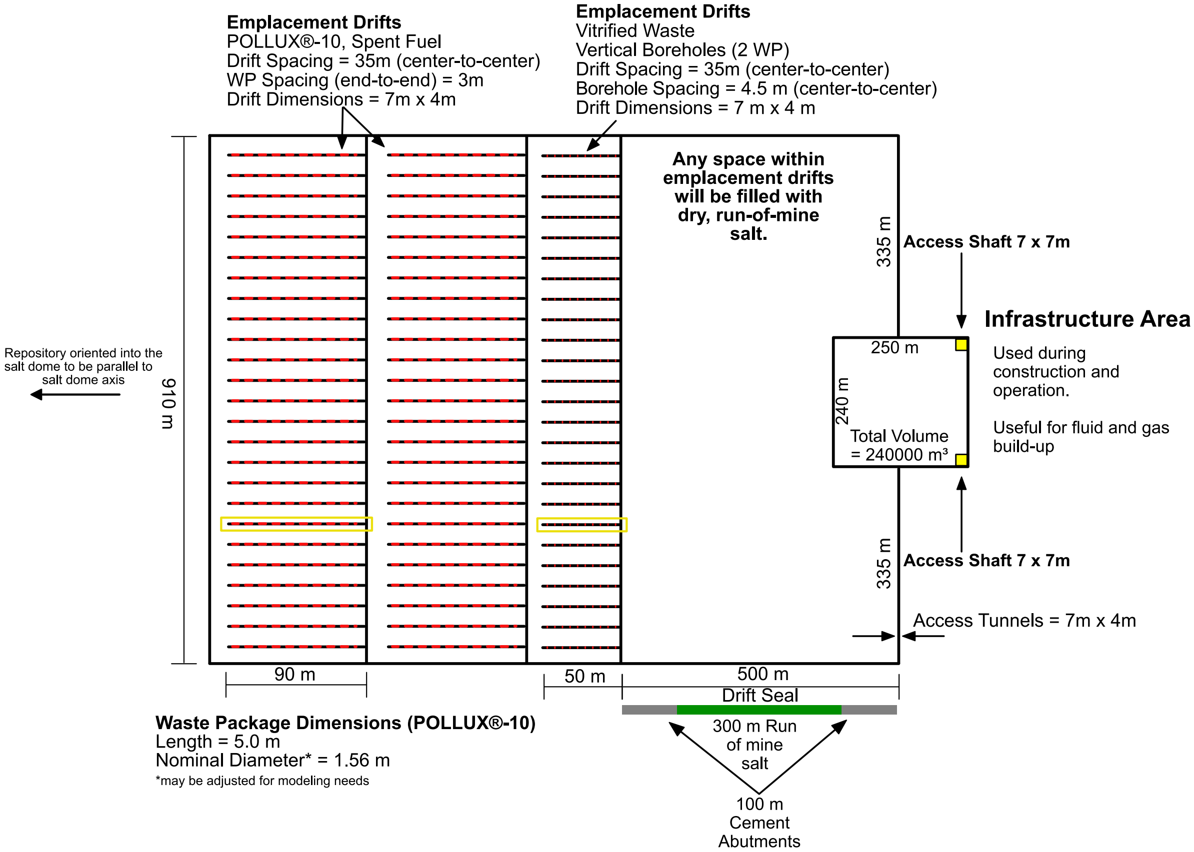

Figure 2-24. **Schematic of the waste repository in a generic salt dome. The drifts outlined in yellow will be for used for comparisons between each teams' results.**

2.2.6 Non-waste Area Seals and Backfill

Two drift seals are placed in the 500-m long tunnels connecting the infrastructure area to the emplacement area. Emplacement drifts and access tunnels are backfilled with dry run-of-mine salt. Due to the compaction of the run-of-mine salt backfill, the backfill will develop a sealing effect over time that is comparable to that of the surrounding, undisturbed geological barrier.

Access to the repository is provided by two shafts connecting the infrastructure area to the ground surface and are utilized during the construction and emplacement phases of disposal. The shaft landing stations and the infrastructure area are backfilled with gravel which is assumed to not compact. The gravel forms a permanent pore storage area to significantly delay increases in brine pressure at the drift seals. Full details are in LaForce et al. (2022).

2.2.7 Shaft Seal

The specifications of the shaft properties are provided as an example of the collaborative conceptual model building that has taken place in Task F2-Salt. The original task specification assumes a homogeneous shaft whose permeability increased by two orders of magnitude at the time of shaft seal failure at 1,000 years. One partner team proposed a layered shaft seal design shown in the illustration in Figure 2-25 as a more suitable level of complexity based on their experience and the capabilities of their modeling software. The top of the shaft is a high-permeability filter, and the uppermost sealing segment (Sealing Element 1) is bentonite, which limits advection due to its low permeability and retards radionuclide transport due to adsorption. The rest of the shaft contains segments designed to seal and segments designed to act as reservoirs for fluid influx.

Test simulations (not shown) were conducted that showed that similar results could be obtained from a layered and heterogeneous model, provided that the homogeneous model properties were updated to be the harmonic average of the permeability and the arithmetic average of the porosity of the layered model. The task specification Revision 8 (LaForce et al. 2022) was updated to include the parameters for the layered model and to update the homogeneous model properties before and after shaft seal failure to ensure consistency between the models.

A second update to the shaft model was also added to clarify boundary condition at the top. Conceptually, a shaft completed all the way to the surface would have low or even zero liquid saturation at the top, but one completed only as far as the base of the overburden would result in a fully saturated liquid top boundary condition. Test simulations (not shown) indicate that the change in the top boundary condition can greatly change the magnitude of flow into the shaft. As many teams are building fully or sequentially coupled models where the shaft and overburden are in separate models, the task specification Revision 8 (LaForce et al. 2022) was updated to clarify that the top of the shaft will be in contact with water-saturated overburden, so a like-to-like comparison can be conducted across all models.

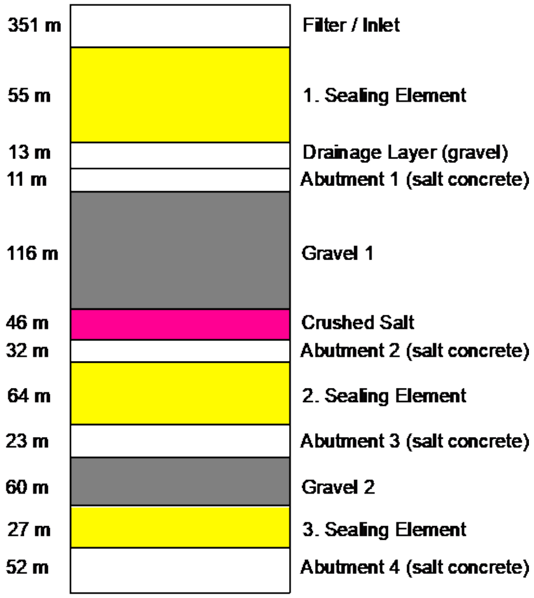

Figure 2-25. Shaft seal for generic salt dome repository (modified from Rübel et al. (2016) by Richard Jayne).

2.2.8 Outputs for Comparison

This section provides a list of outputs for comparison to compare/contrast modeling schemes, numerical models, and assumptions made between the participating teams. In the final report comparisons will be made for a series of radionuclide and fluid fluxes within the repository, shaft and into the overburden. As the model in the current task specification does not contain drift convergence or waste decay heat there is no mechanism to push fluid out of the repository, so comparisons are limited to fluid pressure and fluid flux within the repository. All comparisons will be conducted qualitatively. Four points of comparison are:

- Plot the average liquid pressure and saturation in the shaft as a function of time.
- Plot the average liquid pressure and saturation in the 100-m Sorel cement segment of the drift seal nearest the waste as a function of time.
- Plot the average liquid pressure and saturation in the spent nuclear fuel drift highlighted in Figure 2-24 as a function of time.
- Plot the average liquid pressure and saturation in the high-level waste drift highlighted in Figure 2-24 as a function of time.

2.2.9 Simulation Model Construction

This study combines Voronoi meshing of the Task F2 geologic repository and TH numerical modeling to investigate the pressure and saturation evolution of the repository within domal salt. The workflow used here to create a Voronoi mesh for PFLOTRAN by using two programs; LaGriT (LANL, 2017) and Vorocrust (Abdelkader et al., 2018; 2020). LaGriT is a library of mesh generation and optimization tools in two and three dimensions that was used to create borehole- and drift-bounding surfaces for input into Vorocrust. Figure 2-26 illustrates the surfaces created in LaGriT, which consists of half the repository and one shaft, recalling that the repository was designed to have half symmetry to reduce computational needs. The current model domain is 2,000 m × 2,000 m × 2,000 m consisting of 431,072 grid cells. Vorocrust creates a 3D Voronoi mesh and Figure 2-27 shows a slice down the center of the model domain parallel to the repository at a depth of 795 m and illustrates how the mesh is highly refined around areas of interest and coarsens outward. Figure 2-28A and B are zoomed-in sections of the (A) repository and the (B) disposal drifts to illustrate the mesh refinement within and around the disposal drifts. Vorocrust can resolve the mesh around curved areas of interest while coarsening rapidly away from the area of interest, to reduce the total number of elements and computational burden. Voronoi elements, by construction, result in optimal accuracy for the calculated fluxes in finite volume simulators like PFLOTRAN. Unlike hexahedral meshes, Voronoi meshes do not have a fixed number of connections per element, which leads to a higher connectivity than structured meshes, resulting in more poorly conditioned Jacobian matrices. To address this issue, we used a constrained pressure residual pre-conditioner, which aids with the added numerical challenges associated with a Voronoi mesh (Park et al., 2021).

While steps were taken to reduce the complexity of the meshing and simulations described above, additional assumptions are made to help with numerical convergence:

(1). Currently only the domal salt geologic formation is accounted for explicitly in the model

(2). Drifts are meshed, but individual waste packages are not.

(3). Only one relative permeability model is used for all material types, van Genuchten models from LaForce et al. (2022).

(4). Shaft and drift seals are simplified into one homogeneous material

(5). Liquid saturation is initially set to 20% within the repository, drifts, and shaft

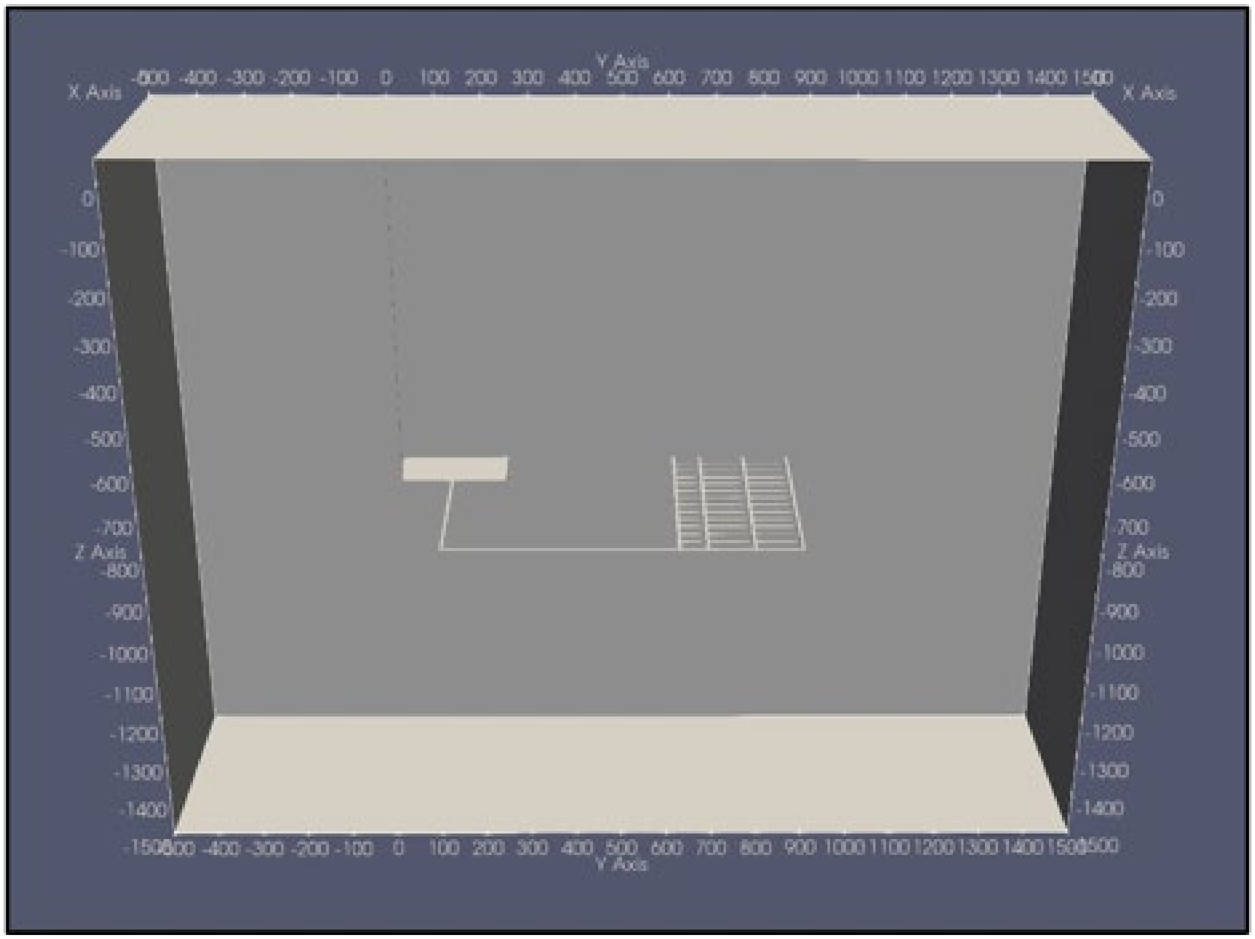

Figure 2-26. **The geologic repository mined components created with LaGriT. This surface object is used by Vorocrust to create the full mesh.**

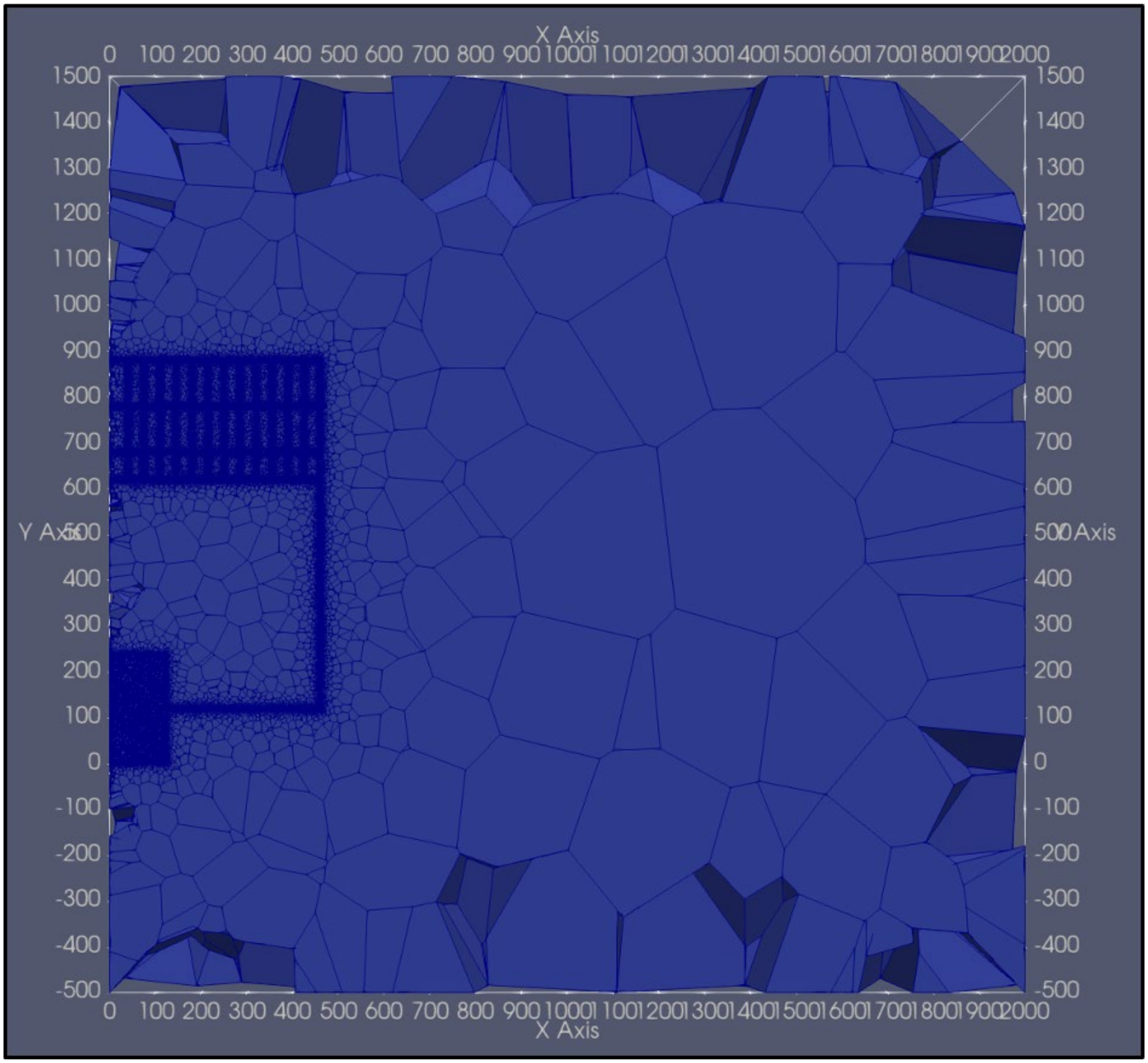

Figure 2-27. Mesh created by Vorocrust. This slice is parallel to the repository at a depth of 795m. Note the high-resolution meshing near the repository and coarsening outwards.

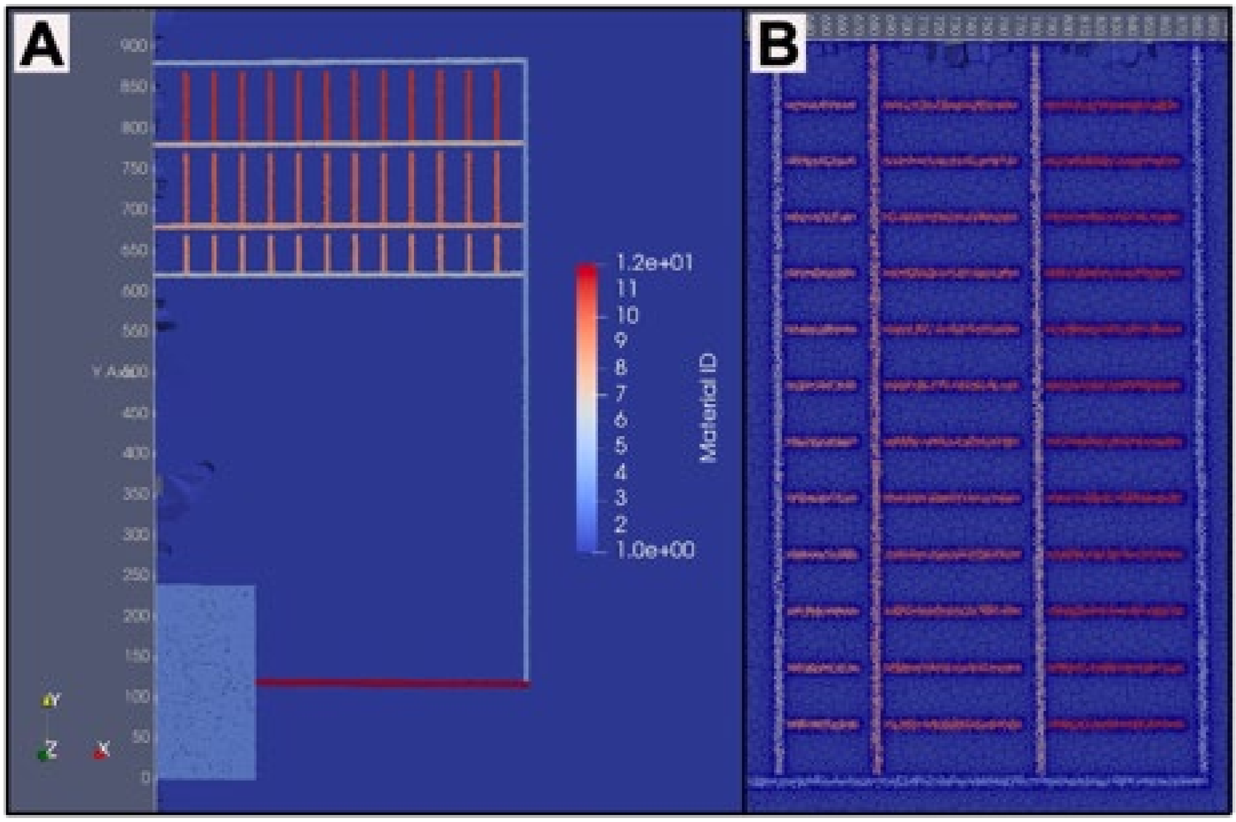

Figure 2-28. Zoomed in slices of the (A) repository and (B) disposal drifts showing the mesh.

2.2.10 Preliminary Results

The preliminary modeling of the Task F2 geologic repository using a 3D Voronoi mesh are illustrated by comparing the pressure and saturation evolution between two different flow modes within PFLOTRAN, using both General (two-phase, two component flow plus energy) and Richards (single phase, variably saturated flow) mode. Figure 2-29 and Figure 2-30 illustrate the wetting up of the repository at 10,000, 20,000, and 30,000 years for General and Richards mode, respectively. Figure 2-31 shows the average pressure and saturation as a function of time for the SNF drift A)-B), the vitrified waste drift C)-D), and the drift seal E)-F) as a function of time. (See Figure 2-24 for location of each region in the repository). The differences between the two modes are fairly small, where at 10,000 years the repository has a slightly higher liquid saturation in General vs. Richards mode. The same observation can be seen at 20,000 and 30,000 years as well. By 40,000 years, the repository is fully liquid saturation in both cases. Figure 2-31 shows that overall, the repository volumes of interest saturate slightly later in General mode.

Shaft saturation plays a critical role in this PA reference case, Figure 2-32 illustrates shaft saturation at three separate time steps at 5,000, 10,000, and 15,000 years. The current simulations are not simulating the shaft seal failure scenario, but the permeability and porosity of the shaft seal in these simulations are roughly at shaft seal failure scenario properties. The flow properties of the drift seals and backfill areas are also homogeneous throughout the model. Figure 2-32 provides an estimate of how long it will take the shaft to saturate during the shaft seal failure scenario of ~15,000 years. Due to the low permeability and brine availability, the major source of fluid for this repository analysis is hypothesized to come from flow down the shaft. While the results presented here are preliminary and are more simplified than the PA case described, these results still provide important information that will affect future simulations.

Additional simulations would be required to quantify the difference in the results between these two modes. The total simulation time differs, to simulate 100,000 years on 180 processors General mode takes 37.3 hours and Richard's mode takes 25.5 hours. As more complexity is built into these models (heterogeneity, multiple relative permeability models, geologic layers, etc.), it is possible that the simulation time difference between the modes will increase. While these results are preliminary, they do provide confidence in the current workflow and model conceptualization presented here.

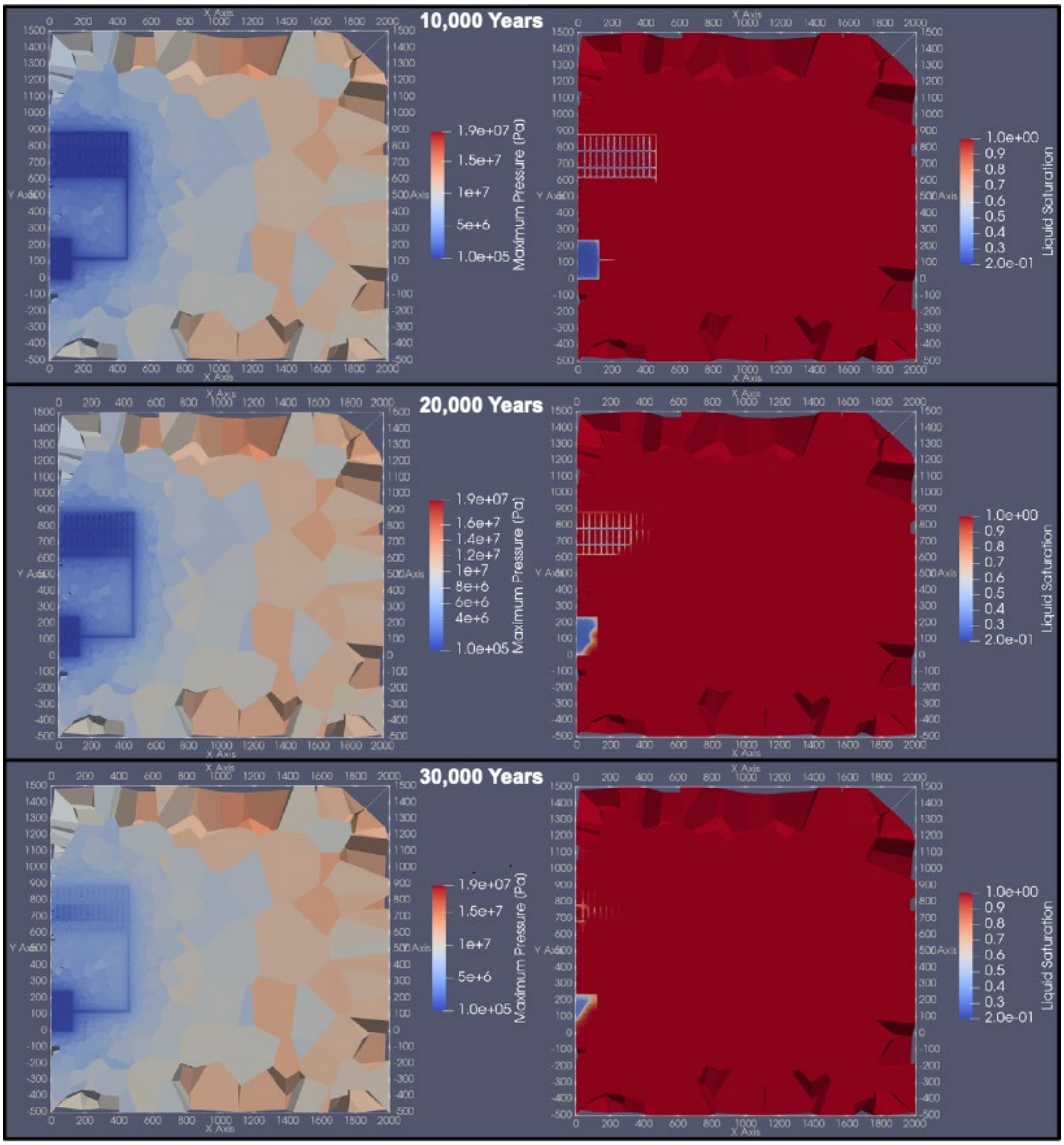

Figure 2-29. General mode results for pressure (left) and saturation (right) at 10,000, 20,000, and 30,000 years.

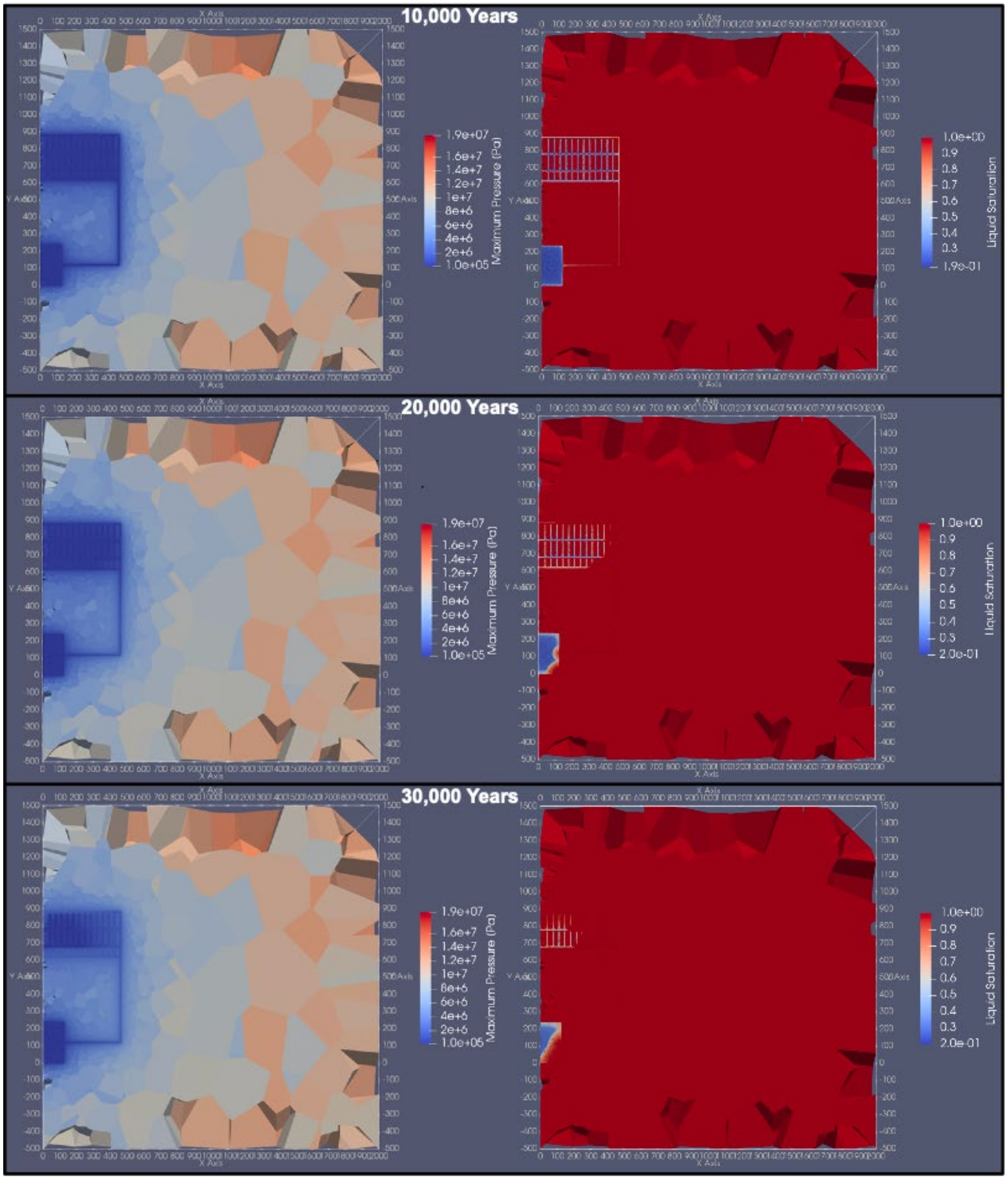

Figure 2-30. **Richard's mode results for pressure (left) and saturation (right) for 10,000, 20,000, and 30,000 years.**

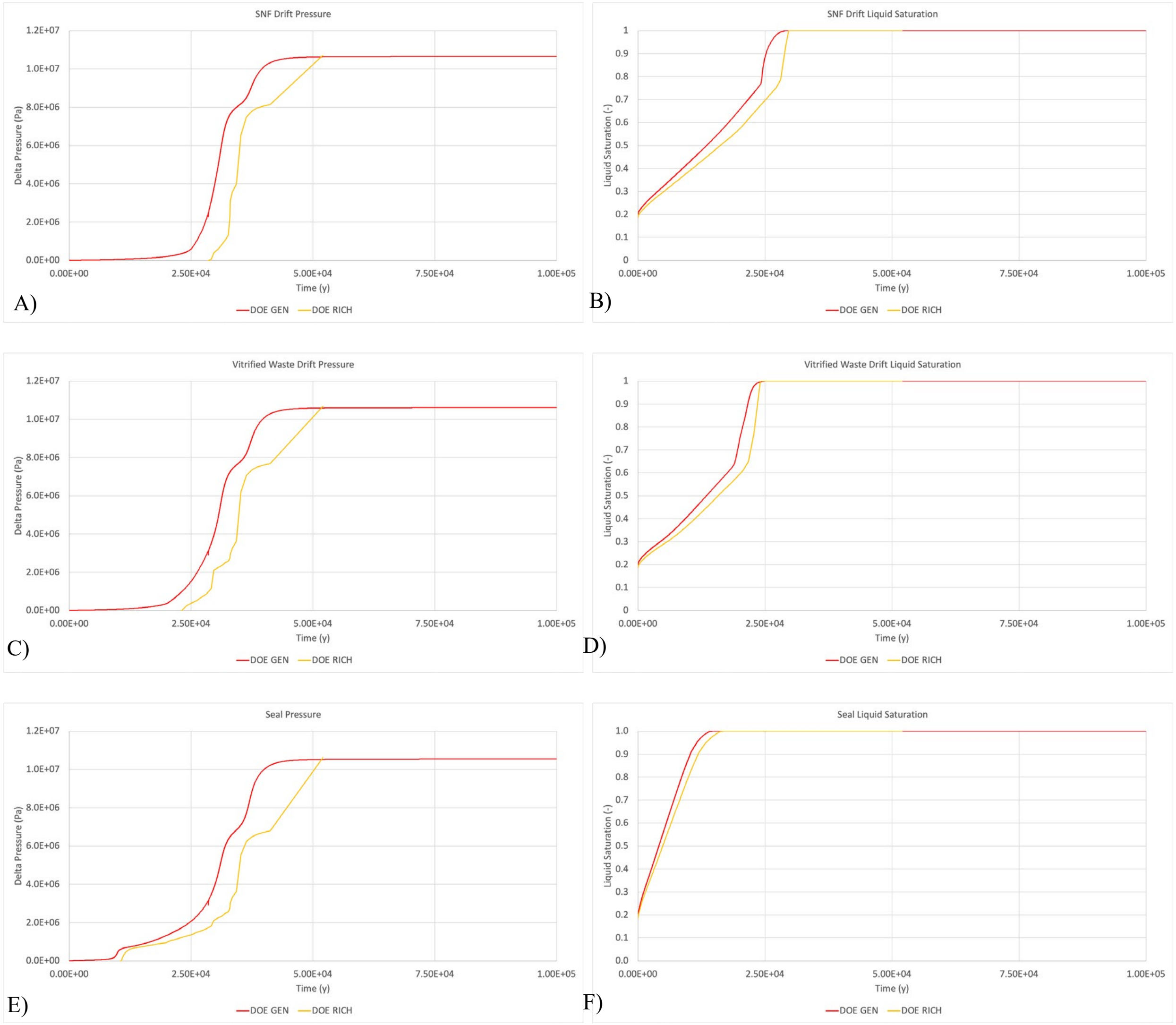

Figure 2-31. Average pressure and saturation for the regions of interest in the model comparison. (A) Pressure in the SNF drift, (B) Liquid saturation in the SNF drift, (C) Pressure in the vitrified waste drift, (D) Liquid saturation in the vitrified drift, (E) Pressure in the drift seal, and (F) Liquid saturation in the drift seal.

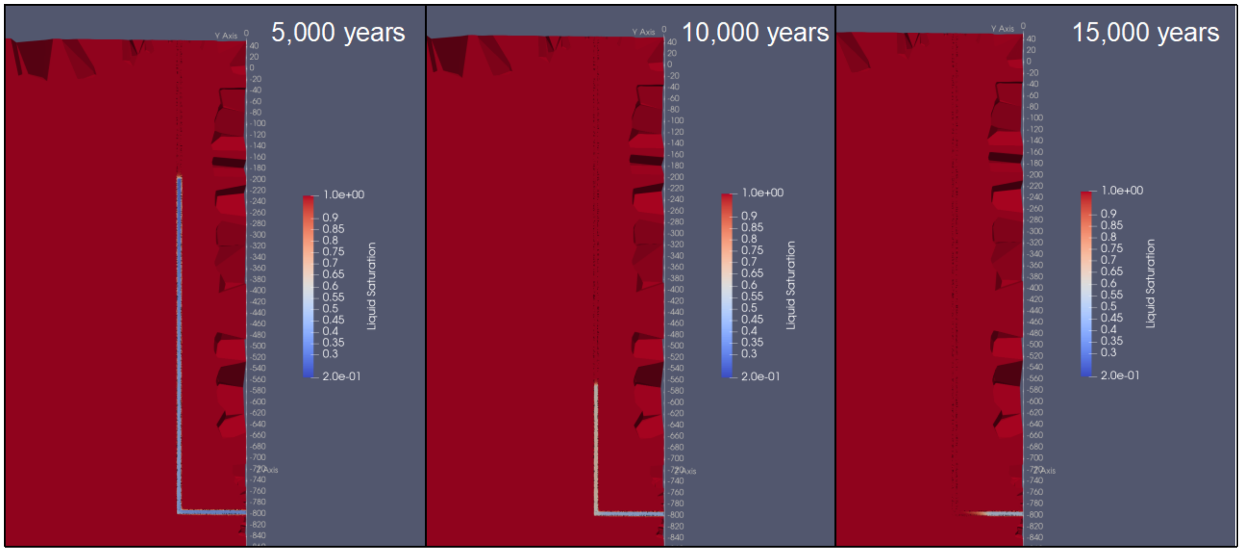

Figure 2-32. Shaft saturation in General mode at 5,000, 10,000, and 15,000 years.

2.2.11 Look Ahead

The numerical methods and model conceptualization utilized here are simplified versions of the task specification. This was done to make trouble-shooting the workflow easier. As a result, there are several assumptions and simplifications that can be changed in order to match the current task specification. These items include: using material properties specified for the disposal drifts, drift seals, and shaft seal; adding in geologic layers including the freshwater aquifer, increasing model domain size to incorporate all geologic layers; and possibly meshing the drifts and shaft seals explicitly to include all materials. Additionally, moving onto the next step in Task F2 will require the addition of creep closure, radionuclide mobilization and transport which will be done with both General and Richards mode of PFLOTRAN to continue model comparisons.

This page intentionally left blank.

3. SMALL-SCALE REFERENCE CASE STUDIES

In the near-field, the EBS and host rock influence each other thermally by heat flow, hydraulically by single- or multi-phase fluid flow, mechanically when the buffer material around the waste package swells, and chemically by exchange of radioactive solutes between groundwater and pore water in the EBS and host rock. Repository excavation disturbs the stress state and physical properties of the intact host rock by inducing fracturing around the excavated area, which is known as the disturbed rock zone (DRZ) and lies between the buffer and undisturbed host rock. Changes in thermal, hydrological, and geochemical characteristics of the DRZ will affect the overall behavior of radioactive waste repositories by redistributing the stress state of the rock and possibly creating additional pathways of radionuclide transport or fluid flow (Tsang et al. (2005), Nasir et al. (2014), Bernier et al. (2017), Zheng et al. (2017)). The coupled thermo-hydro-mechanical-chemical (THMC) behavior of the near-field system may affect advective transport of radionuclides through the repository openings and DRZ as well as diffusive transport into the host rock, impacting the evolution and long-term performance of the repository system.

This study investigates the effect of buffer swelling on solute transport in the presence of heat in the shale-hosted repository system. Mechanically induced DRZ permeability change, based on Two-part Hooke's law model (TPHM; Chen et al. (2015)), as well as temperature-saturation-dependent thermal conductivity are incorporated into the PFLOTRAN THC coupled model. PFLOTRAN is a massively parallel open source, reactive multi-phase flow and transport simulator designed to leverage high-performance computing to simulate subsurface earth system processes (Lichtner & Hammond (2012)). PFLOTRAN has been used for multi-scale and multiphysics PA simulations of deep geologic repository systems (Sevougian et al. (2019b), Mariner et al. (2020), Mariner et al. (2021), LaForce et al. (2020), LaForce et al. (2021)).

This conceptual model accounts for the following processes potentially observed in the near-field: coupled heat and multiphase fluid flow, equilibrium-controlled solute transport via advection and diffusion, and the evolution of rock physical properties in the damage zone in response to buffer swelling. Considering these multiphysics processes for the extremely long performance period (up to 10^6 years) can be computationally challenging, and thus, approximating the geomechanical behavior of the repository system through a reduced-order THMC model can be an efficient alternative to simulate the coupled effects on multiphase flow and transport in the repository system (Chang et al. (2021), Sasaki & Rutqvist (2021)).

3.1 Model Setting

3.1.1 Model Domain

The model domain represents a quarter of a waste package in the shale repository system. The center of the waste package is located at a depth of 500 m below land surface (Figure 3-1A).

Three concentric sections of waste package, buffer, and DRZ 1 m, 2.4 m, and 4.07 m in radius, respectively, are modeled in the 35 m (width) x 10 m (length) x 75 m (height) domain (Figure 3-1B). The buffer dimension is based on the size of a circular drift with a diameter of 4.8 m, and the half-length of waste package is set at 2.5 m. Model width of 35 m represents half the spacing between drifts, while length 10 m is half the distance between waste packages in a drift. With closed lateral boundaries these model dimensions represent the centermost waste package in an infinite array.

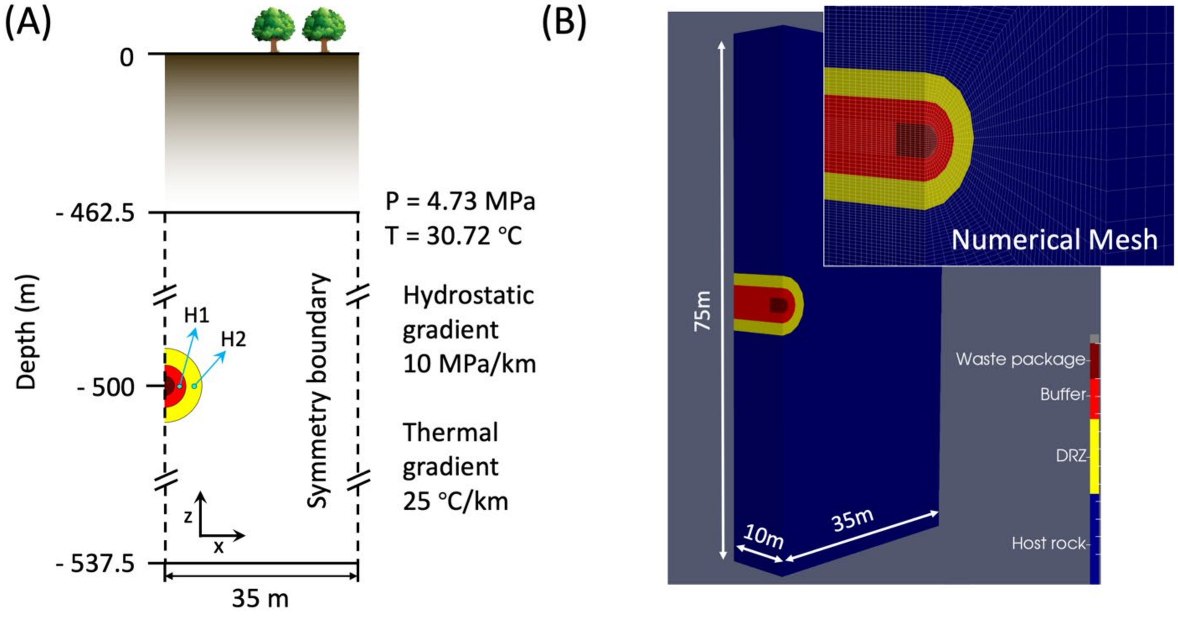

Figure 3-1. Model description and setting. (A) Schematic description of the model domain consisting of waste package (wp), buffer/spacer, DRZ, and shale host rock. (B) Numerical domain with mesh setting. The temporal evolution of concentration of radioactive isotopes are obtained at points H1 and H2 at 2.94 m and 4.315 m in x-direction within the buffer and DRZ, respectively.

Assuming the model domain is a porous medium, the waste package porosity is set equal to the fraction of void space within the section of waste package (50%) in the repository system. The waste package permeability is $1x10^{-16}$ m^2, several orders of magnitude higher than that of the surrounding materials (Table 3-1), so that flow through the waste package is uninhibited, which represents possible water seepage into the waste package. The installed package consists of a stainless-steel canister and a stainless steel overpack, and thus, the thermal properties of stainless steel are implemented for the waste package (Shelton (1934)).

Table 3-1. Model parameter values.

Flow and thermal properties				
	Buffer/Spacer	**DRZ**	**Shale host rock**	**Waste package**
Porosity [-]	0.35	0.2	0.2	0.5
Permeability [m^2]	$1x10^{-20}$	$1x10^{-18}$*	$1x10^{-19}$	$1x10^{-16}$
Density [kg/m^3]	2700	2700	2700	5000
Heat capacity [J/(kg-K)]	830	1005	1005	466
Dry thermal conductivity [W/(K-m)]	0.6	0.6	0.6	16.7
Wet thermal conductivity [W/(K-m)]	1.5	1.2	1.2	16.7
Initial gas saturation [-]	0.35	0.35	0.0	0.6
Residual liquid saturation [-]	0.1	0.1	0.1	0.1
Residual gas saturation [-]	0.1	0.1	0.1	0.1
Van Genuchten saturation function				
Alpha [1/Pa]	$6.25x10^{-8}$	$6.67x10^{-8}$	$6.67x10^{-8}$	$1x10^{-4}$
Lambda [-]	0.375	0.333	0.333	0.5

*The DRZ permeability will converge to the shale permeability with buffer swelling for comparative models implementing the TPHM permeability function.

Geological heterogeneity, often observed in sedimentary basins (e.g., layered system), has been neglected in this small-scale near-field analysis, such that the 75-m thick layer represents a homogeneous portion of shale host rock, with properties appropriate for a sealing shale. The natural barrier system (NBS) comprises the shale formation hosting the repository and the DRZ, defined as the portion of the host rock adjacent to the EBS. Prior to installing waste forms, the localized DRZ experiences durable (but not necessarily permanent) perturbations of hydrological and/or mechanical characteristics of the host rock (e.g., fracture opening) due to excavation for the repository. In the reference model, the initial enhancement of hydraulic diffusivity by excavation-driven fracturing is represented implicitly by assigning one order of magnitude larger permeability to the DRZ than to the undisturbed host rock.

The current set of simulations employs a buffer material with properties appropriate for a compacted mixture of 70% bentonite and 30% quartz sand in the buffer/spacer. The buffer is assigned a porosity of 0.35 and a permeability of 10^{-20} m^2 (Liu et al. (2016)). The bentonite/sand buffer has a water-saturated thermal conductivity of 1.5 W/m/K and a dry thermal conductivity of 0.6 W/m/K (Jobmann & Buntebarth (2009), Wang et al. (2015)). The material properties of the reference case in which hydrological and thermal parameters of all sections are constant over time are given in Table 3.1.

Initial pressure and temperature throughout the model domain are calculated by applying hydrostatic and geothermal gradients (10 kPa/m and 0.025°C/m, respectively) in the vertical direction, assuming temperature of 19°C and atmospheric pressure at the surface (462.5 m above the top of the model domain). For the unsaturated condition, initial liquid saturation (S_{li}) is set to 0.65 for buffer and DRZ, whereas the shale host rock is fully saturated with liquid. By invoking closed symmetry conditions at all side boundaries this represents a waste package that is located in the center of an infinite, symmetrical repository system. The simulation runs 10^3 years.

This study excludes chemical reaction and radioactive decay of nuclides, instead focuses on buffer swelling effects on solute transport by tracer simulation. A single chemical species (Cl^-) is defined as a non-reactive tracer with the solubility limit of 6159.0 mol/m^3-liquid and the precipitated molar density of 37130.2 mol/m^3-mineral (CRC (2020)). The initial molar concentration of Cl^- is set to 10^{-4}, 160, and 332 mol/m^3-liquid for waste package, buffer, and DRZ/shale host rock, respectively (Jove-Colon et al. (2016)).

This near-field model was run in PFLOTRAN GENERAL and NWT (Nuclear Waste Transport) modes, which solve two-phase (liquid-gas) miscible flow and energy conservation, sequentially coupled to solute transport for unsaturated conditions in the waste package, buffer, and DRZ. The numerical domain consists of ~5.4×10^4 unstructured grid cells for spatial discretization of the repository system (subset of Figure 3-1B).

3.1.2 Heat Source

Figure 3-2A shows the transient decay heat curves for 10^6 years from the 10th, 50th, and 75th percentiles of frequency distribution of heat outputs of as-loaded canisters in storage. These are predicted based on the NUHOMS 24PT1 canister installed at the San Onofre Nuclear Independent Spent Fuel Storage Installations (ISFSI) (24PT1-4701D-DSC009), the multi-purpose canister (MPC) installed at the Arkansas ISFSI (MPC-24-MPC-003), and the MPC installed at the Waterford ISFSI (MPC-32-MPC-224), respectively. More details of the selected canisters and procedure for generating the heat curves are described in Jones et al. (2021).

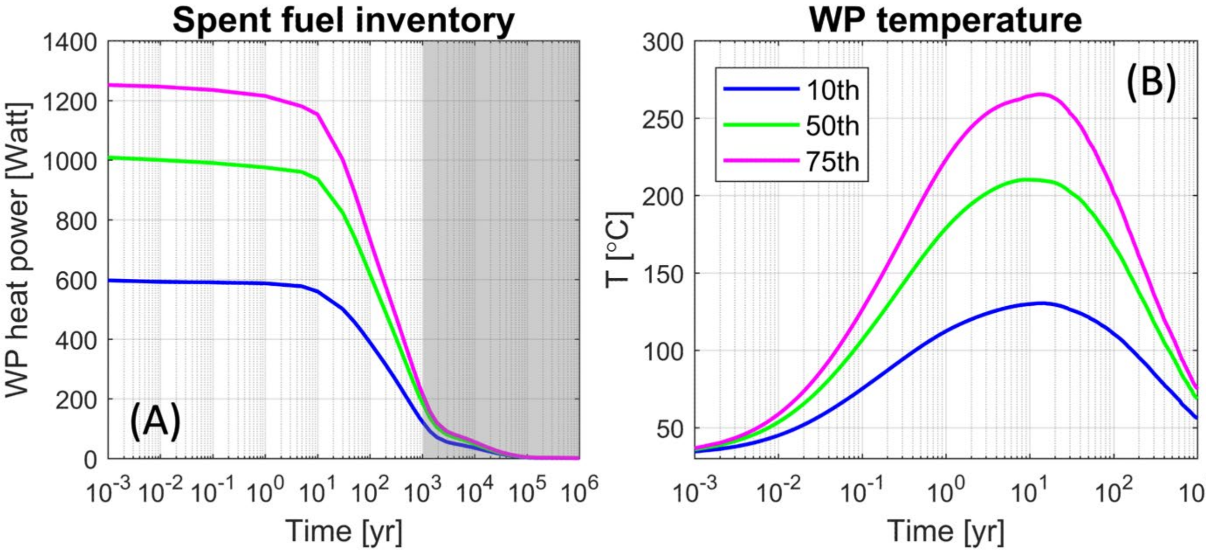

Figure 3-2. Heat source. (A) Transient decay heat curve for waste package heat source term from the 10th, 50th, and 75th percentiles of frequency distribution of heat outputs that are predicted at the selected canisters in Jones et al. (2021). The heat source is scaled based on the volume of a quarter of waste package modeled in this study. (B) Temporal evolution of average temperature within WP for three types of heat source as stored in the shale.

Thermal energy (watts per waste package volume) entering the model domain is updated as a function of time according to values in a lookup table. For the quarter of a single waste package the initial energy is 596.92, 1008.38, and 1251.56 W for the 10th, 50th and 75th percentile, respectively. The 50th percentile heat source is used for the reference case (green line), while the 10th and 75th percentiles of heat source are implemented to see the effect of greater or smaller heat from the waste package on near-field hydro-thermal coupled processes. Figure 3-2B shows the evolution of average temperature within the waste package from three types of heat source. The maximum temperature is reached between 10 and 20 years after the waste package is loaded.

3.1.3 Stress-dependent DRZ Permeability

In the reduced-order simulation, the effective stress acting on the DRZ is approximated by the temporal changes of average liquid saturation (ΔS_l) within the buffer:

$$\Delta\sigma_{eff} = 3K\Delta S_l \beta_{sw}, \qquad \textbf{Eq. (3-1)}$$

where K [Pa] is the bulk modulus of the buffer and β_{sw} [-] is the dimensionless moisture swelling coefficient, approximately 0.238 for a bentonite buffer material. Corresponding evolution of the DRZ permeability as a function of the effective stress is implemented to mimic geomechanical behavior of the DRZ without implementing mechanical components explicitly. Swelling-induced stress and corresponding perturbations in DRZ permeability are estimated as functions of hydrological variables, which evolve in response to heating/cooling from the waste package and imbibition of water from the water-saturated shale host rock. Three models have been suggested to express the changes in permeability as a function of changes in normal stress across fractures for shale rock: (1) exponential function (Dewhurst et al. (1999), Chen et al. (2015)), (2) cubic-law function (Kwon et al. (2001)), and (3) two-part Hooke's law model (TPHM) (Liu et al. (2009)). The effects of three stress-dependent permeability functions on the fluid flow and solute transport associated with the buffer-swelling process were recently investigated by Chang et al. (2021).

In this study, TPHM is implemented in PFLOTRAN, relating DRZ permeability evolution to normal effective stress with specified hydrological and mechanical parameter values. The concept of TPHM represents non-uniform deformation of heterogeneous rock by dividing the rock body into ‘soft’ and ‘hard’ parts to describe different stress-strain behaviors (Liu et al. (2009)). Dividing total porosity into soft and hard parts allows for the superposition of distinct relationships as functions of effective stress which combine to affect the total permeability. In relatively high effective-stress ranges, the hard part of the rock controls permeability, such that the soft part can be neglected (due to micro-crack closure at high stress conditions). The hard-part permeability can be expressed as follows:

$$\kappa_e = \kappa_{e,0} e^{-\beta c_e \phi_{e,0} \Delta\sigma_{eff}} \qquad \textbf{Eq. (3-2)}$$

where κ_e [m^2] and ϕ_e [-] are the stress-dependent hard-part permeability and porosity, c_e [1/MPa] (= 0.185) is the compressibility of the hard part, and β [-] (= 12.5) is a constant stress sensitive coefficient. $\phi_{e,0}$ (= 0.2) is the hard-part porosity under zero effective stress.

Under the relatively low effective-stress condition, the permeability changes mainly due to the deformation of the soft-part porosity, which experiences relatively large deformation, even though the soft-part porosity is a small portion of the total pore volume. Soft part permeability can be expressed as follows:

$$\kappa_t = \alpha \left[\gamma_t \exp\left(-\frac{\Delta\sigma_{eff}}{K_t}\right)\right]^m \qquad \textbf{Eq. (3-3)}$$

where κ_t [m^2] is the soft-part permeability, γ_t [-] (= 0.005) is the volume fraction of the soft part under zero effective stress, α [m^2] (= 1x10^{-16}) and m [-] (= 2.0) are material constants. By superimposing the Eq. (3-2) and Eq. (3-3), the total permeability can be expressed as follows (Zheng et al. (2015)):

$$\kappa = \kappa_{e,0}e^{-\beta c_e \phi_{e,0}\Delta\sigma_{eff}} + \alpha\left[\gamma_t \exp\left(-\frac{\Delta\sigma_{eff}}{K_t}\right)\right]^m \qquad \textbf{Eq. (3-4)}$$

The initial permeability values for the DRZ are unknown, such that the values are assigned as a constant value for the reference case (one order of magnitude less than that of the shale host rock) or computed under assumption that the DRZ permeability will approach that of the host rock as buffer swelling stress reaches the maximum. Note that the DRZ may not completely revert to the intact state by swelling due to inelastic behaviors of fractures and rock matrices, but this assumption provides a physically reasonable endpoint permeability considering mechanical evolution of the DRZ.

3.1.4 Saturation-temperature-dependent Thermal Conductivity

The saturation-temperature-dependent effective thermal conductivity defined by wet (water-saturated) and dry thermal conductivities are as follows (Somerton et al. (1974)):

$$K_{T,eff}(S_l,T) = \left[K_{T,dry} + \sqrt{S_l\left(K_{T,wet} - K_{T,dry}\right)}\right]\left(\frac{T - T_{ref}}{300}\right)^{\gamma} \qquad \textbf{Eq. (3-5)}$$

where $K_{T,eff}$, $K_{T,dry}$, $K_{T,wet}$ [W/m/K] are effective, dry and wet thermal conductivities, respectively, S_l is liquid saturation, T_{ref} is the reference temperature (T_{ref} = -273.15 °C), and γ is the exponent of temperature (γ = -1.18).

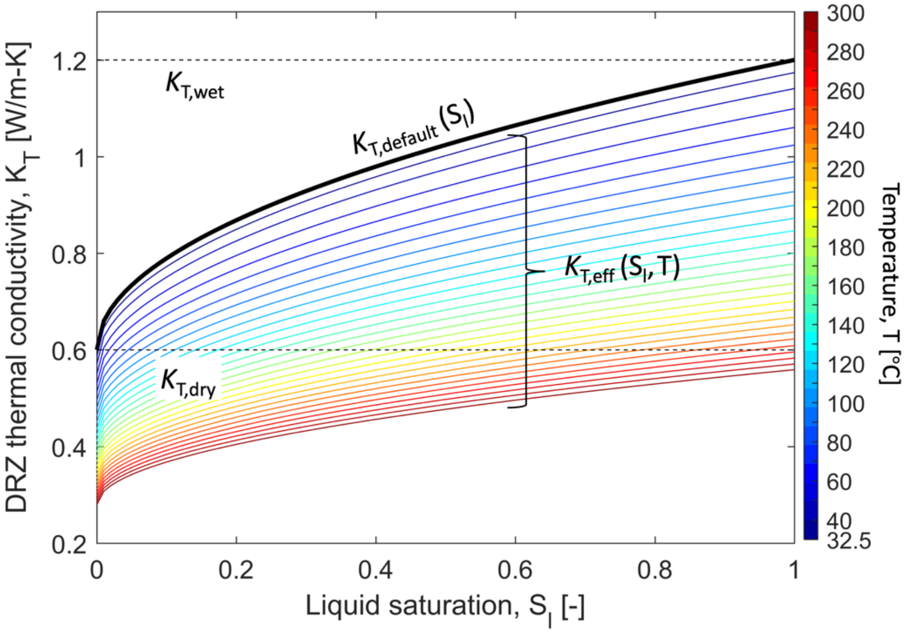

Figure 3-3. Thermal conductivity changes as a function of liquid saturation and temperature. The values of dry and wet thermal conductivities are for the DRZ in this study. The solid

black line represents the default thermal conductivity independent of temperature changes.

Figure 3-3 shows the change of effective thermal conductivity as a function of liquid saturation and temperature. The default case neglects the temperature dependence utilizing the PFLOTRAN default thermal conductivity in Eq. (3-4) instead of the temperature-dependent thermal conductivity shown in Eq. (3-5). The result is shown as a solid black line in Figure 3-3.

3.2 Results

3.2.1 Hydro-thermal Impacts on Tracer Transport

The comparison of results from the buffer and DRZ shows that the DRZ experiences faster re-saturation than the buffer because of larger and more rapid increase of liquid mobility as well as the water inflow directly from the fully saturated host rock (overall larger λ_l and S_l in the DRZ than buffer; Figure 3-4A to Figure 3-4D). The initial imbalance of Cl^- concentrations within the buffer and DRZ drives the tracer transport to achieve an equilibrium state between them while both sections are being heated (Figure 3-4E and Figure 3-4F). Figure 3-5 shows the spatial distribution of Cl^- concentrations at $t = 60$ years for the three types of heat source.

The amount of heat energy impacts the tracer transport. In general, the flow and transport characteristics of the DRZ are more sensitive to the amount of heat from the waste package than ones of the buffer. For the case of 75th percentile of heat source (magenta lines in Figure 3-4), the large mobility within the DRZ (Figure 3-4B) speeds up the tracer transport into the buffer (fastest decrease of Cl^- concentration in Figure 3-4F; the lowest DRZ Cl^- concentration in Figure 3-5C). Simultaneously, dry-out of the waste package as well as stronger outward heat flow accumulates Cl^- within the buffer adjacent to the waste package (the highest buffer Cl- in Figure 3-5C). After 400 years, once the buffer and DRZ are re-saturated and reach the equilibrium state for Cl^- transport, continuous influxes of Cl^- from the shale host rock increase the Cl^- concentration in the DRZ (Figure 3-4F).

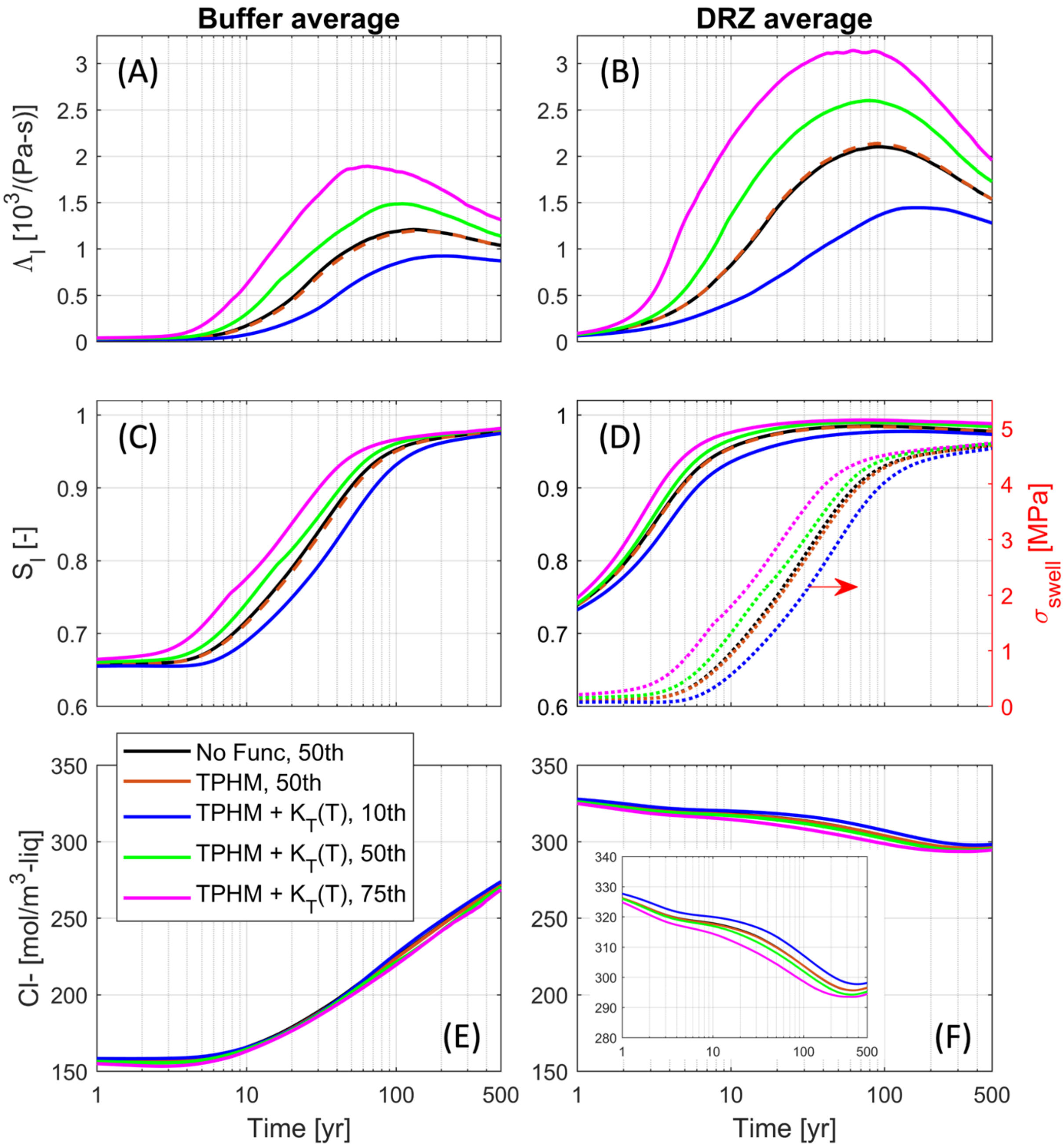

Figure 3-4. Temporal evolution of average (A to B) liquid mobility, (C to D) liquid saturation, and (E to F) aqueous concentration of tracer (Cl^-) within the buffer and DRZ for five cases.

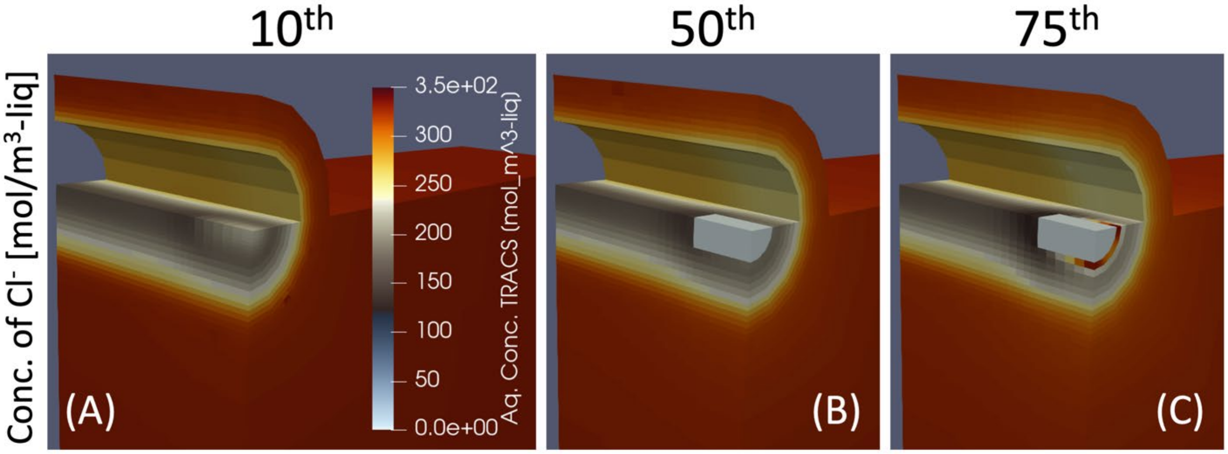

Figure 3-5. **Spatial distribution of aqueous phase concentration of Cl- [mol/m^3-liq] at t = 60 years for three types of heat source.**

Heat transfer and fluid flow in the buffer and DRZ at unsaturated conditions depend on local perturbations of temperature and water content in different parts of each material. It is worthwhile to look into how proximity to the waste package influences the fluid flow and tracer transport associated with heat-driven perturbations of liquid mobility and/or thermal gradients over time.

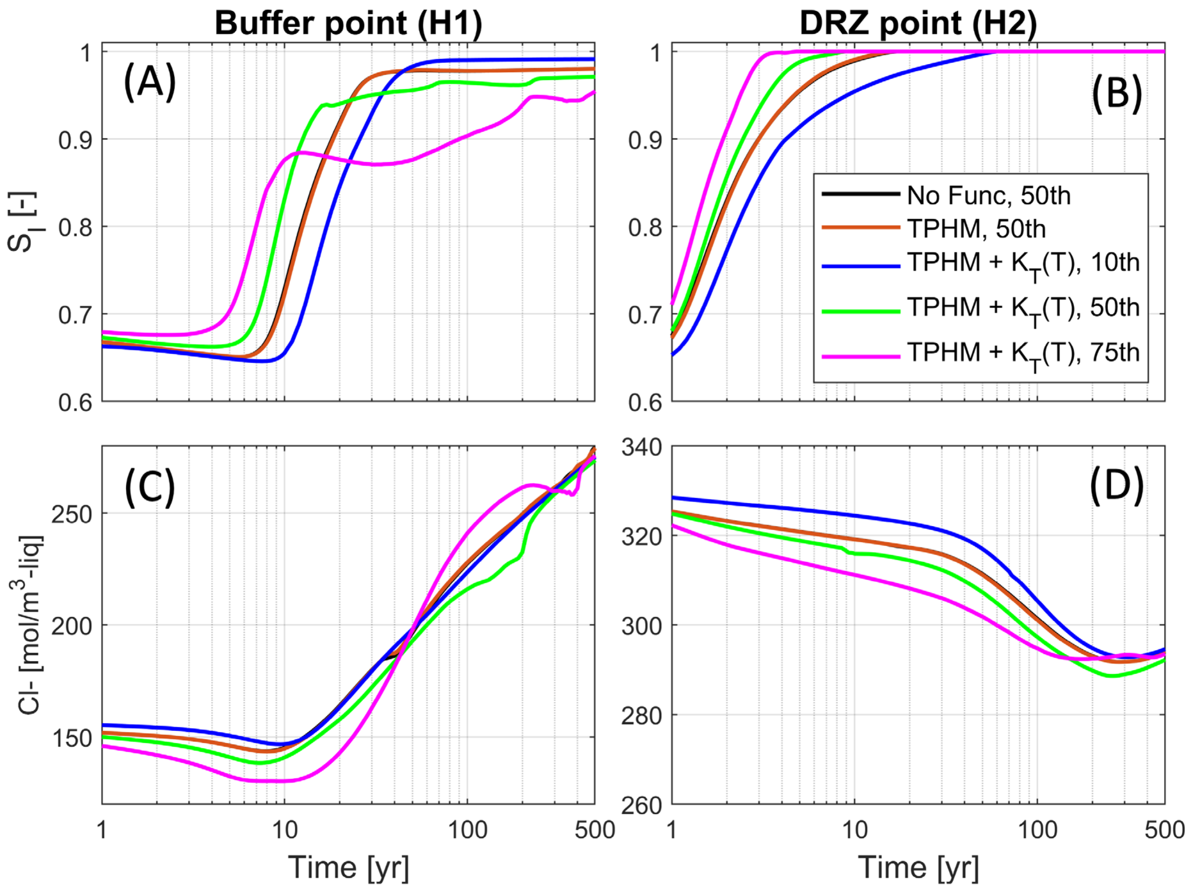

Figure 3-6. **Spatial distribution of (A to B) Liquid saturation and (C to D) aqueous concentration of tracer Cl^- at points H1 and H2 within the buffer and DRZ (refer to Figure 3-1A), respectively for five cases.**

Figure 3-6 shows the evolution of liquid saturation and Cl^- concentration at points H1 and H2 in the buffer and DRZ, closest to the waste package (indicated in Figure 3-1A), for five cases. At the early stage (less than 10 years), the hotter heat source causes faster re-saturation of buffer and DRZ due to the heat-driven increase of liquid mobility (Figure 3-6A and Figure 3-6B). Higher thermal gradients lessen the inflow of Cl^- into the buffer (Figure 3-6C) while larger mobility enhances transport of Cl^- out of the DRZ (Figure 3-6D). As the temperature approaches its maximum (approximately between 10 and 60 years), stronger heat emission causes local evaporation in the buffer that delays the re-saturation process as well as expedites the rate of Cl^- accumulation within the region adjacent to the waste package (magenta lines in Figure 3-6A and Figure 3-6C).

This result indicates that the thermally driven flow of water and/or vapor away from the heat source will redistribute the pore fluids within a repository system after the emplacement of heat-generating nuclear waste. The larger heat output causes more complicated flow dynamics: (1) stronger influx of water into the EBS and subsequent faster re-saturation of the repository system, and (2) localized fluid phase changes, which will influence the transport rate of corrosive species in space and time.

3.2.2 Impact of Numerical Domain Scale

For the near-field analysis, the model domain is vertically shortened to reduce the numerical cost, and both the top and bottom boundaries are set to open boundary conditions to resolve the boundary effects potentially caused by the domain geometry. However, the reduced domain may not describe the full physics of near-field hydro-thermal behaviors because of limiting heat diffusion to greater distance. Thus, the model domain extends vertically from the surface to a depth of 1 km, which is similar to the vertical scale of the field-scale PA model domain (Figure 3-7). Note that the vertically extended domain has the same waste package location, material properties, and hydraulic/thermal gradients for initial conditions as in the reference model (Figure 3-1), such that this comparative study will reveal the effect of the model domain vertical extent on the near-field fluid and thermal impacts of waste package emplacement.

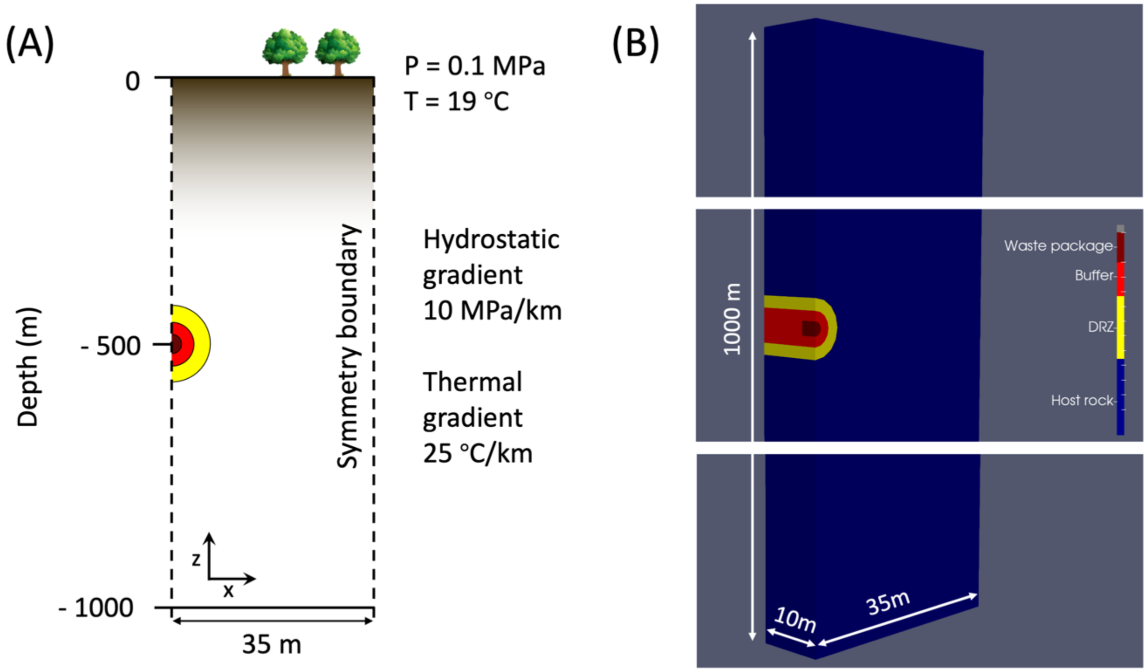

Figure 3-7. Model description and setting. (A) Schematic description of the vertically extended model domain consisting of waste package (wp), buffer/spacer, DRZ, and shale host rock. (B) Numerical domain and geometry.

Figure 3-8 shows the comparison of average temperature, mobility of liquid phase, liquid saturation, and concentration of tracer within the buffer and DRZ for the case of the 50th percentile of heat output with either reduced (green) or extended (purple) model domain.

During the heating phase, the thermally driven fluid flow accelerates the re-saturation process and saturates both buffer and DRZ with over 90% liquid phase until the temperatures reach the maximum. The vertically short or extended domain generate similar thermal impacts during this period as shown in Figure 3-8A and Figure 3-8B, such that the changes liquid saturation and tracer concentration are similar for both cases (Figure 3-8E to Figure 3-8H). The average temperature reaches similar maximum values for both cases, whereas the extended domain delays the relaxation of heat because the boundary condition is further from the heat source (purple lines; Figure 3-8A and Figure 3-8B). Within the buffer, the liquid mobility continues to increase gradually throughout the simulation, corresponding to the delayed heat relaxation in the extended domain (purple; Figure 3-8C). The DRZ also has larger fluid mobility after 100 years compared to the short domain, and mobility decreases with heat decay (Figure 3-8D).

Once heat has peaked and is declining, the extended domain delays the relaxation of heat within the buffer and DRZ that causes variation in thermal impacts on near-field flow and transport characteristics (Figure 3-8C and Figure 3-8D). However, both materials are nearly fully saturated, so this does not cause large differences in liquid saturation and tracer concentration.

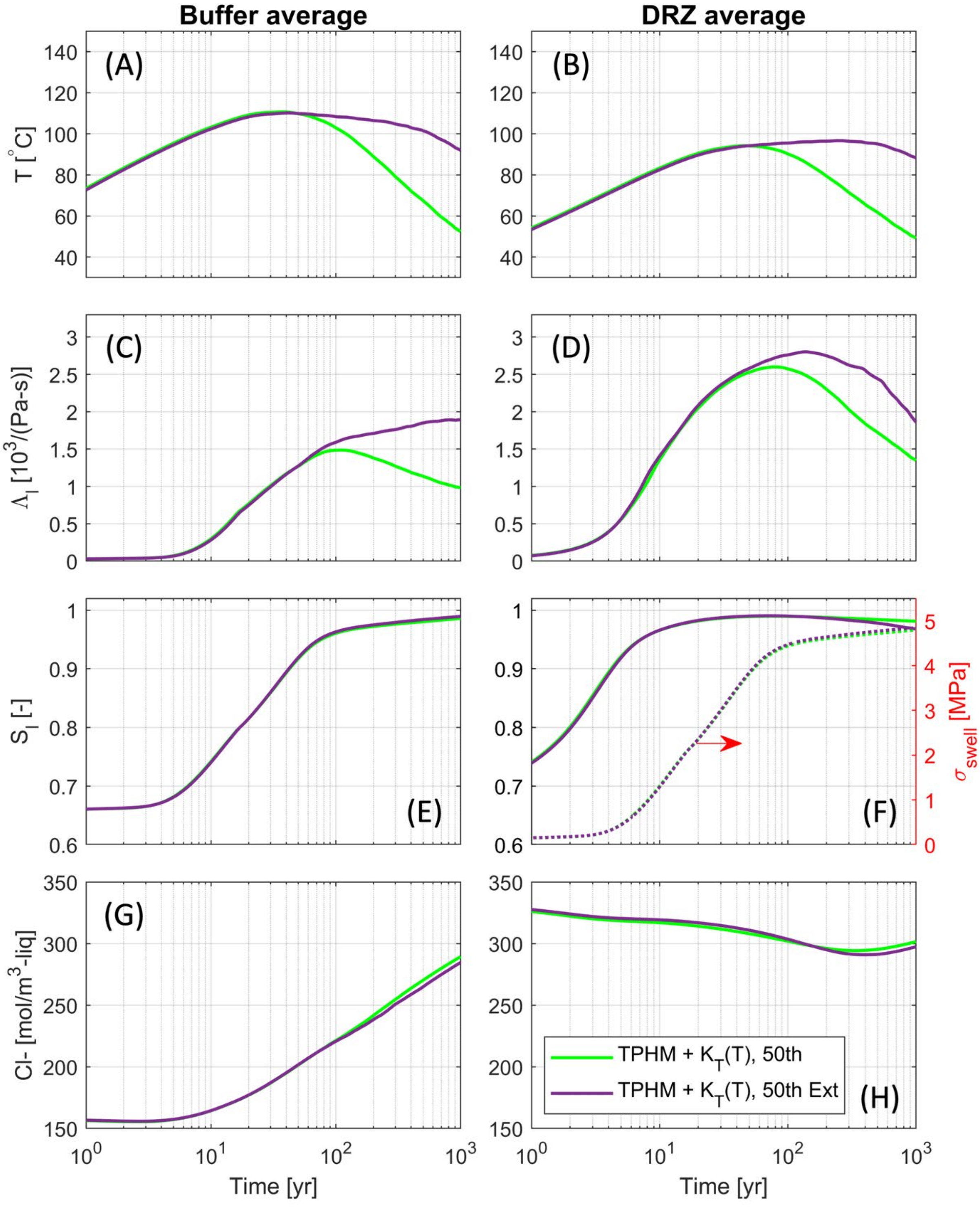

Figure 3-8. The effect of the model domain size. Temporal evolution of average (A to B) temperature, (C to D) mobility of liquid phase, (E to F) liquid saturation, and (G to H) aqueous concentration of tracer (Cl^-) within the buffer and DRZ for the cases of 50th percentiles of heat output with a vertically reduced and extended domain.

3.3 Findings & Future Work

Our simulation results indicate that heat-emitting/decaying of a nuclear waste package will perturb the thermal and hydrological fields around a repository. Thermally-driven flow dynamics and associated changes in thermal and hydraulic properties of the EBS and natural barrier system are approximated by implementing temperature-saturation-dependent thermal conductivity as well as DRZ permeability that changes as a function of effective stress. These can affect the rate of buffer re-saturation and tracer transport corresponding to the heat pulse and phase changes. Integrating thermo-hydro-mechanical parameters into PFLOTRAN enables us to include their impacts on solute transport in the repository system without a fully coupled THMC approach.

This generic study shows that heat-driven perturbations in hydro-thermal characteristics of the geologic repository system have significant impact in the near-field region. The amount of heat emitted from the waste package plays a significant role in controlling the multiphysics coupled response to the buffer swelling. The greater heat will generate:

(1). Larger mobility of the liquid phase, which accelerates the inflow and solute transport into the unsaturated buffer and DRZ from the fully saturated host rock,

(2). Steeper thermal gradients that can result in outward flow within the buffer and DRZ nearest the waste package, and

(3). Lower thermal conductivity that confines more heat within the buffer.

This type of reduced-order model could be used to integrate the effects of multiphysics coupling processes in the near-field into a field-scale performance assessment model corresponding to sequential phases of thermal and mechanical loading-unloading.

The assumptions of current reduced-order models can be modified to represent more realistic near-field coupled processes with geological and operational constraints by:

- Implementing the evolution of the DRZ volume considering fracture dynamics as a function of swelling stress. Pre-defined and constant volume of the DRZ may not be appropriate to describe inelastic mechanical deformation (e.g., healing and sealing) [Tsang et al. (2005)], which can influence the mechanical stability of the repository system for long-term field-scale approaches.

- Considering swelling-driven changes of porosity as a function of hydrological or mechanical parameters, which may influence the evolution of temperature and saturation.

- Validating and generating site-specific relationships between the swelling pressure and deformation based on experimental data of swelling characteristics obtained from a variety of compacted bentonites, which will enhance the accuracy of this reduced-order approach to evaluate the stability of the repository system for different sites.

This page intentionally left blank.

4. Geology and Hydrology of Glacial Deposits to Support Biosphere Modeling in a Crystalline Rock Environment

Pacific Northwest National Laboratory (PNNL) is developing a biosphere model to evaluate dose to human receptors as part of GDSA disposal system modeling (Condon et al. 2020). The biosphere model will be broadly applicable to geologic media and environments being considered in the GDSA generic reference cases (Mariner et al, 2021, Section 3.2.6). Glacial deposits directly overlie crystalline basement rocks in many areas of the northern U.S. that experienced glaciation during the Quaternary Period. This geologic environment is therefore of interest when evaluating geosphere-biosphere interactions as part of development of the biosphere model. The purpose of this section is to provide data related to glacial deposits in a crystalline environment to aid in development of test cases that will be used to benchmark the biosphere model in realistic geologic environments.

Common pathways for movement of radionuclides into the biosphere are through extraction of groundwater from wells and groundwater discharge to surface water features (Condon et al. 2020). In the case of groundwater discharge, radionuclide concentrations in the surface waters will depend partly on the properties of the near-surface geosphere features (e.g., permeability of geologic units) and the degree of mixing that occurs between radionuclide-contaminated groundwater and surface streams or lakes.

In this section we present data from a representative watershed in New England to develop an initial biosphere test case scenario in a crystalline environment. We focus on glacial deposits that overlie crystalline bedrock and how these deposits interface with the biosphere in terms of groundwater contributions to surface streams. We also present data related to potential water sources for crops and the amount of water needed for crop irrigation. Water needs and sources of water for crops are important factors in radionuclide uptake in crops. Other pertinent data in the watershed include precipitation rates and recharge rates to soils and glacial deposits.

The geology, hydrologic setting, and hydrologic properties of glacial deposits in this region are described in LaForce et al. (2021). The watershed used as an example for this study was chosen based on geology that is representative of the region. Nielsen and Locke (2015) present groundwater and streamflow data for the watershed that allow estimates of groundwater contributions to surface streams. The representation of the geology and hydrology of the glacial deposits presented in this section are intended as a simplified and generalized ("generic") example of a geologic environment that can be found in other areas of the northern U.S. Characteristics of the watershed pertinent to biosphere modeling include the hydrologic properties of glacial deposits that overlie the crystalline basement rocks, water well characteristics, and characteristics of surface water features.

4.1 Description of the Example Watershed

The example watershed is located within a few kilometers of the coast of Maine. The lower portion of the watershed nearest the coast lies on a flat coastal plain. Further inland, the watershed transitions to a broadly sloping plateau that is incised by the primary stream and its tributaries (Nielsen and Locke 2015; Figure 4-1). The stream and its tributaries represent local low points in the topography and are potential discharge points for groundwater. The elevation difference from the top to the bottom of the watershed is about 110 meters. Total length of the watershed is about 15 km with an approximate width that is between 2 and 3 km, for a total area of approximately 40 km^2.

Soils in the watershed form at the top of glacial deposits and are mixtures of sand, silt, clay, and organic material. The soils are typically sandy and promote high recharge rates into the underlying glacial deposits, particularly those deposits composed primarily of sand and gravel (Nielsen and Locke 2015). Soils with higher organic content and clay are present at wetlands and are poorly drained.

Land use within the watershed is primarily rural residential with interspersed farmland. Pine forests dominate the landscape with areas of forested wetlands and blueberry barrens (Nielsen and Locke 2015).

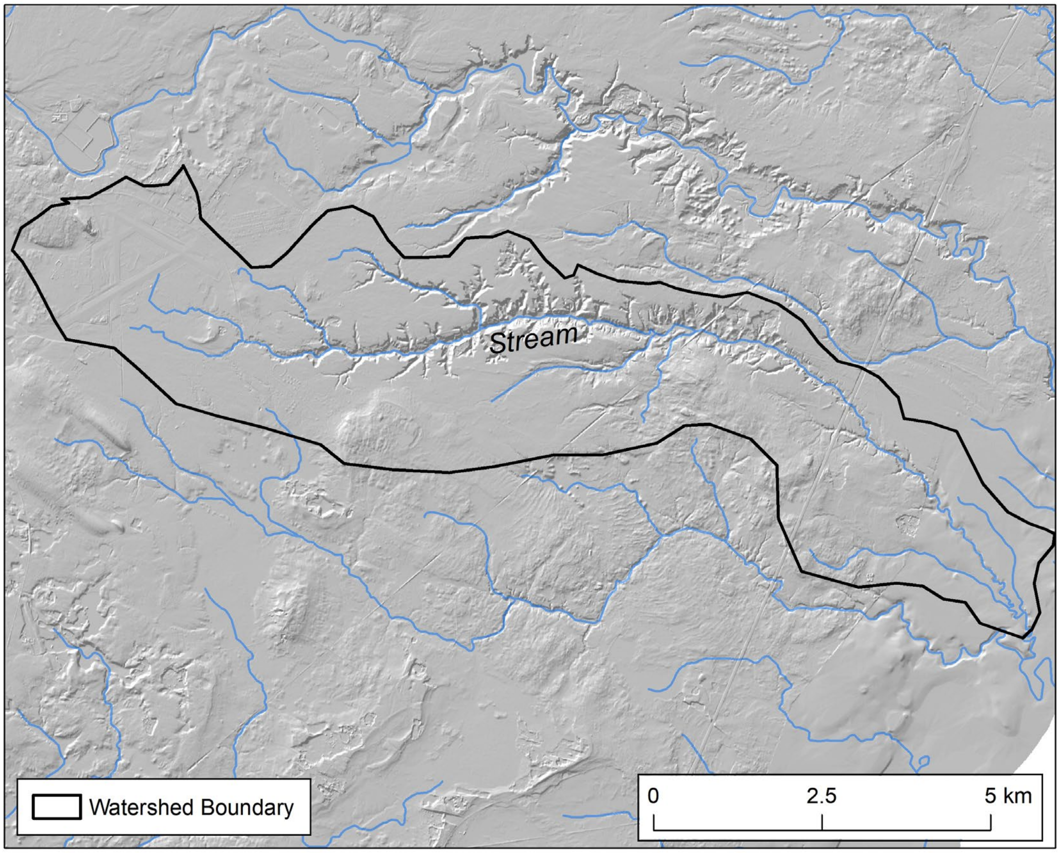

Figure 4-1. Shaded relief map showing the boundary of the watershed and the incision of the glacial deposits by the main stream and its tributaries (streams shown in blue).

4.2 Geology and Hydrology

The geology and hydrology of the watershed is described by Nielsen and Locke (2015) in a study that models groundwater flow and stream depletion within the watershed. The crystalline bedrock of the area consists of Silurian and Ordovician age metamorphic rocks intruded by several granitic plutons of Permian and Devonian age (Hussey et al. 2008). Crystalline rock is not exposed at the surface within the area of the watershed.

Glacial deposits that overlie the crystalline basement rocks can generally be divided into three major units (Figure 4-2 and Figure 4-3). The lowermost unit, directly draping crystalline bedrock, is glacial till with a thickness of up to 7 meters. Clay and silt deposits of the Presumpscot Formation overlie glacial till with a typical thickness of 5-20 meters. The Presumpscot Formation is the most extensive glacial deposit within the watershed. Due to its low permeability, it is a regional aquitard that limits groundwater flow to overlying and underlying units. The youngest glacial deposits within the watershed are sand and gravel glacial outwash deposits that form the shallow aquifer of the area. Sand and gravel deposits have typical thicknesses of 5-20 meters. In most areas of the watershed, the main stream has incised through the sand and gravel deposits into the underlying Presumpscot Formation. Tributaries of the stream are generally less incised and only incise the overlying sand and gravel deposits. Because of their high permeability, sand and gravel deposits are the main pathway for groundwater discharge to the tributaries that supply water to the main stream (Nielsen and Locke 2015). Groundwater flow within the watershed is from west to east and follows the topographic gradient (Nielsen and Locke 2015). Groundwater flows from local topographic highs within sand and gravel units to the nearest discharge points at streams. Permeability and assigned thickness values for the glacial deposits are summarized in Table 4-1.

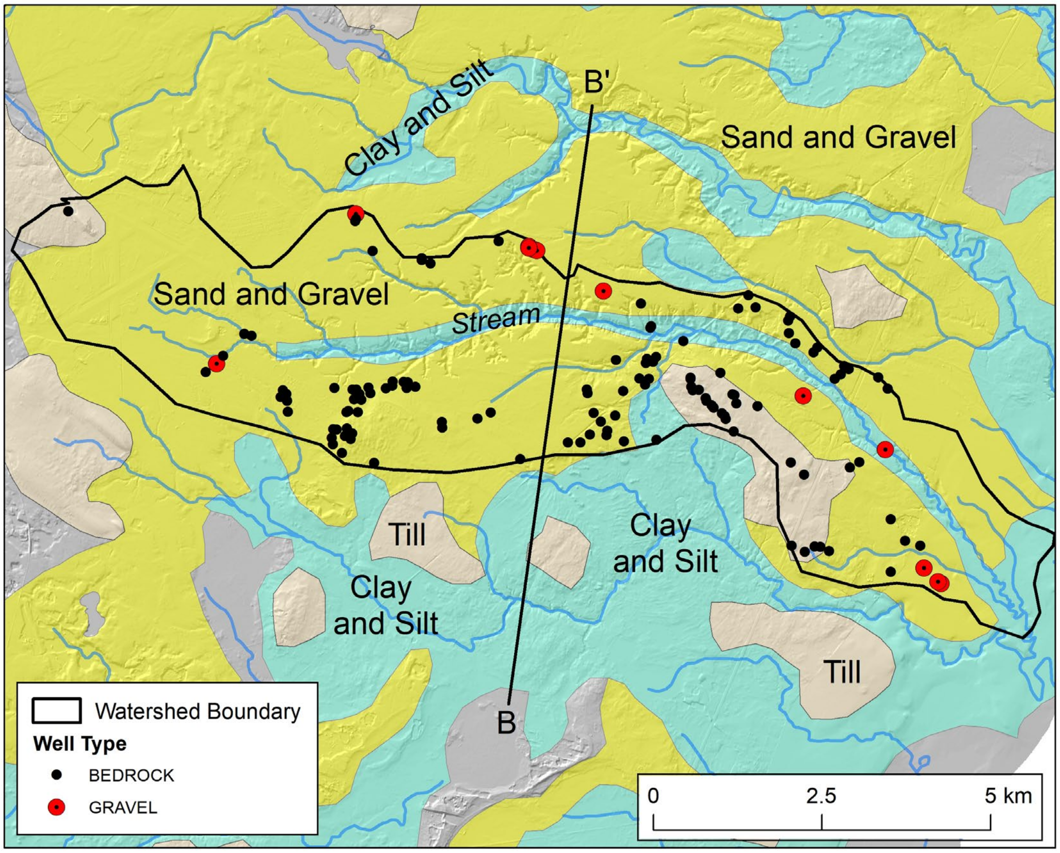

Figure 4-2. **Simplified geologic map of glacial deposits within the region of the watershed and distribution of water wells within the watershed. Line B-B' is the location of the cross-section shown in Figure 4-3.**

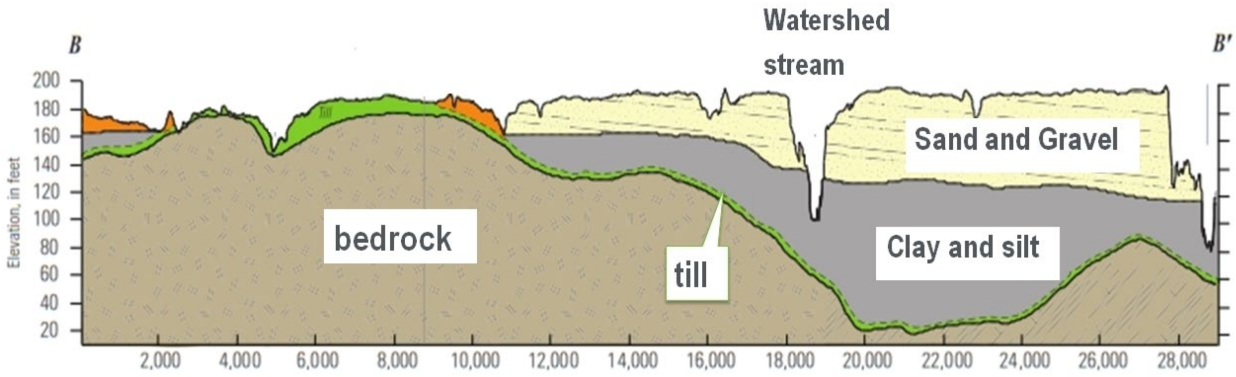

Figure 4-3. Stratigraphic relationships and thicknesses of glacial deposits along geologic cross-section B-B' from Figure 4-2. Modified from Nielsen and Locke (2015).

Table 4-1. Reference permeabilities and thickness of deposits.

Glacial unit	Permeability	Thickness (m)
Till	10^{-14} to 10^{-13} m^2	5
silt and clay	10^{-17} to 10^{-15} m^2	15
sand and gravel	10^{-11} to 10^{-10} m^2	15

4.2.1 Aquifers

Sand and gravel deposits form the shallow aquifer of the watershed (Figure 4-2) The sand and gravel aquifers are the major sources of water for municipal use and to a lesser extent irrigation and domestic use. Well yields range from 10 to several hundred gallons per minute (GPM). The most productive well in the watershed is a municipal well in the sand and gravel aquifer that has a well yield of 150 GPM. Within the region, sand and gravel aquifers typically have yields of 20-30 GPM (LaForce et al. 2021). The next most productive aquifer is the bedrock aquifer which has yields ranging from a few to approximately 100 GPM. The majority of bedrock wells have yields of 10 GPM or less and are generally the main type of well for domestic use. Glacial till is a poor aquifer that typically yields only 1-2 GPM (LaForce et al. 2021).

4.2.2 Water Well Characteristics

A total of 126 water wells are located within the watershed (Figure 4-2). A large majority of these wells (116) are within the crystalline bedrock and ten are shallow wells within gravel deposits (Figure 4-4). All of the bedrock wells are for domestic use, and most have yields of less than 20 GPM. Nine of the ten gravel wells are also for domestic use with the highest yielding well (150 GPM) for municipal use. The average depth of bedrock wells is 91 meters with an average yield of 18 GPM. The average depth of bedrock wells falls within the depth range of high-permeability horizontal fracture zones typical of crystalline rock environments (LaForce et al. 2021). Based on a much smaller sample size, sand and gravel wells have an average depth of 15 meters and an average yield of 27 GPM.

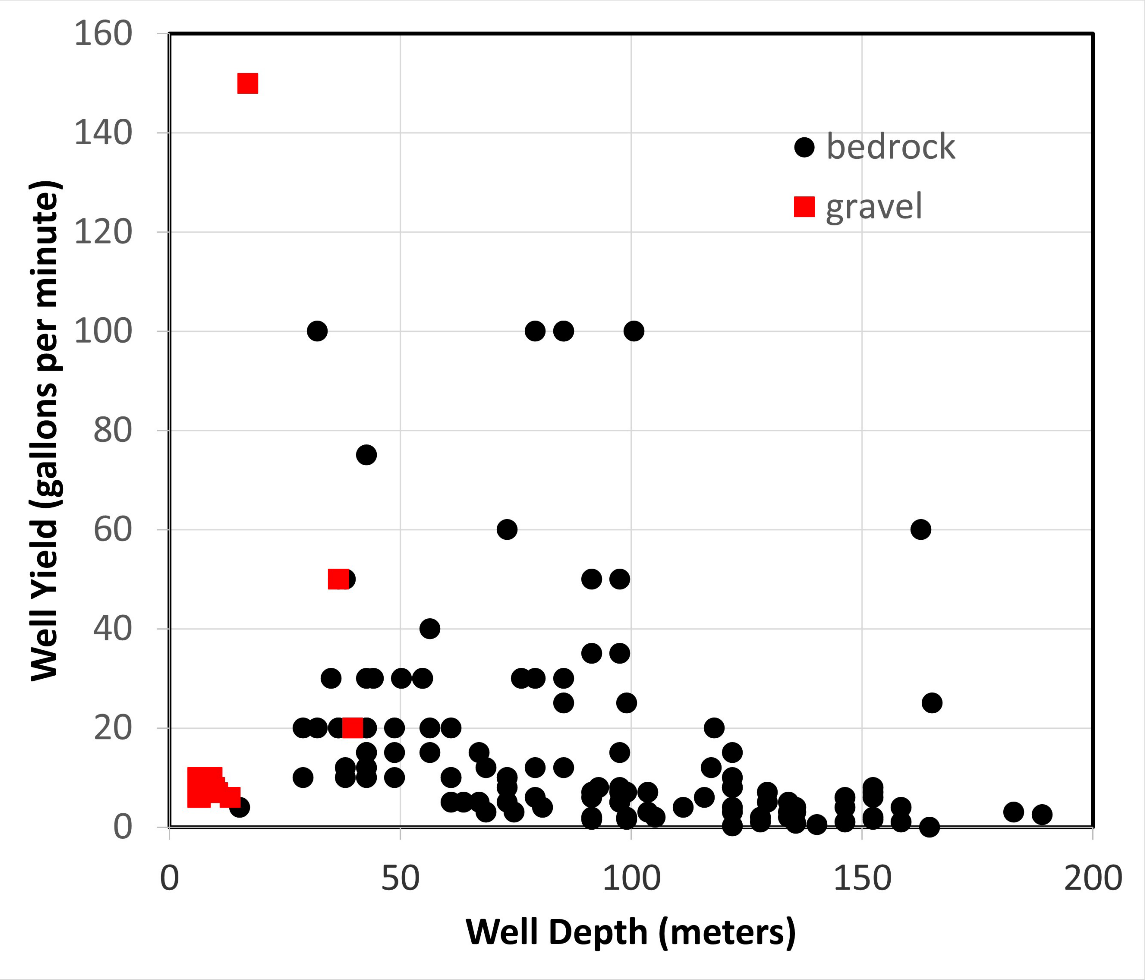

Figure 4-4. **Well Depth versus well yield for bedrock and gravel wells within the example watershed.**

4.2.3 Precipitation and Recharge

Participation in the region of the watershed averages between 115-140 cm (45-55 inches) per year (National Weather Service 2022, https://www.weather.gov/wrh/Climate?wfo=gyx; Nielsen and Locke 2015). Rainfall amounts in the region are fairly consistent from month to month ranging from about 9 to 13 cm (Table 4-2). For the May-September growing season, average precipitation is about 10 cm per month with a range in the average of 9.7 to 11.6 cm.

Recharge to the uppermost permeable sand and gravel deposits in the watershed is approximately 50-60% of total precipitation (Nielson and Locke 2015). For use in biosphere models, we assign a recharge rate of 70 cm per year to the sand and gravel deposits and the overlying soils. The underlying Presumpscot Formation, which is a regional confining unit, has a recharge rate estimated at 1 to 5 cm per year (Nielsen and Locke 2015). We assign the Presumpscot Formation a recharge rate of 2 cm per year. We assign a recharge rate of 12 cm per year for both till and underlying fractured bedrock, from values reported in Nielsen and Locke (2015).

Table 4-2. Monthly Mean Precipitation and Temperature in the area of the watershed.

Month	Total Mean Precipitation (cm)	Mean Temperature (C)
January	9.3	-6.2
February	9.2	-4.8
March	11.9	-0.2
April	11.7	6.4
May	9.7	12.4
June	11.6	17.4
July	10.1	20.4
August	10.0	19.7
September	9.7	15.5
October	13.6	8.9
November	11.3	3.1
December	12.2	-2.6
Annual	130.3	7.5

4.2.4 Groundwater Contribution to Streams

Nielsen and Locke (2015) modeled groundwater and surface water flow to understand potential streamflow depletion from well withdrawals. Streamflow estimates differ depending on the method used to calculate streamflow (Nielson and Locke 2015). However, two methods used by Nielson and Locke (statistical methods using data from multiple watersheds versus direct in-flow stream measurements) yield results that agree within a factor of two for most months of the year (Figure 4-5). Our interest is in how base flow values for the main stream (representing groundwater contribution to stream flow) compare to the overall stream flow. Stream flow is at its lowest in the summer when calculated streamflow values overlap calculated base flow values of 15-20 ft^3/s (Figure 4-5; Nielson and Locke 2015), indicating that a high percentage of the summer streamflow between precipitation events is due to base flow. Based on these estimates, we assign a groundwater contribution of 90-100% (by volume) to total stream flow during the summer crop growing season. Groundwater contribution during the remainder of the year is not as well constrained. It is likely less during the spring when total streamflow is highest and the groundwater contribution is a smaller proportion of the total streamflow, due to higher runoff from snow melt. Although groundwater contribution to streams is less during the spring, we would not expect it to drop to less than 50% of total streamflow.

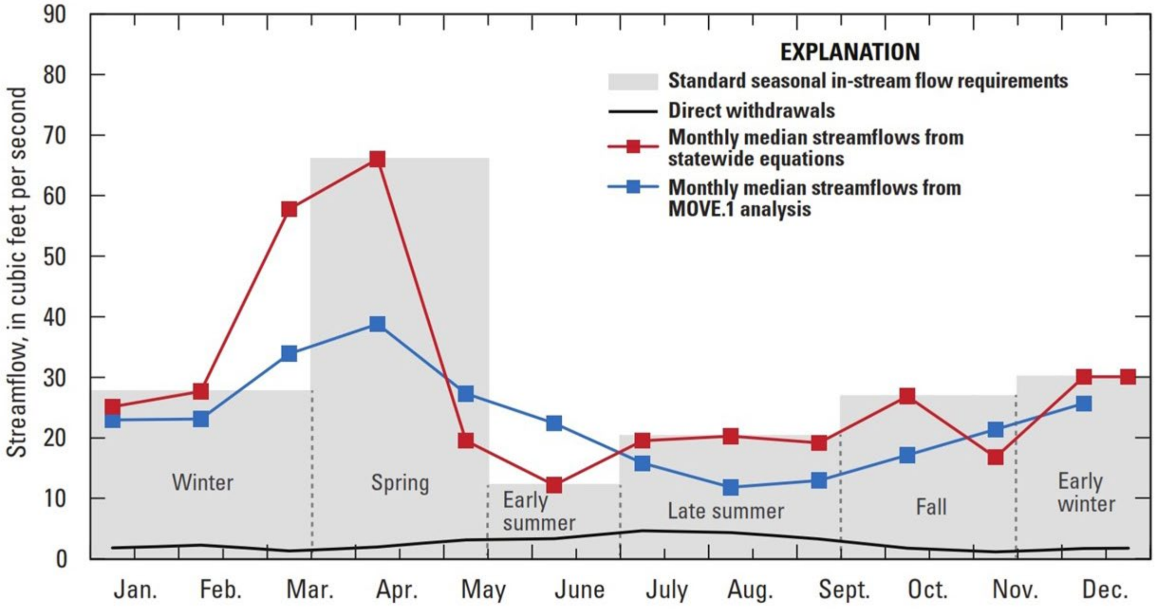

Figure 4-5. Monthly streamflow estimates for the example watershed using two estimation methods, from Nielsen and Locke (2015).

Winter et al. (1998) reports the proportion of groundwater component of stream flow for 54 streams located in different physiographic and climatic regions of the U.S., based on analysis of hydrographic data. The average groundwater component for all the streams from this analysis is 52% (median of 55%). Values range from 14% to 90% with the geologic setting and stratigraphy playing an important role in the contribution of the groundwater component. Streams in areas underlain by thick deposits of low permeability rock (e.g., shale with high clay content) have the lowest contribution of groundwater while those underlain by high permeability gravels and sand deposits have the highest groundwater contribution. In the latter case, groundwater can flow more easily though the permeable deposits to reach streams.

The importance of near-surface stratigraphy to groundwater contribution to streams leads us to consider two different scenarios for the stratigraphy of glacial deposits that influence transfer of radionuclides to streams. These scenarios are depicted schematically in

Figure 4-6 and Figure 4-7. The first scenario is based on the stratigraphy of glacial units represented in the example watershed (

Figure 4-6). The second scenario is based on a simpler stratigraphy where a single layer of till overlies bedrock (Figure 4-7).

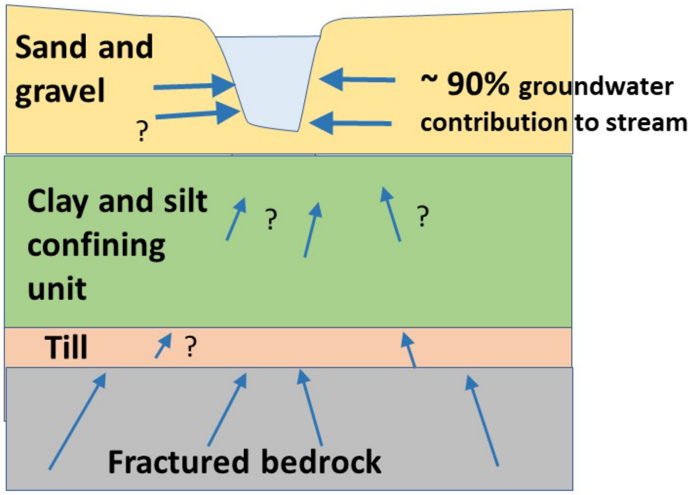

Figure 4-6. Schematic representation of stratigraphy and groundwater flow in a watershed with three types of glacial deposits (not to scale). Groundwater flow from the upper sand and gravel aquifer contributes approximately 90% of the water to the total streamflow. Arrows are general indicators of flow velocities based on differences in permeability. Question marks indicate uncertainty in the amount of radionuclide transport in glacial deposits.

In the watershed example, the presence of permeable sand and gravel deposits at the surface limits runoff and promotes recharge of the shallow aquifer and a greater amount of base flow (groundwater contribution) to streams (Nielsen and Locke 2015). Groundwater contribution values in the range of 90-100% are therefore consistent with the local geology and the analyses presented by Nielsen and Locke (2015). Although much of the main streambed is incised into the underlying silt and clay of the Presumpscot Formation, its tributaries are incised into sand and gravel deposits, which provide the main groundwater flow paths into the main stream (Nielson and Locke 2015). Given the high amount of surface recharge into the shallow aquifer and the possibility of limited flow from below due to the presence of the clay and silt confining unit, it is likely that radionuclides in the shallow aquifer will have significantly lower concentrations compared to water flowing through bedrock fractures.

The second scenario is based on simpler stratigraphy that is typically found farther inland of the example watershed (Figure 4-7). In these areas, the Presumpscot Formation is not present, and till is the dominant glacial deposit that covers the landscape, with lessor deposits of widely spaced sand and gravel deposits. Till deposits are less permeable than the sand and gravel deposits, which would lead to greater surface runoff, lower recharge rates and less groundwater contribution to streams. Due to their lower permeability, recharge rates to till are approximately 25% of recharge rates to sand and gravels deposits (Nielsen and Locke 2015) and discharge rates to streams would be less than from sand and gravel deposits. Based on the range in percent groundwater contribution to streams for the U.S. as a whole (14-90%, Winter et al. 1998), which depends on the permeability of underlying geologic deposits, till would be expected to provide a groundwater contribution to streams that is lower than the sand and gravel deposits. Based on this information, we consider a groundwater contribution from till of approximately 40-50% a reasonable value.

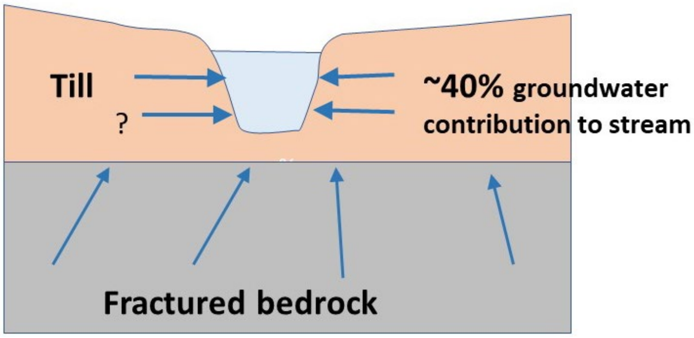

Figure 4-7. Schematic representation of groundwater flow for a simple stratigraphy of till overlying crystalline basement rock. Groundwater flow from till contributes approximately 40% of the water to the total streamflow. Arrows are general indicators of groundwater flow. Question marks indicate uncertainty in the amount of radionuclide transport in glacial deposits.

While estimates of groundwater contributions to streams are given for both scenarios, the radionuclide concentrations in the groundwater contributing to streams will be dependent on flow and transport modeling to estimate radionuclide concentrations in the groundwater of the glacial deposits. The radionuclide concentrations in the sand and gravel deposits are expected to be much lower than those in fractures of the bedrock as radionuclides are transported through the glacial units and diluted in the high-recharge sand and gravel deposits.

4.3 Agricultural Framework

The climate and soils of southern Maine support a variety of crops including leafy vegetables, root vegetables, fruit trees and berries (Central Aroostook Soil and Water Conservation District, 2005). A representative sample of these fruits and vegetables is listed in Table 4-3 along with water needs and sources. The growing season is from May through September and can be extended by the use of greenhouses and other enclosed growing facilities. Average rainfall during the growing season (10 cm per month) typically supplies at least half the water needs for most crops with irrigation supplying the rest.

For the initial watershed scenario, we consider two main exposure pathways, drinking water and water that is taken up and incorporated in crops through irrigation. Drinking water is assumed to be drawn from wells, either in crystalline bedrock or sand and gravel deposits. Irrigation water can be drawn from wells or surface waters (streams, impoundments) that can represent a mixture of groundwater discharge and surface runoff.

4.3.1 Water Sources

Water sources for agriculture are described in Central Aroostook Soil and Water Conservation District (2005). Available water sources in southern Maine include streams, lakes, man-made natural water impoundments (ponds), springs and groundwater wells (Central Aroostook Soil and Water Conservation District 2005). The sources considered for input to the biosphere model are wells, streams and possibly surface impoundments of water drawn from streams or wells which we will assume have the same radionuclide concentration as the well or stream sources. It is not feasible to reliably predict the sources of irrigation water used in a farming area. Depending on the farm location, a combination of wells and surface water sources could be used for irrigation. Water from wells in crystalline bedrock, water from sand and gravel aquifers and water from surface streams would be expected to have decreasing concentrations of radionuclides. It is possible that impoundments of water fed from these sources could have higher concentrations of radionuclides due to water evaporation, but we will not consider this possibility in the present scenarios. We consider three possible water sources for each crop. The first is irrigation water drawn from a sand and gravel aquifer and the second is water drawn from a bedrock well. A third and possibly less likely irrigation source is water from streams. In general streams are not a reliable water sources for irrigation because irrigation demands are greatest in August and September when stream levels are at their lowest (Central Aroostook Soil and Water Conservation District 2005). It is important to be able to estimate radionuclide concentration in streams however, due to the potential use for irrigation and impact on downstream natural habitats or other users.

4.3.2 Water Requirements

Water requirements for representative crops are listed in Table 4-3, based on data presented in Central Aroostook Soil and Water Conservation District (2005). Most crops in the region require about 2.5 cm of water per week and possibly more during critical growing periods. Precipitation during the growing period is approximately equal to crop water needs but crop water needs may not be reliably met on a week-by-week basis or during drier years. Because of high precipitation rates in Maine, irrigation is not employed on all farms or for all crops grown on a farm. In order to include an irrigation component in these scenarios for the biosphere model, we assume the upper range of water needs listed in Table 4-3 and calculate the possible shortfall based on monthly average precipitation rates. Based on these assumptions, irrigation is needed to supply up to an additional 2.5 cm of water per week consistently across most crops. For sandy soils of the watershed, irrigation would be applied at a rate of between 1-2 cm per hour (intake rate of the soil) to prevent ponding and runoff (Central Aroostook Soil and Water Conservation District 2005). In general, the total amount of water available for crops (precipitation plus irrigation) would be sufficient to maintain a soil moisture content of 50-100% (Central Aroostook Soil and Water Conservation District 2005). Concentrations of radionuclides in irrigation water will be based on PFLOTRAN modeling of radionuclide concentrations in well water from either crystalline basement or the sand and gravel aquifers.

Table 4-3. Water Requirements and Sources for Representative Crops in the May-September growing season.

Crop	Root depth	Water needs	Potential Irrigation needs	Water sources
beans	0.3-0.6 m	2.5-5 cm per week	2.5 cm per week	bedrock or sand and gravel well (or stream)
lettuce	0.3-0.6 m	2.5-5 cm per week	2.5 cm per week	bedrock or sand and gravel well (or stream)
broccoli	0.3-0.6 m	2.5-5 cm per week	2.5 cm per week	bedrock or sand and gravel well (or stream)
potatoes	0.3-0.6 m	2.5-5 cm per week	2.5 cm per week	bedrock or sand and gravel well (or stream)
apples	Varies (2-3 m)	5 gallons per tree per week (2.5 cm per week)	0 cm given average rainfall	bedrock or sand and gravel well (or stream)
corn	0.7-1.0 m	2-4 cm per week	1.5 cm per week	bedrock or sand and gravel well (or stream)
strawberries	0.3-0.6 m	2.5-5 cm per week	2.5 cm per week	bedrock or sand and gravel well (or stream)

4.4 Consideration of Future Climate and Landscape Evolution Scenarios

Future climate and landscape evolution scenarios will be evaluated as part of development and application of the biosphere model. In this section we briefly describe some of the factors that may need to be considered for scenarios that are applicable to regions subjected to glaciation and a periglacial climate.

4.4.1 Periglacial Climate

Section 4 has focused on conditions applicable to the present climate in coastal Maine, but the biosphere model will also have to consider colder periglacial climate conditions. We assume that humans will not occupy areas with thick ice sheets that occur during a full glacial climate.

The following are a few of the conditions that are expected to apply in a periglacial climate:

(1). Humans living in a periglacial climate are organized in a hunter-gatherer society with agriculture playing a much diminished or non-existent role (Condon et al. 2020).

(2). Permafrost will be an important feature of the geosphere/biosphere system with key parameters being the depth of frozen ground and its effect on barriers and groundwater movement. This will require a consideration of modeling needs for radionuclide transport where frozen ground is present.

(3). Because of difficulties in drilling water wells in permafrost, surface water sources may replace wells for drinking water with ice from lakes or rivers that is harvested in the fall and stored for use during the winter. This mode of acquiring drinking water is practiced today by communities in periglacial climates (Dickens, 1959).

4.4.2 Landscape Evolution

Landscape evolution in the far future is complex in an area subject to glaciation and is impossible to predict in any detail. The current glacial sediments are geologically young and in the short term (prior to the next glacial period) are subject to erosion and incision as the region continues to experience crustal uplift from glacial rebound. As incision progresses, stream beds can come in contact with stratigraphically lower and less permeable glacial deposits within the watershed which would tend to decrease the groundwater contribution to the stream. In the longer term (including the next glacial cycle) the current sediments may be completely removed and replaced by a new generation of sediments by the advancement and retreat of future glaciers. Glacial advance and retreat will also likely determine the location and characteristics of future lakes and streams. Each new glacial advance and retreat has the capacity to create a new glacial landscape, but with overall similarities to previous landscapes. In detail however, these landscapes will differ in the distribution and characteristics of glacial sediments and surface water features, which will impact the concentrations and distribution of radionuclides in the biosphere.

At Forsmark, Sweden, landscape evolution is thought to depend on two main processes, climate variations (glacial cycles) and vertical crustal movements (glacial advancement and retreat) leading to shoreline displacement (Lindborg, 2010). These same processes apply in southern Maine. For example, the Presumpscot Formation is a marine clay and silt deposit that has been uplifted in the past 10,000 years to a terrestrial position in the current landscape. Erosion and redistribution of glacial deposits play a role in how groundwater is recharged at higher elevations and discharged into topographic lows over time. These processes will affect radionuclide transport in the biosphere in future times.

Understanding these processes in any detail in a specific geologic and topographic setting is challenging and requires development of a set of landscape development tools to predict how erosion and sedimentation change the landscape over time (Lindborg 2010). Development of a set of landscape development tools would require a considerable effort and may not be beneficial until likely sites are being considered or selected, as site specific features of the landscape would play a part in determining how landscape evolution is modeled.

4.5 Conclusions

Glacial deposits overlie crystalline basement rocks in areas of the northern US that were glaciated during the Quaternary Period. Glacial deposits in these areas therefore represent a common geologic interface between the deeper geosphere (various types of bedrock) and the ecosystems of the biosphere. Transfer of radionuclides from crystalline basement rocks and glacial deposits to the biosphere occurs through extraction of groundwater from wells and discharge of shallow groundwater directly into streams and other surface water features. Of interest to the biosphere model is the proportion of groundwater (carrying radionuclides) that contributes to surface waters such as streams or lakes, thereby defining the concentration of radionuclides in the surface waters. Based on the example watershed and stream system described in this section, groundwater from highly permeable, near-surface aquifers such as sand and gravel deposits can contribute 90-100% of the water in the total streamflow. In comparison, less permeable till deposits that overlie crystalline basement rocks in areas outside of the watershed are estimated to supply approximately 40-50% of total streamflow where sand and gravel deposits are not present.

A sampling of crops grown in the region of the watershed indicates that most crops require 2.5 to 5 cm of water per week during the growing season with the highest amounts needed during critical growth periods. Assuming the highest values, and typical precipitation rates of 2.5 cm per week during the growing season, irrigation is necessary to supply an additional 2.5 cm of water per week for most crops. This amount of irrigation water can be supplied by wells, or less likely, by withdrawal from streams.

Although we can estimate the contribution of groundwater from different sources as a component of stream flow, radionuclide concentrations obtained from PFLOTRAN modeling will be needed to support the biosphere model. Modeling of radionuclide concentrations in sand and gravel and till deposits will allow estimates of radionuclide concentrations in surface waters when combined with estimates of groundwater contributions to streams.

5. UNSATURATED ALLUVIUM

This section presents an update of the unsaturated zone (UZ) alluvium reference case first introduced in Mariner et al. (2018), continued in Sevougian et al. (2019a), Sevougian et al. (2019b), and most recently in LaForce et al. (2021). The present study is focused on setting up more realistic simulations with the use of recently developed PFLOTRAN solvers, options, and transport mode. This includes setting a more realistic grain density value for the upper basin fill DRZ, running simulations with a corrected version of the Newton Trust-Region Dogleg Cauchy (NTRDC) nonlinear solver, and implementing the use of the newly developed PFLOTRAN transport mode called nuclear waste transport (NWT).

This reference case considers thick alluvial valleys of the Great Basin in the western United States and the low-permeability playa/lacustrine sediments found there. Several features of this type of host rock are favorable to waste isolation, including low groundwater fluxes, low permeability, and low water saturation. This type of environment is favorable to the disposal of DPCs since low water saturation greatly reduces the possibility of criticality events. Mariner et al. (2018) goes into detail of the natural barrier system, movement of water through sediments, and the physical and chemical characteristics of the host rock. The next sections touch on the model setting, description of the model domain, repository layout, simulation set up, results of completed runs, and future work considerations.

5.1 Model Setting

Two schematics, shown in Figure 5-1 and Figure 5-2, take their inspiration from the thick alluvial valleys of the Great Basin in the western U.S. Figure 5-1 is a schematic of the hydrology and geology of a UZ repository (Mariner et al., 2018). Figure 5-2 shows the cross section of a UZ model where the repository is represented by the red block at a depth of 250 m and lies within the UZ that is between a depth of 0 m to 450 m. Within the UZ, there are impermeable fine-grained playa sediments, fluvial deposits, and the upper basin fill (UBF) consisting of unconsolidated gravel, sand, silt, and clay. The saturated zone (SZ) is located below the UZ at a depth of 450 m to 1,000 m. The SZ consists of an alluvial aquifer at a depth of 450 m to 500 m. The top of the SZ is a higher-permeability sand/gravel aquifer that lies at the base of the UBF and above the lower basin fill (LBF) at a depth between 500 m to 1,000 m which is made up of consolidated gravel, sand, silt, and clay.

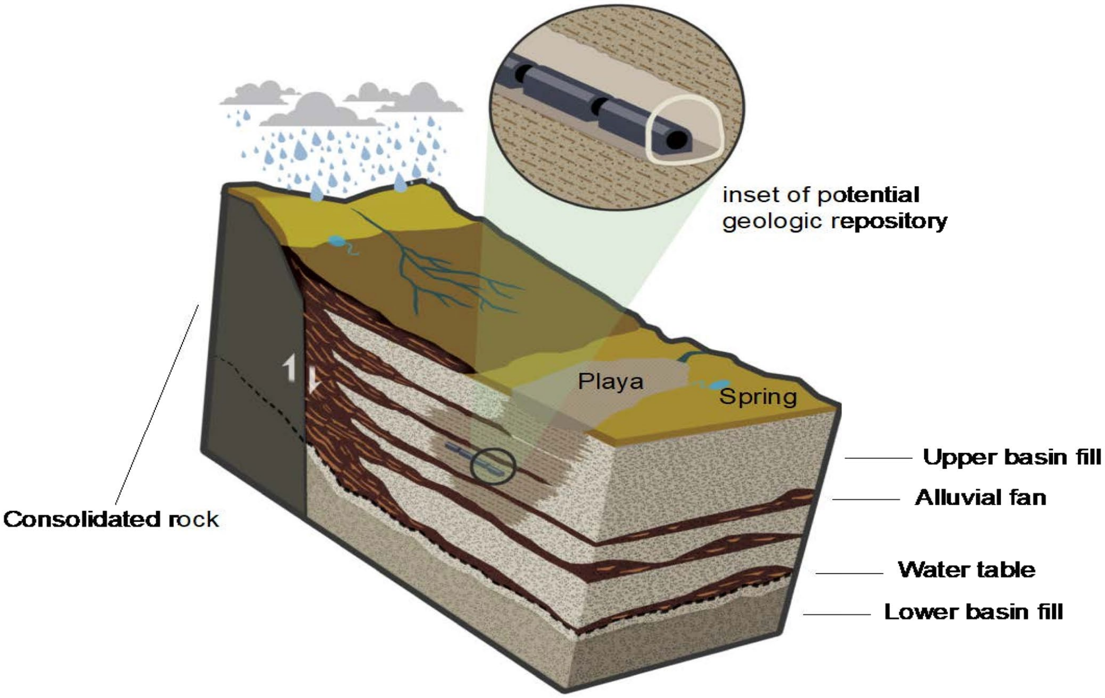

Figure 5-1. **A schematic showing a potential unsaturated zone geologic repository. Figure 5-2 of Mariner et al. (2018). A possible location for a repository would be in the playa deposits, which are impermeable fine-grained sediments and are located towards the center of this schematic. Also notice the lithologic heterogeneity depicted here that is expected in basin-fill valleys where alluvial fans, fluvial systems, spring discharge areas, and playas are common features.**

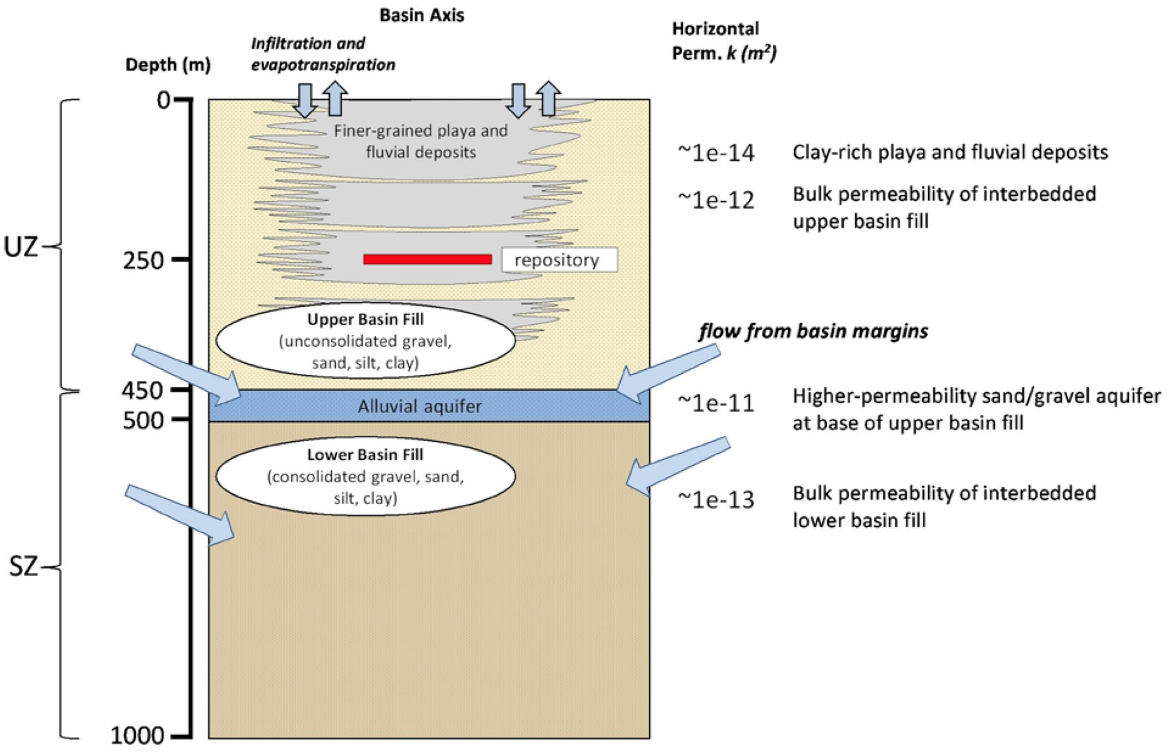

Figure 5-2. **Schematic cross section of the unsaturated zone model (Mariner et al., 2018). UZ = unsaturated zone; SZ = saturated zone**

5.2 Simulation

The mesh for the model domain originally proposed by Mariner et al. (2018) for field-scale simulations of the UZ reference case has been slightly modified due to a “zig-zag” issue in the DRZ edge that has been addressed for the deterministic simulations presented in this section and discussed in Section 5.3 of LaForce et al. (2021). The configuration for the model domain used this year, shown in Figure 5-3, is colored by material ID and has the same domain size of 3915 m x 1065 m x 1005 m as in Mariner et al. (2018) and most recently in LaForce et al., (2021). The repository lies within the Upper Basin Fill Confining (ubf_conf) sediment which is material ID 3, colored in turquoise.

Figure 5-4 shows an XY slice through the repository that is colored by material ID. In this model the repository is assumed to be 250 meters below the surface. The zoom box on the top left of the figure shows four waste packages (WPs) in red, buffer in yellow, DRZ in burgundy, and ubf_conf in turquoise.

Many preliminary simulations with varying PFLOTRAN solver options were run. The two final simulations being compared use 24-PWR, 100 y OoR, 40 GW-d/MTU burn-up WPs in a field-scale half-symmetry model with 27 drifts and 25 WPs per drift (675 24-PWR waste packages for half-symmetry). Drift spacing is 50 m, and center-to-center spacing of packages along the drift is 20 m. The model has no-flow boundary condition at the south face, which acts as a reflector, meaning the total number of WPs represented in the model is 1350. The field-scale PA unstructured mesh used for the final simulations was gridded with Cubit (Skroch et al., 2021) and has 2,996,313 grid cells, nearly 600k more than the mesh used prior to LaForce et al. (2021). Simulations of two-phase flow and temperature are run with PFLOTRAN (Hammond et al., 2014). Model domain visualizations have been generated using ParaView (Ayachit, 2015).

Initially, simulations were run up to 100k years using older PFLOTRAN solvers (Sevougian et al, 2019a, b) and smoothed characteristic curve options. The updated simulations presented later in this section are the 10 mm/yr infiltration case previously used in LaForce et al. (2021) and were run with the latest PFLOTRAN version which included a corrected NTRDC solver. The updated runs consist of two PFLOTRAN simulations that differ only in the subsurface transport mode used. The first uses the traditional GIRT mode and the second uses the recently developed NWT mode. These simulations were set up to have a final time of 100k years using 540 cores of a parallel HPC cluster.

The first simulation consists of two steps. This is necessary because the waste packages in the UZ model completely dry out at early time and GIRT mode cannot handle dry out anywhere in the model. In the first step, the simulation was set up without transport and run up to 100k years. Liquid saturation results were inspected in this simulation and it was determined that by 2,200 years, no cells in the model had a saturation value equal to zero. A checkpoint file was generated at 2,200 years simulation time using the CHECKPOINT keyword for the first part of the simulation. The second step used the RESTART keyword to continue running the simulation where it left off and included GIRT mode transport with a single tracer. This is considered an acceptable approximation to the full simulation including transport because at 2,200 years radionuclides would be in or near the nearly-dry waste packages, and without mobile water present there is no mechanism for transport away from them. The simulation was run to 100k years using GIRT mode from this restart time of 2,200 years. The first simulation completed in 33.1 hours (first step 17.6 hours + second step 15.5 hours).

The second simulation uses NWT mode from the beginning of the simulation, as NWT can handle complete dry out. This simulation failed to complete in the 96-hour window on the parallel HPC cluster and reached 8,464 years simulation time.

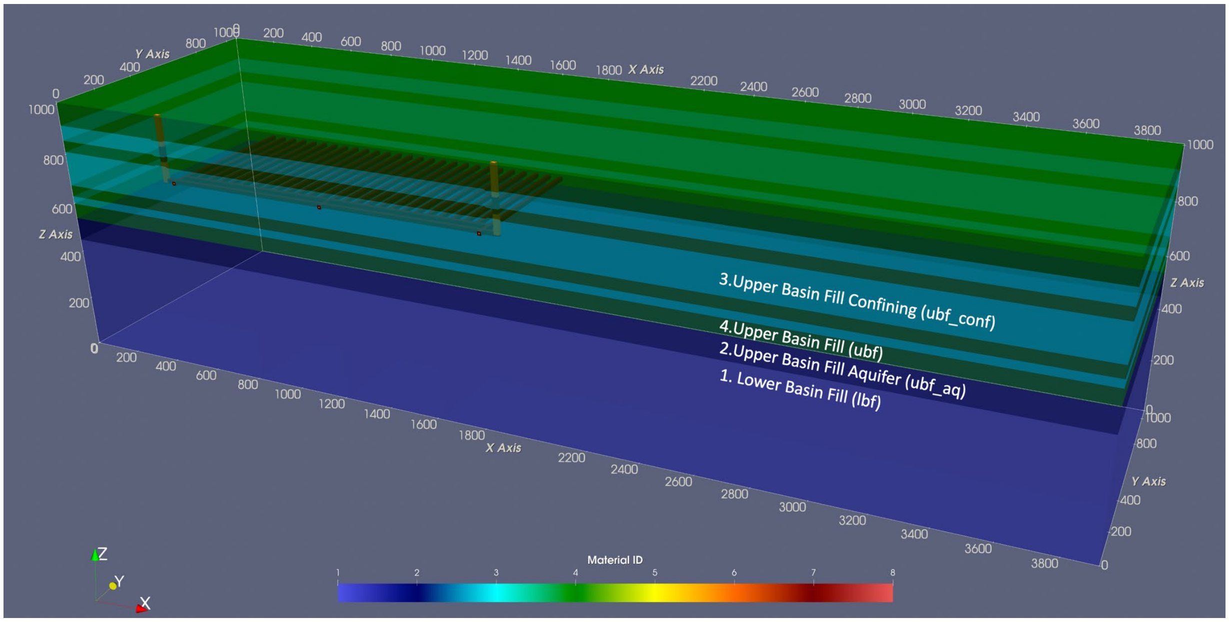

Figure 5-3. **Configuration of the repository and natural barrier system generated using Cubit, simulated in PFLOTRAN and visualized on ParaView. Turquoise color (material ID 3) represents the ubf_conf units (the centermost contains the repository as seen there), green (material ID 4) represents UBF, dark blue (material ID 2) represents the UBF aquifer, and blue (material ID 1) represents LBF. Distances along the axes are in meters, where 1000 m is land surface and 0 m is the bottom of the model domain. The left side of the figure represents a western direction.**

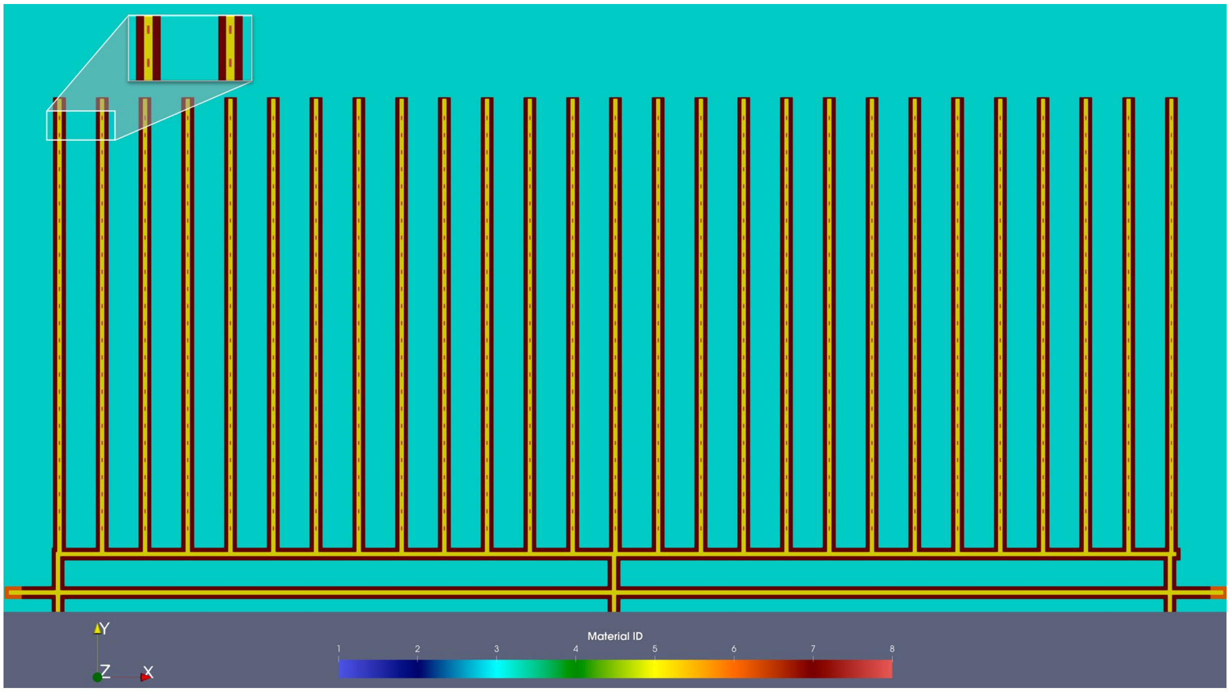

Figure 5-4. **XY slice through the repository colored by material ID. The repository is assumed to be 250 meters below the surface. The zoom in box on the top left shows a close-up of four waste packages (WPs), colored in red, buffer in yellow, DRZ in burgundy, and ubf_conf in turquoise. Visualized using ParaView.**

5.2.1 Newton Trust-Region Dogleg Cauchy Nonlinear Solver Update

Recent updates to the PFLOTRAN NTRDC solver (Nole et al., 2022) resolved an issue of negative liquid saturation that was observed in the FY21 runs (LaForce et al, 2021). Latest results are presented Section 5.3, which show that liquid saturation rescaled over all timesteps is no longer negative.

5.2.2 Nuclear Waste Transport Mode

The NWT mode is similar to the GIRT reactive transport mode, except for the manner in which the chemistry block and the Newton solver block for transport are set up within the PFLOTRAN input deck. NWT was designed to be used with WIPP flow mode, which is isothermal two-phase flow. The mode assumes equilibrium chemical processes, meaning there will not be rates or any kind of database that will need to be provided. NWT – PFLOTRAN Documentation (2022) provides more information regarding this specific mode and its usage.

5.2.3 Initial Conditions

The initial pressure is atmospheric at the top of the model domain. The initial temperature conditions are a surface temperature of 25°C and a natural geothermal temperature gradient of 0.025°C/m. The east and west boundary conditions are based on equilibrated one-dimensional simulations corresponding to these constraints. The full model domain temperature, pressure and saturation are simulated without drifts, waste packages or damage zone until a convergence tolerance is reached. This guarantees a quasi-steady-state initial condition for the simulations with infiltration.

5.2.4 Boundary Conditions

The bottom condition for the model is set to be Dirichlet so it is open to fluid flow and has temperature of 44 °C to create a geothermal gradient. These parameters are taken from the previously used input deck used in Mariner et al. (2018). As in previous work (Sevougian et al., 2019b; LaForce et al., 2021), there is no cross-repository flux at this time, but it will be considered for future PA modeling. At the top boundary the water infiltration rate is set to 10 mm/yr.

5.2.5 Material Properties

Material properties are discussed in Sections 4.1 and 4.2 of Sevougian et al. (2019a). Values used in the simulations are summarized in Table 5-1 below, which has been modified from Table 5-1 in LaForce et al. (2021). The only parameter modification is setting a more realistic grain density value for the upper basin fill DRZ which was previously set to 1600, and now set to 2700.

Table 5-1. Parameter values used in simulations (Modified from LaForce et al. 2021, Table 5-1). Modification made was setting a more realistic grain density value for the upper basin fill DRZ.

Model Region	Permeability (m^2)	Porosity ϕ	Tortuosity exponent[1] τ	Saturated Thermal Conductivity (W/m/K)	Unsaturated Thermal Conductivity (W/m/K)	Heat Capacity (J/kg/K)	Grain Density (kg/m^3)
Upper basin fill (UBF)	1×10^{-12}	0.40	1.4	2.0	1.0	830	2700
Upper confining zone (ubf_conf)	1×10^{-14}	0.40	1.4	2.0	1.0	830	2700
Basin fill below water table (LBF)	1×10^{-11}	0.40	1.4	2.0	1.0	830	2700
Confining zone below water table	1×10^{-13}	0.40	1.4	2.0	1.0	830	2700
Upper basin fill DRZ	1×10^{-11}	0.435	1.4	2.0	1.0	830	2700
Backfill	1×10^{-13}	0.40	1.4	2.0	1.0	830	2700
Waste Package (WP)	1×10^{-13}	0.50	1	16.7	16.7	488	5000

[1] $\tau = \phi^{1.4}$ (Van Loon and Mibus 2015)

5.3 Simulation Results and Discussion

Figure 5-5 shows the temperature, gas saturation, gas pressure, and liquid saturation as a function of log time at a single observation point called "Fwp_inside", which is inside the centermost WP of the half-symmetry repository for the PFLOTRAN simulations. These plots show differences in results between the past "FY21" PFLOTRAN NTRDC solver run and the updated version that was used for the "GIRT" and "NWT" simulations. It should be noted that the "NWT" run completed 8,463 years of simulation time out of the set final time of 100k years within the HPC wall clock time of 96 hours and that data is presented within these plots.

Table 5-2 lists results for these runs at specific times of interest. Initial values for temperature, gas pressure, liquid saturation, and gas saturation were the same for all three simulations. No differences were seen when looking at the available data for temperature, gas saturation, gas pressure and liquid saturation results for the “GIRT” and “NWT” simulations, as expected. Differences between the “FY21” and new simulations can be seen early in the simulations as water begins to boil off. The most noticeable difference is within the gas pressure plot in which the “GIRT” and “NWT” simulations see a constant increase up until 0.4 years and reached a max value of 192,735 Pa. This was not the case in the “FY21” simulation that saw a slight decrease and overall larger gas pressure up until 0.5 years that reached a maximum value of 196,080 Pa. When comparing the new simulation results to “FY21”, Table 5-2 shows that in the new simulations dry out happens a little over seven days sooner and resaturation begins eight years sooner, at year 1,771. The differences in results are due to changes in the NTRDC solver as well as the updated grain density value used within the backfill in the newest simulations.

Figure 5-6 shows a visual at 300 years for the “NWT” simulation that is colored by liquid saturation. Previously for the “FY21” run, the scale showed that liquid saturation data range resulted in a negative saturation for the bottom value (-2.3e-02) in some waste packages. This small numerical error is now resolved. The newest runs now show a 0.0e+00 saturation bottom value and a maximum saturation value of 5.4e-01 which differs by only 0.1e-01 when compared to the older “FY21” run.

The total tracer molar concentration of a row of WPs in the center of the repository at five snapshots in time are shown in Figure 5-7, along with a visual showing the material layers in the area of interest for the “GIRT” simulation. At 2,350 years, the tracer is the repository region, and the concentration is highest towards the center of the WPs as shown in the inset zoom of the centermost WP called “Fwp_inside”. Concentration at this centermost observation point and time shows an orange/red color matching the upper range of tracer molar concentrations of 2.30×10^{2} (M). By 3,000 years, the tracer has begun to transport below the repository due to infiltration driving downward flux. By 4,000 years, the tracer has continued to diffusively transport and reached the upper boundary of material ID 2, the upper basin fill aquifer (ubf_aq) that has a permeability of 1×10^{-11} m^2. By 10,200 years, the tracer molar concentration has decreased in the repository area but is still flowing into the ubf_aq layer. By the end of the simulation at 100k years, tracer concentrations are negligible.

A plot of total tracer molar concentration history at the observation point “Fwp_inside” for the “GIRT” simulation is shown in Figure 5-8. This plot shows that tracer concentration rapidly increases to a maximum value at 2,200 years, as it is released into the waste package. It then decreases with time and has reached background levels by the end of the simulation. Tracer results for the “NWT” mode PFLOTRAN simulation are not included in this report as it is still a work in progress. The “FY21” simulation is also not shown as it did not include any tracer transport.

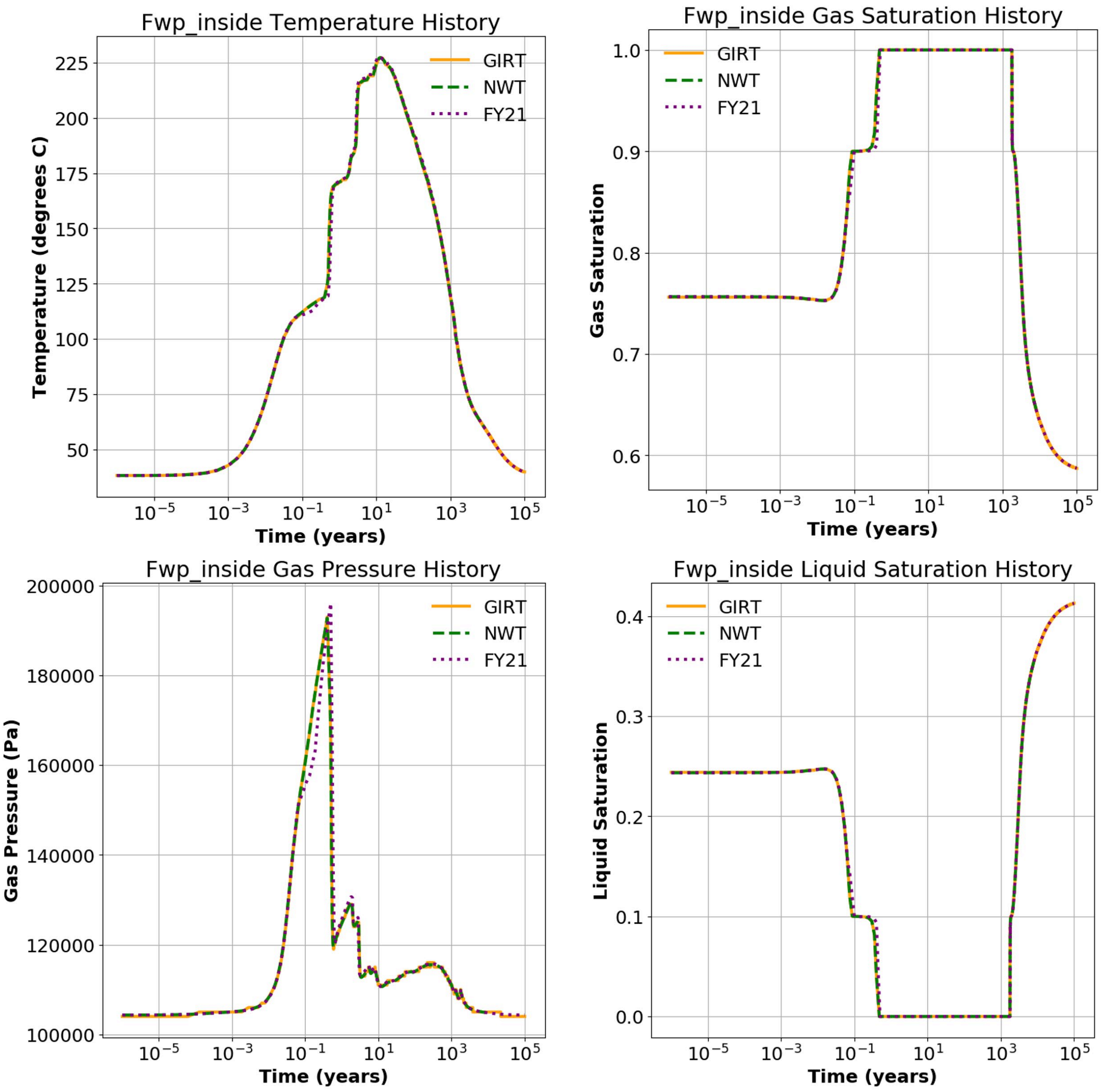

Figure 5-5. Temperature, gas saturation, gas pressure and liquid saturation history plots at observation point "Fwp_inside" for the three PFLOTRAN simulations.

Table 5-2. Results for the PFLOTRAN simulations at observation point "Fwp_inside".

Simulation:	**GIRT**	**NWT**	**FY21**
Initial temperature:	38.2°C	38.2°C	38.2°C
Maximum temperature:	227.3°C at 12.8 years	227.3°C at 12.8 years	227.6°C at 11.7 years
Temperature at 100K years:	39.8°C	Simulation did not complete	39.8°C
Initial gas pressure:	104,321 Pa	104,321 Pa	104,321 Pa
Maximum gas pressure:	192,735 Pa at 0.4 years	192,735 Pa at 0.4 years	196,080 Pa at 0.5 years
Gas pressure at 100K years:	104,339 Pa	Simulation did not complete	104,339 Pa
Initial liquid saturation:	0.24	0.24	0.24
Liquid saturation goes to zero:	from year 0.48 to year 1,771	from year 0.48 to year 1,771	from year 0.5 to year 1,779
Liquid saturation at 100K years:	0.41	Simulation did not complete	0.41
Initial gas saturation:	0.76	0.76	0.76
Gas saturation at value 1:	from year 0.48 to year 1,771	from year 0.48 to year 1,771	from year 0.5 to year 1,779
Gas saturation at 100K years:	0.59	Simulation did not complete	0.59

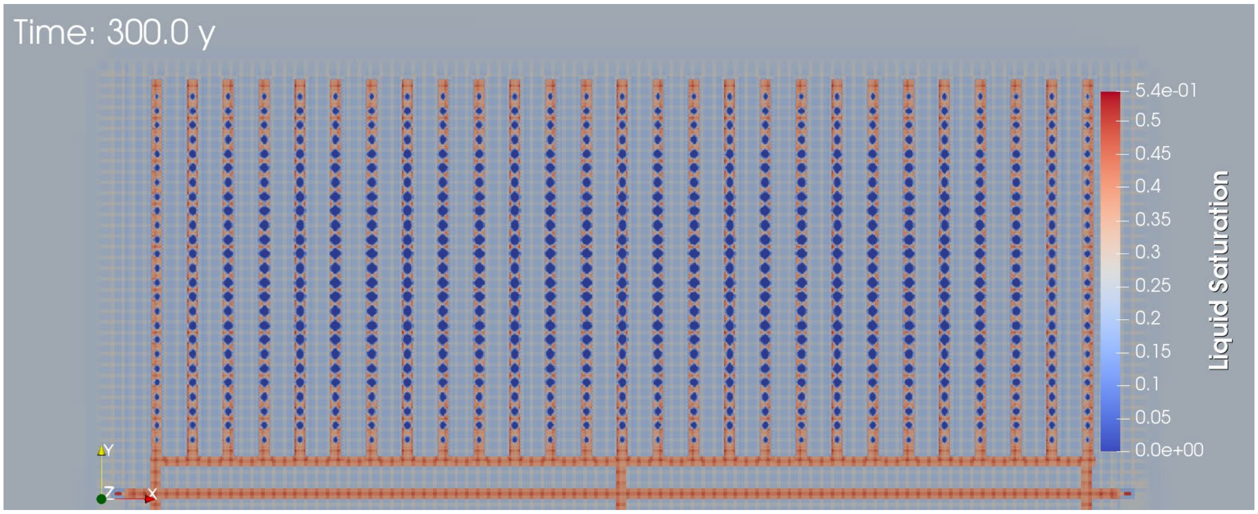

Figure 5-6. XY slice through the repository colored by liquid saturation at 300 years for the NWT simulation. Saturation range has been rescaled over all timesteps and no longer shows a negative lower range value as FY21 runs did.

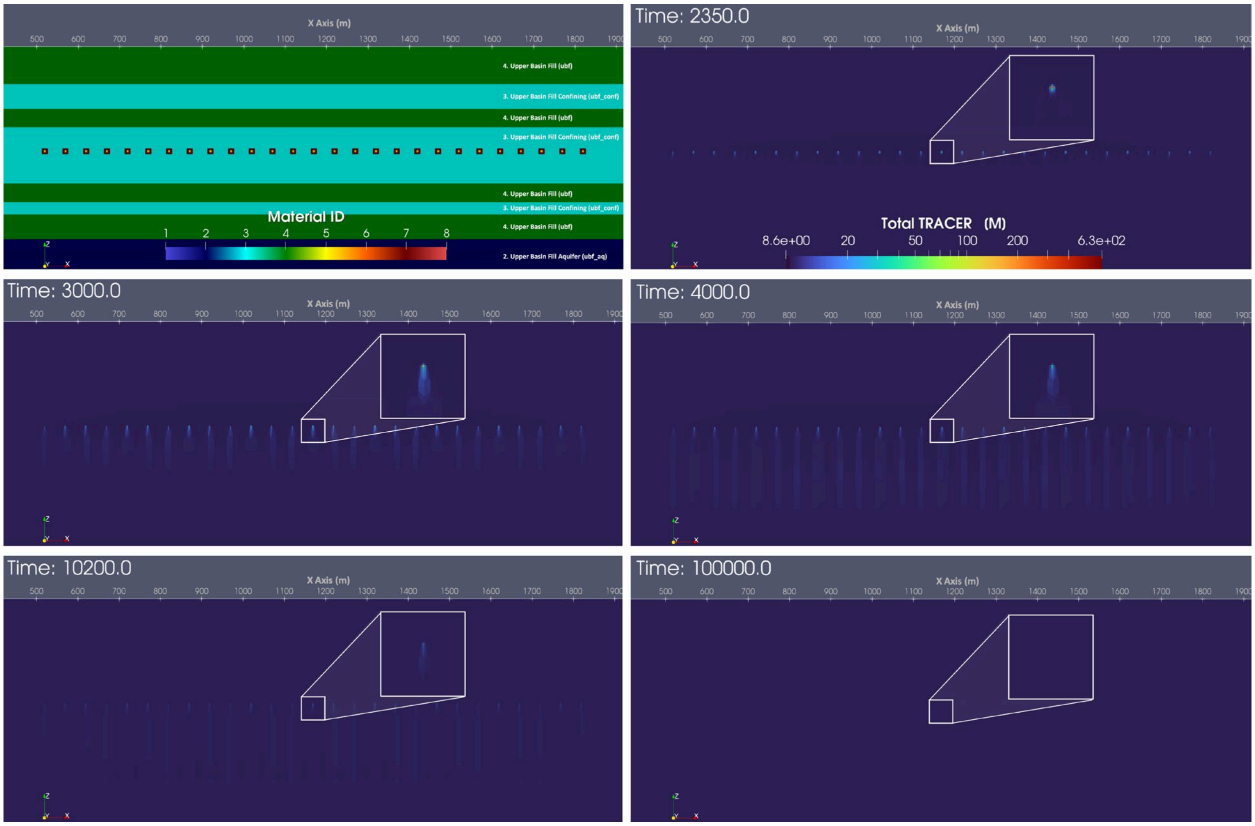

Figure 5-7. XZ slice through the center of the repository at “Fwp_inside” colored by Material ID (top left) and Total Tracer (M) at 2350, 3000, 4000, 10200, and 100k years for the “GIRT” simulation. Tracer concentration range has been rescaled over all timesteps.

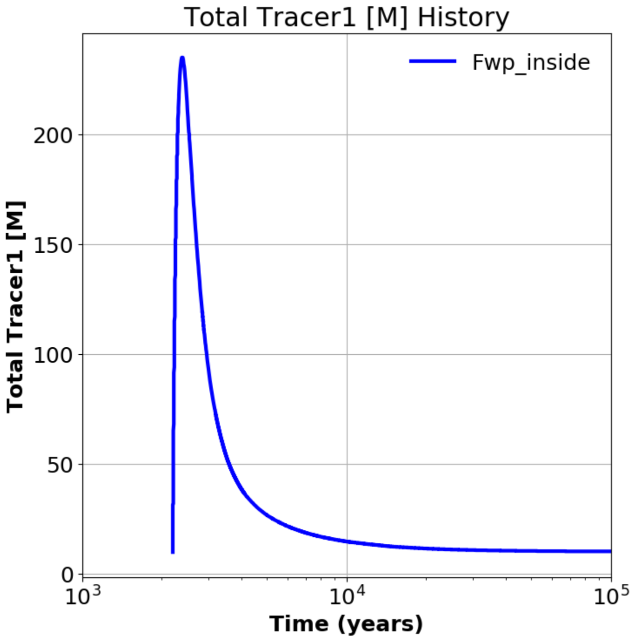

Figure 5-8. Total Tracer molar concentration history at observation point "Fwp_inside" for the "GIRT" simulation.

5.4 Conclusions and Considerations for Future Work

This section provided updated UZ model simulations including tracer transport in GIRT and NWT mode. An improved prediction of liquid saturation at dry out was achieved by using the most recent developments in the NTRDC solver. Flow results were shown, comparing the three different simulations. GIRT mode tracer concentration transport results were shown for a single simulation.

The next steps for the unsaturated alluvium model are to continue to the use of transport models (both GIRT and NWT) and implement the use of nuclides instead of tracers. It will also be necessary to implement flow from west to east of the model and set up UZ simulations using the GDSA Next Generation Workflow (NGW) as described in Section 3.2.1 of Mariner et al. (2020) to include uncertainty quantification (UQ) and sensitivity analysis (SA).

This page intentionally left blank.

6. NEW WASTE FORM SOURCE TERMS

In current PA simulations, all hypothetical DPC waste packages of each type (e.g., 24 or 37 PWR) have identical radionuclide inventory and thermal output (i.e., decay heat). The waste package thermal properties are based on scaled inventories for CSNF from Carter et al (2013) Rev 6 Table C-1 for either 40 or 60 (i.e., high-burnup) GWd/MTU burnup fuel. However, the estimated decay heat was unrealistic as it assumed a uniform loading of 60 GWd/MTU assemblies. As of writing, no commercial reactors irradiate fuel to 60 GWd/MTU. Additionally, to aid in thermal management during onsite storage, handling and final disposal, it is more likely that a waste package will contain a range of assembly burnups as opposed to a uniform high-burnup (i.e., 60 GWd/MTU) loading. To this end, a more realistic DPC inventory and thermal output for future PA simulations was modeled using an as-loaded 32 PWR assembly DPC currently in storage.

6.1 SNL ORIGEN modelling of Spent Fuel Cask

To create a realistic estimate of the decay heat of a notional spent fuel cask, a combined irradiation/decay simulation of a loaded spent fuel cask (Fort et al., 2019) was performed using the Oak Ridge Isotope Generation (ORIGEN) module of the SCALE code system (Wieselquist et al., 2020). SCALE is a widely used code system for nuclear safety analysis and design maintained by Oak Ridge National Laboratory (ORNL). ORIGEN is a combined depletion and decay module used to calculate fission product and activation nuclide inventories and their associated properties (e.g., decay heat). For this work, SCALE 6.2.3 was used.

Burnup and enrichment data from a Pacific Northwest National Laboratory (PNNL) thermal simulation of the TN-32B fuel cask (henceforth referred to as the TN-32B data) was used to generate ORIGEN input. The data is shown in Figure 6-1 (reproduced from Fig. 3-1 in Fort et al., 2019) and presented in Table 6-1. The assembly enrichments and power histories shown in Figure 6-1 were originally provided to ORNL by fuel vendors and Dominion, a nuclear power plant site operator. The burnup and enrichment data from the PNNL thermal simulation was used for this work as it is a realistic representation of a real-world spent fuel cask loading.

The ORIGEN decay heat calculation was performed in three steps. First, individual cross-section libraries were generated by interpolating SCALE's standard "w17x17" 17x17 PWR cross-section libraries using SCALE's built-in Automatic Rapid Process (ARP) utility. The cross-section libraries were interpolated to 60 GWd/MTU using the assembly-specific enrichment. A moderator density of 0.723 g/cm^3 was used. Using the cross-section libraries, each assembly was irradiated to its target burnup using a continuous irradiation cycle (i.e., decay during refueling outages was not modeled). Then, the nuclide inventories from the individual assembly irradiation cases were combined using ORIGEN's "blend" function. The "blended" mixture contains all irradiated material loaded into the notional fuel cask. The resulting mixture was decayed using evenly spaced linear timesteps from 0 years to 100 years and evenly spaced logarithmic timesteps from 100 years to 1,000,000 years.

The data in Fort et al. (2019) report did not include the assembly fuel or cladding masses but did specify that the assemblies were a 17x17 design. Thus, two simplifying assumptions were used for the mass calculations. First, all fuel assemblies were assumed to be generic Westinghouse 17x17 designs. The assemblies in the PNNL reference cask are a mix of Orano and Westinghouse designs, but all assemblies in the reference cask are 17x17 designs (Fort et al., 2019). The Westinghouse 17x17 design was chosen as the generic representation as the Westinghouse AP1000 Design Control Document (DCD) is publicly available (Westinghouse, 2012) and contains enough information to estimate the mass of a single Westinghouse 17x17 assembly using data from the Westinghouse AP600 design. Second, all cladding was assumed to be Zircaloy-4. According to the AP1000 DCD, the AP600 uses Zircaloy-4 or ZIRLO^{TM} cladding. It is not unreasonable to assume that the reported cladding mass was for either Zircaloy-4 or ZIRLO^{TM} cladding and may be incorrect for other cladding types. Furthermore, the isotopic composition of Zircaloy-4 cladding is readily available.

Core loading data for the Westinghouse AP600 design from Table 4-1.1 in the Westinghouse AP1000 DCD (Westinghouse, 2012) was used to estimate the fuel and cladding assembly mass shown in Table 6-2. A summary of the calculations is shown in Table 6-1. As previously discussed, the AP600 uses a standard Westinghouse 17x17 fuel assembly design (i.e., not Westinghouse 17x17 XL Robust fuel). To estimate the assembly fuel and cladding masses, the reported total core fuel loading of 75913.22 kg UO_2 (reported in the DCD as 167,360 lbm) was divided by 145, the total number of assemblies in the AP600 core to give 523.54 kg of UO_2 per assembly. The isotopic masses of ^{235}U and ^{238}U were calculated from the UO_2 mass on a per-assembly basis using stoichiometry. The cladding mass per assembly of 111.22 kg was estimated in a similar manner by dividing the total cladding mass of 16127.48 kg (reported in the DCD as 35,555 lbm) by 145 assemblies. The nuclide masses of the cladding were estimating using Zircaloy-4 nuclide weight fractions reported by McConn et al. (2011).

Table 6-1. Tabulated data from PNNL thermal simulation of a TN-32B spent fuel cask used for ORIGEN simulations.

Cell #	Assembly ID	Burnup (GWd/MTU)	Enrichment (wt%)
1	6T0	54.2	4.25
2	3K7	53.4	4.55
3	3T6	54.3	4.25
4	6F2	51.9	4.25
5	3F6	52.1	4.25
6	30A	52	4.55
7	22B	51.2	4.55
8	20B	50.5	4.55
9	5K6	53.3	4.55
10	5D5	55.5	4.2
11	5D9	54.6	4.2
12	28B	51	4.55
13	F40	50.6	3.59
14	57A	52.2	4.55
15	30B	50.6	4.55
16	3K4	51.8	4.55
17	5K7	53.3	4.55
18	50B	50.9	4.55
19	3U9	53.1	4.45
20	0A4	50	4.0
21	15B	51	4.55
22	6K4	51.9	4.55
23	3T2	55.1	4.25
24	3U4	52.9	4.45
25	56B	51	4.55
26	54B	51.3	4.55
27	6V0	53.5	4.4
28	3U6	53	4.45
29	4V4	51.2	4.4
30	5K1	53	4.55
31	5T9	54.9	4.25
32	4F1	52.3	4.25

Table 6-2. Assembly nuclide/isotopic masses used for ORIGEN simulation input.

Material	Parameter	Value
UO_2	Total mass in AP600 core (kg)	75913.22
	Mass (kg)	523.54
	U mass (kg)	461.49
	U^{235} and U^{238} mass (kg)	Depends on assembly-specific enrichment
	O from UO2 (kg)	62.05
Zircaloy-4	Cladding in AP600 core (kg)	16127.48
	Mass (kg)	111.22
	O mass (kg)	0.13
	Cr mass (kg)	0.11
	Fe mass (kg)	0.22
	Zr mass (kg)	109.21
	Sn mass (kg)	1.55

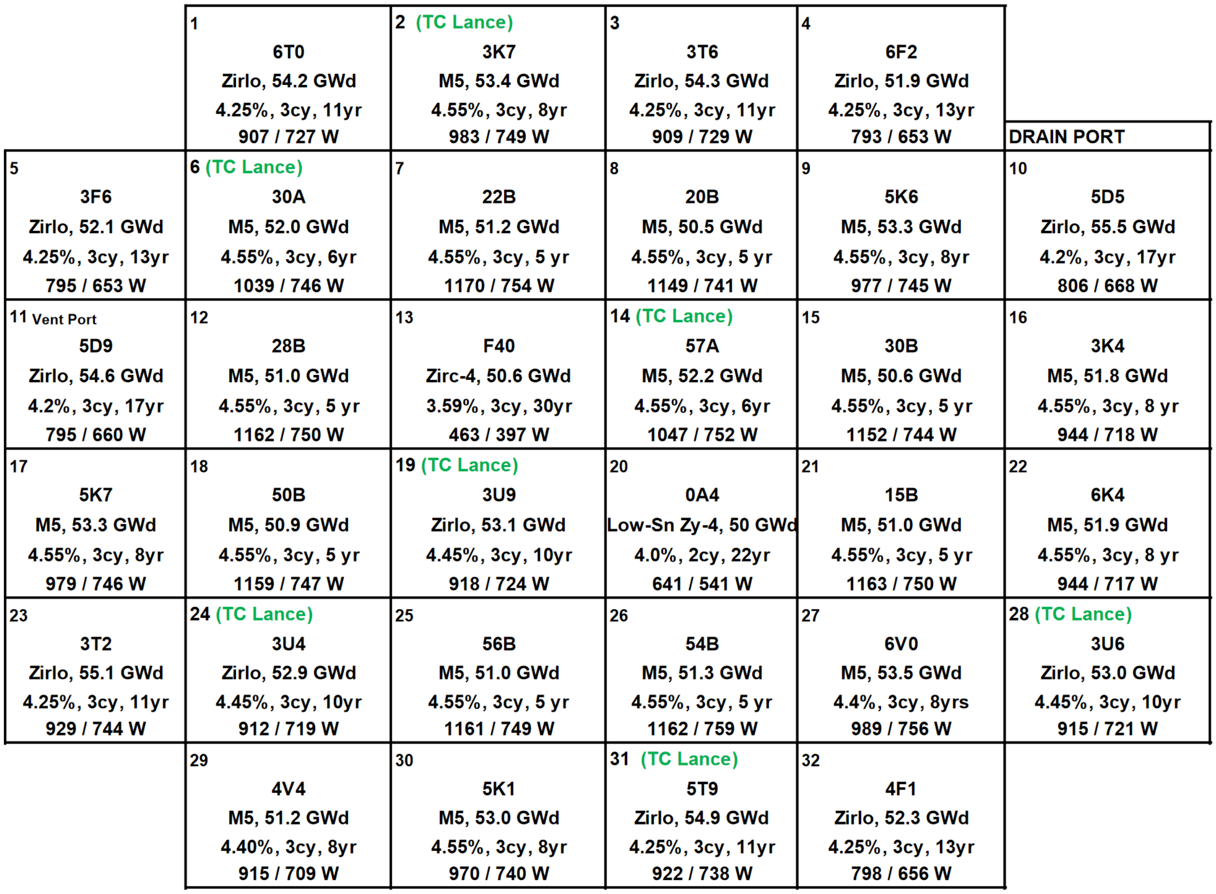

	1 6T0 Zirlo, 54.2 GWd 4.25%, 3cy, 11yr 907 / 727 W	2 (TC Lance) 3K7 M5, 53.4 GWd 4.55%, 3cy, 8yr 983 / 749 W	3 3T6 Zirlo, 54.3 GWd 4.25%, 3cy, 11yr 909 / 729 W	4 6F2 Zirlo, 51.9 GWd 4.25%, 3cy, 13yr 793 / 653 W	DRAIN PORT
5 3F6 Zirlo, 52.1 GWd 4.25%, 3cy, 13yr 795 / 653 W	6 (TC Lance) 30A M5, 52.0 GWd 4.55%, 3cy, 6yr 1039 / 746 W	7 22B M5, 51.2 GWd 4.55%, 3cy, 5 yr 1170 / 754 W	8 20B M5, 50.5 GWd 4.55%, 3cy, 5 yr 1149 / 741 W	9 5K6 M5, 53.3 GWd 4.55%, 3cy, 8yr 977 / 745 W	10 5D5 Zirlo, 55.5 GWd 4.2%, 3cy, 17yr 806 / 668 W
11 Vent Port 5D9 Zirlo, 54.6 GWd 4.2%, 3cy, 17yr 795 / 660 W	12 28B M5, 51.0 GWd 4.55%, 3cy, 5 yr 1162 / 750 W	13 F40 Zirc-4, 50.6 GWd 3.59%, 3cy, 30yr 463 / 397 W	14 (TC Lance) 57A M5, 52.2 GWd 4.55%, 3cy, 6yr 1047 / 752 W	15 30B M5, 50.6 GWd 4.55%, 3cy, 5 yr 1152 / 744 W	16 3K4 M5, 51.8 GWd 4.55%, 3cy, 8 yr 944 / 718 W
17 5K7 M5, 53.3 GWd 4.55%, 3cy, 8yr 979 / 746 W	18 50B M5, 50.9 GWd 4.55%, 3cy, 5 yr 1159 / 747 W	19 (TC Lance) 3U9 Zirlo, 53.1 GWd 4.45%, 3cy, 10yr 918 / 724 W	20 0A4 Low-Sn Zy-4, 50 GWd 4.0%, 2cy, 22yr 641 / 541 W	21 15B M5, 51.0 GWd 4.55%, 3cy, 5 yr 1163 / 750 W	22 6K4 M5, 51.9 GWd 4.55%, 3cy, 8 yr 944 / 717 W
23 3T2 Zirlo, 55.1 GWd 4.25%, 3cy, 11yr 929 / 744 W	24 (TC Lance) 3U4 Zirlo, 52.9 GWd 4.45%, 3cy, 10yr 912 / 719 W	25 56B M5, 51.0 GWd 4.55%, 3cy, 5 yr 1161 / 749 W	26 54B M5, 51.3 GWd 4.55%, 3cy, 5 yr 1162 / 759 W	27 6V0 M5, 53.5 GWd 4.4%, 3cy, 8yrs 989 / 756 W	28 (TC Lance) 3U6 Zirlo, 53.0 GWd 4.45%, 3cy, 10yr 915 / 721 W
	29 4V4 M5, 51.2 GWd 4.40%, 3cy, 8yr 915 / 709 W	30 5K1 M5, 53.0 GWd 4.55%, 3cy, 8yr 970 / 740 W	31 (TC Lance) 5T9 Zirlo, 54.9 GWd 4.25%, 3cy, 11yr 922 / 738 W	32 4F1 Zirlo, 52.3 GWd 4.25%, 3cy, 13yr 798 / 656 W	

Figure 6-1. Reference data from PNNL thermal simulation of a TN-32B spent fuel cask. (After Fort et al., 2019)

6.1.1 ORIGEN modelling results

A subset of the radionuclide inventory from the ORIGEN simulation of the 32 assembly DPC is shown in Table 6-3. These radionuclides are the most likely to be included in the waste form in repository performance assessment simulations. They are highly radioactive, long-lived, and/or highly mobile in the subsurface environment, or represent part of the decay chain for radionuclides of primary concern.

Figure 6-2 shows the decay heat curves for actinides, non-actinides (i.e., light nuclides and fission products), and all nuclides for the simulated TN-23B canister. Because the x-axis is logarithmic, the decay heat at 0 years is not displayed. Initially, 95% of the total decay heat is produced by non-actinide nuclides. However, after about 55 years of decay, both the actinides and non-actinides produce equivalent amounts of decay heat. After 55 years, the non-actinides decay away, and by 300 years, effectively 100% of the decay heat is produced by actinides. As actinides are expected to drive long-term decay heat trends, these results help verify the ORIEGN simulations performed for this work.

As a second check, characteristics of the DPC simulated for this work were compared to the DPC characteristics in Fort et al., (2019) shown in Figure 6-1. The average cooling time of the assemblies in Figure 6-1 is approximately 10 years, and the summed decay heat from all assemblies in Figure 6-1 is 30.6 MW. In comparison, the decay heat of the simulated DPC at 10 years is 29.6 MW (i.e., 3% absolute error). The error for this specific comparison at 10 years was not viewed as significant. Unfortunately, there was not enough data provided in Fort et al., (2019) to perform a more detailed comparison of the simulation results.

Figure 6-3 shows a comparison of the hypothetical 37 assembly DPC (assumed uniform 60 GWd/MTU) used for previous studies (Sevougian et al., 2019; LaForce et al., 2020, 2021) and the 32 assembly DPC produced as part of this work. From 100 years to 1000 years, the decay heats of the two DPCs are comparable, but after 1000 years, the decay heat of the 37 assembly DPC is noticeably higher. For example, between 4000 to 5000 years, the decay heat of the 37 assembly DPC is about 66% higher than the decay heat of the simulated 32 assembly DPC. The differences are a result of the different masses in each DPC as well as the lower average burnup of the simulated 32 assembly DPC.

The purpose of Figure 6-3 is to illustrate how high the decay heat of the hypothetical 37 assembly DPC was. Figure 6-4 shows a more reasonable comparison of the decay heats for the simulated 32 assembly DPC and a mass-scaled version of the 37 assembly DPC decay heat curve used for recent simulations in Sevougian et al. (2019), LaForce et al. (2020, 2021). The decay heat of the original DPC was scaled by 0.86 (i.e., 32/37) to provide a reasonable comparison to the simulated 32 assembly DPC. The mass scaling assumes a homogenous DPC composition.

As can be seen in Figure 6-4, the decay heat of the simulated 32 assembly DPC is very similar to the hypothetical, mass-scaled 37 assembly DPC decay heat curve. Between 100 to 1100 years, the decay heat curves do not show any notable differences, although the simulated 32 assembly DPC decay heat is slightly higher than the mass-scaled 37 assembly DPC between 200 to 1000 years. From 1,000 years onwards, the mass-scaled 37 assembly DPC is slightly hotter than the 32 assembly DPC. The largest difference between the two decay heat curves occurs around 5000 years when the mass-scaled 37 assembly curve is approximately 33% greater than the simulated 32 assembly curve (i.e., 400 W versus 300 W, respectively). For simulations considering the integrated decay heat (i.e., total decay energy), the slightly lower decay heat of the simulated 32 assembly DPC may be significant.

A final comparison is shown in Figure 6-5. Figure 6-5 is the same as Figure 6-4 except that the 32 assembly DPC has been scaled by 86% (i.e., 0.435/0.461). The scaling reflects the difference between the metric tons of initial heavy metal (MTIHM) per assembly in the simulated 32 assembly DPC (0.461

MTIHM/assembly) and the 37 assembly DPC (0.435 MTIHM/assembly). When comparing the total decay heats, scaling the mass of the 32 assembly DPC provides a more accurate comparison. The main point of Figure 6-5 is to demonstrate that the decay heat of the mass-scaled 37 assembly DPC is still high compared on a per MTIHM basis and the scaling the 37 assembly DPC decay heat may still lead to overestimating decay heat in PA simulations.

Table 6-3. Mass of select nuclides in simulated 32 assembly DPC at 0.0 yrs.

Isotope	Mass (kg)
^{241}Am	0.67
^{243}Am	3.52
^{238}Pu	5.28
^{239}Pu	90.92
^{240}Pu	38.63
^{242}Pu	14.23
^{237}Np	10.68
^{233}U	8.4×10^{-6}
^{234}U	0.06
^{236}U	88.81
^{238}U	13565.51
^{229}Th	8.7×10^{-9}
^{230}Th	1.7×10^{-7}
^{226}Ra	2.6×10^{-12}
^{36}Cl	2.5×10^{-29}
^{99}Tc	17.78
^{129}I	3.60
^{135}Cs	7.58

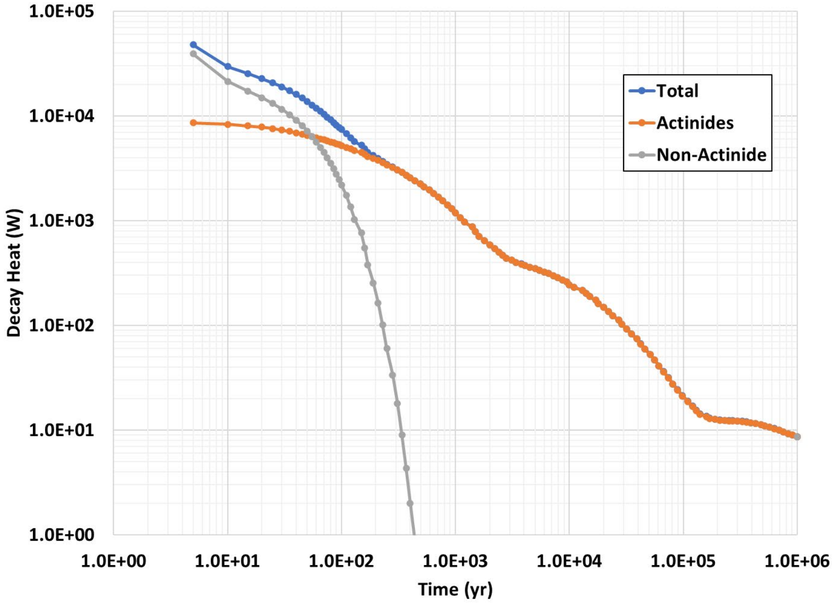

Figure 6-2. **Thermal energy output vs time for the 18 individual radionuclides and total decay heat for the simulated 32 PWR assembly DPC.**

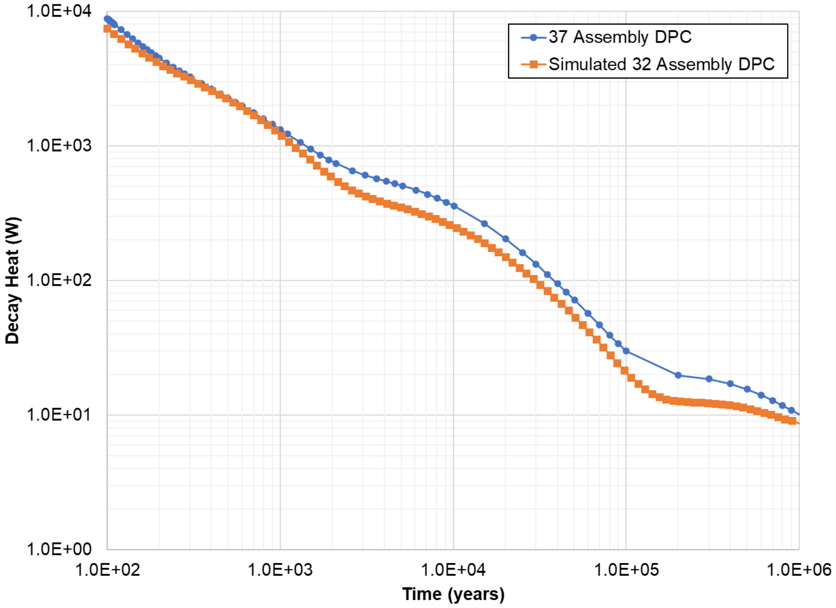

Figure 6-3. **Comparison of the decay heats of the simulated 32 assembly DPC and the hypothetical 37 assembly DPC used in previous PA simulations.**

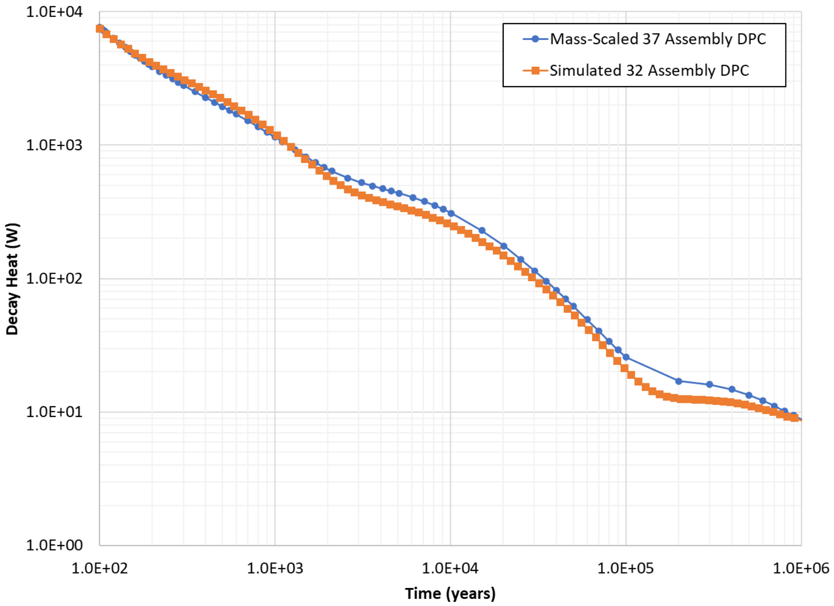

Figure 6-4. **Comparison of the decay heats of the simulated 32 assembly DPC and the hypothetical 37 assembly DPC used in previous PA simulations scaled to 32 assemblies.**

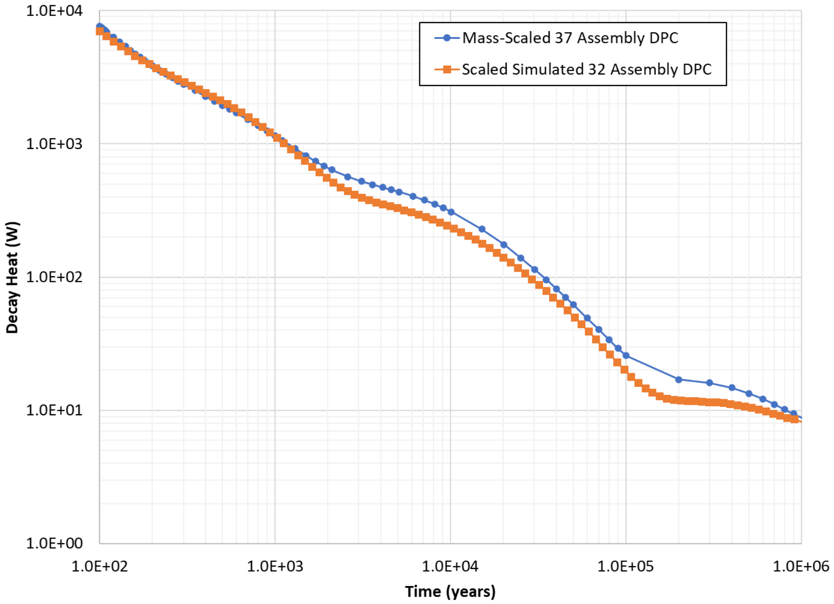

Figure 6-5. **Comparison of the decay heats of the mass-scaled simulated 32 assembly DPC and the hypothetical 37 assembly DPC used in previous PA simulations scaled to 0.435 MTIHM/assembly.**

6.1.2 Comparison with existing PWR model

Comparison of the thermal output from Fort et al. (2019) with simulations by Oak Ridge National Laboratory in Jones et al, (2021), Table 1-2, verifies that the TN-32 DPC likely lies between the 75%-90% of DPCs in inventory (Price, 2022). The similarity of the thermal output between the as-loaded high-burnup spent fuel from (Fort et al, 2019) confirms that the hypothetical 37 assembly DPC is not representative of the average DPC in inventory, but neither is it unrealistically hot.

6.2 ORNL ORIGEN Modelling SNF Decay

In FY 2022 we also reached out to researchers at Oak Ridge National Laboratory (ORNL) about creating more representative heat of decay files for future PA analysis. ORNL provided ORIGEN modelling scenarios for a hypothetical Westinghouse 17x17 commercial power reactor and five sets of assembly depletion parameters. The selected burnup and enrichment values are shown in Table 6-4, and the full simulation details from ORNL are provided in the Appendix: DPC calculations from ORNL.

ORNL researchers provided the enrichment for fuel cooled for 55 years for use to initialize future PA simulations. The top of the table of isotopes is shown in the Appendix.

Table 6-4. Selected Burnup and Enrichment Values.

Burnup (MWD/MTU)	Irradiation Time (days)	Enrichment (wt. %)
45000	1108.92	3
50000	1232.13	3.2
55000	1355.35	3.5
60000	1478.56	3.8
65000	1601.77	4.1

6.2.1 Comparison with existing PWR decay heat

Figure 6-6 shows a comparison of the decay heat for four of the hypothetical PWRs. All the simulated heats are scaled to 32 PWR to be consistent with Figure 6-4. The decay heat output used in previous PA simulations calculated at 5 years and then at the assumed beginning of the PA simulations at 100-year OoR, with no timesteps in between. After 100 years the heat output from the previous DPC is very similar to the hypothetical DPC decay heat. It is slightly lower at 500 years and slightly higher around 5,000-100,000 years. This confirms that the 60GWd/MTU heat source in the previous PA calculations is consistent with DPCs loaded with high burn-up fuel from updated ORIGEN simulations.

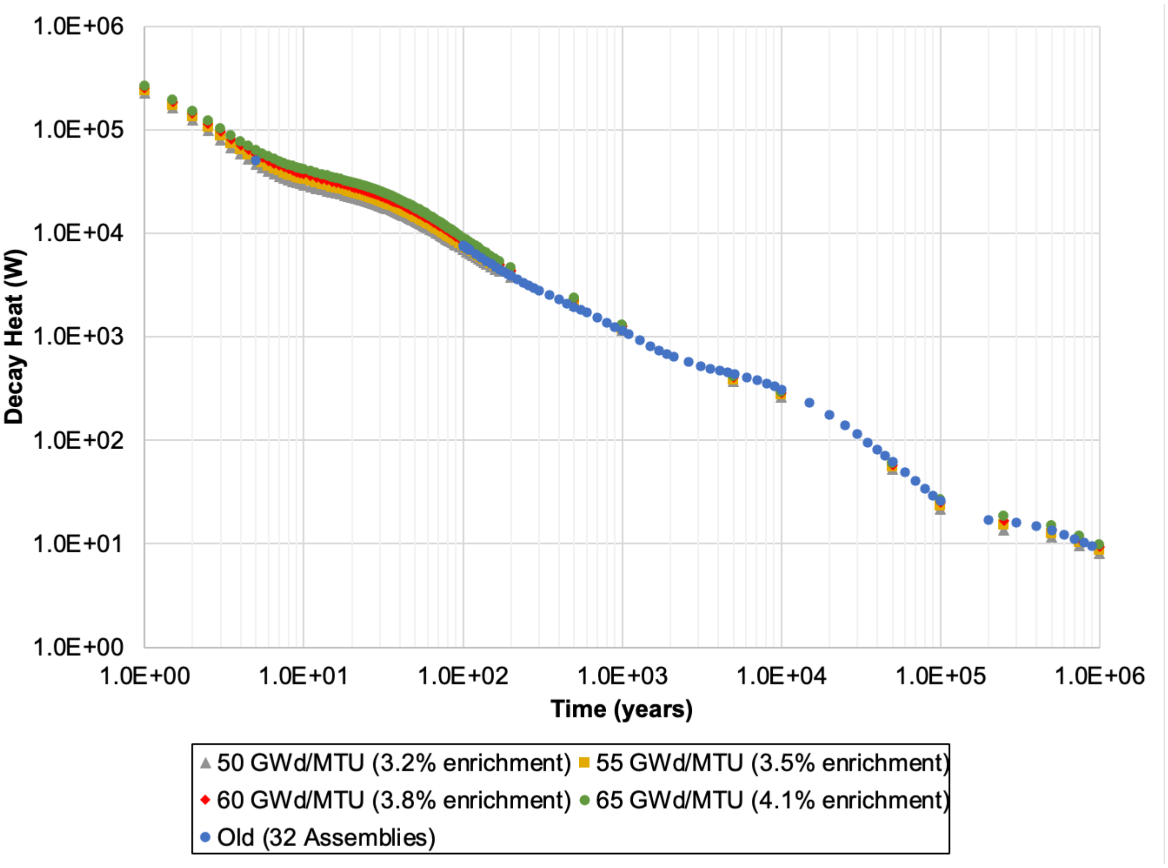

Figure 6-6. **Comparison of the decay heat of 4 hypothetical DPCs with burnup and enrichment shown and the heat source used in previous PA simulations. Both are scaled to 32 PWR.**

6.3 Conclusions and Future Work

The two preceding analyses confirm that the 37 PWR DPC heat source utilized in previous GDSA PA simulations is consistent with ORIGEN simulations on real and hypothetical DPCs filled with high burn-up fuel. This validates the existing hypothetical 37 PWR DPC for use in simulations, but also indicates that it is not representative of an ‘average’ waste package.

Future PA simulations should include uncertainty sampling from a distribution of PWRs with a range of predicted decay heats that are representative of the range of thermal output of in-storage DPCs. Some of the required data is available from a separate project on DPC thermal analysis, which has the decay heats for the 10%, 50%, 75%, 90%, 95% and 99% hottest waste packages in inventory (Jones et al., 2021). Alternately, the necessary data could be generated by SNL or ORNL project partners.

A realistic distribution of decay heat will result in a lower average heat load in the repository than previous GDSA RSA PA simulations. However, sampling of decay heat is more complex than traditional sampling over a normal distribution. One operational constraint that should be included in the sampling to avoid unrealistic localized heating in the PA model is to require that hot DPCs not be allowed next to each other in the repository. Theoretically this constraint can be handled by sampling all waste packages, placing the hottest DPCs in the model and then forcing the neighboring waste packages to be lower thermal load DPCs. However, this method biases the distribution of the DPCs in the repository and is more challenging to implement than a purely random distribution.

PA simulations utilizing a sampled approach to creating radionuclide and heat sources will also contain DPCs that are even hotter than currently considered. This may cause challenges in the PA simulation framework because of very high local heat at the hottest DPCs.

This page intentionally left blank.

7. VOROCRUST MESHING AND SIMULATION

VoroCrust development and simulation on Voronoi meshes continued this year. The two main accomplishments in this task were:

(1). Creation and release of an open-source version of VoroCrust (Abdelkader et al., 2020) called "VoroCrust-Meshing" that contains the capability necessary for simulation in PFLOTRAN (Lichtner et al., 2020) and visualization of the results in ParaView 5.9 (Ahrens et al., 2005).

(2). Performance Assessment (PA) case using VoroCrust meshes in PFLOTRAN simulations that includes geological structure based on a geological framework model (GFM) in the uncertainty analysis for a simplified case.

7.1 Improvements to VoroCrust

VoroCrust is a software framework developed at SNL. It deploys Voronoi-based methods for a wide range of applications including meshing, sampling, optimization, uncertainty quantification, and machine learning, as shown in Figure 7-1. VoroCrust's meshing algorithm is the first provably correct algorithm for conforming Voronoi meshing of non-convex and non-manifold domains with guarantees on the quality of both surface and volume elements (Abdelkader et al., 2020).

VoroCrust provides meshing solutions to the GDSA Framework that no other software can provide. Flow and transport codes such as TOUGH2, FEHM, PFLOTRAN, and MODFLOW achieve more accurate solutions on orthogonal meshes (see LaForce et al., 2021). Voronoi meshes are one type of mesh that can deliver provably orthogonal meshes that satisfy this requirement. Conforming Voronoi tessellations are difficult to produce if the geometry is complex, as is often the case for subsurface simulations which require meshing a combination of engineered and natural features. VoroCrust-Meshing is a push button technique that automatically generates meshes of closed input volumes with provable quality.

The VoroCrust team was tasked in FY2022 to release the meshing piece as an open-source code on GitHub. This required redesigning the architecture of the VoroCrust framework which included the following tasks:

(1). Separate the meshing code into a standalone package that could be released under an open-source license to GDSA customers and collaborators.

(2). Establish a GitHub repository at https://github.com/sandialabs and develop a release strategy to update its code from the internal VoroCrust gitlab repository where the development takes place.

(3). Rewrite methods within the VoroCrust-Meshing code to ensure VoroCrust functionalities that are not needed for meshing and that are either Sandia proprietary or in an exploratory research phase are not released.

(4). Remove redundant code (search trees and background grid refinement).

(5). Update the user manual with instructions for general users.

(6). Work with Sandia legal on getting a new open-source license for the VoroCrust-Meshing code that meets the GDSA requirements and conforms to the current VoroCrust patents.

The code was restructured and a new system is introduced in VoroCrust where there are libraries and applications. VoroCrust-Meshing is now one of these applications. A portion of the meshing code has been rewritten to enable a standalone distribution. Currently work is underway with the legal department at Sandia National Laboratories to obtain the needed open-source license to release that piece of the code. The release of the first version of VoroCrust-Meshing is expected in September 2022.

In addition to this main task, the VoroCrust team continued to provide user support to the GDSA analysts to enable them to use/test VoroCrust-Meshing efficiently. Time has been dedicated to make sure that the VoroCrust code works well and installation has been tested on a variety of Mac, Linux and Windows operating system releases to meet the GDSA requirements.

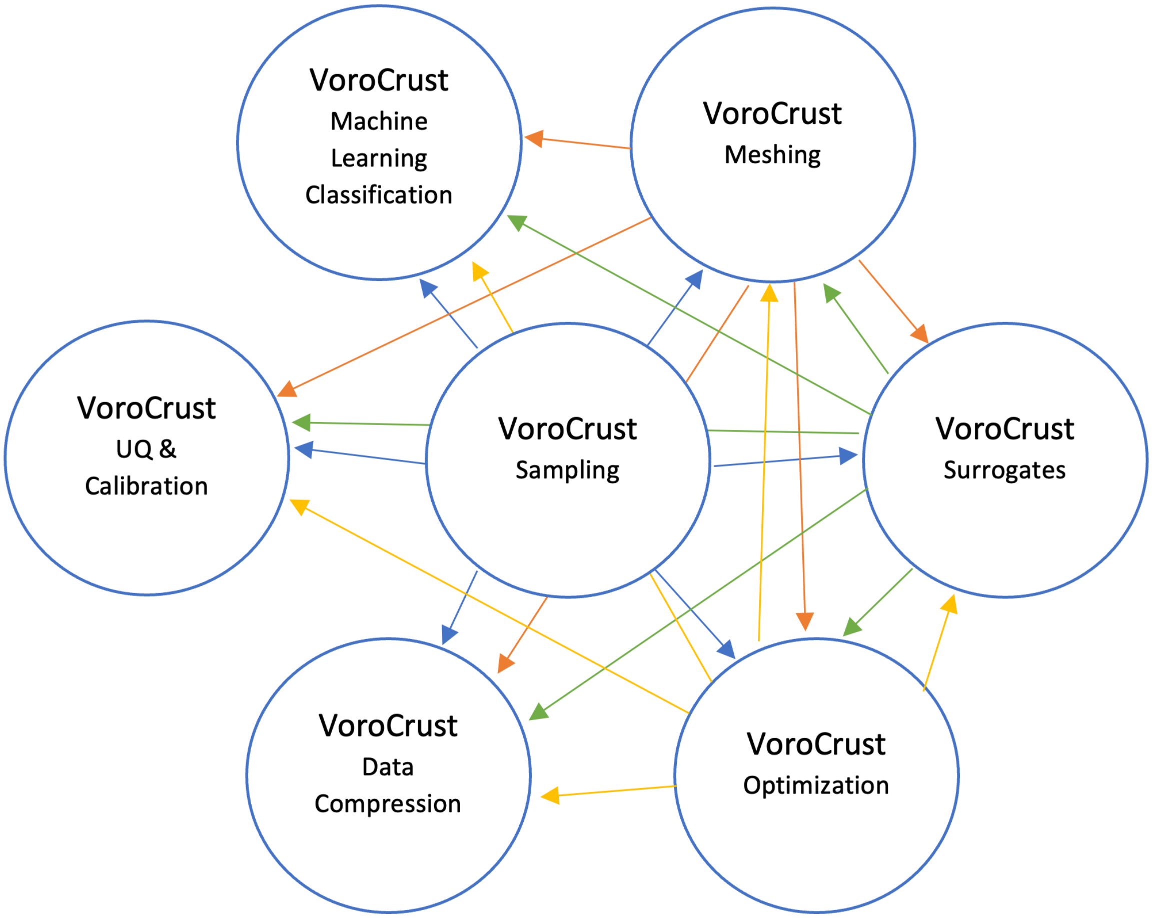

Figure 7-1. **At the beginning of this fiscal year, VoroCrust was a set of C++ classes that had different functionality and a wide range of applications. There was a great deal of interdependency between the different classes. VoroCrust has a commercial license which poses constraints on distribution of the code outside Sandia National Laboratories and did not meet the needs of the GDSA to distribute the code as part of its open-source earth science package.**

7.2 Shale Performance Assessment

In this section, a simplified PA example that includes geological uncertainty is developed and simulated. This work represents the first time a GFM has been directly used in a GDSA PA simulation. This proof-of-concept is a critical first step towards incorporating geological realism into PA calculations.

An example of the workflow under development is shown in Figure 7-2. For each realization, Dakota (Adams et al., 2021) Latin Hypercube Sampling (LHS) is run to sample each of the uncertain parameters and choose one of the 87 mesh realizations of the geological model. A unique geological model is sampled for each set of flow parameters so that all uncertainties are epistemic. The model volumes for each geological realization are created in LaGriT (Los Alamos Grid Toolbox, 2017) and meshed in VoroCrust (Abdelkader et al., 2020). PFLOTRAN (Lichtner et al., 2020) simulations are populated with the sampled stochastic flow parameters and run for each realization of the model. The process of meshing the model and creating the PFLOTRAN input deck for a single realization of the uncertainty scenarios is mostly automated at the present time and discussed in detail below. The uncertainty analysis piece of the workflow is not complete at this time, as it is currently too time intensive to run a sufficiently large number of simulations required for a robust statistical analysis.

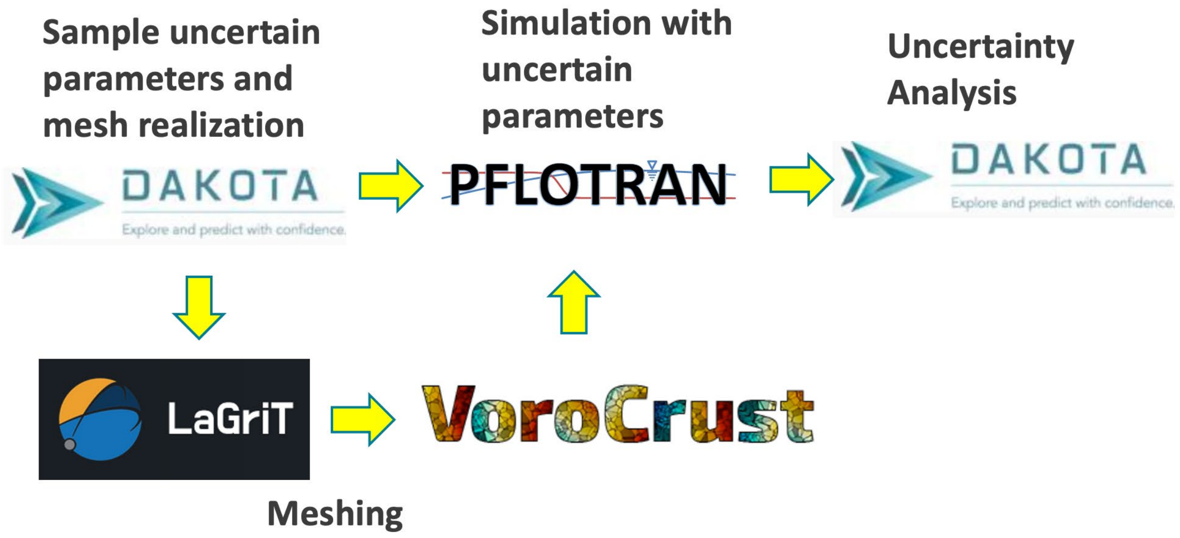

Figure 7-2. Schematic of the current workflow for incorporating geological uncertainty into simplified PA.

7.2.1 Simplifications

The geological models for simulating the shale repository are 7 km by 2.5 km sections clipped out of the GFM model of the Pierre Shale presented in Section 5.1 of Sevougian et al. (2019b). The shale GFM model is reproduced in the top of Figure 7-3. The simulation model and uncertain parameters are consistent with previous shale cases in Mariner et al. (2017) Section 4, Sevougian et al. (2019b) Section 5.3, and Swiler et al. (2019) Section 7 as far as possible. However, the example PA case is simplified from the previous shale PA cases in two ways that make the simulation models and results less realistic than those from previous cases.

First, the entire repository and surrounding damage zones are represented as a single, rectangular source term containing the repository footprint. The region has buffer properties, with higher porosity and lower permeability than the shale host rock. This simplification is necessary is because it is not yet possible to mesh 2,575 individual waste packages in VoroCrust without creating a simulation mesh far too large to simulate on. (VoroCrust meshing of individual waste packages is possible but remains an area of future work.) Not explicitly including the engineered backfill around each waste package means that this case is likely to over-predict the transport of radionuclides away from the repository as compared with the previous models that explicitly include backfill and waste package properties. With a single representative repository volume, it is also impossible to look at uncertainty in engineered properties or waste package degradation time and only far-field quantities of interest can be assessed.

Second, isothermal transport is represented by two tracers with properties representative of ^{129}I, as it is typically the radionuclide that travels the furthest in PA simulations (Mariner et al., 2017; Swiler et al. 2019; LaForce et al. 2020). Tracer 1 is instantly released at the start of the simulation, and Tracer 2 is released at a constant rate to represent radionuclide release as the waste packages degrade. This is the same transport model as used in the DECOVALEX PA cases in Section 2.1 of this report. The assumption of isothermal transport is implemented using the ISOTHERMAL card, which allows GENERAL mode simulations to run faster due to having fewer degrees of freedom. GENERAL mode was used in Sevougian et al. (2019b) and Swiler et al. (2019) and TH mode was used in Mariner et al. (2017), all of which included thermal affects. Ignoring waste package heating is likely to cause an under-prediction of tracer transport near the repository because heat-driven flux of fluid away from waste packages is an important mechanism for radionuclide transport away from the repository at early time.

Biosphere is also not considered in the current model. Monitoring points at several depths 5 km downstream of the repository are used to study radionuclide release.

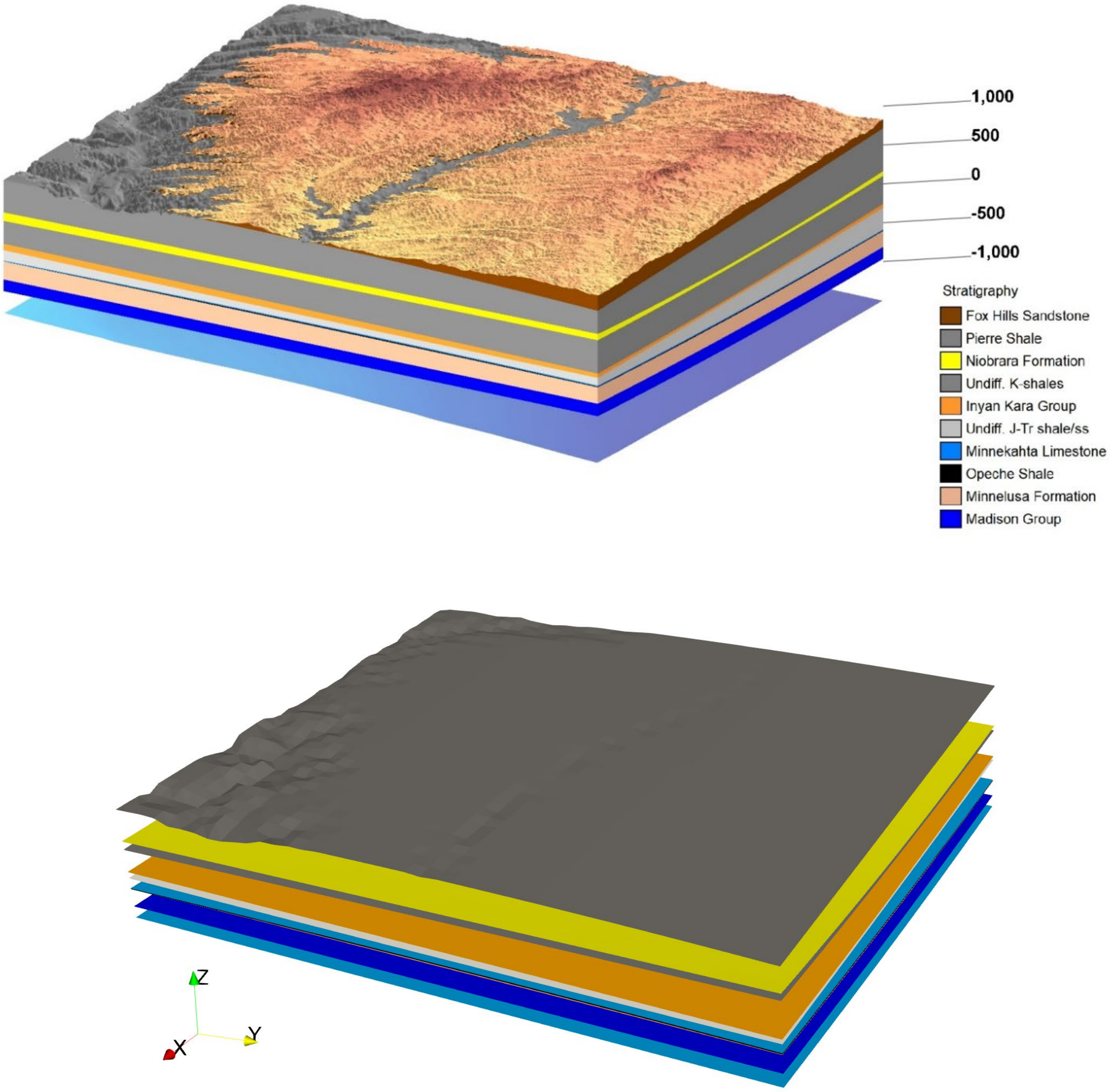

Figure 7-3. Top: Geological framework model of the Pierre Shale sequence stratigraphy at 10x vertical exaggeration at 250 m grid resolution (after Sevougian et al., 2019b). Bottom: Subsurface geological horizons at 10x vertical exaggeration upscaled to 1000 m grid resolution (Overburden Top surface not included). The dimensions of the region are 69 km (E-W) by 83 km (N-S). Stratigraphy color scale is the same for both subfigures.

7.2.2 Geosphere/Natural Barriers

The natural barrier properties from Mariner et al. (2017) are assumed to be suitable for the present PA simulations and are shown in Table 7-1. Mariner et al. (2017) built their model to be loosely consistent with the properties of the same shale used to construct the GFM, shown in the top of Figure 7-3. Section 5.1 of Sevougian et al (2019b) discusses the development of the GFM in detail, so it is only briefly described here.

7.2.2.1 Shale GFM

The hypothetical shale host rock is a thick marine shale interbedded with silt, sandstone, and limestone. The Host Shale for the repository has a thickness of 250-589 m in the area of interest, making it an excellent geological barrier to radionuclide transport. The Overburden sandstone overlays the Host Shale in much of the GFM but is eroded away in some locations by a river channel feature, as can be seen in the top of Figure 7-3. Within the Host Shale is a thin Silty Shale interval with higher permeability that may allow for radionuclide transport away from the repository. Below the Silty Shale is the Underlying Shale, another thick shale sequence that provides a barrier to radionuclide transport. Below the second shale is the Limestone, which is a regional aquifer that may allow for transport away from the repository, as was seen in the deterministic shale case in Section 5.3 of Sevougian et al (2019b). Below the Limestone aquifer is another shale sequence, the Lower Shale. Figure 7-3 shows several lithologies below the Lower Shale but based on the results shown in Mariner et al. (2017) and Sevougian et al. (2019b), they are unlikely to impact radionuclide transport and are omitted from the current simplified PA models.

Table 7-1. Parameter values used in deterministic simulation, reproduced from Mariner et al., (2017). Thermal properties are not included as current simulations are isothermal.

Model Region	Permeability (m^2)	Porosity	τ	Effective Diffusion Coefficient[2] (m^2/s)	Grain Density (kg/m^3)
Overburden	1×10^{-15}	0.20	0.11	2.2×10^{11}	2700
Host Shale and Underlying Shale	1×10^{-19}	0.20	0.11	2.2×10^{11}	2700
Silty Shale	1×10^{-17}	0.20	0.11	2.2×10^{11}	2700
Lower Shale	1×10^{-20}	0.10	0.04	4.0×10^{12}	2700
Limestone	1×10^{-14}	0.10	0.04	4.0×10^{12}	2700
Repository Region	1×10^{-20}	0.35	0.23	8.1×10^{11}	2700

[1] Effective diffusion coefficient = $D_w \phi r s$, where the free water diffusion coefficient (*Dw*) = 1 x 10^{-9} m^2/s (Li and Gregory, 1974) and saturation (*s*) = 1

[2] $r = \phi^{1.4}$ (Van Loon and Mibus, 2015)

[3] $r = \phi^{1/3}$ (Millington, 1959)

7.2.2.2 Uncertainty in Stratigraphy of a GFM

All geological features in the subsurface have a degree of uncertainty associated with them due to our limited ability to gather data in the subsurface. Figure 7-3 shows a GFM of the shale stratigraphy (top) and the geological horizons in the model (bottom) (Sevougian et al., 2019b). A geological horizon is defined as: "An informal term used to denote a surface in or of rock, or a distinctive layer of rock that might be represented by a reflection in seismic data" (https://glossary.oilfield.slb.com/en/terms/h/horizon).

The exact locations of geological horizons are known at wells from well logging but must be interpolated 100's of meters to 10's of kilometers between wells. It may be up to a geologist's professional judgement whether a particular horizon is continuous between two wells. Seismic images of the subsurface are created based on the travel time of seismic waves through rock, and interpretation of seismic data depends on assumptions about rock material properties that are at best known at discrete well locations. Ideally, well logs and seismic data are interpreted jointly to improve the accuracy of subsurface maps, but uncertainty in the location of geological horizons and rock properties away from wells and the repository always exists.

7.2.3 Multiple PA-Scale Geological Models from the GFM

In this section, the process of developing a suite of 7.0 km x 2.5 km models for PA simulations is presented. These models are 1.0 km wider than previous PA simulations because there is no symmetry in the geologically uncertain system, and so a reflective boundary cannot be used. The 2.5 km width allows simulation of a repository that is effectively half the size of the previous PA models and maintains the same distance from the repository to the open model boundaries.

7.2.3.1 Searching for suitable PA-scale model regions

In PA, the exact location of the repository is known and only the locations of geological horizons away from the repository contain uncertainty. We only have a single realization of the GFM, so to create a suite of pseudo-uncertain realizations for the geological horizons, 7.0 km × 2.5 km submodels of the GFM model are created and the difference between these models is used as a proxy for subsurface uncertainty. Each model will contain different horizon locations on the surface and in the subsurface due to their differing locations.

A Python script is used to clip the entire Overburden Top surface into 297 non-overlapping 7 km x 2.5 km rectangular submodels. The larger dimension (7 km) of the submodels is in the x-direction so that the model points in the downstream (positive x) direction of the surface river feature (See Figure 7-3). By doing this we are implicitly assuming that subsurface transport will follow the same flow direction as the surface water flow. Each submodel is then screened for suitability for the repository based on two criteria:

(1). The Overburden Top surface must be present over the entire PA model region. The currently scripted methodology will only work if all horizons are continuous across the model. This also ensures that:

   a. The repository is deep enough in the subsurface without being too close to the Silty Shale formation.

   b. It will be possible to monitor tracer concentration 5 km downstream of the repository in the overlying Overburden sediments.

(2). The average height of the Overburden Top is at least 15 m higher at the small-x boundary than the average height at the large-x boundary. This is to ensure that the dominant surface flow direction is the positive x-direction and that the monitoring point 5 km away from the repository is plausibly in the downstream direction.

Application of these constraints to the shale GFM results in 87 prospective PA-scale model regions that can be meshed out of the original 297.

7.2.4 Deterministic Case

7.2.4.1 Partially automated creation of a model realization

An example of the workflow under development is shown in Figure 7-2. Dakota (Adams et al., 2021) is run to get the sampled parameters and choose the realization of the geological model prior to starting to build the simulation model. The sampled flow parameters are the permeability of the Overburden, Limestone Aquifer and Silty Shale and porosity of the Host Shale, as shown in Table 7-3. The process of meshing and creating the PFLOTRAN (Lichtner et al., 2020) input deck for a single realization of the uncertainty scenarios is mostly automated. The existing scripts include some hard-coding specific to the current model. The main Python script is called ***setupModelv4.py*** and executes the following steps:

(1). Open the file of uncertain parameters and read in the 4 sampled parameters and mesh realization number (See Table 7-3). Read in the x- and y-coordinates for the desired mesh realization.

(2). Call subfunction ***make_shale_sector_v3.py*** and clip the GFM model to the correct (x,y) range for the surfaces in the PA model. (Figure 7-4 a)

(3). Call subfunction ***make_shale_smaller_avs_v2.py*** to convert the surfaces into Audio and Video Coding Standard (avs) file format so that they can be imported into LaGriT (Los Alamos Grid Toolbox, 2017) for creation of the simulation mesh volumes.

(4). Write and execute the two scripts necessary to create the model volumes in LaGriT. These scripts are hard-coded to include only a pre-selected subset of the surfaces, as shown in Figure 7-4 a. These surfaces are chosen to capture the three thin formations that are potential flow paths: Overburden, Silty Shale, and Limestone aquifer and have thick, homogeneous shales everywhere else (Figure 7-4 b).

   a. Initially, ***stack_subset.lgi*** is updated with the correct x- and y- coordinates.
   b. Second, ***extract_surface.lgi*** is copied over as it is identical for every model.
   c. Both LaGrit scripts are executed by the main Python script calling a bash script and the reservoir volume ***.stl*** file is created.

(5). A VoroCrust directory is created that includes:

   d. The VoroCrust executable file and ***vorocrust2pflotran.py*** for converting the VoroCrust mesh to PFLOTRAN UNSTRUCTURED_EXPLICIT format. These are the same for every realization.
   e. A repository volume file, where the repository center is at height z = 447 m. The repository is a slightly different depth below the ground surface for every realization because the height of the Overburden varies between realizations. Repository depths vary from around 250 m to 400 m.

(6). A simulation directory is created that includes the PFLOTRAN input deck with the four sampled parameters in place and ***pflotran2exodus.py***, for visualizing the final simulation results in ParaView.

The steps that currently must be conducted by hand are:

- Prior to running VoroCrust, the stereolithography (.stl) file produced by LaGriT is converted into a wave-front object (.obj) file to read into VoroCrust. This must be done by the user opening the .stl file in ParaView (Ahrens et al., 2005) and saving it as an .obj file of the same name in the VoroCrust directory.

- VoroCrust is then run and the ***mesh.vcg*** file must be converted to PFLOTRAN UNSTRUCTURED_EXPLICIT (.uge) mesh format. The ***.uge*** and ***.ex*** files are copied into the simulation/grid directory manually.

- Prior to running PFLOTRAN, the exact location of the desired monitoring points in the input deck must be manually added by the user.

There is no reason that these three steps could not be automated, but it is an area of future work. Figure 7-4 shows the development of the simulation mesh for the base case PA model from the workflow above. The properties in this model correspond to the first set of sampled parameters (Realization 1) given by Dakota.

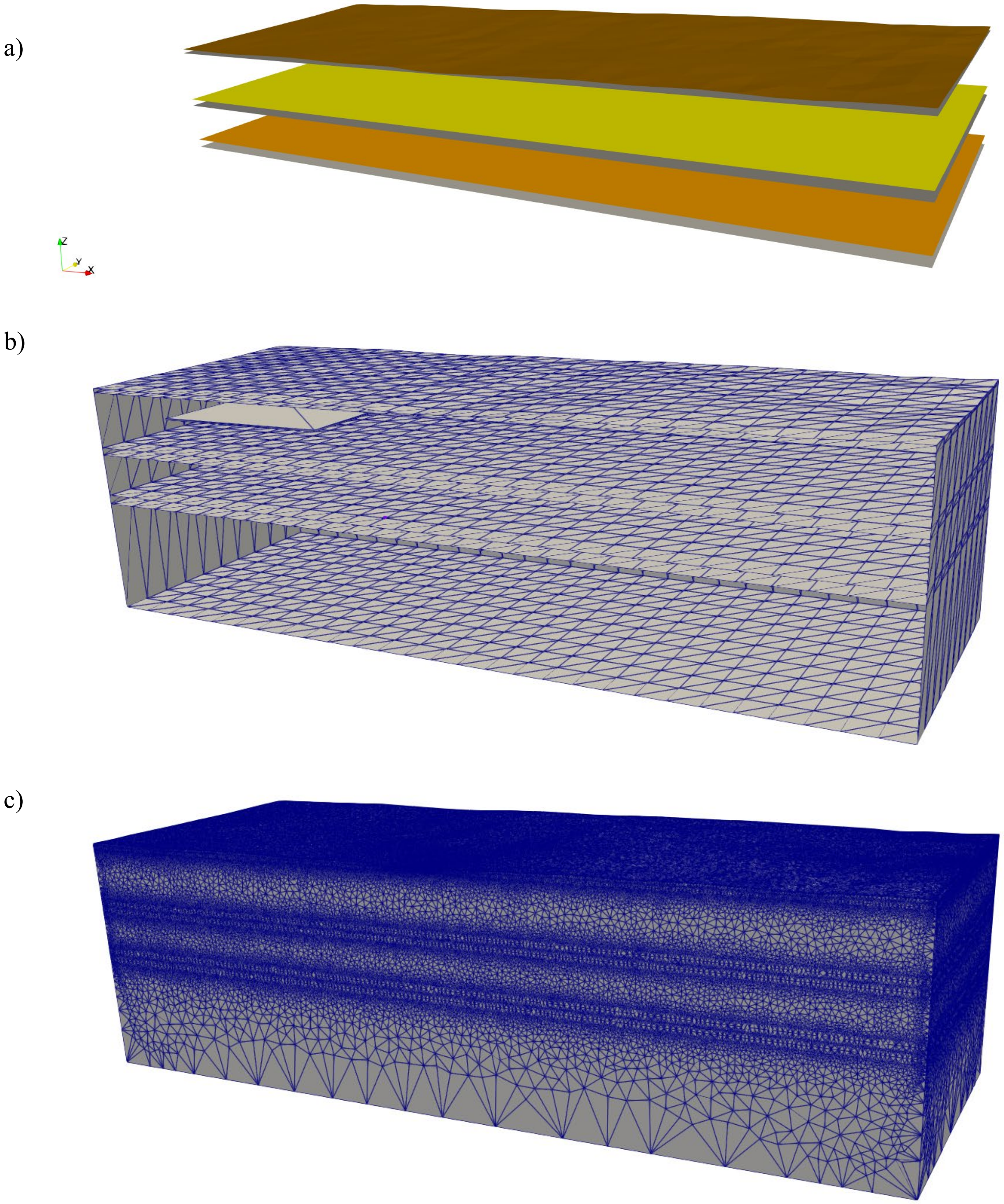
a)
z
y
x
b)
c)

d)

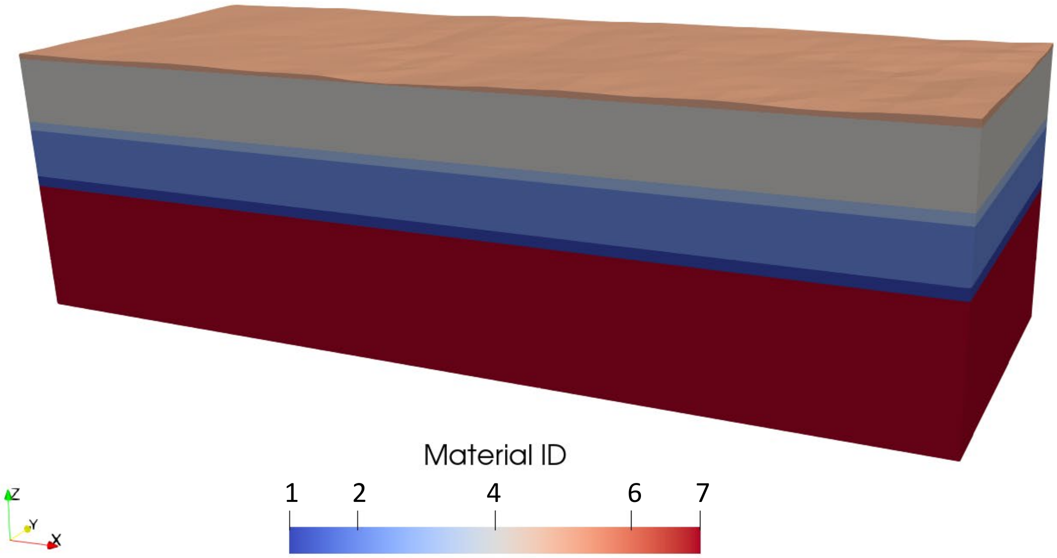

Figure 7-4. Development of an example simulation mesh for the base case (Realization r1). (a) Surfaces selected for the PA model. From the top they are Top Overburden, Top Host Shale, Top Silty Shale, Top Underlying Shale, Top Limestone aquifer, and Top Lower Shale. A flat model base is added at z = -1200 m. (b) Model volume and surfaces from LaGriT clipped to show the box containing the repository box in the interior. (c) VoroCrust simulation surface mesh. (d) VoroCrust simulation mesh showing colored by material ID where 1 = Limestone, 2 = Underlying Shale, 3 = Silty Shale, 4 = Host Shale, 5 = Overburden, 6 = repository (not shown), and 7 = Lower Shale.

7.2.4.2 Deterministic Model Meshing Results

The breakdown of the volume and the number of grid cells in each formation volume for the base case is shown in Table 7-2. The volume of the input region and volume of each region as meshed are also shown. The small difference between the input and meshed volumes demonstrates that the mesh is a high-quality representation of the input volumes.

In the creation of this mesh, VoroCrust was allowed to make grid cells as large as possible everywhere in the domain. As a result, regions with large volumes such as the Underlying and Lower Shales do not necessarily have a large number of grid cells (see Table 7-2). Conversley, the thinnest regions tend to have a disproportionately large number of grid cells because VoroCrust meshes are always isotropic, meaning that a region with small vertical extent, such as the Overburden (see Figure 7-5) and repository (see Figure 7-4 b), will have a large number of cells because cell size in the x and y directions are limited by the small vertical thickness. The Host Shale requires the largest number of grid cells of any region because it is the second-largest input volume and also surrounds the finely-meshed repository region.

The unrestricted mesh size results in extremely large grid cells in the interior of the Host Shale and Underlying Shale, as can be seen in Figure 7-4 c). The largest grid cell in the model is in the Lower Shale and is 3.15×10^7 m^3, which is likely too large to fully resolve transport of radionuclides in this region. For comparison, in the shale PA in Sevougian et al. (2019b) and Mariner et al. (2017), the largest cells in the CUBIT (Skroch et al., 2021) mesh were 15 m on a side, for a volume of 3,375 m^3, which is four orders of magnitude smaller. It is unlikely that Voronoi cells will need to be that small to capture the transport of radionuclides due to superiority of the flow field resolution in simulations on randomized Voronoi meshes. However, a convergence study would need to be done to ensure sufficient mesh resolution for a realistic PA case of the shale model without unnecessarily slowing the simulation down with excess grid cells.

Figure 7-5 (a) shows the model volumes created in LaGriT for the Overburden formation in the base case at 10x vertical exaggeration to show the detail of the topography of the structure. The top surface of the Overburden is at least 15 m higher, on average at x=0 m than at x=7,000 m, as this was a screening criterion for model selection. This does not mean that the Overburden formation is thicker at the small x boundary, only that it is higher. Indeed, the Overburden appears thicker at the x = 7,000 m boundary. The screening criteria also did not guarantee that the slope was uniform, and the base case shows a low spot in the middle of the model where the Overburden top surface is lower than either boundary and the formation is very thin. The thin vertical extent of the Overburden volume results in a large number of very small grid cells in the VoroCrust mesh at this location, as can be seen in Figure 7-5 (b) and (c). The smallest cell in the model has a volume of 0.478 m^3 and is in the Overburden in this region.

The ability of PFLOTRAN to simulate on meshes that have grid cells ranging over 8 orders of magnitude is a testament to both the high quality of the meshes and the capabilities of PFLOTRAN to simulation on very difficult simulation domains.

Table 7-2. Model meshing results for the base case (Realization r1) mesh. Material IDs correspond to Figure 7-4 c.

Model Region	Input Volume (m^3)	Meshed Volume (m^3)	Relative difference $\frac{abs(V_{in}-V_m)}{V_{in}}$ (-)	Number of Grid Cells
Overburden (ID 5)	6.8390×10^8	6.8353×10^8	5.40×10^{-4}	295,696
Host Shale (ID 4)	8.2916×10^9	8.2912×10^9	4.28×10^{-5}	642,293
Silty Shale (ID 3)	1.2143×10^9	1.2142×10^9	9.88×10^{-5}	94,481
Underlying Shale (ID 2)	6.2624×10^9	6.2619×10^9	7.82×10^{-5}	129,830
Limestone (ID 1)	1.3601×10^9	1.3600×10^9	9.56×10^{-5}	78,848
Lower Shale (ID 7)	1.6878×10^{10}	1.6872×10^{10}	3.08×10^{-4}	65,056
Repository (ID 6)	3.7515×10^7	3.7509×10^7	1.65×10^{-4}	221,284
Full Model	3.4727×10^{10}	3.4721×10^{10}	1.92×10^{-4}	1,527,491

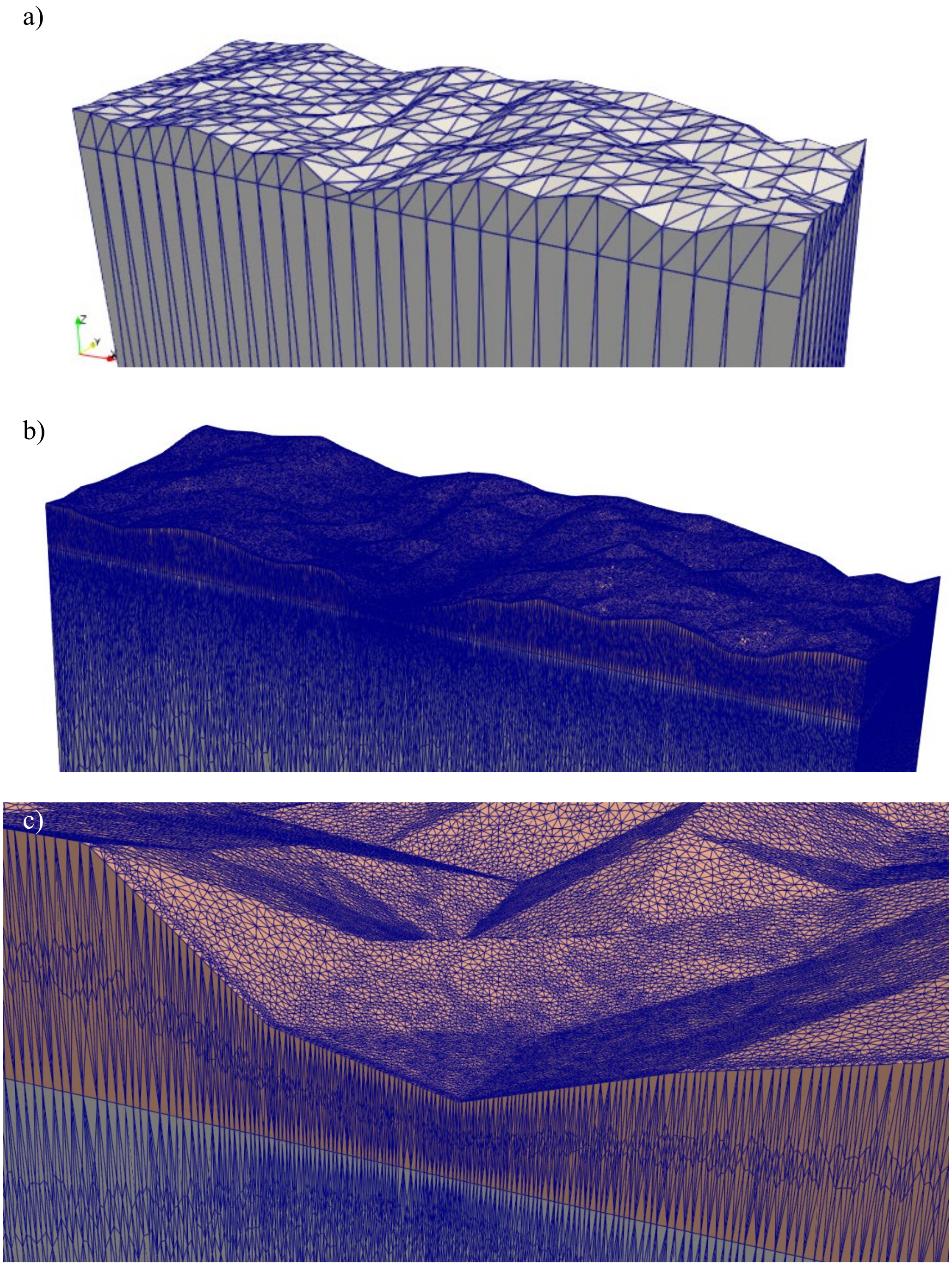

Figure 7-5. **The Overburden formation for the base case (Realization r1) of the shale PA model at 10x vertical exaggeration. (a) Model volume from LaGriT. (b) Voronoi surface mesh generated by VoroCrust-meshing. (c) Detail of the surface mesh at the thinnest point in the Overburden.**

7.2.4.3 Deterministic Model Numerical Implementation

The initial condition for the simulation model is hydrostatic with head gradient in the x-direction of 15 m/7,000 m = 0.0021 m/m, which is higher than the 0.0013 m/m gradient in Mariner et al. (2017), Sevougian et al. (2019b) and Swiler et al. (2019). The boundary conditions are set to the initial conditions so that the flow field is in the positive x-direction and is constant throughout the simulation. The material properties used for the deterministic simulations are taken from Mariner et al. (2017) and shown in Table 7-1 except for the sampled properties, which are sampled according to the distributions given in Table 7-3. The example case is Realization 1 of the Dakota samples, and the parameters are shown in Table 7-4.

Simulations are run using PFLOTRAN's GENERAL mode with the temperature equation turned off using the ISOTHERMAL card. Though the simulations are fully-saturated, characteristic curves are required. Capillary pressure are the same for every region and use the van Genuchten function with liquid residual 10%, M=0.2 and Alpha = 0.5 for all formations (Lichtner et al., 2020). The liquid and gas relative permeabilities are also the same in every region Mualem-van Genuchten curves with residual saturation of both phases at 10% and van Genuchten parameter M=0.6.

The engineered barriers are significantly simplified from Mariner et al. (2017), Swiler et al. (2019), and Sevougian et al. (2019b). The dimensions of the repository volume are 1,640 × 1,525 × 15 m. This is the same x- and y- dimensions as the repository in Mariner et al. (2017), and the vertical thickness is the height of the drifts and the damage zones above and below the repository in that work. The damage zone is included in the repository volume vertically because it is implicitly included in the x and y dimensions and also to avoid having a very thin feature in the model, which would result in a significantly larger number of grid cells in the Voronoi mesh, as discussed in the preceding section. The repository is assumed to be a homogeneous volume with the properties shown in Table 7-1, which are the properties of the buffer in Mariner et al. (2017). Though most of the repository volume contains Host Shale and disturbed rock zone, buffer properties are chosen as the buffer completely surrounds the waste packages in each drift and neglecting the low permeability of the buffer could result in unrealistically early release of tracer. The higher porosity of the buffer as compared with the Host Shale results in the repository volume holding more water than would be expected.

Both tracers in the simulation have properties representative of ^{129}I, as it is typically the radionuclide that behaves most like an ideal tracer and travels the furthest due to its low sorption onto rocks, high solubility, (see Tables 4-5, 4-6 of Mariner et al, 2017), and very long half-life (1.57×10^7 years). Radioactive decay of the tracers is not included in the present model. The radionuclide is assumed to have an instant release fraction of 10% while the other 90% is slowly released out of the repository as the spent nuclear fuel (SNF) dissolves at a rate of 10^{-7}/yr. Tracer 1 represents the instant release fraction while Tracer 2 represents the slow-release fraction. This is the same instant release fraction and mode SNF dissolution rate used in Mariner et al. (2017) and the Crystalline case in Section 2 of this report.

Table 7-3. Sampled parameters and their distributions. (Mariner et al., 2017).

Parameter	Range	Units	Distribution
Overburden Permeability	$10^{-15} – 10^{-13}$	m^2	log uniform
Limestone Permeability	$10^{-17} – 10^{-14}$	m^2	log uniform
Silty Shale Permeability	$10^{-17} – 10^{-15}$	m^2	log uniform
Host Shale Porosity	0.1 – 0.25	-	uniform
Realization ID	-	uniform	

Table 7-4. Results of DAKOTA sampling for 10 realizations of the shale PA model. Geological model ID is sampled with other parameters, the model is meshed and finally simulated.

Realization number	Geological realization ID (-)	Host Rock Porosity (-)	Overburden permeability (m^2)	Limestone permeability (m^2)	Silty Shale Permeability (m^2)
r1	72	0.196	1.65×10^{-15}	2.18×10^{-16}	1.56×10^{-17}
r2	69	0.189	5.66×10^{-14}	6.35×10^{-17}	2.59×10^{-16}
r3	53	0.143	9.17×10^{-14}	3.94×10^{-16}	3.34×10^{-17}
r4	83	0.124	1.11×10^{-15}	1.45×10^{-16}	5.88×10^{-16}
r5	5	0.217	3.36×10^{-15}	2.41×10^{-17}	6.54×10^{-17}
r6	49	0.247	1.37×10^{-14}	9.93×10^{-15}	1.03×10^{-16}
r7	39	0.159	4.26×10^{-15}	6.53×10^{-16}	1.72×10^{-16}
r8	17	0.107	7.47×10^{-15}	2.27×10^{-15}	1.70×10^{-17}
r9	21	0.165	2.12×10^{-14}	4.97×10^{-15}	9.28×10^{-16}
r10	30	0.228	3.81×10^{-14}	1.80×10^{-17}	4.31×10^{-17}

7.2.4.4 Monitoring Tracer Transport

Transport of tracer away from the repository is monitored at four locations. Three of the locations monitor tracer concentrations as a function of time at points 5 km downstream of the center of the repository at the location x = 6,120 m, y = 1,250 m. They are located above the repository in the Overburden, in the Silty Shale below the repository and in the Limestone aquifer below the repository. These three locations were chosen because tracer transport downstream is most likely to occur in these formations. The depth of the monitoring points is different for every simulation because the stratigraphic layers are different in each model. Tracer concentration at the center of the repository and the mass of tracer in the repository as a function of time is also calculated in the simulations. This enables calculation of the residence time of Tracer 1, which is a measure of how well the simplified engineered barrier and the immediately surrounding host rock natural barrier are working.

7.2.5 Stochastic Cases

Ten realizations of the model are created for the purpose of demonstrating the workflow and the resulting parameters given by Dakota LHS sampling are shown in Table 7-4. This sample is not large enough to create valid statistical distributions for quantitative analysis. (For comparison, Mariner et al. (2017) and Swiler et al. (2019) each ran 50 probabilistic simulations of the shale PA case.)

The sampled parameters and their distributions are shown in Table 7-3. Host Shale porosity and Limestone permeability are far-field properties sampled in Mariner et al. (2017). Overburden and Silty Shale permeability formations have not been sampled in previous analyses but have been chosen because of the potential for tracer transport through them. The fifth sampled parameter is the realization of the geology of the shale. The realizations are ordered by the x and y coordinates in the original GFM, with y as the fastest increasing index, which is intended to be arbitrary. All mesh realizations are thus considered equally-likely so they are sampled from a uniform distribution. The other material properties are shown in Table 7-1.

All grids are constructed using the workflow described in Section 7.2.4.1. The top surface of realizations 2-9 are shown with 10× vertical exaggeration in Figure 7-6, while Realization 1 was shown in the top of Figure 7-5. As can be seen, there is considerable variability between the models. In particular, Realizations r1 and r4 have very thin overburden, which will increase the size and complexity of the VoroCrust mesh relative to the other models. Realization 8 has the thickest overburden and also has significant slope downward in the positive y-direction.

Recall that the PA models were screened so that they have at least 15 m average surface height difference between the small x and large x boundaries. In the simulation models the head gradient is 15 m/ 7,000 m in the x-direction, regardless of the actual difference in model height. Some of the models such as Realization r9 (see Figure 7-6) have much more than 15 m height difference across them, which implies the potential for higher groundwater flux through the Silty Shale, Limestone aquifer, and Overburden formations. However, the constant-flux simplification is necessary for the current workflow.

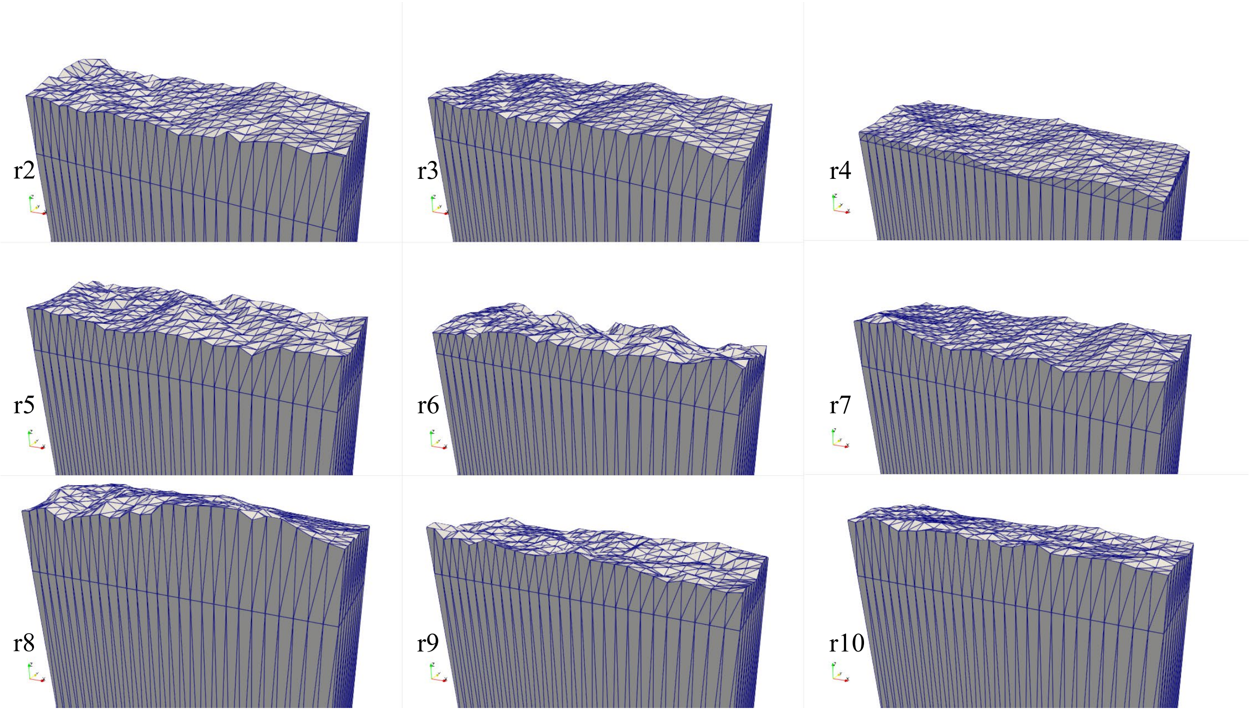

Figure 7-6. Top surface of Realizations 2-10 of the shale PA model at 10x vertical exaggeration.

7.2.6 Simulation Results

7.2.6.1 Deterministic Results

The tracer concentration in the reservoir above 1×10^{-11} (M) at six snapshots in time is shown in Figure 7-7. At the first time, t = 1 year, all of Tracer 1 is in the repository region and the concentration of Tracer 2 is below the 1×10^{-11} (M) threshold concentration, even in the repository. The oblong shape of the high-concentration tracer regions in the reservoir indicates that transport of Tracer 1 is almost entirely diffusive until 100,000 years, while transport of Tracer 2 is almost entirely diffusive until 200,000 years. Both tracers begin to spread advectively when they reach the Overburden formation because of the Overburden's relatively high permeability of 1.65×10^{-15} m^2. Neither tracer moves advectively in the Silty Shale layer because the sampled permeability in the realization is 1.56×10^{-17} m^2, the lowest of any of the ten realizations of the PA model. Both tracers take 500,000 years for concentrations above 1×10^{-11} (M) to reach the Limestone aquifer and show modest advective transport in the aquifer by 1,000,000 years.

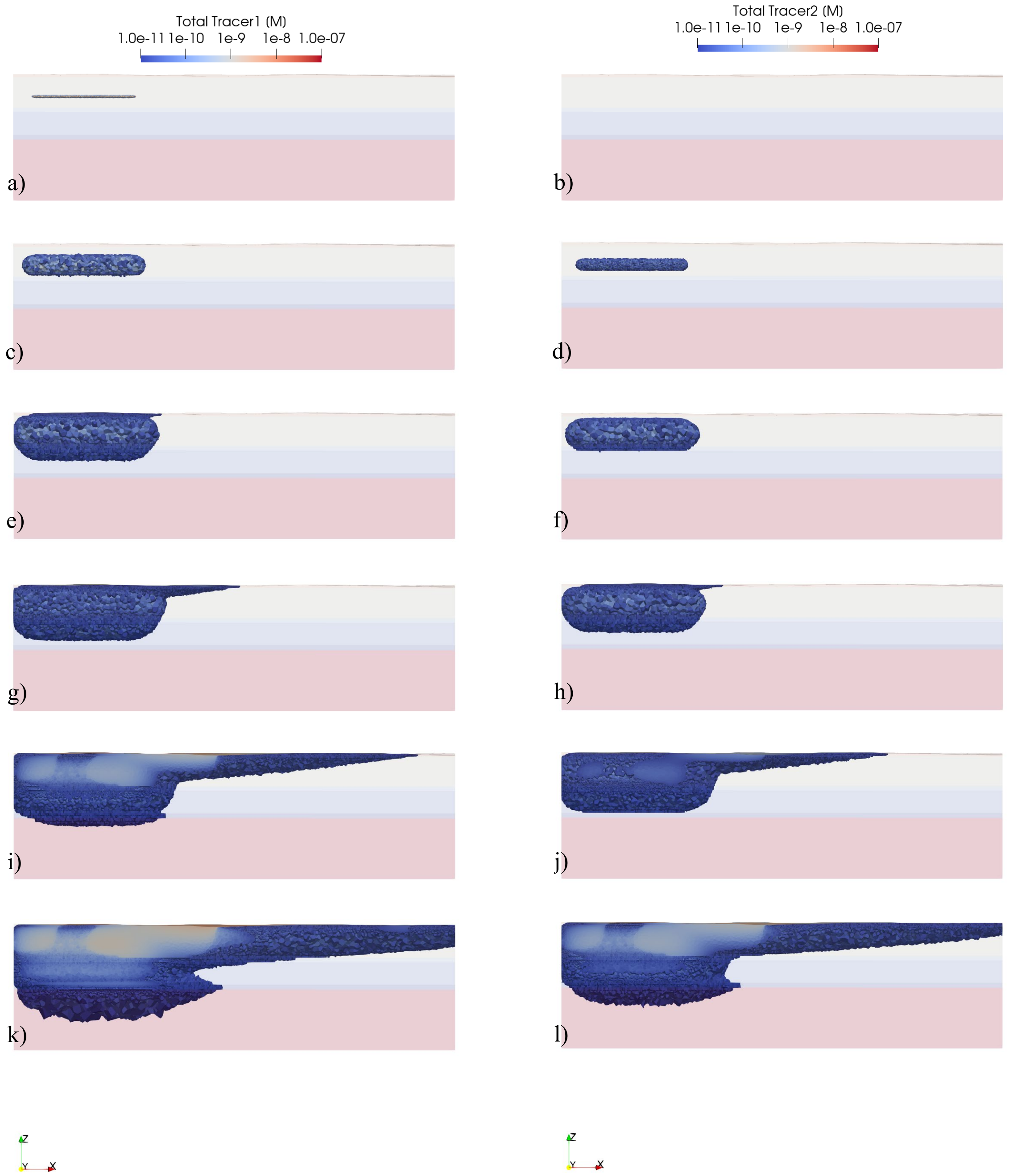

Figure 7-7. **Tracer 1 (left) and Tracer 2 (right) in the reservoir for the base case (r1). Tracer concentrations above 1×10^{-11} (M) are overlain on the full model colored according to Material ID. Times are a-b) 1 years; c-d) 10,000 years; e-f) 100,000 years; g-h) 200,000 years; i-j) 500,000 years; k-l) 1,000,000 years.**

7.2.6.2 Probabilistic Results

All 10 realizations of the PA model were successfully run to completion. The simulation results are presented with only qualitative analysis. Figure 7-8 shows the tracer concentrations at the three monitoring points 5 km downstream of the repository, Figure 7-9 shows the tracer concentration in the repository, and Figure 7-10 shows the total mass of tracer in the repository as a function of time.

7.2.6.2.1 Simulation Statistics

Table 7-5 shows the gridding and simulation statistics for the 10 realizations of the model. All simulations were run on a single node with 32 cores of a parallel super-computer for comparison purposes, regardless of the number of grid cells in the model.

The number of grid cells in each model shown in Table 7-5 is determined largely by the thickness of the Overburden formation because it is the volume in the models with the highest aspect ratio (horizontal/vertical extent), as discussed above. The Overburden thickness of the 10 realizations is shown in Figure 7-5 and Figure 7-6. The Overburden of r4 has a minimum thickness of just 4.83 m at (x,y) = (3250, 250) m, making it by far the thinnest feature in any model, and results in over 2.5 million grid cells. Realization r1 has the second thinnest overburden and second largest grid, with over 1.5 million cells. The realization with the fewest grid cells is r8 which has 1.1 million cells and one of the thickest overburden layers. The simulation times shown in Table 7-5 follow the same trend as the number of grid cells. Simulation r4 had the longest computation time by a wide margin at 145 minutes, r1 the second-longest at 85 minutes, and r8 the shortest at 64 minutes.

Though the number of grid cells and their impact on computation time are a numerical artifact of the VoroCrust meshing method, this result has implications for future PA work. Small features in models, which may be randomly generated, can have significant impact on model size and computation time. When more complex models are run simulation times will be significantly longer and automatically generating VoroCrust meshes will result in a wider range of computation times than have been encountered in previous GDSA PA models.

Table 7-5. Simulation statistics for the shale uncertain simulations

Realization number	Grid cells (-)	Computation time (min)	Mean residence time Tracer 1 (yr)
r1	1,527,491	85.22	4.15×10^3
r2	1,421,426	83.86	4.35×10^3
r3	1,438,742	83.05	6.65×10^3
r4	2,536,453	145.2	8.40×10^3
r5	1,225,174	67.33	3.60×10^3
r6	1,380,880	80.81	3.05×10^3
r7	1,471,792	78.96	5.65×10^3
r8	1,142,050	63.66	1.15×10^4
r9	1,303,975	77.12	5.30×10^3
r10	1,183,375	70.38	3.35×10^3

7.2.6.2.2 Tracer Results

All the simulations show a tendency to have the highest tracer concentration 5 km downstream in the Overburden, rather than in the Silty Shale, Limestone aquifer, or the Host Shale, as seen in Figure 7-8. This is likely because for the first 100,000-200,000 years, movement of tracers is dominated by diffusion through the Host Shale and the repository is much closer to the Overburden than it is to the Limestone aquifer in all the realizations. Also, for radionuclides to reach the Limestone they must pass through the Silty Shale formation, which may be a transport path for advection in the positive x-direction and prevent the tracers from migrating deeper into the subsurface to the Limestone.

There is a clear trend in Figure 7-8 that in realizations r1 and r4 the tracers begin to increase in concentration at all three downstream monitoring points much later than the other 8 models, while in r2 and r3 tracer concentrations increase the earliest at the Overburden (Figure 7-8 a-b) and Silty Shale (Figure 7-8 c-d) monitoring points. The most obvious difference between the r1/r4 and r2/r3 in the properties given in Table 7-4 is that r2 and r3 have higher Overburden permeability than r1 and r4, which could lead to increased flow through the Overburden. Tracer 1 in the reservoir for Realization r1 is shown on the left of Figure 7-7, while for Realization r2 it is shown in Figure 7-11. In r2, Tracer 1 concentrations above 1×10^{-11} (M) have already advected to the end of the Overburden by 100,000 years, while in r1 Tracer 1 is still diffusing through the Host Shale at that time. After 1,000,000 years the tracer profile in the reservoir for r1 and r2 are much more similar, but the r1 simulation has greater diffusion into the Lower Shale and much more advection through the Limestone aquifer. This is consistent with the earlier breakthrough of Tracer 1 at the Overburden and Silty Shale observation points in Realization r2.

Models r6, r8 and r9 have breakthrough of concentrations above 1×10^{-11} (M) significantly earlier than the other models at the Limestone aquifer monitoring point. Table 7-4 shows that these three realizations have the highest Limestone permeability, which may contribute to this result. Figure 7-12 shows Tracer 1 in the reservoir for the realization in r8. In r8, Tracer 1 is still being transported by diffusion through the shale after 100,000 years, but after 1,000,000 years Tracer 1 concentrations above 1×10^{-11} (M) have advected to the end of the model in both the Overburden and the Limestone aquifer. This preferential flow of Tracer 1 through the Limestone aquifer corroborates with the tracers appearing early in at the Limestone observation point (Figure 7-8 e-f).

Figure 7-9 shows the concentration of the tracers as a function of time in the center of the repository while Figure 7-10 shows the total mass of tracer in the repository for the first 100,000 years of the simulation. The concentration and mass of Tracer 1 decline with time, as it is instantly released into the model. Conversely, the concentration and mass of Tracer 2 in the repository constantly increases as it is released into the model at a rate faster than it is diffused out of the repository. After 100,000 years two-thirds to three-quarters of Tracer 1 is outside the repository, while most of Tracer 2 has yet to be released into the model.

Table 7-5 shows the median residence time of Tracer 1 in the repository region for all the realizations. Median residence time is defined as the time it takes half the tracer mass to leave the repository volume and is a measure of the effectiveness of the engineered barriers and surrounding host rock barrier. In this PA model, which models the entire repository area as buffer material, the mean residence times are between 3.05×10^3 years (r6) and 1.15×10^4 years (r8). This correlates with r6 having the highest shale porosity and r8 having the lowest.

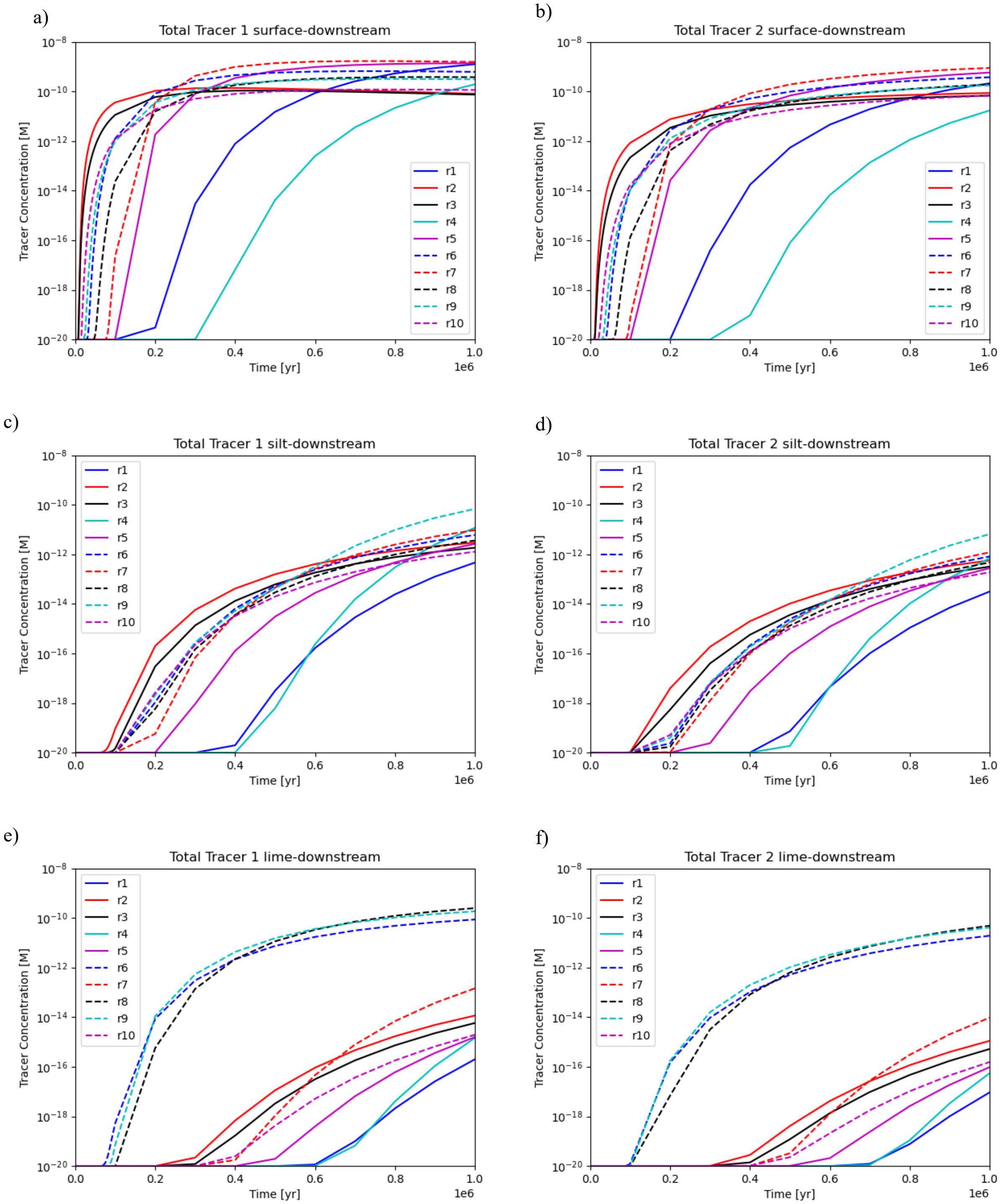

Figure 7-8. **Concentration of the instant release Tracer 1 (left) and slow-release Tracer 2 (right) at the three downstream monitoring locations as a function of time for the million year simulation. a)-b) Tracers in the Overburden. c)-d) Tracers in the Silty Shale. e)-f) Tracers in the Limestone aquifer.**

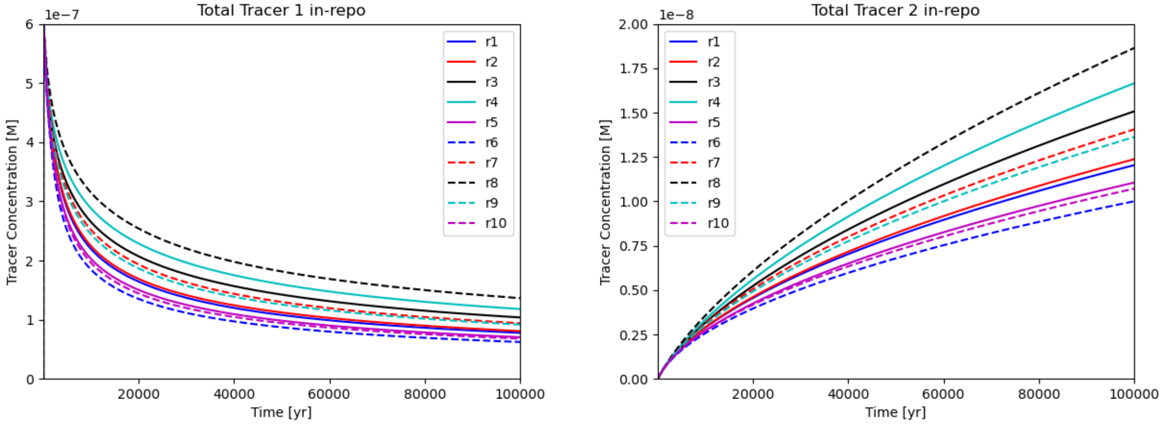

Figure 7-9. **Concentration of the instant release Tracer 1 (left) and slow-release Tracer 2 (right) at the monitoring point in the middle of the repository as a function of time for the first 100,000 years of the simulation. Note: Vertical scale on the subplots is not the same.**

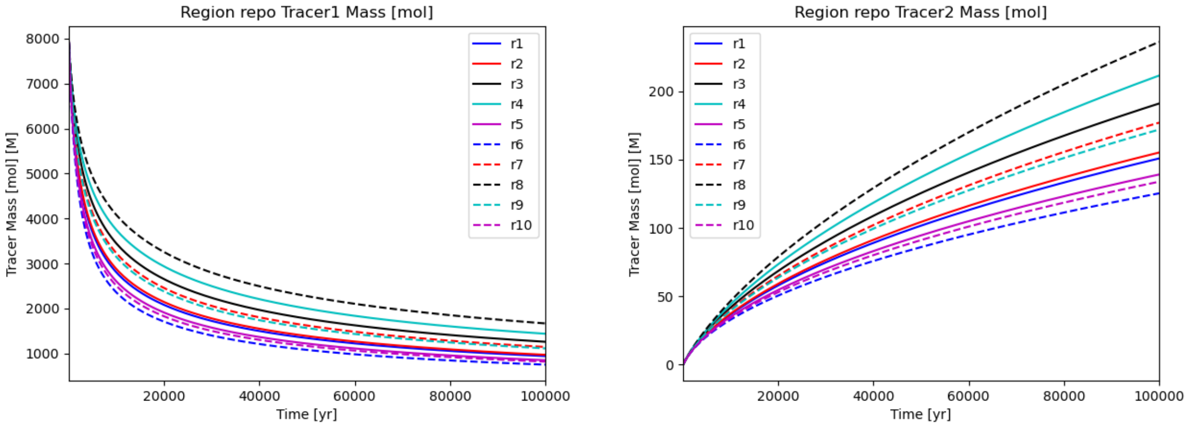

Figure 7-10. **Total mass of the instant release Tracer 1 (left) and slow-release Tracer 2 (right) in the repository volume as a function of time for the first 100,000 years of the simulation. Vertical scale on the subplots is not the same.**

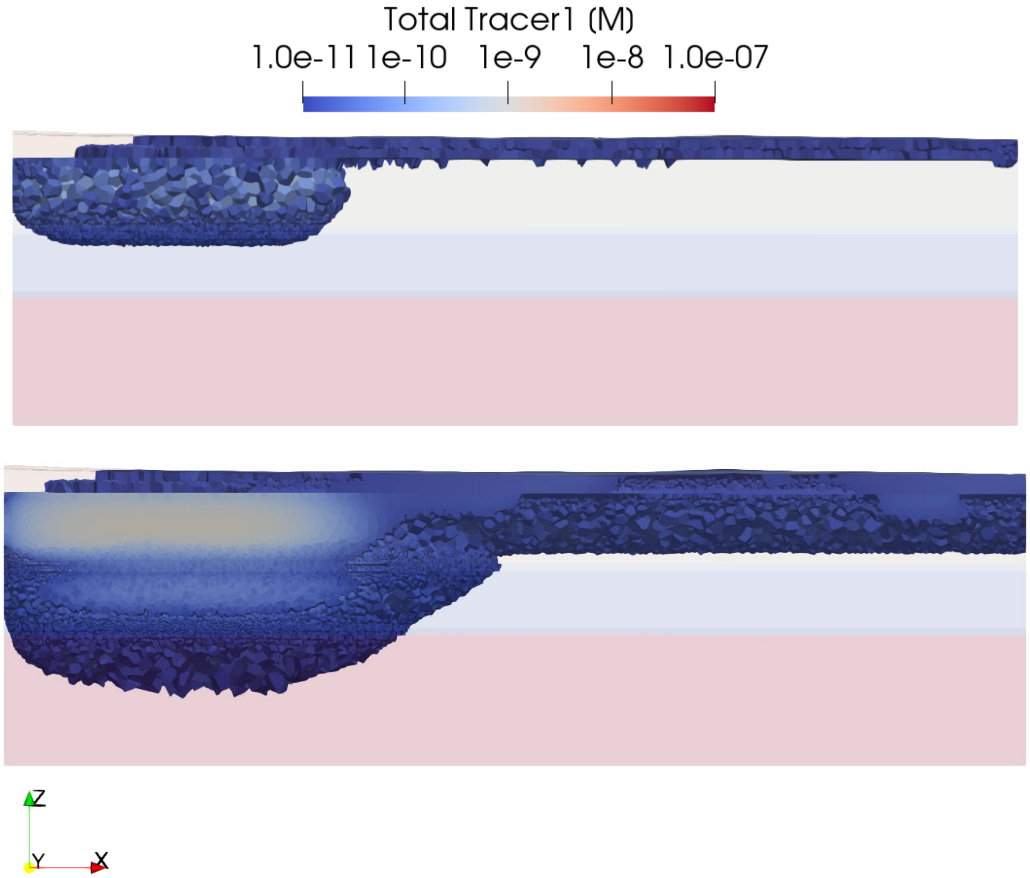

Figure 7-11. Tracer 1 in the reservoir for realization r2 of the model. Tracer concentrations above 1×10^{-11} (M) are overlain on the full model colored according to Material ID. Times are Top: 100,000 years; Bottom: 1,000,000 years.

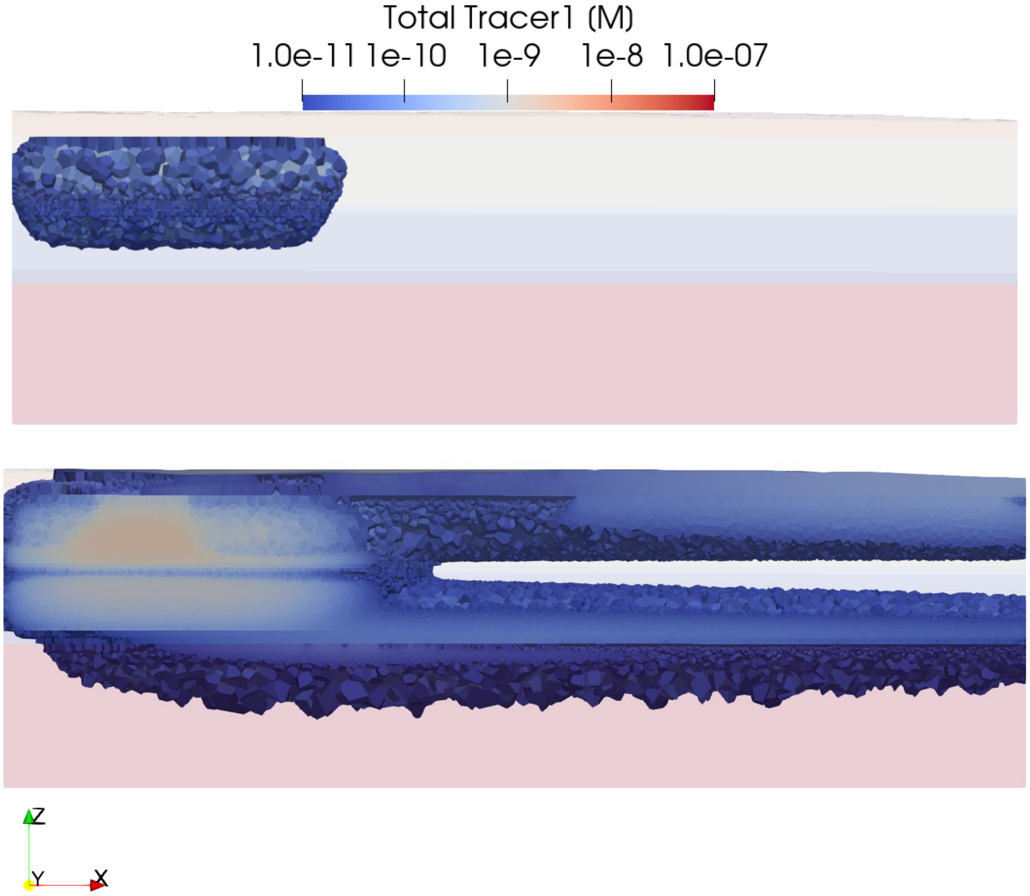

Figure 7-12. **Tracer 1 in the reservoir for realization r8 of the model. Tracer concentrations above 1×10^{-11} (M) are overlain on the full model colored according to Material ID. Times are Top: 100,000 years; Bottom: 1,000,000 years.**

7.2.6.3 Comparison with Previous Shale PA case

The simulation models that are generated from the Shale GFM are different from previous shale PA cases (Swiler et al., 2019; Mariner et al., 2017; Sevougian et al., 2019b) in several ways, and the simulation results reflect these differences. Figure 7-13 shows the simulation domain of Swiler et al. (2019). Comparison of Figure 7-13 and Figure 7-4 (b) and (d) shows that the repository is in a different stratigraphic section of the model. In both cases the repository is approximately 400 m below the top of the simulation domain, but in the current model the Host and Underlying Shales are much thicker, so that 400 m depth makes the repository in the Host Shale above the Silty Shale layer, while in the previous models 400 m depth made the repository between the Silty Shale and the underlying Limestone aquifer (Swiler et al., 2019; Mariner et al., 2017; Sevougian et al., 2019b).

Swiler et al., (2019) has a ^{129}I instant release fraction of 10% at the time a waste package breaches, which may be anytime during the million years simulation as shown in Swiler et al. (2019) Table 7.1. Tracer 1 in the present work represents the same mass as the instant release fraction, but is released at the start of the simulation. Moreover, the additional 90% of the ^{129}I is released in Swiler et al., (2019) as the waste packages degrade over geologic time.

The ^{129}I concentrations at two monitoring points from Swiler et al. (2019) are shown in Figure 7-14. Comparison of these plots with Figure 7-8 (a) and (e) shows that there is a large difference in trend between the profiles. While Swiler et al. (2019) observed ^{129}I in the limestone about 200,000 years earlier than the Overburden, the current models have Tracer 1 appear around 30,000 years earlier in the Overburden than in the Limestone. This reversal is likely attributable to the increased distance to the Limestone aquifer in the new models. Interestingly, Tracer 1 and ^{129}I start to appear in the Limestone aquifer at around the same time in both models, which may be attributable to the higher background fluid flux in the present model, or the simplification of the repository. The distribution of the Tracer curves in the Limestone in Figure 7-8(e) appears to be skewed toward later time than the distribution in Swiler et al. (2019) in Figure 7-14.

In this comparison it is important to recall that Swiler et al. (2019) had 90% delayed release ^{129}I as well as the instant release fraction of 10% at the time of waste package breach, while Tracer 1 is all released instantly at the start of the simulation. Hence it is not appropriate to compare maximum concentrations or late-time curves of the ^{129}I in Swiler et al. (2019) with the Tracer 1 curves in the present work.

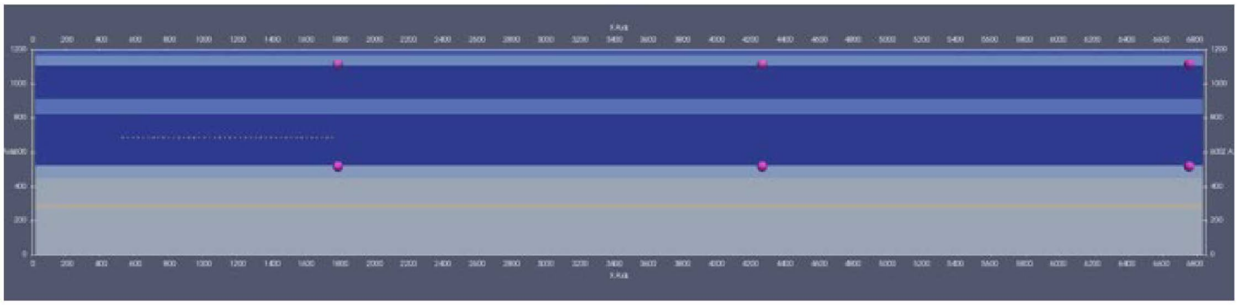

Figure 7-13. Figure 7.2 from Swiler et al., (2019): 2-D cross section of 3-D model domain showing aquifer observation points (pink dots). From top to bottom and left to right: sand_obs 1, sand_obs2, sand_obs3, lime obs 1, lime_obs2, lime obs3.

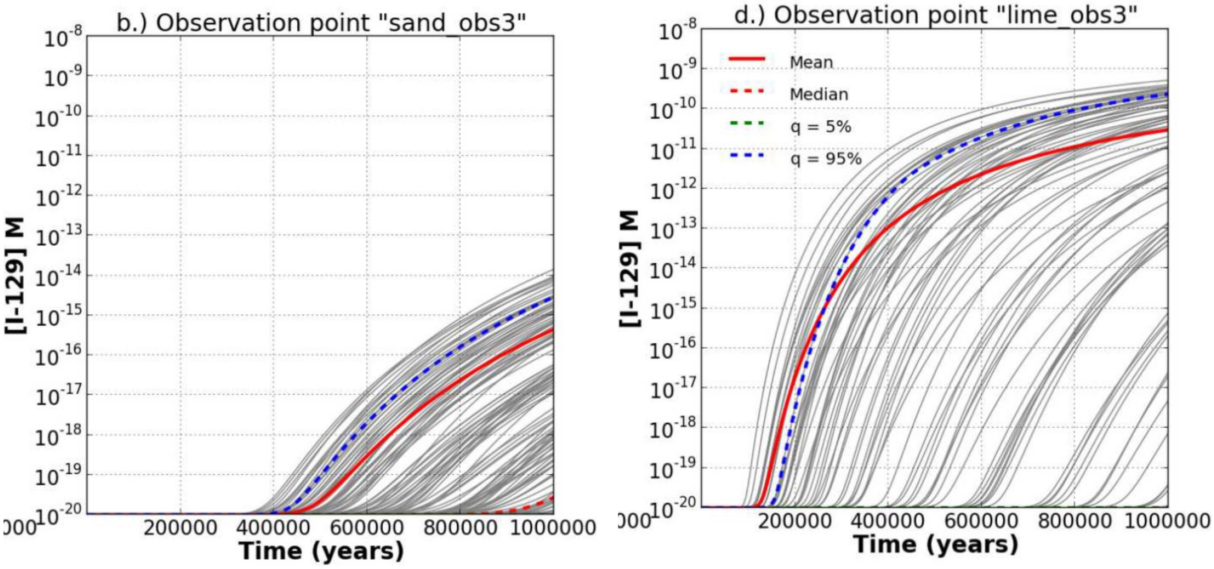

Figure 7-14. ^{129}I concentrations at observation points from Figure 7.3 of Swiler et al. (2019). Only the plots of 'sand_obs3' and 'lime_obs3' are shown as they are the closest to our Overburden and Limestone aquifer monitoring points, respectively.

7.3 Conclusions and Future Work

The first part of this section has provided an update on VoroCrust-Meshing software development that will lead to the release of an open-source version of the software before the end of FY22. The second section demonstrated a prototype PA simulation analysis that demonstrates how VoroCrust-meshing could be used as part of an automated workflow for SA/UQ. The example case was loosely based on the previous shale GDSA PA cases (Sevougian et al. 2019b; Swiler et al., 2019; Mariner et al, 2017) and utilized the shale GFM model from Sevougian et al. (2019b). Ten models were generated and simulated utilizing Dakota Latin-hypercube sampling in a partially-automated process scripted in Python. There are several conceptual simplifications and differences in the stratigraphy that prevent direct comparison of the new and old PA simulations, but the results appear to be qualitatively consistent with the current understanding of the shale PA.

The next step for the prototype stochastic shale PA is to fully-automate the model building and simulation process and move the workflow from Python scripts to the Sandia next generation workflow (NGW) module of the Sandia Analysis Workbench (Mariner et al., 2021; Orient et al., 2019), as has been done for the Crystalline PA case (Swiler et al, 2021). This will enable simulation of a sufficiently large number of realizations to perform a robust statistical analysis on the results. Future simulation studies should also include an assessment of the impact of grid resolution and random mesh realization on quantities of interest and account for two-phase flow and the heat generated by the waste packages. A more appropriate method for creating models with uncertainty in the geological structure is also needed, as there should be little to no uncertainty in surface topography in the models. In the longer term it will be necessary to mesh down to the level of individual waste packages and populate the engineered barriers with sampled properties, as was done in previous stochastic PA calculations in Mariner et al. (2017) and Swiler et al. (2019).

This page intentionally left blank.

8. SUMMARY AND CONCLUSIONS

This report describes specific activities in FY2022 associated with the Geologic Disposal Safety Assessment (GDSA) Repository Systems Analysis (RSA) work package within the SFWST Campaign. The overall objective of the GDSA RSA work package is to develop generic deep geologic repository concepts and system performance assessment (PA) models in several host-rock environments, and to simulate and analyze these generic repository concepts and models using the GDSA Framework toolkit (Mariner et al. 2021), and other tools as needed.

The GDSA RSA work package has continued to lead Task F1-crystalline and Task F2-salt of the DECOVALEX 2023 project on behalf of the SFWST campaign. Development of the task specification is nearly complete, and a version has been made publicly available (LaForce et al, 2022). The SNL simulations on both tasks are well underway. Task F1-crystalline tracer simulations have been conducted for all 10 realizations of the fracture network and are being analyzed. Task F2-salt fluid-flow simulations have been completed on a simplified model of the repository, and a more complete model including geology is under development.

Near-waste package simulations have continued. This year the impact of thermal effects on fluid flow and tracer transport in the presence of DRZ evolution have been conducted. The new simulations use two of PFLOTRAN's newly implemented capabilities; temperature-dependent thermal conductivity and NWT transport mode. The simulations use waste package heat representative of the 10th, 50th and 75th hottest waste packages in inventory. They show counter-intuitively that there is increased tracer transport towards a hotter waste package, due to the higher mobility of water at increased temperature.

Near-surface geology and hydrology of glacial sediments overlying crystalline formations in support of the GDSA biosphere modelling effort (Condon et al, 2020) has continued. Emphasis this year was on irrigation and municipal water use needs of the region and understanding the groundwater contribution to surface and irrigation water.

Simulations on the new UZ model this year focused on adding tracer transport to this numerically challenging problem. Simulations with PFLOTRAN's new NWT transport mode were initially conducted but took too long to complete. An alternative coupled in time approach was implemented to enable use of PFLOTRAN's GIRT transport mode. GIRT is much faster than NWT on the UZ case but cannot handle complete dry out in the simulation domain, requiring a sequentially-coupled approach to allow for completion of a deterministic UZ simulation with tracer transport. The simulations show that tracer transport is primarily downwards due to the constant infiltration rate in the model. Tracer concentration was diluted to low values by the time it reached the aquifer below the model.

Two ORIGEN modelling studies on energy output and radionuclide inventory for SNF DPCs were conducted this year. One was by project partners at ORNL, and the other by SNL staff. The purpose of these studies was to examine how representative the hypothetical high-thermal output 37 PWR DPC used in PA simulations as compared with real and hypothetical high-energy waste packages. The studies showed that the hypothetical 37 PWR DPC used in previous PA is not unrealistically hot, but it is too hot to be representative of an 'average' as-loaded DPC in inventory.

A simplified shale PA model with uncertainty in the locations of geological horizons was developed using PFLOTRAN simulations on VoroCrust meshes. The intent of the study is to serve as a proof of concept for how geological uncertainty could be incorporated into PA simulation modelling including uncertainty. Simulations on 10 stochastic realizations of the model were completed using a partially-automated workflow. Simulation results were compared with the previous shale PA uncertainty study (Swiler et al, 2019).

8.1 Future Work

Future work in FY2023 will continue to focus on developing the technical bases for representing generic repository concepts in GDSA Framework simulations for deep geologic disposal in any of four possible host-rock environments: argillite, crystalline, bedded salt, and unsaturated zone formations. The following tasks are of particular interest:

- Finalize the DECOVALEX 2023 task specification. Run simulations for the final crystalline and salt models and compare the results with partner teams.

- Continue simulations of near waste package flow and transport for waste packages representative of as-loaded DPCs in inventory. This may include consideration of additional possible host-rock environments or adding radionuclides to the simulation study.

- Completing the unsaturated alluvium simulation with tracers using the PFLOTRAN's new NWT transport mode.

- Fully automating the shale PA model with more realistic geological uncertainty. This will require implementing VoroCrust mesh generation into the Sandia next generation workflow (NGW) developed by the GDSA Framework work package and utilized in crystalline PA cases by the GDSA SA/UQ work package. Development of a model with the same degree of complexity as the previous shale PA model in Swiler et al. (2019) will require additional VoroCrust development to allow for meshing of individual waste packages.

9. References

Abdelkader, A., Bajaj, C.L., Ebeida, M., Mahmoud, A.H., Mitchell, S.A., Owens, J.D., & Rushdi, A.A. (2018). Sampling conditions for conforming Voronoi meshing by the VoroCrust algorithm. Leibniz international proceedings in informatics 99.

Abdelkader, A., Bajaj, C.L., Ebeida, M.S., Mahmoud, A.H., Mitchell, S.A., Owens, J.D., & Rushdi, A.A. (2020). VoroCrust: Voronoi meshing without clipping. ACM Transactions on Graphics (TOG) 39(3):1–16.

Adams, B.M., Bohnhoff, W.J., Dalbey, K.R., Ebeida, M.S., Eddy, J.P., Eldred, M.S., Hooper, R.W., Hough, P.D., Hu, K.T., Jakeman, J.D., Khalil, M., Maupin, K.A., Monschke, J.A., Ridgway, E.M., Rushdi, A.A., Seidl, D.T., Stephens, J.A., Swiler, L.P., and Winokur, J.G. (2021). "Dakota, A Multilevel Parallel Object-Oriented Framework for Design Optimization, Parameter Estimation, Uncertainty Quantification, and Sensitivity Analysis: Version 6.15 User's Manual," Sandia Technical Report SAND2020-12495, November 2021.

Ahrens, J., Geveci, B., and Law, C. (2005). ParaView: An End-User Tool for Large Data Visualization, Visualization Handbook. Elsevier

Ayachit, U. (2015). *The ParaView Guide: A Parallel Visualization Application*. Kitware, ISBN 978-1930934306

Bear, J., Tsang, C., & Marsily, D. G. (1993). *Flow and Contaminant Transport in Fractured Rock* (1st ed.). Academic Press.

Bernier, F., Lemy, F., de Cannière, P., & Detilleux, V. (2017). Implications of safety requirements for the treatment of THMC processes in geological disposal systems for radioactive waste. *Journal of Rock Mechanics and Geotechnical Engineering*, *9*(3), 428–434. https://doi.org/10.1016/j.jrmge.2017.04.001

Bertrams, N., Bollingerfehr, W., Eickemeier, R., Fahland, S. Flügge, J., Frenzel, B., Hammer, J., Kindlein, J. Liu, W., Maßmann, J., Mayer, K.-M., Mönig, J., Mrugalla, S., Müller-Hoeppe, N., Reinhold, K., Rübel, A., Schubarth-Engel- schall, N., Simo, E., Thiedau, J., Thiemeyer, T., Weber, J.R., Wolf, J. (2020). *Grundlagen zur Bewertung eines Endlagersystems in flach lagernden Salzformationen (S1) - Ergebnisse aus dem Vorhaben RESUS*. BGE TEC 2020.

Beuth, T., Bracke, G., Buhmann, D., Dresbach, C., Keller, S., Krone, J., Lommerzheim, A., Mönig, A., Mrugalla, S., Rübel, A., and Wolf, J. (2012). *Szenarienentwicklunng: Methodic und Anwendung. Bericht zum Arbeitspaket 8. Vorläufige Sicherheitsanalyse für den Standort Gorleben*, Gesellschaft für Anlagen und Reaktorsicherheit (GRS) mbH, GRS-284, Köln, ISBN 978-3939355-60-1.

Bollingerfehr, W., Filbert, W., Pöhler, M., Tholen, M., and Wehrmann, J. (2008). *Konzeptionelle Endlagerplanung und Zusammen- stellung des endzulagernden Inventars (Design planning of a final repository and summary of the inventory to be stored) – Project ISIBEL*, Peine, April 2008.

Bollingerfehr, W., Buhmann, D., and Doerr, S. (2017). *Evaluation of methods and tools to develop safety concepts and to demonstrate safety for an HLW repository in salt*. Final Report (No. TEC-03-2017-AB). DBE Technology GmbH.

Bollingerfehr, W., Bertrams, N., Buhmann, D., Eickemeier, R., Fahland, S., Filbert, W., Hammer, J., Kindlein, J., Knauth, M., and Wenting, L. (2018). *Concept developments for a generic repository for heat-generating waste in bedded salt formations in Germany*. Synthesis Report (No. BGE TEC 2018-13). BGE TECHNOLOGY GmbH.

Carter, J., Luptak, A. J., Gastelum, J., Stockman, C. T., and Miller, A. (2013). *Fuel Cycle Potential Waste Inventory for Disposition*. FCR&D-USED-2010-000031 Rev 6. Savannah River National Laboratory, Aiken, SC.

Central Aroostook Soil and Water Conservation District, (2005). *Maine Irrigation Guide 2005*. Linda Alverson, Executive Director, Presque Isle.

Chang, K. W., Nole, M., & Stein, E. R. (2021). Reduced-order modeling of near-field THMC coupled processes for nuclear waste repositories in shale. *Computers and Geotechnics*, *138*, 104326. https://doi.org/10.1016/j.compgeo.2021.104326

Chen, D., Pan, Z., & Ye, Z. (2015). Dependence of gas shale fracture permeability on effective stress and reservoir pressure: Model match and insights. *Fuel*, *139*, 383–392. https://doi.org/10.1016/j.fuel.2014.09.018

Choi, H. J., Lee, J. Y., & Choi, J. (2013). Development Of Geological Disposal Systems For Spent Fuels and High-level Radioactive Wastes in Korea. *Nuclear Engineering and Technology*, *45*(1), 29–40. https://doi.org/10.5516/net.06.2012.006

Clayton, D., Freeze, G., Hadgu, T., Hardin, E., Lee, J. Prouty, J., Rogers, R., Nutt, W. M., Birkholzer, J., Liu, H. H., Zheng, L., and Chu, S. (2011). *Generic Disposal System Modeling - Fiscal Year 2011 Progress Report.* SAND 2011-5828P; FCRD-USED-2011-000184. Sandia National Laboratories, Albuquerque, NM.

Condon C. A., Napier, B. A., Ghosh, S., Weaver, W. C., Varnum-Lowry, C. B. (2020). *GDSA Biosphere Model Software Requirements Document*. M3SF-20PN010304091, PNNL-30280. Pacific Northwest National Laboratory. Richland, WA.

Lide, D. R., & Kehiaian, H. V. (2020). *CRC Handbook of Thermophysical and Thermochemical Data*. Amsterdam University Press.

Dewhurst, D. N., Aplin, A. C., & Sarda, J. P. (1999). Influence of clay fraction on pore-scale properties and hydraulic conductivity of experimentally compacted mudstones. *Journal of Geophysical Research: Solid Earth*, *104*(B12), 29261–29274. https://doi.org/10.1029/1999jb900276

Dickens, H. B. (1959). Water supply and sewage disposal in permafrost areas of northern Canada. *Polar Record*, *9*(62), 421–432. https://doi.org/10.1017/s0032247400066377

DOE (U.S. Department of Energy). 2012. *Used Fuel Disposition Campaign Disposal Research and Development Roadmap*. FCR&D-USED-2011-000065, REV 1, U.S. DOE Office of Nuclear Energy, Used Fuel Disposition, Washington, D.C.

Follin, S., Hartley, L., Jackson, P., Joyce, S., Roberts, D., and Swift B. (2007). *Hydrogeological characterization and modeling of deformation zones and fracture domains, Forsmark modelling stage 2.2*. SKB R-07-48. Svensk Kärnbränslehantering AB, Stockholm, Sweden.

Fort, J.A., Richmond, D.J., Cuta, J.M., Suffield S.R. (2019). *Thermal Modeling of the TN-32B Cask for the High Burnup Spent Fuel Data Project.* Technical Report PNNL-28915. Pacific Northwest National Laboratory. Richland, WA.

Freeze, G., Gardner, P., Vaughn, P., Sevougian, S.D., Mariner, P., Mousseau, V. and Hammond, G. (2013). *Enhancements to Generic Disposal System Modeling Capabilities*. FCRD-UFD-2014-000062. SAND2013-10532P. Sandia National Laboratories, Albuquerque, NM.

Hammond, G. E., Lichtner, P. C., and Mills, R. T. (2014). Evaluating the performance of parallel subsurface simulators: An illustrative example with PFLOTRAN. *Water Resources Research*, *50*(1), 208–228. https://doi.org/10.1002/2012wr013483

Hussey, A.M., II, Bothner, W.A., and Thompson, P.J., 2008, *Bedrock geology of the Kittery 1:100,000 quadrangle, Maine and New Hampshire: Maine* Geological Survey Open-File no. 08–78, scale 1:100,000.

Hyman, J. D., Karra, S., Makedonska, N., Gable, C. W., Painter, S. L., & Viswanathan, H. S. (2015). dfnWorks: A discrete fracture network framework for modeling subsurface flow and transport. *Computers & Geosciences*, *84*, 10–19. https://doi.org/10.1016/j.cageo.2015.08.001

Jobmann, M., & Buntebarth, G. (2009). Influence of graphite and quartz addition on the thermo–physical properties of bentonite for sealing heat-generating radioactive waste. *Applied Clay Science*, *44*(3–4), 206–210. https://doi.org/10.1016/j.clay.2009.01.016

Jones, P., Chang, K.W., Hardin, E. (2021). DPC Disposal Thermal Scoping Analysis. SAND2021-7515R, Sandia National Laboratories, Albuquerque, NM, USA.

Jove-Colon, C.F., Hammond, G.E., Kuhlman, K.L., Zheng, L., Kim, K., Xu, H., Rutqvist, J., Caporuscio, F.A., Norskog, K.E., Maner, J., Palaich, S., Cheshire, M., Zavarin, M., Wolery, T.J., Atkins-Duffin, C., Jerden, J., Copple, J.M., Cruse, T., Ebert, W. (2016). Evaluation of Used Fuel Disposition in Clay-Bearing Rock. SAND2016-10311R, Sandia National Laboratories, Albuquerque, NM, USA.

Joyce, S., Simpson, T., Hartley, L., Applegate, D., Hoek, J., Jackson, P., Swan, D., Marsic, N., and Follin, S. (2010). *Groundwater flow modelling of periods with temperate climate conditions - Forsmark*. SKB R-09-20. Svensk Kärnbränslehantering AB, Stockholm, Sweden.

Kwon, O., Kronenberg, A. K., Gangi, A. F., & Johnson, B. (2001). Permeability of Wilcox shale and its effective pressure law. *Journal of Geophysical Research: Solid Earth*, *106*(B9), 19339–19353. https://doi.org/10.1029/2001jb000273

LaForce, T., Chang, K.W., Perry, F.V., Lowry, T.S., Basurto, E., Jayne, R., Brooks, D., Jordan, S., Stein, E., Leone, R., and Nole, M. (2020). *GDSA Repository Systems Analysis Investigations in FY2020*. M2SF-20SN010304052, SAND2020-12028 R. Sandia National Laboratories, Albuquerque, NM.

LaForce, T., Basurto, E., Chang, K.W., Jayne, R., Leone, R., Nole, M., Perry, F.V., Stein, E. (2021) *GDSA Repository Systems Analysis Investigations in FY2021*. SAND2021-11691 R, Sandia National Laboratories, Albuquerque, NM.

LaForce, T., R.S. Jayne, R. Leone, Stein, E., Nguyen, S. (2022). D*ECOVALEX-2023 Task F Specification Revision 8.* SAND2022-6944 R. Sandia National Laboratories, Albuquerque, NM.

Lichtner, P.C., Hammond, G.E. (2012). Quick Reference Guide: PFLOTRAN 2.0: Multiphase-Multicomponent-Multiscale Massively Parallel Reactive Transport Code. LA-CC-09-047, Los Alamos National Laboratory, Los Alamos, NM, USA.

Lichtner, P. C., Hammond, G. E., Lu C., Karra, S., Bisht, G., Andre, B., Mills, R. T., Kumar, J., Frederick, J. M. (2020) PFLOTRAN Web page. http://www.pflotran.org

Lindborg, T., ed. (2010). *Landscape Forsmark—Data, methodology and results for SR-Site*. Svensm Karnbranslehantering AB. SKB TR-10-05. Stockholm, Sweden. Report. 252 pp.

Liu, H. H., Rutqvist, J., & Berryman, J. G. (2009). On the relationship between stress and elastic strain for porous and fractured rock. *International Journal of Rock Mechanics and Mining Sciences*, *46*(2), 289–296. https://doi.org/10.1016/j.ijrmms.2008.04.005

Liu, J. F., Song, Y., Skoczylas, F., & Liu, J. (2016). Gas migration through water-saturated bentonite–sand mixtures, COx argillite, and their interfaces. *Canadian Geotechnical Journal*, *53*(1), 60–71. https://doi.org/10.1139/cgj-2014-0412

Los Alamos National Laboratory. (2017). Los Alamos grid toolbox, LaGriT. http://lagrit.lanl.gov.

Mariner, P.E., Berg, T.M., Chang, K.W., Debusschere, B.J., Eckert, A.C., Harvey, J., LaForce, T.C., Leone, R.C., Mills, M.M., Nole, M.A., Park, H.D., Perry, F.V., Seidl, D.T., Swiler, L.P. (2021). *GDSA Framework Development and Process Model Integration FY2021*. SAND2021-12626 R. Sandia National Laboratories, Albuquerque, NM.

Mariner,P.E., Nole, M.A., Basurto, E., Berg, T.M., Chang, K.W., Debusschere, B.J., Eckert, A.C., Ebeida M.S., Gross*, M., Hammond, G.E., Harvey, J., Jordan, S.H., Kuhlman K.L., LaForce, T.C., Leone, R.C., McLendon III, W.C., Mills, M.M., Park, H.D., Perry, F.V., Salazar III, A., Seidl, D.T., Sevougian, S.D., Stein, E.R., Swiler, L.P. (2020). *Advances in GDSA Framework Development and Process Model Integration*. SAND2020-10787 R. Sandia National Laboratories, Albuquerque, NM.

Mariner, P. E., Connolly, L. A., Cunningham, L. J., Debusschere, B. J., Dobson, D. C., Frederick, J. M., Hammond, G. E., Jordan, S. H., LaForce, T. C., Nole, M. A., Park, H. D., Perry, F. V., Rogers, R. D., Seidl, D. T., Sevougian, S. D., Stein, E. R., Swift, P. N., Swiler, L. P., Vo, J., and Wallace, M. G. (2019). *Progress in Deep Geologic Safety Assessment in the U.S. since 2010*, M2SF-19SN010304041. U.S. Department of Energy, Spent Fuel and Waste Science and Technology Campaign, Office of Spent Fuel and Waste Disposition. Washington, DC.

Mariner, P. E., Stein, E. R., Sevougian, S. D., Cunningham, L. J., Frederick, J. M., Hammond, G. E., Lowry, T. S., Jordan, S., and Basurto, E. (2018). *Advances in Geologic Disposal Safety Assessment and an Unsaturated Alluvium Reference Case*, SFWD-SFWST-2018-000509, SAND2018-11858R. Sandia National Laboratories, Albuquerque, NM.

Mariner, P. E., Stein, E. R., Frederick, J. M., Sevougian, S. D., and Hammond, G. E. (2017). *Advances in Geologic Disposal System Modeling and Shale Reference Cases*. SFWD-SFWST-2017-000044 / SAND2017-10304R. Sandia National Laboratories, Albuquerque, NM.

Mariner, P. E., Stein, E. R., Frederick, J. M., Sevougian, S. D., Hammond, G. E., and Fascitelli, D. G. (2016). *Advances in Geologic Disposal System Modeling and Application to Crystalline Rock*. FCRDUFD-2016-000440, SAND2016-96107R. Sandia National Laboratories, Albuquerque, NM.

Mariner, P. E., Gardner, W. P., Hammond, G. E., Sevougian, S. D. and Stein, E. R. (2015). *Application of Generic Disposal System Models*. SAND2015-10037R; FCRD-UFD-2015-000126. Sandia National Laboratories, Albuquerque, NM.

McConn Jr, R.J., Gesh, C.J., Pagh, R.T., Rucker, R.A., Williams III R.G. *(*2011). *Compendium of Material Composition Data for Radiation Transport Modeling Revision 1.* Technical Report PIET-43741-TM-963/PNNL-15870 Rev. 1 Pacific Northwest National Laboratory. Richland, WA.

Nasir, O., Fall, M., & Evgin, E. (2014). A simulator for modeling of porosity and permeability changes in near field sedimentary host rocks for nuclear waste under climate change influences. *Tunnelling and Underground Space Technology*, *42*, 122–135. https://doi.org/10.1016/j.tust.2014.02.010

Nielsen, M.G., and Locke, D.B. (2015). *Simulation of groundwater flow and streamflow depletion in the Branch Brook, Merriland River, and parts of the Mousam River watersheds in southern Maine: U.S. Geological Survey Scientific Investigations Report 2014–5235*. 78 p.

Nole, M., Beskardes, G.D., Fukuyama, D., Leone, R.C., Mariner, P., Park, H.D., Paul, M., Salazar, A., Hammond, G.E., Lichtner, P.C. (2022). PFLOTRAN Development FY2022. SAND2022- XXXX R. Sandia National Laboratories, Albuquerque, New Mexico, August 1, 2022.

NWMO. (2012). *Used Fuel Repository Conceptual Design and Postclosure Safety Assessment in Crystalline Rock*. NWMO TR-2012-16. Nuclear Waste Management Organization, Toronto, Ontario.

NWT - PLOTRAN Documentation. (2022). PFLOTRAN. Retrieved July 26, 2022, from https://www.pflotran.org/documentation/user_guide/cards/simulation/subsurface_transport_modes/nuclear_waste_transport_card.html#nuclear-waste-transport-card

Orient, G.E., Clay, R.L., Friedman-Hill, E.J., Pebay, P.P., Ridgway, E.M. (2019) Sensitivity and Uncertainty Workflow of Full System SIERRA Models Supporting High Consequence Applications SAND2019-11311.

Park, H. D., Hammond, G. E., Valocchi, A. J., & LaForce, T. (2021). Linear and nonlinear solvers for simulating multiphase flow within large-scale engineered subsurface systems. *Advances in Water Resources*, *156*, 104029. https://doi.org/10.1016/j.advwatres.2021.104029

Pettersson, S. and Lönnerberg, B. (2008). *Final Repository for Spent Nuclear Fuel in Granite - The KBS-3V Concept in Sweden and Finland.* Paper presented at the International Conference Underground Disposal Unit Design & Emplacement Processes for a Deep Geological Repository, Prague. 16-18 June 2008.

Price, Laura, (2022). Personal Communication, July 12, 2022.

Radulescu, G., Brandon, G. and Kaushik, B. (2021). *Fuel Assembly Reference Information for SNF Radiation Source Term Calculations*. ORNL/SPR-2021/2093. United States: N. p., 2021. Web. doi:10.2172/1819561.

Rübel, A., Buhmann, D., Kindlein, J. and Lauke, T. (2016). *Performance assessment of sealing systems. Conceptual and integrated modelling of plugs and seals* (No. GRS-415). Gesellschaft fuer Anlagen-und Reaktorsicherheit (GRS) gGmbH.

Sasaki, T., & Rutqvist, J. (2021). Estimation of stress and stress-induced permeability change in a geological nuclear waste repository in a thermo-hydrologically coupled simulation. *Computers and Geotechnics*, *129*, 103866. https://doi.org/10.1016/j.compgeo.2020.103866

Sassani, D. Birkholzer, J., Camphouse, R., Freeze, G., Stein, E. (2021). *SFWST Disposal Research R&D 5-Year Plan- FY2021* Update. SAND2021-12491 R. Sandia National Laboratories, Albuquerque, NM and Lawrence Berkeley National Laboratory.

Sevougian, S. D., Stein, E. R., LaForce, T., Perry, F. V., Lowry, T. S., Cunningham, L. J., Nole, M., Haukwa, C. B., Chang, K. W. and Mariner, P. E. (2019a). *GDSA Repository Systems Analysis Progress Report*. SAND2019-5189R. Sandia National Laboratories, Albuquerque, NM.

Sevougian, S. D., Stein, E. R., LaForce, T., Perry, F. V., Nole, M., Haukwa, C. B., and Chang, K. W. (2019b). *GDSA Repository Systems Analysis FY19 Update*. SAND2019-11942R. Sandia National Laboratories, Albuquerque, NM.

Sevougian, S. D., Mariner, P. E., Connolly, L. A., MacKinnon, R. J., Roger, R. D., Dobson, D. C., and Prouty, J. L. (2019c). *DOE SFWST Campaign R&D Roadmap Update.* M2SF-19SN010304042 SAND2019-5179R. Sandia National Laboratories, Albuquerque, NM.

Sevougian, S. D., Stein, E. R., Gross, M. B., Hammond, G. E., Frederick, J. M. and Mariner, P. E. (2016). *Status of Progress Made Toward Safety Analysis and Technical Site Evaluations for DOE Managed HLW and SNF*. SAND2016-11232 R; FCRD-UFD-2016-000082, Rev. 1. Sandia National Laboratories, Albuquerque, NM.

Sevougian, S. D., Freeze, G. A., Gardner, W. P., Hammond, G. E. and Mariner, P. E. (2014). *Performance Assessment Modeling and Sensitivity Analyses of Generic Disposal System*

Concepts. FCRD-UFD-2014- 000320, SAND2014-17658. Sandia National Laboratories, Albuquerque, NM.

Sevougian, S. D., Freeze, G. A., Vaughn, P., Mariner, P. E., and Gardner, W.P. (2013). *Update to the Salt R&D Reference Case*. FCRD-UFD-2013-000368. SAND2013-8255P. Sandia National Laboratories, Albuquerque, NM.

Sevougian, S. D., Freeze, G. A., Gross, M. B., Lee, J., Leigh, C. D., Mariner, P. E., MacKinnon, R. J. and Vaughn, P. (2012). *TSPA Model Development and Sensitivity Analysis of Processes Affecting Performance of a Salt Repository for Disposal of Heat-Generating Nuclear Waste*. FCRD-UFD-2012-000320 Rev. 0. U.S. Department of Energy, Office of Used Nuclear Fuel Disposition, Washington, DC.

Shelton, S. (1934). Thermal conductivity of some irons and steels over the temperature range 100 to 500 C. *Bureau of Standards Journal of Research*, *12*(4), 441. https://doi.org/10.6028/jres.012.042

Skroch, M., Owen S. J., Staten, M.L., Quadros, R.W., Hanks, B., Clark, B., Hensley, T., Ernst, C., Morris, R., McBride, C., Stimpson, C., Perry, J., Richardson, M., and Merkley, K. (2021) *CUBIT geometry and mesh generation toolkit 15.9 user documentation*. Technical Report SAND2021-12663 W, Sandia National Laboratories. Albuquerque, NM.

Somerton, W., Keese, J., & Chu, S. (1974). Thermal Behavior of Unconsolidated Oil Sands. *Society of Petroleum Engineers Journal*, *14*(05), 513–521. https://doi.org/10.2118/4506-pa

Stein, E. R., Frederick, J. M., Hammond, G. E., Kuhlmann, K. L., Mariner, P. E., and Sevougian, S. D. (2017). *Modeling Coupled Reactive Flow Processes in Fractured Crystalline Rock*. Paper presented at the International High-Level Radioactive Waste Management Conference, Charlotte, NC. April 9-13, 2017.

Sweeney, M. R., Gable, C. W., Karra, S., Stauffer, P. H., Pawar, R. J., & Hyman, J. D. (2020). Upscaled discrete fracture matrix model (UDFM): an octree-refined continuum representation of fractured porous media. *Computational Geosciences*, *24*(1), 293–310. https://doi.org/10.1007/s10596-019-09921-9

Swiler, L.P., Helton, J.C., Basurto, E., Brooks, D.M., Mariner, P.E., Moore, L.M., Mohanty, S., Sevougian, S.D., and Stein, E.R. (2019). Status Report on Uncertainty Quantification and Sensitivity Analysis Tools in the Geologic Disposal Safety Assessment (GDSA) Framework, SAND2019-13835R.

Swiler, L. P., Basurto, E., Brooks, D. M., Eckert, A.C., Mariner, P. E., Portone, T., and Stein, E. R. (2020). *Advances in Uncertainty Quantification and Sensitivity Analysis Methods and Applications in GDSA Framework*. SAND2020-10802 R. Sandia National Laboratories, Albuquerque, NM.

Swiler, L., Basurto, E., Brooks, D., Eckert, A., Leone, R., Mariner P., Portone, T., Smith, M., Stein, E. (2021), Uncertainty and Sensitivity Analysis Methods and Applications in the GDSA Framework (FY2021). SAND2021-9903R.

TPC (Taiwan Power Company). (2017). *The Technical Feasibility Assessment Report on Spent Nuclear Fuel Final Disposal*. Main Report. Taiwan Power Company, Taipei, Taiwan.

Tsang, C. F., Bernier, F., & Davies, C. (2005). Geohydromechanical processes in the Excavation Damaged Zone in crystalline rock, rock salt, and indurated and plastic clays—in the context of radioactive waste disposal. *International Journal of Rock Mechanics and Mining Sciences*, *42*(1), 109–125. https://doi.org/10.1016/j.ijrmms.2004.08.003

van Loon, L. R., & Mibus, J. (2015). A modified version of Archie's law to estimate effective diffusion coefficients of radionuclides in argillaceous rocks and its application in safety analysis studies. *Applied Geochemistry*, *59*, 85–94. https://doi.org/10.1016/j.apgeochem.2015.04.002

Vaughn, P., Sevougian, S. D., Hardin, E. L., Mariner, P. E., and Gross, M. B. (2013). *Reference Case for Generic Disposal of HLW and SNF in Salt, in Proceedings of the 2013 International High-Level Radioactive Waste Management Conference*, Albuquerque, NM, April 28 – May 2, 2013, American Nuclear Society, La Grange Park, Illinois. (www.ans.org).

Wang, M., Chen, Y. F., Zhou, S., Hu, R., & Zhou, C. B. (2015). A homogenization-based model for the effective thermal conductivity of bentonite–sand-based buffer material. *International Communications in Heat and Mass Transfer*, *68*, 43–49. https://doi.org/10.1016/j.icheatmasstransfer.2015.08.007

Westinghouse. (2012). AP1000 Design Control Document, Rev 16, Tier 2 Chapter 4 -Reactor. https://www.nrc.gov/docs/ML0715/ML071580895.pdf . Accessed 8/19/22

Whitmarsh, C L. (1962). *Revie of Zircaloy-2 and Zircaloy-4 Properties Relevant to N.S. Savannah Reactor Design*. ORNL-3281, United States: N. p., 1962. Web. doi:10.2172/4827123.

Wieselquist, W.A., Lefebvre, R.A., and Matthew, J.A. (2020). *SCALE Code System*. ORNL/TM-2005/39. United States: N. p., 2020. Web. doi:10.2172/1616812.

Winter, T., Harvey, J., Franke, O., and William, A. (1998). *Ground water and surface water: a single resource*. U.S. Geological Survey Circular 1139. 87 p.

Wieselquist, W. A., Lefebvre, R. A., and Jessee, M. A. Eds. (2020). *SCALE Code System*, ORNL/TM-2005/39, Version 6.2.4, Oak Ridge National Laboratory, Oak Ridge, TN.

Zheng, J., Zheng, L., Liu, H. H., & Ju, Y. (2015). Relationships between permeability, porosity and effective stress for low-permeability sedimentary rock. *International Journal of Rock Mechanics and Mining Sciences*, *78*, 304–318. https://doi.org/10.1016/j.ijrmms.2015.04.025

Zheng, L., Rutqvist, J., Xu, H., & Birkholzer, J. T. (2017). Coupled THMC models for bentonite in an argillite repository for nuclear waste: Illitization and its effect on swelling stress under high temperature. *Engineering Geology*, *230*, 118–129. https://doi.org/10.1016/j.enggeo.2017.10.002

This page intentionally left blank.

Appendix A

DPC Calculations from ORNL

The text below shows the report from ORNL on ORIGEN calculations they conducted for us.

PWR Decay Heat

SCALE 6.2 (Wieselquist et al., 2020) is used to calculate decay heat PWR 17x17 spent fuel. Isotopic composition is provided for selected cooling times.

Introduction

For these calculations, pre-generated ARP libraries provided with the SCALE 6.2 distribution are used. The SCALE 6.2 ARP module creates burnup-dependent ORIGEN cross-section libraries by interpolating over reactor cross-section libraries generated in advance using reactor physics transport methods. The reactor cross-section libraries distributed in SCALE include Westinghouse 17×17 commercial power reactor design and a range of fuel assembly depletion parameters. Using the above-mentioned libraries, the ORIGAMI module of SCALE 6.2 was used to perform ORIGEN calculations in order to represent the isotopic distribution of fuel within an assembly in more detail. This approach provides an efficient mechanism to perform standalone reactor depletion calculations using pre-generated ORIGEN libraries which contain self-shielded, collapsed one-group cross sections as a function of selected independent variables such as burnup, enrichment, and moderator density.

Input Data

Table A-1 provides a summary of input data used to develop the ORIGAMI input files. The fuel dimensions are from Radulescu (2021). A bounding uranium weight is selected based on Radulescu (2021). The cladding composition is from (Whitmarsh, 1962). Cladding weights are calculated based on fuel rod dimensions and are shown in Table 6-4. Burnups are selected to represent the typical discharge burnup range and enrichments are selected as lower bounds expected for the corresponding enrichments. The list of selected burnups and enrichments is provided in Table 6-4. Cooling time steps progressively become larger for longer times to capture decay heat over time with smaller time steps shortly after discharge and longer time steps later after discharge. The cooling time steps are summarized in Table A-2.

Table A-1. Fuel Assembly Input parameters

WE 17 × 17		
Active length (cm)	365.76	
Number of Fuel Rods	264	
Clad ID	0.8357	
Clad OD (cm)	0.9500	
Density (g/cm3)	6.5500	
Clad Mass (kg)	101.3833	
MTU	0.4692	
Clad Weight (kg/mtu)	216.0770	
Clad Material	Zirc4	
Specific Power (mw/mtu)	40.58	
Cladding Composition	**%**	**kg/mtu**
Sn	1.7	3.6733
Fe	0.18	0.3889
Cr	0.15	0.3241
Zr	97.97	211.6907

Table A-2. Cooling time steps as a function of cooling time

Cooling Time (years)	Cooling Time Step (years)
0-10	0.5
10-60	1
60-90	2
100-140	5
140-170	10
170-200	30

Input files

An example ORIGAMI input file is shown in Table A-3. Library “w17x17” represents Westinghouse 17x17 library per Table 5.3.1 of the SCALE manual (Wieselquist et al., 2020). The fuel mixture is defined as 100% UO2 fuel with a U-235 enrichment of 3 wt %. Enrichment is adjusted for each ORIGAMI calculation. Heavy metal mass is set per Table A-1. Non-fuel composition is set per Table 6-4 and is entered per metric ton of uranium, therefore fracnf is not required in the options block. Specific power is set per Table A-1 and the burn value is calculated based on burnup and specific power as (45000 MWdays/MTU) / (40.58 MW/MTU) = 1108.92 days. This value is adjusted for each ORIGAMI calculation. Decay cycles (power=0) are then listed with required cooling time steps in days. Some lines are omitted for brevity. Finally, for each calculation, the data are requested in terms of grams and decay heat for each nuclide.

Results

The ORIGAMI output files are postprocessed using a Python script. The isotopic composition is provided for fuel with a cooling time of 55 years. Note that only isotopes with concentrations above 1 gram are listed. Decay heat is provided for all time steps listed in Table A-2. The format of the file is CSV (comma-separated-values) which can be imported to other programs. For a preview the files can be opened in Excel or a text editor (Notepad). The file formats are described in Table A-4 and Table A-5.

Table A-3. Example ORIGAMI input file

```
=origami
title='Westinghouse 17x17 45000 GWD/MTU 3.0 wt%'
libs=[ w17x17 ]
fuelcomp{
   uox(fuel){ enrich = 3.0 }
   mix(1){ comps[fuel=100] }
}
options{ mtu=0.469 ft71=all output=cycle}

nonfuel=[zr=211.69 sn=3.673 fe=0.3889 cr=0.3241]
hist[
cycle{ power=40.58 burn=1108.92 nlib=4 down=0 }
cycle{ power=0 burn=0  down=182.5}
(lines omitted)
cycle{ power=0 burn=0  down=182.5}
cycle{ power=0 burn=0  down=365}
(lines omitted)
cycle{ power=0 burn=0  down=365}
cycle{ power=0 burn=0  down=730}
(lines omitted)
cycle{ power=0 burn=0  down=730}
cycle{ power=0 burn=0  down=1825}
(lines omitted)
cycle{ power=0 burn=0  down=1825}
cycle{ power=0 burn=0  down=3650}
(lines omitted)
cycle{ power=0 burn=0  down=3650}
cycle{ power=0 burn=0  down=10950}
]
print{ nuc {
units=[grams watts] }
}
end
```

Table A-4. Output Files Format. File: decay_heat.csv – contains decay heat data for 0 to 200 years. The file has a header of 5 lines. The lines contain the variable name in the first column followed by 5 columns of input data. Line 6 is the header for decay heat results. Line 7 and below are results, again in 6 columns where the first column is the decay time in years and columns 2-6 are results in Watts for each corresponding header column. The start of the file is shown.

Fuel Type	**WE17**	**WE17**	**WE17**	**WE17**	**WE17**
Enrichment (wt.%)	3	3.2	3.5	3.8	4.1
Burnup (GWD/MTU)	45000	50000	55000	60000	65000
Specific Power (W/kg)	40.58	40.58	40.58	40.58	40.58
Uranium Weight (MTU)	0.4692	0.4692	0.4692	0.4692	0.4692
Cooling Time (years)	**Decay Heat (W)**				
0	1149500	1148800	1149000	1149100	1149200
0.5	10896	11494	12025	12531	13018
1	6562.6	7039.1	7462.1	7871.1	8268.8

Table A-5. File: isotopes.csv – contains isotopic composition for 55 years cooled fuel. The file has a header of 6 lines. The lines contain the variable name in the first column followed by 5 columns of input data. Line 7 is the header for isotopic composition results. Lines 8 and beyond are results, again in 6 columns where the first column is the isotope name and columns 2-6 are results in grams of isotope for each header column. The start of the file is shown.

Fuel Type	**WE17**	**WE17**	**WE17**	**WE17**	**WE17**
Enrichment (wt.%)	3	3.2	3.5	3.8	4.1
Burnup (GWD/MTU)	45000	50000	55000	60000	65000
Specific Power (W/kg)	40.58	40.58	40.58	40.58	40.58
Cooling Time (years)	55	55	55	55	55
Uranium Weight (MTU)	0.4692	0.4692	0.4692	0.4692	0.4692
Isotope	**Weight (grams)**				
He-4 (g)	5.591	6.5348	7.4531	8.4202	9.4325
C-13 (g)	5.2382	5.8515	6.4143	6.9802	7.549
O-16 (g)	62890	62891	62893	62894	62896